



# LUND UNIVERSITY

## Swelling and Microstructure of Nanoplatelet Systems

Thuresson, Axel

2017

[Link to publication](#)

*Citation for published version (APA):*

Thuresson, A. (2017). *Swelling and Microstructure of Nanoplatelet Systems*. Lund University, Faculty of Science, Department of Chemistry, Theoretical Chemistry.

*Total number of authors:*

1

### General rights

Unless other specific re-use rights are stated the following general rights apply:

Copyright and moral rights for the publications made accessible in the public portal are retained by the authors and/or other copyright owners and it is a condition of accessing publications that users recognise and abide by the legal requirements associated with these rights.

- Users may download and print one copy of any publication from the public portal for the purpose of private study or research.
- You may not further distribute the material or use it for any profit-making activity or commercial gain
- You may freely distribute the URL identifying the publication in the public portal

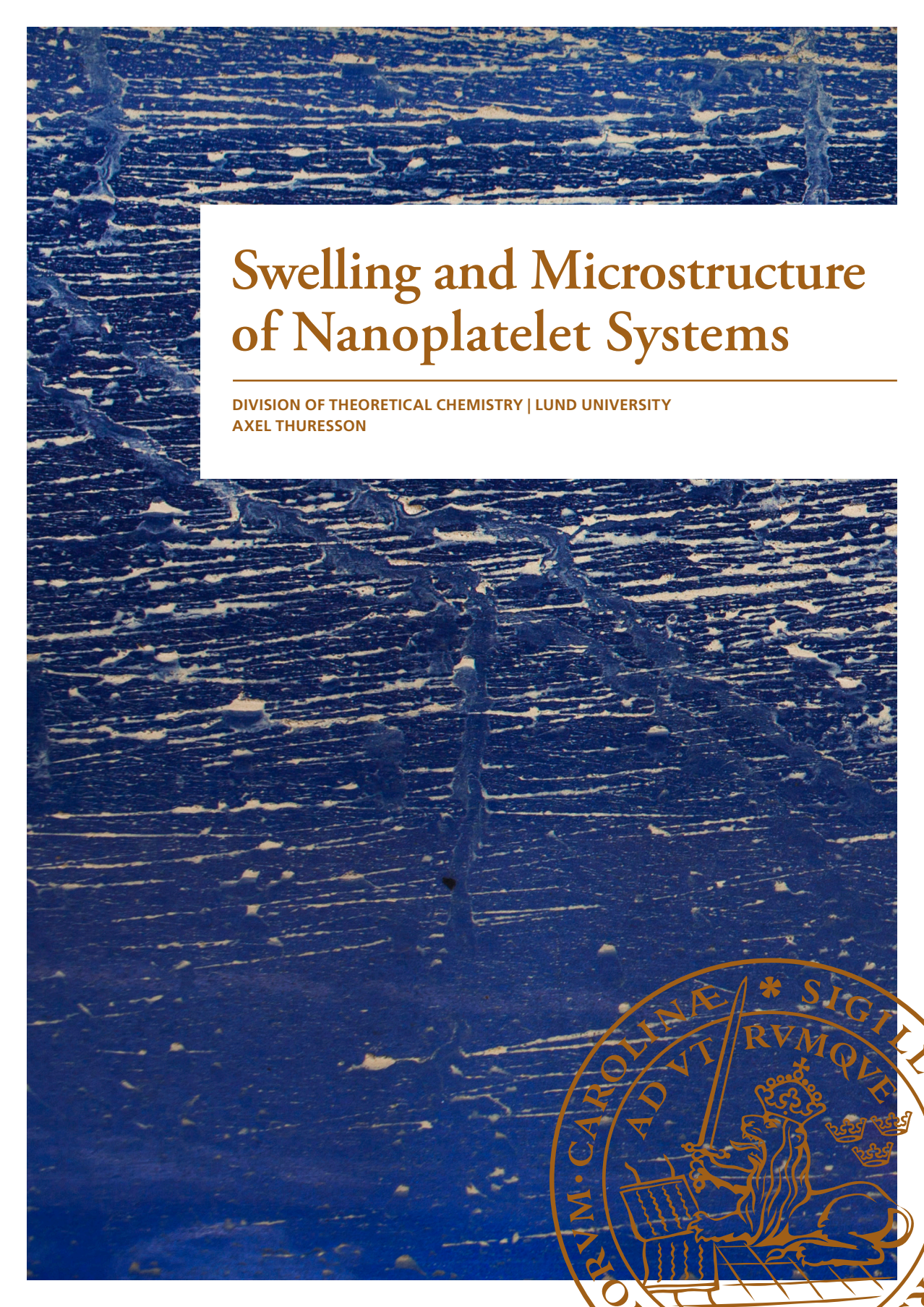
Read more about Creative commons licenses: <https://creativecommons.org/licenses/>

### Take down policy

If you believe that this document breaches copyright please contact us providing details, and we will remove access to the work immediately and investigate your claim.

LUND UNIVERSITY

PO Box 117  
221 00 Lund  
+46 46-222 00 00



# Swelling and Microstructure of Nanoplatelet Systems

DIVISION OF THEORETICAL CHEMISTRY | LUND UNIVERSITY  
AXEL THURESSON





# Swelling and Microstructure of Nanoplatelet Systems

Axel Thuresson

Division of Theoretical Chemistry  
Lund University, Sweden



**LUND**  
UNIVERSITY

Doctoral Thesis

The faculty opponent is Prof. Jon Otto Fossum, Norwegian University of  
Science and Technology

This thesis will be publicly defended on 2nd of June 2017, at 10.15, in lecture hall C of  
the Center for Chemistry and Chemical Engineering (Kemicentrum), Lund.

Organization <b>LUND UNIVERSITY</b> Center for Chemistry and Chemical Engineering P. O. Box 124 SE-221 00 LUND Sweden		Document name <b>DOCTORAL DISSERTATION</b>	
Author(s) Axel Thuresson		Date of disputation 2017-06-02	
		Sponsoring organization eSSENCE, the Swedish national strategic e-science research program.	
Title and subtitle Swelling and Microstructure of Nanoplatelet Systems			
Abstract <p>Many clay minerals consist of charged nanoplatelets that swell in an aqueous solution. The swelling and the microstructure depend on the type of clay mineral but are also dependent on, for example, the ionic composition and the temperature of the solution. The synthetic clay mineral Laponite and the natural clay mineral montmorillonite have been studied experimentally and theoretically. The swelling has been studied by swelling pressure measurements in a test cell and the microstructure has been studied by small angle X-ray scattering (SAXS), and cryogenic transmission electron microscopy (cryo-TEM). Theoretically, Metropolis Monte Carlo (MC) simulations and molecular dynamics (MD) simulations were used to study the electrostatic interactions between the platelets and an adsorbing polymer was also included. Coarse-grained models have been used to represent the platelets, the ions, and the polymers. This thesis can be divided into three parts:</p> <p>In the first part, the tactoid formation (platelets aggregating face-to-face with an equidistant separation) and the microstructure of negatively charged platelets were investigated by simulations. Tactoid formation was promoted by increasing the platelet surface charge density, the platelet size, the ion valency, and the salt concentration. With enough added salt, an isodesmic model was suggested that gives a monotonically decaying distribution of aggregation numbers.</p> <p>In the second part, the tactoid formation and the microstructure were investigated with respect to the platelet size for flocculated Laponite and montmorillonite at elevated salt concentrations, with and without the addition of the polymer polyethylene glycol (PEG). The smaller Laponite platelets give rise to a more disordered microstructure compared to the larger montmorillonite platelets. The number of platelets per tactoid increased with the addition of PEG. The simulations suggested that the role of the salt is to screen the repulsive interactions between the platelets, and the role of the polymer is to bridge between the platelets.</p> <p>In the third part, the temperature response of Na/Ca montmorillonite was investigated. It was found that the swelling pressure increased with increased temperature if sodium is the dominating counterion whereas the opposite was found if calcium is the dominating counterion. The simulations predicted this behavior and it was shown that the results could be explained by a single equation.</p>			
Key words Nanoplatelets, Model clay system, Coarse grained models, Statistical mechanics, MC simulations, MD simulations, SAXS, Cryo-TEM, Laponite, Montmorillonite, Swelling, Tactoid			
Classification system and/or index terms (if any)			
Supplementary bibliographical information		Language English	
ISSN and key title		ISBN 978-91-7422-522-8 (print) 978-91-7422-523-5 (pdf)	
Recipient's notes		Number of pages 130	Price
		Security classification	

I, the undersigned, being the copyright owner of the abstract of the above-mentioned dissertation, hereby grant to all reference sources the permission to publish and disseminate the abstract of the above-mentioned dissertation.

Signature



Date April 24, 2017

# Swelling and Microstructure of Nanoplatelet Systems

Axel Thuresson

Division of Theoretical Chemistry  
Lund University, Sweden



**LUND**  
UNIVERSITY

**Cover illustration front:** "Mood Splash Texture", taken from [wildtextures.com](http://wildtextures.com)

**Funding information:** eSSENCE, the Swedish national strategic e-science research program.

© Axel Thuresson 2017

Faculty of Science, Center for Chemistry and Chemical Engineering

ISBN: 978-91-7422-522-8 (print)

ISBN: 978-91-7422-523-5 (pdf)

Printed in Sweden by Media-Tryck, Lund University, Lund 2017



Media-Tryck is an environmentally certified and ISO 14001 certified provider of printed material. Read more about our environmental work at [www.mediatryck.lu.se](http://www.mediatryck.lu.se)

MADE IN SWEDEN 

*Till Narda, Leonardo  
och mina föräldrar*



# Contents

List of publications . . . . .	iii
Acknowledgements . . . . .	v
Populärvetenskaplig sammanfattning . . . . .	vi
<b>Swelling and Microstructure of Nanoplatelet Systems</b>	<b>I</b>
1 Introduction . . . . .	1
1.1 Clays and clay minerals . . . . .	2
1.1.1 Montmorillonite . . . . .	3
1.1.2 Laponite . . . . .	5
1.2 Polymer-clay composites . . . . .	5
1.2.1 Polyethylene oxide . . . . .	7
2 Experimental . . . . .	7
2.1 Purification and ionic exchange of bentonite clay . . . . .	7
2.2 Small angle X-ray scattering . . . . .	8
2.3 Cryo-TEM . . . . .	10
2.4 Free swelling in dialysis pocket . . . . .	11
2.5 Swelling pressure in a test cell . . . . .	12
3 Theoretical . . . . .	14
3.1 Statistical mechanics and thermodynamics . . . . .	14
3.1.1 Statistical thermodynamics . . . . .	15
3.1.2 Classical statistical mechanics . . . . .	17
3.2 Intermolecular interactions . . . . .	17
3.2.1 Coulomb interactions . . . . .	18
3.2.2 Poisson-Boltzmann equation . . . . .	18
3.2.3 From weak coupling to strong coupling . . . . .	20
3.2.4 Short-ranged interactions . . . . .	24
3.2.5 Effective pair potentials . . . . .	26
3.3 Coarse-grained modeling . . . . .	27
3.3.1 Clay platelets and ions . . . . .	27
3.3.2 Polyethylene oxide . . . . .	29
3.4 Monte Carlo simulations . . . . .	30
3.4.1 Metropolis method . . . . .	31

	3.4.2	Trial moves . . . . .	32
	3.5	Molecular dynamics simulations . . . . .	33
	3.6	Simulation techniques . . . . .	35
	3.6.1	Boundary conditions . . . . .	35
4		Main Results of the Research Papers . . . . .	36
	4.1	Paper I: Monte Carlo Simulations of Parallel Charged Platelets as an Approach to Tactoid Formation in Clay. . . . .	37
	4.2	Paper II: Interaction and Aggregation of Charged Platelets in Electrolyte Solutions: A Coarse-Graining Approach. . . . .	38
	4.3	Paper III: Flocculated Laponite-PEG/PEO Dispersions with Monovalent Salt, a SAXS and Simulation Study. . . . .	39
	4.4	Paper IV: Flocculated Laponite-PEG/PEO Dispersions with Multivalent Salt: A SAXS, Cryo-TEM, and Computer Simulation Study. . . . .	40
	4.5	Paper v: Anomalous Temperature Behavior in Clay Swelling due to Ion-Ion Correlations. . . . .	41
	4.6	Paper VI: Temperature Response of Charged Colloidal Particles by Mixing Counterions Utilizing $\text{Ca}^{2+}/\text{Na}^{+}$ Montmorillonite as Model System. . . . .	41
5		Conclusions and Future Perspectives . . . . .	42
6		References . . . . .	44
<b>Scientific Publications</b>			<b>47</b>
	Author Contributions . . . . .		47
	Paper I: Monte Carlo Simulations of Parallel Charged Platelets as an Approach to Tactoid Formation in Clay. . . . .		47
	Paper II: Interaction and Aggregation of Charged Platelets in Electrolyte Solutions: A Coarse-Graining Approach. . . . .		47
	Paper III: Flocculated Laponite-PEG/PEO Dispersions with Monovalent Salt, a SAXS and Simulation Study. . . . .		47
	Paper IV: Flocculated Laponite-PEG/PEO Dispersions with Multivalent Salt: A SAXS, Cryo-TEM, and Computer Simulation Study. . . . .		48
	Paper v: Anomalous Temperature Behavior in Clay Swelling due to Ion-Ion Correlations. . . . .		48
	Paper VI: Temperature Response of Charged Colloidal Particles by Mixing Counterions Utilizing $\text{Ca}^{2+}/\text{Na}^{+}$ Montmorillonite as Model System. . . . .		48

## List of publications

This thesis is based on the following publications, referred to by their Roman numerals:

- I **Monte Carlo Simulations of Parallel Charged Platelets as an Approach to Tactoid Formation in Clay.**  
A. Thuresson, M. Ullner, T. Åkesson, C. Labbez and B. Jönsson  
Langmuir, 2013, 29, pp. 9216–9223
- II **Interaction and Aggregation of Charged Platelets in Electrolyte Solutions: A Coarse-Graining Approach.**  
A. Thuresson, M. Ullner and M. Turesson  
Journal of Physical Chemistry B, 2014, 118, pp. 7405–7413
- III **Flocculated Laponite-PEG/PEO Dispersions with Monovalent Salt, a SAXS and Simulation Study.**  
A. Thuresson, M. Segad, M. Turesson and M. Skepö  
Journal of Colloid and Interface Science, 2016, 466, pp. 330–342
- IV **Flocculated Laponite-PEG/PEO Dispersions with Multivalent Salt: A SAXS, Cryo-TEM, and Computer Simulation Study.**  
A. Thuresson, M. Segad, T. S. Plivelic and M. Skepö  
Journal of Physical Chemistry C, 2017, 121, pp. 7387–7396
- V **Anomalous Temperature Behavior in Clay Swelling due to Ion-Ion Correlations.**  
A. Thuresson, O. Karnland and B. Jönsson  
Europhysics Letters, 2016, 114, pp. 38002
- VI **Temperature Response of Charged Colloidal Particles by Mixing Counterions Utilizing  $\text{Ca}^{2+}/\text{Na}^{+}$  Montmorillonite as Model System.**  
A. Thuresson, M. Jansson, T. S. Plivelic and M. Skepö  
Journal of Physical Chemistry C, 2017, 121, pp. 7951–7958

All papers are reproduced with permission of their respective publishers.

Publications not included in this thesis:

**Faunus—a Flexible Framework for Monte Carlo Simulation.**

B. Stenqvist, A. **Thuresson**, A. Kurut, R. Vácha and M. Lund  
Molecular Simulation, 2013, 39, pp. 1233–1239

**Dielectric Response from Lattices of Dipoles with Fixed Orientation.**

A. **Thuresson** and G. Karlström  
The Journal of Chemical Physics, 2014, 141, pp. 234505

**Slow-Light-Based Optical Frequency Shifter.**

Q. Li, Y. Bao, A. **Thuresson**, A. N. Nilsson, L. Rippe and S. Kröll  
Physical Review A, 2016, 93, pp. 043832

**Using Electric Fields for Pulse Compression and Group Velocity Control.**

Q. Li, A. Kinos, A. **Thuresson**, L. Rippe and S. Kröll  
Physical Review A, 2017, 95, pp. 032104

**Aggregation Behavior of Aqueous Cellulose Nanocrystals: The Effect of Inorganic Salts.**

T. Phan-Xuan, A. **Thuresson**, M. Skepö, A. Labrador, R. Bordes and A. Matic  
Cellulose, 2016, 23, pp. 3653–3663

## Acknowledgements

Many years have past since I started working at Theoretical Chemistry. I have had the opportunity to collaborate with a lot of people that have been supporting me during different periods of my PhD studies. I would like to mention the persons that I think helped me the most.

Marie Skepö, thanks for the endless support, guidance and for your positive attitude towards everything in life.

Magnus Ullner, thanks for giving me the chance to become a PhD student, for helping me whenever I got stuck with theory and always corrected my bad English.

Bo Jönsson, thanks for sharing your wisdom and always being patient with me.

Torbjörn Åkesson, thanks for all fruitful discussions that we had, I really enjoyed discussing with you.

Ola Karlund, thanks for always having time for interesting discussions and for allowing me to work in the lab at Clay Technology.

Thanks to everyone who helped me at Clay Technology.

Martin Turesson, thanks for your supervision back in the days and for introducing me to Gromacs.

Maria Jansson, thanks for allowing me to be your co-supervisor during your master project, I really enjoyed it.

Thanks to Mo Segad and Tomás Plivelic for your experimental expertizes and thanks to Christophe Labbez for your interesting ideas for the simulations.

To all former/current PhD students and post docs, thanks for all the great moments at the teokem Thursdays with games and pizza.

Finally, thanks to my family and friends for all support through these years.

## Populärvetenskaplig sammanfattning

De flesta anser nog att kemi och speciellt teoretisk kemi är ett mycket komplext ämne, medan lera nog anses som ett begripligt koncept. Det man kanske inte tänker på är att många leror utgörs till stor del av elektrostatiskt laddade nanopartiklar där dess beteende kan förstås genom just ämnena kemi och teoretisk kemi. De laddade nanopartiklarna, även kallade lerplattor, är formade som tunna pannkakor och har en tjocklek som är en miljardels meter. Diametern kan variera och är mellan fem till tusen gånger större än tjockleken. Detta kan jämföras med ett A4-ark där kortsidan är två tusen gånger större än tjockleken.

Lera har en otrolig mängd tillämpningar, exempelvis vid kärnavfallshantering, papperstillverkning, och vid borrning efter gas och olja. Sverige planerar att slutförvara det farliga radioaktiva avfallet från de svenska kärnkraftverken i kopparkapslar som sedan bäddas in i bentonitlera 500 m under marken. Bentonitlera utgörs till stor del av lerplattor som är av lermineralen montmorillonit. Tanken är att bentonitleran ska skydda kopparkapseln både fysiskt och kemiskt under väldigt lång tid (upp till en miljon år) tills det anses vara ofarligt för människan. Eftersom grundvattnets innehåll och temperaturen varierar över tiden är det viktigt att utvärdera lerans egenskaper, för att få en förståelse kring hur och varför den beter sig som den gör.

Lera används också som fyllnadsämne vid papperstillverkning för att öka papprets vithet och ogenomskinlighet. Bentonitlera tillsätts till vatten i vissa fall vid borrning efter gas och olja, delvis för att smörja och kyla borren, men även p.g.a. att leran är tixotrop (låg viskositet vid rörelse och hög viskositet vid upphörd rörelse). När man slutar pumpa upp det material man vill avlägsna ifrån borrhålet så stelnar leran vilket förhindrar stenar att falla till botten av borrhålet. Däremot vill man inte att leran som finns nere i marken ska lösas upp och svälla för mycket när man borrar eftersom det kan minska borrhastigheten. Därför tillsätter man andra material för att förhindra denna process. Därmed är det viktigt att förstå varför och hur dessa material interagerar med leran.

De lermineraller som har undersökts i denna avhandling sväller när man lägger dem i vatten. Svällningen beror på typen av lera men är också beroende på t.ex. vilken surhetsgrad, typ av salt, salthalt, och temperatur. Det är effekten av de tre senare som har undersökts i denna avhandling i olika sammanhang. För att få en så bra förståelse som möjligt har experiment och datorsimuleringar kombinerats. De experimentella tekniker som använts är lågvinkel röntgenspridning (SAXS), elektronmikroskopi (cryo-TEM), och svälltrycksmätningar. Eftersom lerplattorna inte kan ses med blotta ögat så har SAXS och cryo-TEM använts för att få en inblick i hur lerplattorna växelverkar samt hur de organiserar sig i förhållande till varandra, dvs. man studerar mikrostrukturen hos lerplattorna. Svälltrycksmätningar används för att mäta det osmotiska trycket en lera ger

upphov till för en given volymsfraktion och genom att göra dessa mätningar så får man en uppfattning om vilka krafter som finns i systemet. Datorsimuleringar har använts för att försöka förutsäga och förstå de mekanismer som ger leran dess egenskaper. Den här avhandlingen är indelad i tre studier:

Den första studien fokuserar på datorsimuleringar där effekten av lerplattornas laddning, storlek och flexibilitet samt typ av salt och dess koncentration påverkar hur lerplattorna aggregerar till en större partikel, s.k. taktoid. En taktoid kan ses som en bunt pappersark.

Den andra delen handlar om hur den syntetiska lermineralen Laponit skiljer sig mot montmorillonit vid hög saltkoncentration. Laponitplattorna har en mycket mindre diameter än montmorillonitplattorna vilket ger upphov till en mer oordnad mikrostruktur för Laponit. SAXS och cryo-TEM mätningar visade att mikrostrukturen blev mer ordnad då man tillsatte en polymer. Med hjälp av datorsimuleringar så föreslogs en bryggningmekanism, dvs. polymeren drar ihop plattorna och skapar en extra attraktion i systemet vilket ger upphov till större taktoider och en mer ordnad mikrostruktur.

I den tredje och sista delen av avhandlingen undersöktes temperaturresponsen hos montmorillonit med hjälp av svälltrycksmätningar och SAXS. När de negativt laddade lerplattorna kompenseras av natriumjoner ökar trycket med ökad temperatur. Om natriumjonerna byts ut mot kalciumjoner minskar trycket med ökad temperatur. Simuleringarna kunde förklara de experimentella resultaten och det visade sig att mekanismen kan förstås endast genom en enda ekvation.



# Swelling and Microstructure of Nanoplatelet Systems

## I Introduction

Particles within the size range of about 1 nm to 1  $\mu\text{m}$  are usually denoted as colloidal particles. A colloidal dispersion is a system where particles of colloidal size are dispersed in another phase. In a colloidal dispersion, the particles must be evenly distributed, hence the force between the particles is repulsive (the particles push each other apart). On the other hand, if the force is attractive, the particles might flocculate (the particles aggregate and form flocs), which eventually leads to a phase separation between the dispersion medium and the colloids. When a charged colloidal particle is dissolved in an aqueous or polar solvent, the counterions will be released and form an electrical double layer. The first layer is the charged surface of the colloid, and the second layer is the counterions that screen the first layer. When two charged colloids approach each other, their double layers will overlap, which leads to a repulsive force due to the confinement (entropic loss) of the counterions. If salt is introduced into the system, the repulsion is effectively screened (reduced) between the colloids. At high enough salt concentration, the repulsion is reduced enough such that the attractive short-ranged van der Waals forces dominate, which leads to flocculation of the particles. On the other hand, if the counterions are multivalent and the colloids are highly charged, a short-ranged attractive interaction can appear due to electrostatic ion-ion correlation interactions, which also could lead to the same phenomena, i.e., flocculation. The properties of many clay minerals (e.g. montmorillonite and Laponite) are well described, at least in a qualitative sense, with the above mentioned mechanisms.

## 1.1 Clays and clay minerals

Clay science is an old and multidisciplinary field and to date there is no uniform nomenclature for the terms clay and clay mineral. Before the modern analytical techniques were available to characterize the material, there were difficulties to characterize the small-sized particles that contain various degrees of crystal imperfection, which led to problems with the nomenclature. Since the 1950s, attempts have been made on an international level to unify the nomenclature (Bailey (1980)). One definition of a clay is: a naturally occurring material composed primarily of fine-grained minerals (the upper size of a clay is chosen to about 2-4  $\mu\text{m}$ ), which is generally plastic at appropriate water contents, and will harden when dried or fired. A clay mineral can be defined as: phyllosilicate minerals and minerals which impart plasticity to clay and which harden upon drying or firing (Guggenheim & Martin (1995)).

The family of phyllosilicates (or silicate layers) that represents clay minerals has a tetrahedral sheet of composition  $X_2O_5$  (where X is commonly  $\text{Si}^{4+}$ ,  $\text{Al}^{3+}$ , or  $\text{Fe}^{3+}$ ) linked to an octahedral sheet that usually consists of groups of coordinated cations, or individual cations (Bailey (1980)). Clay minerals are divided into two main types, 1:1 (TO) and 2:1 (TOT). The 1:1 layer is about 0.7 nm thick and consists of a tetrahedral sheet and an octahedral sheet. An example of a 1:1 clay mineral is kaolinite with ideal chemical formula  $\text{Al}_2\text{Si}_2\text{O}_5(\text{OH})_4$ . A schematic picture of the structure can be seen in Fig. 1.

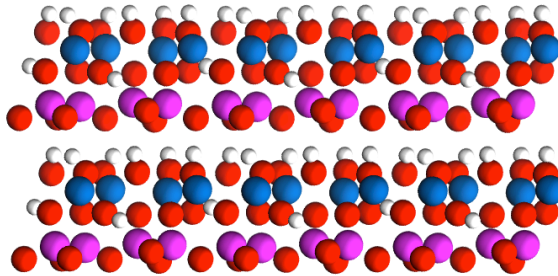


**Figure 1:** Schematic picture of two kaolinite layers. Aluminum and silicon are represented as blue and purple spheres, respectively. Oxygen and hydrogen are represented as red and white spheres, respectively.

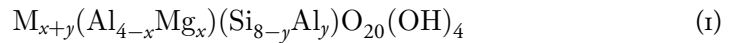
Kaolinite is a non-swelling clay mineral due to the strong attraction between adjacent layers, i.e., hydrogen bonding between the OH groups of the octahedral sheet and the oxygens of the tetrahedral sheet (Grim (1953)). Moreover, kaolinite is dioctahedral since there are two trivalent cations in the octahedral sheet. The alternative is to have three divalent cations and the structure is then denoted as trioctahedral. The 2:1 layer, denoted

as clay *platelet*, is about 1 nm thick and consists of two tetrahedral sheets sandwiching a central octahedral sheet. One of the most important features of a 2:1 clay mineral is the permanent surface charge density. The origin of the latter arises from: (i) substitution of  $\text{Si}^{4+}$  by  $\text{Al}^{3+}$  in the tetrahedral sheet; (ii) substitution of  $\text{Al}^{3+}$  or  $\text{Mg}^{2+}$  by lower charge cations in the octahedral sheet, or (iii) vacancies. To maintain electroneutrality, exchangeable counterions are located between the platelets. Hydroxyl groups are located at the broken edges of the clay platelets, which can have a positive, negative, or neutral charge depending on the pH (Bergaya et al. (2006)).

Several configurations of the clay platelets in a clay have been proposed due to the interplay between the negative surface charge and positively charged edges such as the *House-of-Cards* configuration, where the adjacent platelets are in a T configuration, and the *Overlapping Coins* configuration, where band-like structures are formed (Delhomme et al. (2012)).

### 1.1.1 Montmorillonite

Montmorillonite is an example of a natural dioctahedral 2:1 clay mineral with the ideal chemical formula (Karnland et al. (2006)):



where M is a monovalent counterion,  $x$  is the number of  $\text{Al}^{3+}$  ions in the octahedral sheet substituted by  $\text{Mg}^{2+}$ , and  $y$  is the number of  $\text{Si}^{4+}$  ions in the tetrahedral sheet substituted by  $\text{Al}^{3+}$ . The surface charge density can vary depending on the substitution parameters  $x$  and  $y$ . A schematic picture of the structure can be seen in Fig. 2.

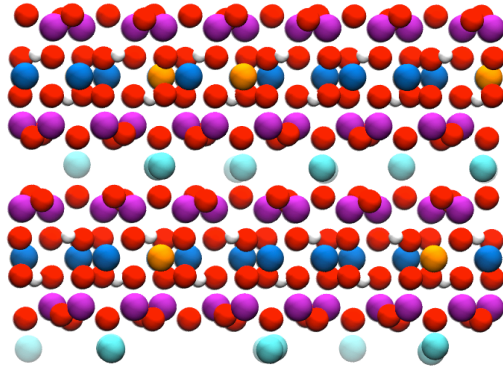


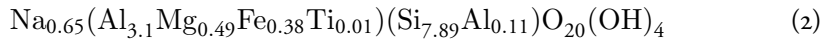
Figure 2: Schematic picture of two montmorillonite layers. Aluminum, magnesium, and silicon are represented as blue, orange, and purple spheres, respectively. Oxygen and hydrogen are represented as red and white spheres, respectively. The counterions are represented as cyan spheres.

The montmorillonite platelets are polydisperse in diameter and are typically found in the range  $\sim 5\text{-}1000$  nm (Michot et al. (2004)). Montmorillonite belongs to the smectite group and the negative charge per  $\text{O}_{20}(\text{OH})_4$ -unit is between 0.4 and 1.2 unit charges ( $0.4 < (x + y) < 1.2$ ). In Eq. (1), the negative charge is neutralized by  $(x + y)$  monovalent counterions, M (e.g.  $\text{K}^+$ ,  $\text{Li}^+$ , and  $\text{Na}^+$ ), although it should be noted that the valency of the counterions can be exchanged. For example, the monovalent counterions can be replaced with multivalent counterions (e.g.  $\text{Ca}^{2+}$ ,  $\text{Mg}^{2+}$ , and  $\text{La}^{3+}$ ) as described in Section 2.1. With multivalent counterions, tactoids are formed, i.e., the clay platelets aggregate in a face-to-face configuration with an equidistant separation of about 2 nm (Michot et al. (2004); Segad et al. (2015)).

The main properties of clay minerals in the smectite group are: (i) high specific surface area, (ii) moderate layer charge, (iii) clay platelets of colloidal size, (iv) high degree of stacking disorder, and (v) clay platelets can dissociate and swell extensively with monovalent counterions (e.g.  $\text{Li}^+$  or  $\text{Na}^+$ ) in water (Bergaya et al. (2006)).

A natural bentonite clay, such as MX-80, has a high content of the clay mineral montmorillonite and the counterions are usually a mixture of monovalent and divalent counterions. The dominating counterion in a natural bentonite is often used to describe the clay since it, to a large extent, determines the swelling property in water. MX-80 is a Wyoming bentonite produced by American Colloid Company. It contains about 80% montmorillonite and is described as a sodium bentonite since sodium is the dominating counterion. Sodium saturated montmorillonite from MX-80 has the chemical formula

(Karnland et al. (2006)):



MX-80 is a candidate for use as a barrier material in the final deposit of highly radioactive spent nuclear fuel. The clay barrier should fulfill the following properties: (i) high swelling capacity to self-seal itself around the canister, (ii) low hydraulic conductivity to minimize any mass transport to and from the canister to avoid corrosion of the canister and, in case a canister breaks, the radioactive material should leak out as slowly as possible, (iii) appropriate plasticity and stiffness to keep the canister in place but also reduce the force from any rock movement, (iv) long-term stability since it will take up to one million years until the radioactive material is harmless to humans, and (v) high thermal conductivity to dissipate the heat from the radioactive material (Svensson (2015); SKB (2011); Karnland et al. (2006)).

### 1.1.2 Laponite

Laponite is a trioctahedral synthetic clay mineral with the ideal chemical formula:



The diameter of Laponite platelets are  $\sim 25$  nm and the thickness  $\sim 1$  nm (BYK (2016)). Hence, the Laponite platelets are much smaller than the montmorillonite platelets where the average diameter has been estimated to  $\sim 250$  nm (Michot et al. (2004)). Laponite is widely used as a rheology-modifier in applications such as paints, household cleaners, and personal products. Laponite is a smectite, and has properties similar to montmorillonite, but the chemical stability of Laponite is rather limited around pH 10. Laponite has been considered to be a model system for investigating several physical mechanisms and its phase diagram has been under debate for more than two decades (Ruzicka & Zaccarelli (2011)). The main reason to use Laponite in this thesis is that the average diameter of the platelets are much smaller than the average diameter of montmorillonite. Thus, the effect of the platelet size can be investigated.

## 1.2 Polymer-clay composites

A polymer is a large molecule composed of many repeating units. DNA and cellulose are examples of natural polymers, whereas polyvinyl chloride (PVC) and polystyrene (PS) are examples of synthetic polymers.

A composite material is defined as a combination of two or more materials that are physically distinct and dispersed in a controlled way to achieve optimum properties,

which are superior to those of the individual components. Polymer-clay composites are typically used to enhance the polymer properties in five areas: mechanical, barrier, flame retardant, electrical, and biodegradable. Schematic pictures of polymers and stacked clay platelets (in a face-to-face configuration) represented as connected beads forming a polymer chain and a set of connected spheres forming a platelet, respectively, can be seen in Figs. 3a-3b. Three types of classifications are used to describe the microstructure as shown in Fig. 3: (c) If the polymer does not enter between the clay platelets the composite is *conventional*, i.e., the spacing between the platelets remain unchanged, (d) if the polymer enters between the clay platelets although the platelets remain stacked the composite is *intercalated*, i.e., the spacing between the platelets is increasing, and (e) if the clay platelets are pushed apart due to the addition of the polymer the composite is *exfoliated*, i.e., the separation between the platelets is large and the structure is disordered (Chen et al. (2008)).

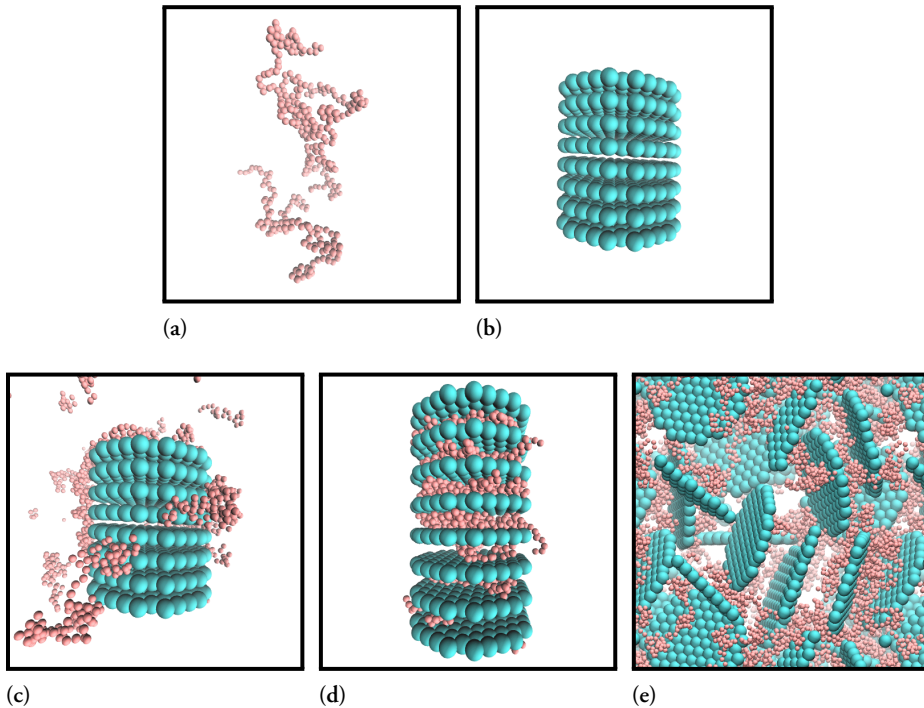


**Figure 3:** Schematic picture of (a) polymers and (b) stacked clay platelets. A polymer is represented as a set of connected red spheres and a platelet is represented as a monolayer of connected cyan spheres. Three classifications that describe the microstructure between polymers and clay platelets. (c) Conventional composites, (d) intercalated composites, and (e) exfoliated composites.

Water-based drilling fluids (WBDF) are being used to a large extent in the exploration for oil and gas wells due to its environmental advantage over oil-based and synthetic-

based fluids. The disadvantage of WBDF compared to oil-based or synthetic-based fluids is the increased clay swelling that can create wellbore instability and consequently leads to an increased production cost. Uncharged polymers, such as polyethylene oxide (PEO), can be used to reduce the clay swelling where the polymer intercalate between the clay platelets (Anderson et al. (2010)).

### 1.2.1 Polyethylene oxide

PEO, also known as polyethylene glycol (PEG), is a synthetic polymer with molecular structure  $\text{HO}-(\text{CH}_2-\text{CH}_2-\text{O})_n-\text{H}$  where the repeating ethylene oxide unit ( $\text{CH}_2-\text{CH}_2-\text{O}$ ) has a molecular weight of 44 g/mol. PEO/PEG is a water-soluble polymer that is widely used in biotechnology and life science industry (Choi et al. (2014)).

In Paper III and Paper IV, PEG was added to Laponite and montmorillonite to investigate the tactoid formation at high salt concentrations.

## 2 Experimental

### 2.1 Purification and ionic exchange of bentonite clay

Two types of raw clays have been used in this thesis. The first, MX-80, is a bentonite from Wyoming, Montana, and/or South Dakota in the USA (see Section 1.1.1); and the second, WB, is clay from Wadi Bashira in Iraq (Segad (2013)). These clays were chosen since they have a natural domination by counterions of different valency, were MX-80 is dominated by sodium ions ( $\text{Na}^+$ ), and WB is dominated by calcium ions ( $\text{Ca}^{2+}$ ).

To purify a raw bentonite clay, it is necessary to remove the majority of the accessory minerals (e.g. quartz, feldspars, gypsum, and calcite). This can be done by dispersing the clay in deionized water to allow the larger particles ( $>2 \mu\text{m}$ ) to sediment (and/or centrifuge to speed up the process) and thereafter recover the supernatant. To perform a cationic exchange, the clay is washed three times by either 1 M NaCl or 0.5 M  $\text{CaCl}_2$  in order to exchange the counterions to either sodium or calcium. To remove the excess salt, the clay suspension is dialyzed in a large volume of deionized water, which is repeatedly replaced until the conductivity is below  $10 \mu\text{S}/\text{cm}$ . MX-80 was purified in Paper IV, Paper V and Paper VI and is named X-montmorillonite where X is either  $\text{Na}^+$  or  $\text{Ca}^{2+}$  depending on the type of counterion of the clay.

## 2.2 Small angle X-ray scattering

Small angle X-ray scattering (SAXS) is a suitable technique to study the microstructure of a sample on the colloidal scale. The information that can be extracted with SAXS is for example the shape of particles as well as the interaction and distances between them. Typical information that can be extracted from clay in water is the size of the platelets, distances between the platelets, size of the aggregates, and fractal dimensions. X-rays are primarily scattered by electrons and the scattered photons will interfere constructively or destructively depending on the different electron densities in the sample. A coherent monochromatic beam of X-rays with wavelength,  $\lambda$ , is sent through a sample with wavevector  $\mathbf{k}_i$ , and the outgoing scattered beam has wavevector  $\mathbf{k}_s$ . The scattering intensity,  $I(q)$ , is recorded on a 2D detector, and is represented as a function of magnitude of the scattering vector  $q$  where  $q = |\mathbf{q}| = |\mathbf{k}_s - \mathbf{k}_i| = 4\pi \sin(\theta)/\lambda$  and  $2\theta$  is the scattering angle (Glatter & Kratky (1982)). A schematic picture is shown in Fig. 4.

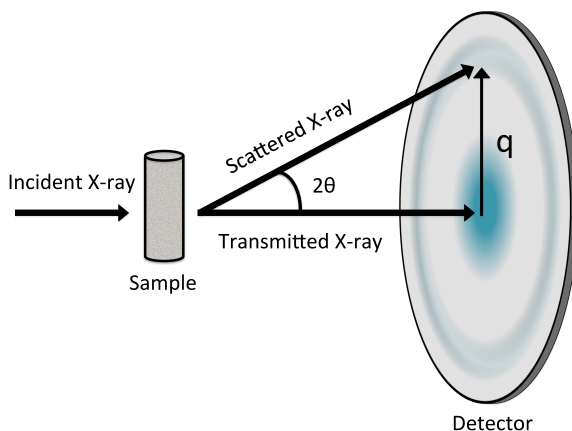


Figure 4: Schematic picture of SAXS. An incident beam is sent through a sample. The scattering angle between the transmitted beam and scattered beam is denoted as  $2\theta$  and the corresponding  $q$ -vector is shown on the 2D detector (given that the scattering angle is small).

For systems composed of spherical particles, the scattering intensity can be decomposed into two separate functions  $I(q) \propto P(q)S(q)$  where  $P(q)$  is the form factor and  $S(q)$  is the structure factor. For dilute samples, the size and shape of the particles can be extracted from the form factor since  $S(q) \approx 1$ , i.e., no structure or negligible intermolecular interactions in the system (Schnablegger & Singh (2013)). Once the form factor is known, the structure factor for more dense samples can be extracted where information about the interaction and the distances between the particles can be extracted. The decomposition of the scattering intensity is an approximation for anisotropic objects such as clay platelets. A more accurate comparison can be done by calculating the *total structure factor* (Gutiérrez & Johansson (2002)) from simulations and compare it

to the experimental scattering intensity. This has been done in Paper III.

Clay platelets that are aggregated in a face-to-face configuration give rise to a Bragg peak due to the periodicity of the system. The distance between the platelets can be found by Bragg's law:  $d = 2\pi/q_{max}$ , where  $q_{max}$  is  $q$  at the maximum of the peak (Schnablegger & Singh (2013)). The full width at half maximum (FWHM) of the Bragg peak is related to the size of the aggregates, i.e., the number of clay platelets per aggregate. The average number of platelets per tactoid,  $\langle N \rangle$ , according to the Scherrer equation (Patterson (1939)) is,

$$\langle N \rangle d = \frac{K\lambda}{\Delta\theta \cos(\theta)} \quad (4)$$

where  $d$  is the spacing between the platelets,  $K \approx 0.9$  is the Scherrer constant,  $\Delta\theta = \theta_2 - \theta_1$  is the FWHM of the Bragg peak between the angles  $\theta_1$  and  $\theta_2$ , and  $2\theta$  is the Bragg angle. For small angles ( $\cos(\theta) \approx 1$ , and  $\sin(\theta) \approx \theta$ ) the FWHM of the Bragg peak is  $\Delta\theta \approx \sin(\theta_2) - \sin(\theta_1)$  and the Scherrer equation can be approximated as,

$$\langle N \rangle \approx \frac{q_{max}}{2\pi(\sin(\theta_2) - \sin(\theta_1))/\lambda} = \frac{q_{max}}{(\Delta q)/2} = \frac{q_{max}}{w} \quad (5)$$

where the Scherrer constant is set to one, and  $\Delta q = 2w$  is the FWHM in units of  $\text{nm}^{-1}$ . The FWHM of the Bragg peak has been estimated by two different methods in this thesis. The first method was to fit a Lorentzian function to the structure factor where it is assumed that it is possible to decompose the scattering intensity, in  $P(q)$  and  $S(q)$ . Moreover, the form factor is assumed to be  $P(q) \propto q^{-2}$ . The fitting occurs between  $q_{max} \pm 0.5 \text{ nm}^{-1}$  (Segad (2013)),

$$q^2 I(q) = A \frac{w}{(q - q_{max})^2 + w^2} + B \quad (6)$$

where A and B are fitting parameters. The second method was to subtract a polynomial function,  $C(q)$ , for the background contribution around the Bragg peak (Mauroy et al. (2013)), and fit the peak to a Lorentzian function:

$$I(q) - C(q) = A \frac{w}{(q - q_{max})^2 + w^2} \quad (7)$$

where A is a fitting parameter. Both methods gave the same result for the montmorillonite samples whereas the second method gave more reasonable results for the Laponite samples. The reason that the second method is more reliable is probably related to the fact that  $C(q)$  can more accurately describe the form factor than the assumption  $P(q) \propto q^{-2}$ . Thus, for platelets with a large aspect ratio (e.g. montmorillonite) and where the peak is relatively narrow, any of the two methods can be used. For platelets with a low aspect ratio (e.g. Laponite) and in the case where the peak is very wide it is important to use a more accurate description.

### 2.3 Cryo-TEM

Cryogenic transmission electron microscopy (cryo-TEM) is a microscopy technique where the size, the shape, and the microstructure of particles on the colloidal scale can be investigated. A description of the technique with many examples of how cryo-TEM has been utilized can be found in the following reference: Almgren et al. (2000). The specimens were prepared as thin liquid films (thinner than 300 nm) on lacey carbon filmed copper grids, and frozen rapidly in order to preserve the microstructure as it was at room temperature. In general, the microstructure of clays can only be studied qualitatively with this technique since it is difficult to prepare a homogeneous thin film. Moreover, in the case of flocculated clays, which are dense, the single platelets could only be distinguished from each other in the parts of the flocs where the particle density was low enough. Sample preparation was done in a CEVS (controlled environment vitrification system), freeze plunged into liquid ethane ( $-180\text{ }^{\circ}\text{C}$ ), and then stored in liquid nitrogen. The microscope used was a Philips CM120 cryo-TEM operated at 120 kV and equipped with a cryo holder (Oxford Instruments CT-3500). Images were recorded with a GIF 100 (Gatan imaging filter). Fig. 5 shows two images where the microstructure of Laponite in 1 M NaCl, with and without PEG20k, can be seen. The thin dark lines are the Laponite platelets that are oriented more or less orthogonal to the film. One pixel corresponds to  $\sim 0.5\text{ nm}$ , and the thickness of the dark lines was found to be approximately two–three pixels; hence, a thickness of two pixels corresponds to the thickness of a single platelet. Some platelets are found in a face-to-face configuration (the platelets form tactoids), as indicated by the red circles. By comparing Fig. 5a and Fig. 5b, it can be seen that the number of platelets per tactoid is larger with the addition of PEG20k (Fig. 5b). Flocculated Laponite-PEG20k dispersions were studied in Paper III and Paper IV.

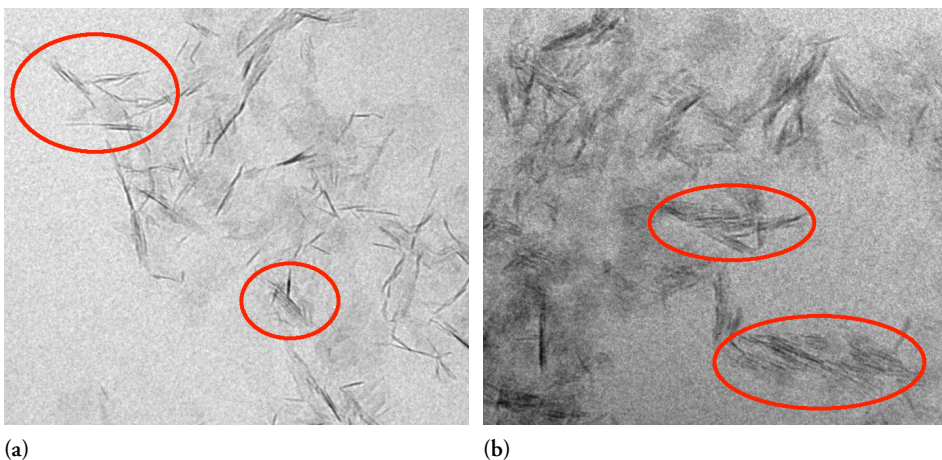


**Figure 5:** Cryo-TEM images for flocculated and sedimented Laponite. The think dark lines are the Laponite platelets seen side-on. (a) 0.25 wt% Laponite in 1 M NaCl and 0 wt% PEG20k. (b) 0.25wt% Laponite in 1 M NaCl and 5wt% PEG20k. The width of the images corresponds to 320 nm.

## 2.4 Free swelling in dialysis pocket

The rate of swelling and maximum uptake of water can be found in a free swelling experiment. The rate of swelling can reveal the swelling dynamics, i.e., to verify if the swelling is a diffusion controlled process (the uptake of water varies linearly with square root of time) or show deviations from it that could indicate that a slow phase transition occurs (Martin et al. (2006); Segad et al. (2010)). The maximum uptake of water can reveal information about the intermolecular interactions between the particles.

One gram of clay is placed inside a cylindrical dialysis membrane and both ends of the membrane are closed by, for example, clips or knots. The membrane is then quickly dipped into the water container and the weight is registered as a reference weight. The amount of water that enters into the clay can then be monitored over time. To set the temperature of the experiment and maintain constant conditions, the water container was placed inside an incubator. A schematic picture is shown in Fig. 6.

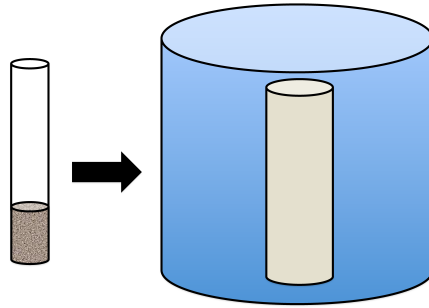


Figure 6: Schematic picture of a free swelling experiment. Clay is placed inside a cylindrical dialysis membrane and both ends of the membrane are closed (left). The cylindrical dialysis membrane is then placed inside a water container and water will enter into the clay (right).

If the colloidal particles repel each other by long-range electrostatic interactions, such as in Na-montmorillonite, the maximum uptake of water is usually not possible to find, i.e., the swelling is infinite. On the other hand, if the colloidal particles attract each other, such as in Ca-montmorillonite, the maximum uptake of water can be found, i.e., the swelling is finite (Segad et al. (2010)). To be able to find the maximum uptake of water for both Na-montmorillonite and Ca-montmorillonite, a stressing polymer can be added to the reservoir of water such that the external osmotic pressure is larger than zero (Martin et al. (2006); Michot et al. (2004)). The maximum uptake of water of the clay is then found when the osmotic pressure of the clay is equal to the external osmotic pressure. In Paper v, we were interested in the swelling of clay at different temperatures. If a stressing polymer would be used, the external osmotic pressure would not be independent of the temperature for a fixed concentration of polymer. To compensate for this effect, different concentrations of polymer at different temperatures would have to be used. This did not seem like a promising route since the uncertainties would be too large due to the fact that the temperature effect of clay is rather small. Hence, the rate of swelling for Na-montmorillonite at two different temperatures was the only property that could be achieved from the free swelling experiment. A different approach to find the temperature response of clay is to limit the volume and measure the swelling pressure as described in Section 2.5.

## 2.5 Swelling pressure in a test cell

The swelling pressure or the net osmotic pressure of clay in water can be measured as a function of volume fraction and temperature in a test cell placed inside an incubator (Karnland et al. (2006); Birgersson et al. (2010)). A schematic picture of the test cell is shown in Fig. 7a. A few grams of clay are placed in a cylindrical cell with a radius

of 1 cm surrounded by two semi-permeable membranes, one at the bottom and one at the top. The semi-permeable membranes will keep the clay inside the cell but let the water and the ions diffuse freely between the two compartments. The clay is set in equilibrium with the bulk solution by slowly circulating water through the pipes. The clay is confined inside a predefined volume by a piston that is attached to a force transducer. Knowing the area of the cell,  $A = 0.01^2\pi \text{ m}^2$  and measuring the force,  $F$ , the swelling pressure is calculated as  $P = F/A \text{ N/m}^2$ . By studying the swelling pressure over time, it is possible to find a stable value of the swelling pressure for the given volume fraction and temperature of the sample (the clay is then assumed to be in equilibrium with the bulk). A typical equilibration process at 25°C of the swelling pressure (in units of kPa) of Na-montmorillonite and Ca-montmorillonite in water as a function of time is shown in Fig. 7b.

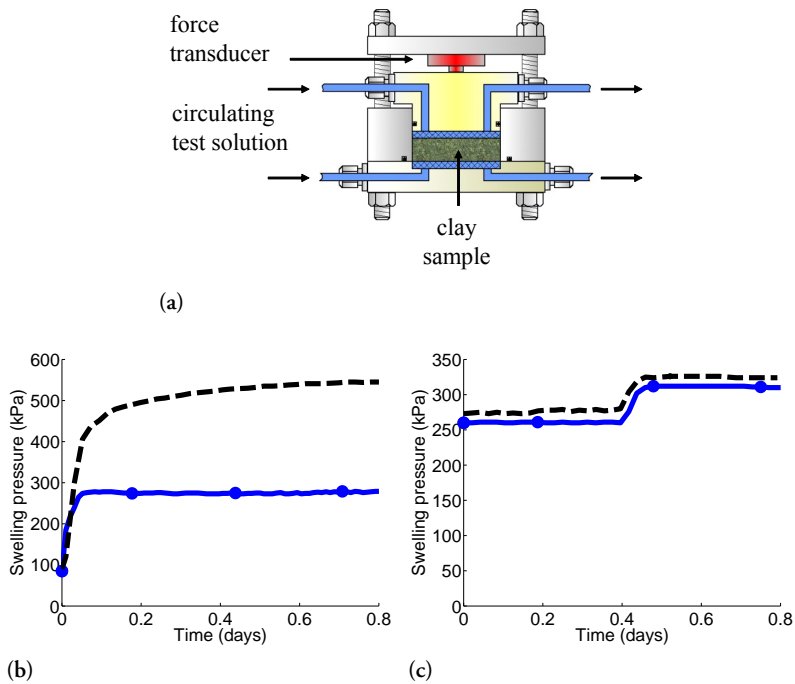


**Figure 7:** (a) A schematic picture of the test cell (Karnland et al. (2006)). (b) Equilibration of Na-montmorillonite (black dashed), and Ca-montmorillonite (blue circle) in water at 25°C. (c) Temperature response of Ca-montmorillonite with (black dashed) and without (blue circle) aluminum cylinder to account for the difference in thermal expansion of the cell. The temperature is changing from 25 °C to 5 °C at 0.4 days.

To find the water ratio,  $w = m_w/m_s$ , of the samples where  $m_w$  is the mass of the water and  $m_s$  is the mass of the solids, the test cell was disassembled and the total mass of the clay water sample was measured  $m_{tot} = m_w + m_s$ . The sample was then dried in an oven at 105°C for 24h and the mass of the solids was recovered. Knowing the density of the

clay,  $D_s = 2750 \text{ kg/m}^3$ , and the density of water,  $D_w = 1000 \text{ kg/m}^3$ , the dry density of the clay can be calculated as  $D_d = m_s/V_{tot} = D_w/(w + D_w/D_s) \text{ kg/m}^3$ , and the volume fraction is  $\phi = D_d/D_s$  (Karnland et al. (2006)).

The advantage of this experimental technique is that the uncertainty of measuring the water ratio does not affect the measured temperature response since the temperature is changed *in situ*. In Fig. 7a, it can be seen that the test cell consists of two separate systems, an outer system that confines the inner system, and an inner system which is measuring the force. The outer system consists of screws attached to a hollow stainless steel cylinder, and the inner system consists of two semi-permeable membranes and a piston. Initially it was found that the thermal expansion of the two systems were not equal, i.e., the confined volume changes with temperature. A ceramic plate, which is known to have a low thermal expansion, was confined in the cell and gave rise to a pressure response of  $\sim -1 \text{ kPa/}^\circ\text{C}$  from  $25^\circ\text{C}$  to  $5^\circ\text{C}$  where the total pressure was  $400 \text{ kPa}$  at  $25^\circ\text{C}$  and hence the length of the confined part is increasing with temperature. The solution to minimize the effect of this artifact was to insert a solid aluminum cylinder (aluminum has a larger thermal expansion coefficient than stainless steel) of appropriate length under the force transducer in order to compensate the relative temperature response between the inner and outer system. Thereby the pressure response was reduced to  $\sim +0.2 \text{ kPa/}^\circ\text{C}$  from  $25^\circ\text{C}$  to  $5^\circ\text{C}$  where the total pressure was  $400 \text{ kPa}$  at  $25^\circ\text{C}$ . The temperature response of Ca-montmorillonite was then measured both with and without the solid aluminum cylinder and gave a pressure response of  $-2.5 \text{ kPa/}^\circ\text{C}$  and  $-2.6 \text{ kPa/}^\circ\text{C}$  from  $25^\circ\text{C}$  to  $5^\circ\text{C}$  where the total pressure was  $270 \text{ kPa}$  at  $25^\circ\text{C}$ , respectively (see Fig. 7c). The conclusions from these measurements were that: (i) The change in volume is small and does not seem to play a big role, and (ii) a compensation of the pressure response with temperature from a solid reference system, such as a ceramic plate, is problematic and probably not possible because clay in water is an osmotic system, i.e., if the volume of the cell is changing slightly so does the water content.

## 3 Theoretical

### 3.1 Statistical mechanics and thermodynamics

Statistical thermodynamics provides a connection between thermodynamic properties of a system and its content, i.e., the particles of the system and their interactions. Some examples of thermodynamic properties are energy, volume, particle number (extensive properties), and pressure, temperature, and density (intensive properties). This section is intended to be an overview of some key concepts of statistical mechanics and thermodynamics, for a more detailed and in-depth description, the following references are recommended: Callen (1985); Hill (1986).

### 3.1.1 Statistical thermodynamics

To derive some useful concepts of statistical thermodynamics, we start by introducing the *phase space*, which is the space where all possible states of a system is represented. For example, in a classical system with  $N$  particles, the phase space is a  $6N$ -dimensional space where each state is represented as a vector that describes the position  $(x, y, z)$  and the momenta  $(p_x, p_y, p_z)$  of all  $N$  particles. At *thermodynamic equilibrium*, which is reached after a long time, there is no macroscopic flow of matter or energy within a system or between systems. Thus, if a certain property of a system is measured over a long time, it is expected to have a constant average value at equilibrium. A thermodynamical *ensemble* is the set of all possible states of a system at equilibrium and according to the *ergodic hypothesis* the average value measured over a long time is equal to the *ensemble* average, i.e., all parts of the phase space have been visited.

An *isolated* system, is a system which is completely disconnected such that no matter or energy can go in or out of the system, i.e., the number of particles ( $N$ ), volume ( $V$ ), and total energy ( $U$ ) are constant. The set of all possible states of an isolated system is called the *microcanonical* ensemble where the entropy ( $S$ ) is given by,

$$S = k_B \ln \Omega_{N,V,U} \quad (8)$$

where  $k_B$  is the Boltzmann constant, and the *microcanonical partition function*,  $\Omega_{N,V,U}$ , is the number of possible states for a constant number of particles, volume, and energy. At equilibrium, the entropy has reached its maximum, and if the function  $S$  is known, thermodynamic properties of the system such as the temperature and pressure can be found. From an experimental point of view, the microcanonical ensemble is not very useful by itself since an isolated system is rarely investigated. More useful ensembles are for example the *canonical* ensemble, the *isobaric* ensemble, and the *grand canonical* ensemble. In the canonical ensemble the number of particles, volume, and temperature ( $T$ ) are constant. The canonical partition function is defined as,

$$Q_{N,V,T} = \sum_i \Omega_{N,V,U_i} e^{-\beta U_i} \quad (9)$$

where the sum is over all energy levels,  $N$ ,  $V$ , and  $T$  are constant, and  $\beta = 1/(k_B T)$ . In the isobaric ensemble the number of particles, pressure ( $P$ ), and temperature are constant. The isobaric partition function is defined as,

$$\Delta_{N,P,T} = \sum_i Q_{N,V_i,T} e^{-\beta P V_i} \quad (10)$$

where the sum is over all volumes and  $N$ ,  $T$ , and  $P$  are constant. In the grand canonical ensemble the chemical potential ( $\mu$ ), volume, and temperature are constant. The grand

canonical partition function is defined as,

$$\Xi_{\mu,V,T} = \sum_i Q_{N_i,V,T} e^{-\beta\mu N_i} \quad (11)$$

where the sum is over all numbers of particles and  $V$ ,  $T$ , and  $\mu$  are constant. Note that the test cell described in Section 2.5 can be considered to be a grand canonical system where the volume and temperature are constant but water and salt can be exchanged with the reservoir. In a salt-free system, where  $N$  is considered to be the clay platelets and its counterions, the test cell can be considered to be a canonical system. The use of implicit water (the water molecules are represented as a continuous medium) in the simulations of Paper v made it possible to compare simulations within the canonical ensemble with the experimental findings.

The usefulness of the canonical partition function is demonstrated below by calculating the average pressure within the canonical ensemble,  $\langle P \rangle$ , such that a comparison can be made by the experimentally measured swelling pressure from the test cell. The probability,  $\rho_i$ , of state with energy  $U_i$  is

$$\rho_i = \frac{e^{-\beta U_i}}{Q_{N,V,T}}. \quad (12)$$

The average pressure within the canonical ensemble is then found by

$$\langle P \rangle = \sum_i P_i \rho_i \quad (13)$$

where the sum is over all states, and  $P_i = -\frac{\partial U_i}{\partial V}$  is the pressure for the  $i$ :th configuration. The *Helmholtz free energy* can be expressed as,

$$A = -k_B T \ln Q_{N,V,T}. \quad (14)$$

The Helmholtz free energy plays a similar role within the canonical ensemble as the entropy (Eq. (8)) within the microcanonical ensemble. Notice that there is a minus sign difference between Eq. (8) and Eq. (14), and hence at equilibrium, the Helmholtz free energy is minimized. If the Helmholtz free energy is known, the pressure,  $\langle P \rangle$ , can be calculated as,

$$\langle P \rangle = -\left(\frac{\partial A}{\partial V}\right)_{T,N} \quad (15)$$

where the equation above and Eq. (13) are equivalent. Following the thermodynamic definition of Helmholtz free energy

$$A = \langle U \rangle - TS \quad (16)$$

where  $\langle U \rangle$  is the average energy of the system. Eq. (16) was used in Paper v to explain the temperature response of montmorillonite. Furthermore, the relation will be utilized in Section 3.2.3 where the origin of the attractive ion-ion correlations is explained in detail.

### 3.1.2 Classical statistical mechanics

The classical approach to calculate the partition functions is to replace the set of states on the quantum level with a classical continuum approach. As an example, Eq. (9) is replaced by,

$$Q_{class} = \frac{1}{N! \Lambda^{3N}} \int_V e^{-\beta U(\mathbf{\Gamma})} d\mathbf{\Gamma} \quad (17)$$

where  $\mathbf{\Gamma}$  is a  $3N$ -dimensional vector that describes the  $x$ ,  $y$ , and  $z$  coordinates of the  $N$  particles that exist in the system,  $U(\mathbf{\Gamma})$  is the potential energy of the system as a function of the particle positions, and the integral is over the entire volume for each and every particle. The kinetic part of the system has been integrated beforehand and the result is included in the de Broglie wavelength,  $\Lambda$ . The pressure in Eq. (13) can now be written as,

$$\langle P \rangle = \frac{\int_V P(\mathbf{\Gamma}) e^{-\beta U(\mathbf{\Gamma})} d\mathbf{\Gamma}}{Z_N} \quad (18)$$

where  $Z_N = \int_V e^{-\beta U(\mathbf{\Gamma})} d\mathbf{\Gamma}$  is the *configuration integral*, and  $P(\mathbf{\Gamma})$  is the pressure as a function of the particle positions,  $\mathbf{\Gamma}$ .

### 3.2 Intermolecular interactions

The molecular interactions in a system can be divided into intra- and intermolecular interactions. The intramolecular interactions, for example, describe the chemical bonds within a molecule. The intermolecular interactions describe the interactions between molecules or colloidal particles. The interplay between attractive and repulsive forces from these interactions are used to, for example, explain why colloids are pushed apart to form a colloidal dispersion under certain circumstances and why in some cases flocculation occurs.

In many cases, and especially for large systems, it is not possible to include all particles to calculate thermodynamic properties of a system. Hence, approximations and simplifications are used to try to capture and understand the relevant physics of a system that gives rise to a certain behavior. In a real colloidal system, the colloidal particles are dispersed in a medium where the medium is composed of molecules (Fig. 8a). A common example of an approximation that is used for colloidal systems is to treat the solvent implicitly, i.e., the solvent is represented as a continuum throughout space (Fig. 8b).

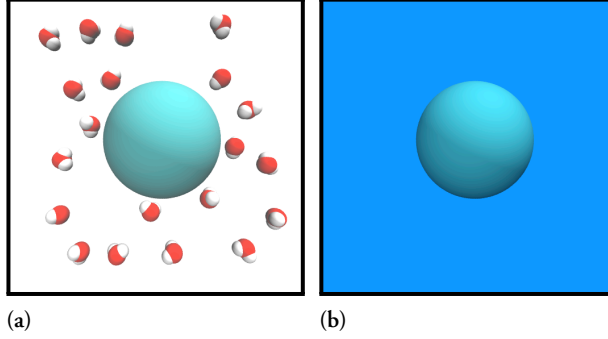


**Figure 8:** Schematic picture of (a) a real system where the solvent are composed of molecules (represented as red and white spheres, i.e., water molecules) and (b) a system where the solvent is treated implicitly (represented as the blue background color). The colloidal particle is represented as a cyan sphere.

### 3.2.1 Coulomb interactions

Two charged particles  $i$  and  $j$  at a fixed distance,  $r_{ij}$ , will interact according to Coulomb's law,

$$u(r_{ij}) = \frac{q_i q_j}{4\pi\epsilon_0 r_{ij}} \quad (19)$$

where  $q_i$  is the charge of particle  $i$ , and  $\epsilon_0 \approx 8.854 \cdot 10^{12} \text{ C}^2/(\text{Jm})$  is the permittivity of vacuum. If the two charged particles are immersed in a polar solvent such as water, the pair interaction between the two particles is given by,

$$\beta w(r_{ij}) = \beta \frac{q_i q_j}{4\pi\epsilon_0 \epsilon_r(T) r_{ij}} = \frac{l_B z_i z_j}{r_{ij}} \quad (20)$$

where  $l_B = \beta e^2 / (4\pi\epsilon_0 \epsilon_r(T))$  is the Bjerrum length,  $e$  is the elementary charge,  $z_i = q_i/e$  is the valency of particle  $i$ , and  $\epsilon_r(T)$  is the dielectric constant of the solvent, which is dependent on the temperature (Israelachvili (2011)). Eq. (20) is a free energy since the interactions with the water molecules have been averaged, i.e., the water is treated implicitly. If the solvent is water, it can be shown that the Bjerrum length increases with temperature due to the temperature-dependent dielectric constant. This fact was utilized in Paper v and Paper vi to explain the temperature response of Na-montmorillonite and Ca-montmorillonite in water. Note that all simulations in this thesis assume that the dielectric constant is uniform throughout space.

### 3.2.2 Poisson-Boltzmann equation

The Poisson-Boltzmann (PB) equation is extremely useful to understand the physics in many charged colloidal systems. As will be demonstrated below, the PB equation

explains how charged colloids can form a colloidal dispersion and how additional salt changes the intermolecular electrostatic interaction. By combining the Poisson's equation and the Boltzmann distribution, the PB equation is given as,

$$\epsilon_r \epsilon_0 \Delta \Phi(\mathbf{r}) = - \sum_i q_i c_i e^{-\beta q_i \Phi(\mathbf{r})} \quad (21)$$

where  $\Delta$  is the Laplace operator,  $\Phi(\mathbf{r})$  is the *mean* electrostatic potential at the position  $\mathbf{r}$ , and  $c_i$  is the concentration of the ionic species  $i$  with charge  $q_i$ . The PB equation relies on a mean-field approximation where each ion interacts with the mean electrostatic potential.

At low electrostatic potential, the PB equation can be Taylor expanded to the first order which gives the linearized PB equation. By solving the linearized PB equation in spherical geometry, the interaction potential between two charged particles is,

$$\beta w(r_{ij}) = l_B z_i z_j \frac{e^{-\kappa r_{ij}}}{r_{ij}} \quad (22)$$

where  $1/\kappa$  is the Debye screening length, and  $\kappa^2 = 4\pi l_B \sum_i z_i^2 c_i$  (Evans & Wennerström (1999)). The physical insight of Eq. (22) is that the addition of salt into a system is simply Coulomb's law (Eq. (20)) multiplied by  $e^{-\kappa r_{ij}}$ . Thus, salt effectively screens (reduces) the long-ranged electrostatic interaction between charged particles. The electrostatic interaction becomes more short-ranged if the salt concentration and/or the valency of the salt increase, i.e., the Debye screening length decrease. As an example, for 1:1 salt (e.g. NaCl) in water at room temperature, the Debye screening length at 1 mM and 100 mM is about 10 nm and 1 nm, respectively.

As explained in Section 3.3.1, two parallel clay platelets can be modeled as two uniformly charged surfaces where the ions are located in between the two surfaces (see Fig. 13). The PB equation can be solved exactly for two equally charged surfaces in the salt-free case, i.e., only counterions are present. The osmotic pressure,  $\Pi$ , which is equal to the pressure,  $P$ , in the salt-free case, is given by the so-called mid-plane approach (Evans & Wennerström (1999)),

$$\Pi_{PB} = P_{PB} = k_B T c(0) \quad (23)$$

where  $c(0) = 2k_B T s^2 \epsilon_r \epsilon_0 / (z e h)^2$  is the concentration of the counterions at the mid-plane,  $s \tan s = |\sigma| z e h / (2k_B T \epsilon_r \epsilon_0)$ ,  $h$  is the separation between the charged surfaces,  $\sigma$  is the surface charge density where the charges are smeared out on each surface, and  $z$  is the valency of the counterions. Notice that the concentration of the counterions is always positive, in particular at the mid-plane, hence, the PB equation will always give a positive pressure (repulsive force) between two equally charged surfaces (see Fig. 11c). The fact that the charged colloids repel each other explains how a colloidal dispersion

can be formed. The counterions of the colloids as well as salt have been treated explicitly in all simulations in this thesis due to the fact that the PB equation does not include the ion-ion correlations, which can give a negative osmotic pressure (attractive force) at short separations between highly charged colloids mediated by multivalent ions (Jönsson & Wennerström (2001)). The essence of ion-ion correlations will be explained in the following section.

### 3.2.3 From weak coupling to strong coupling

We start off by considering two equally charged surfaces as in the previous section. The PB equation is asymptotically exact in the limit of weak coupling, i.e., long distances between the surfaces, low surface charge, and low counterion valence. The strong coupling (SC) theory is asymptotically exact in the opposite limit, i.e., short distances between the surfaces, high surface charge, and high counterion valence. The limits can be found by considering the coupling parameter,

$$\Xi = 2\pi z^3 \ell_B^2 \sigma_s \propto \frac{z^3 \sigma_s}{(\epsilon_r T)^2} \quad (24)$$

where  $\sigma_s$  is the surface charge number density. The SC theory is valid for  $\Xi \rightarrow \infty$  (the SC limit), and the PB equation is valid for small values of  $\Xi$ . Moreover, the SC theory is valid if the lateral distance,  $\alpha$ , between the ions is larger than the separation,  $h$ , between the surfaces, i.e.,  $h < \alpha$ . Two different scenarios of two charged surfaces mediated by the counterions are shown in Fig. 9. The SC theory is valid in case (a) where  $h < \alpha$ , and the PB equation is valid in case (b). Each ion interacts with a diffuse cloud of other ions in Fig. 9b, whereas the ions move almost independently along the vertical direction in Fig. 9a due to the strong ion-ion correlations (the structure of the ions is dominated by the mutual repulsion between them) (Netz (2001)).

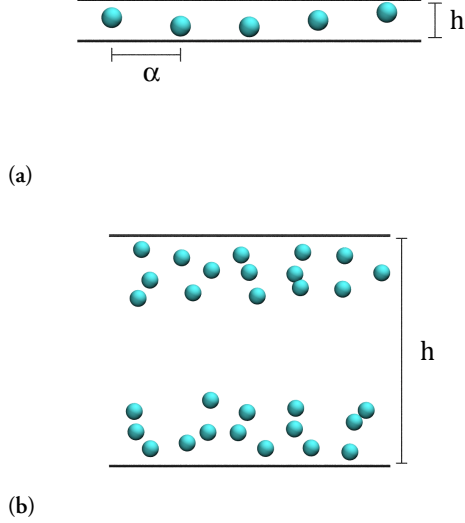


**Figure 9:** Schematic picture of two charged surfaces (represented as the horizontal black lines) mediated by the counterions (represented as the cyan spheres). (a) The lateral distance,  $\alpha$ , between the ions is larger than the separation,  $h$ , between the two charged surfaces. (b) The charged surfaces attract two separate layers of counterions and the lateral distance between the ions is small.

In the SC limit, a cylinder can be cut out from the system that contains only *one* counterion located within the volume  $Mh$ , where  $h$  is the length of the cylinder, and  $M$  is the area of each circular end. All other counterions are neglected since their impact on the free energy is negligible in the SC limit (see Fig. 9a). By using Eq. (16), the Helmholtz free energy can be calculated if the average energy,  $\langle U \rangle$ , and the entropy,  $S$ , can be found. The interaction between an infinite charged surface and an ion is  $\beta w_{\text{surface-ion}} = 2\pi l_B z \sigma_s x$ , where  $x > 0$  is the distance to the surface. If the distances to the two surfaces and the ion are  $x$  and  $(h - x)$ , respectively, the total interaction between the surfaces and the ion is  $\beta w_{\text{surfaces-ion}} = 2\pi l_B z \sigma_s (x + (h - x)) = 2\pi l_B z \sigma_s h$ . Notice that the surfaces-ion interactions only depend on the surface-surface separation  $h$  (there is no net force acting on the ion), and that the force between the surfaces and the ion ( $F_{\text{surfaces-ion}} = -\partial w_{\text{surfaces-ion}} / \partial h$ ) is attractive. The system is electro-neutral, hence the sum of the total charge of the two surfaces and the charge of the ion is zero ( $z = 2\sigma_s M$ ). Hence, the interaction between the two surfaces is then  $\beta w_{\text{surface-surface}} = -2\pi M l_B \sigma_s^2 h$ . The total average energy is,

$$\beta \langle U \rangle = \beta w_{\text{surface-surface}} + \beta w_{\text{surfaces-ion}} = 2\pi M l_B \sigma_s^2 h. \quad (25)$$

The number of available states of the ion is given by the volume,  $V = hM$ , divided by a constant:  $S = k_B \ln(V/C)$  where  $C$  is a constant. The Helmholtz free energy according

to Eq. (16) is given by,

$$\beta A_{SC}(h) = 2\pi l_B \sigma_s^2 h M - \ln(hM/C) \quad (26)$$

and the pressure (the force divided by the area) can be calculated as

$$\begin{aligned} \beta P_{SC} &= -\beta \left( \frac{\partial A_{SC}/M}{\partial h} \right) = -2\pi l_B \sigma_s^2 + \frac{1}{hM} = 2\sigma_s \left( -\pi l_B \sigma_s + \frac{1}{zh} \right) \\ P_{SC} &= -\frac{2\pi e^2 \sigma_s^2}{4\pi \epsilon_0 \epsilon_r(T)} + \frac{2\sigma_s k_B T}{zh}. \end{aligned} \quad (27)$$

Notice that the pressure from the SC theory and the pressure from the PB equation (Eq. (23)) are completely different. At large separations, the pressure in the SC theory is always negative (i.e. attractive force, in contrast to a repulsive force found from the PB equation) due to the dominant electrostatic attraction. At very short separations the entropic pressure, due to the confined counterion, dominates and the pressure becomes repulsive (see Fig. 11b). Suppose that the surfaces are initially far apart, the attractive force will bring the surfaces closer and closer until the force becomes repulsive. The equilibrium separation between the surfaces is found when the pressure is zero ( $P = 0$ ), i.e.,  $h = 1/(\pi l_B z \sigma_s)$ . (Netz (2001)) The SC theory gives an explanation to why tactoids are formed in montmorillonite when the counterions are multivalent. However, the theory also predicts that tactoids are formed when the counterions are monovalent, which is not the case. Hence, it is important to know the assumptions of a theory and realize when the SC theory is valid and when the PB equation is valid by considering the value of the coupling parameter  $\Xi$  of the system. For a more in-depth description and comparison between the PB equation, the SC theory, and simulations, the following reference is recommended: Moreira & Netz (2002).

A model that qualitatively describes both weakly and strongly coupled systems is the so-called *simple model* (SM), which has been shown to capture the essential physics between two charged surfaces at short separations (Jönsson et al. (2005)). The SM is akin to the SC theory, where the only difference between the two models is that the SM assumes that the cylinder that contains the single counterion is closed, i.e., the surfaces are now finite circular disks and all interactions outside the cylinder are neglected. To obtain a simple analytical expression while still maintaining the qualitative results, the system is transformed into a one-dimensional system. Thus, the finite discs are replaced by point charges equal to  $-ze/2$ . The point charges are fixed at a distance  $-\delta$  and  $h + \delta$  such that the potential from the point charge is equal to the potential from the disc at the end points, which gives  $\sigma = ze/(8\pi\delta^2)$  (see Fig. 10).

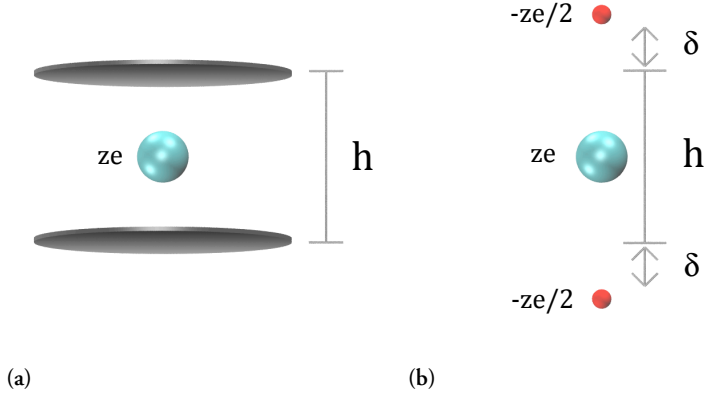


Figure 10: (a) A single counterion (represented as a cyan sphere) confined between two charged circular disks. (b) Simplifying the model in (a) into a one-dimensional system with two fixed “surface” charges (represented as red spheres) and one mobile counterion of valency  $z$  confined to a line of length  $h$ . The displacement of the surface charges,  $\delta$ , is supposed to mimic the surface charge density.

The energy can be estimated by locating the counterion in the middle between the “surfaces” and the entropy is overestimated by assuming that the distribution is uniform (notice that this is true for infinite surfaces as shown in the derivation of SC theory). The average energy can be calculated by simply summing up the interactions between the three charges. The entropic contribution in the one-dimensional system is  $S = k_B \ln(h/C)$  where  $C$  is a constant. The Helmholtz free energy is then given by (Jönsson et al. (2005), Paper v),

$$\beta A_{SM}(h) = -\frac{7}{4} \frac{l_B z^2}{h + 2\delta} - \ln(h/C) \quad (28)$$

and the pressure can be calculated as,

$$\begin{aligned} \beta P_{SM} &= -\beta \left( \frac{\partial A_{SM}/M}{\partial h} \right) = -\frac{7}{4} \frac{l_B z^2/M}{(h + 2\delta)^2} + \frac{1}{hM} = 2\sigma_s \left( -\frac{7}{4} \frac{l_B z}{(h + 2\delta)^2} + \frac{1}{zh} \right) \\ P_{SM} &= -\frac{7}{2} \frac{ze^2 \sigma_s}{4\pi \epsilon_0 \epsilon_r(T) (h + 2\delta)^2} + \frac{2\sigma_s k_B T}{zh}. \end{aligned} \quad (29)$$

Similar to the SC theory there is a competition between an attractive electrostatic component and a repulsive entropic component. The main difference between the SC theory and the SM is that the electrostatic component is distance-dependent and scales with the valency of the counterion. At equilibrium, the pressure should be zero, which is found only for  $z^3 l_B^2 \sigma_s \geq 128/(49\pi) \approx 0.83$ . Note that the left-hand side of the inequality is proportional to the coupling parameter,  $\Xi$ . Hence, in the SM, the pressure is positive for all separations where  $\Xi < 256/49 \approx 5$ . For  $\Xi \geq 5$ , the pressure becomes

negative at intermediate separations, and at very short separations the positive entropic component dominates.

An example of the SM is to consider clay in water at room temperature ( $l_B \approx 0.7$  nm) where the surface number charge density is assumed to be  $\sigma_s = 1$  nm $^{-2}$ , which is a rough estimate of the surface number charge density of montmorillonite. By using the inequality above, the pressure is purely positive (the clay platelets swell significantly) for  $z < 1.2$ , i.e., if the counterions are monovalent ( $z = 1$ ). For multivalent ions ( $z \geq 2$ ), the pressure is negative at intermediate separations and tactoids are formed. The equilibrium separation in between the platelets is found at  $P = 0$  (see Fig. 11a). As a comparison, the corresponding pressures within the SC theory, and PB equation, are shown in Fig. 11b, and Fig. 11c, respectively. Finally, the attractive ion-ion correlations can be understood by the competition between an attractive electrostatic component and a repulsive entropic component. By increasing the coupling parameter over a certain threshold, e.g. increasing the valency of the counterions, increasing the surface charge density, and/or reducing  $\epsilon_r$  (exchange the solvent with a less polar solvent), the force between two colloids can be changed from repulsive for all separations to attractive at intermediate separations.

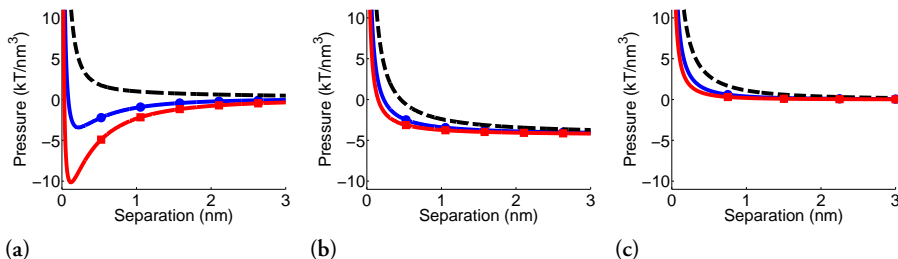


Figure 11: Pressure between two charged surfaces as a function of the separation within the (a) SM (Eq. (29)), (b) SC theory (Eq. (27)), and PB equation (Eq. (23)) for  $l_B = 0.7$  nm and  $\sigma_s = 1$  nm $^{-2}$ . The surfaces are neutralized by monovalent counterions (black dashed), divalent counterions (blue circle), and trivalent counterions (red square).

### 3.2.4 Short-ranged interactions

In addition to the long-ranged interactions, e.g. the electrostatic interactions, other types of interactions, which are short-ranged (short-ranged potentials decay as  $r^{-n}$  where  $n > 3$ ), exist between molecules. The Pauli exclusion principle states that two or more identical fermions can not occupy the same quantum state. The principle implies that two interacting atoms or molecules repel each other at close distances since electrons are fermions. Two simple potentials that describes this type of interaction are the *hard sphere* potential and the *truncated and shifted Lennard-Jones* potential (see Fig. 12). The

hard-sphere potential between two particles  $i$  and  $j$  is defined as,

$$u(r_{ij}) = \begin{cases} +\infty & \text{if } r_{ij} < \sigma_{ij} \\ 0 & \text{otherwise} \end{cases} \quad (30)$$

where  $\sigma_{ij} = (d_i + d_j)/2$ , and  $d_i$  is the diameter of particle  $i$ . The truncated and shifted Lennard-Jones potential is strictly repulsive and is defined as,

$$u(r_{ij}) = \begin{cases} \epsilon \left( \left( \frac{\sigma_{ij}}{r_{ij}} \right)^{12} - 2 \left( \frac{\sigma_{ij}}{r_{ij}} \right)^6 + 1 \right) & \text{if } r_{ij} < \sigma_{ij} \\ 0 & \text{otherwise} \end{cases} \quad (31)$$

where  $\epsilon$  determines the strength of the interaction. The reason to choose Eq. (31) over Eq. (30) is that Eq. (30) is a continuous function with a continuous derivative (the force) which is required for the molecular dynamics simulation (described in Section 3.5) package that was used in this thesis. Molecules and atoms are also attracted to each other by the so called van der Waals forces which are a collection of interactions that are proportional to  $r^{-6}$ . The van der Waals forces arise from three different origins: the Keesom force (rotational average between two dipoles), the Debye force (rotational average between a dipole and a corresponding induced dipole), and the London dispersion force (instantaneous induced dipoles). A convenient and popular way to combine the Pauli exclusion principle with the van der Waals forces is the Lennard-Jones (LJ) potential defined as,

$$u(r_{ij}) = 4\epsilon \left( \left( \frac{\sigma_{ij}}{r_{ij}} \right)^{12} - \left( \frac{\sigma_{ij}}{r_{ij}} \right)^6 \right) \quad (32)$$

where  $\epsilon$  determines the strength of the interaction, and the minimum value  $-\epsilon$  of the potential is found at  $r_{ij} = 2^{1/6}\sigma_{ij}$  (see Fig. 12). A description using the PB equation for the electrostatic interactions and the van der Waals forces for the short ranged interactions is known as the DLVO-theory (Derjaguin & Landau (1941); Verwey & Overbeek (1948)).

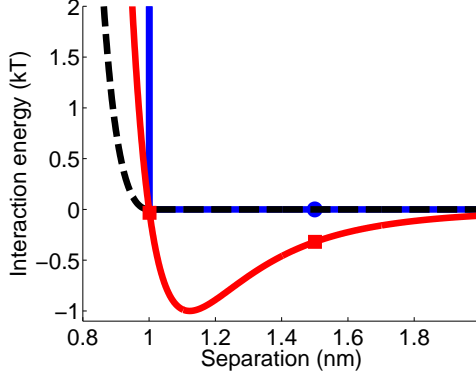


Figure 12: Comparison between the short-ranged interaction potentials with  $\epsilon = 1$  kT, and  $\sigma = 1$  nm: The hard-sphere potential (blue circle), truncated and shifted Lennard-Jones potential (black dashed), and Lennard-Jones potential (red square).

### 3.2.5 Effective pair potentials

Descriptions of the interaction between two point charges where the solvent (Eq. (20)) or the solvent and the salt (Eq. (22)) are treated implicitly are examples of *effective* pair potentials. In general terms, an effective pair potential, also known as the potential of mean force,  $W(r)$ , as a function of the separation,  $r$ , is defined as,

$$W(r) = - \int_{\infty}^r \bar{F}(r') dr' \quad (33)$$

where  $\bar{F}(r') = \langle F(r'; \mathbf{s}) \rangle$  is the mean force between the particles at a distance  $r'$ , and  $\mathbf{s}$  is the degrees of freedom that has been averaged over. In a dilute suspension, the effective pair potential between two particles (two-body system) is usually enough to understand the full system (many-body system) since the interactions between three particles or more are negligible.

In the case of charged colloids, the effective pair potential is considered between two colloids and the degrees of freedom of, for example, ions and polymers are integrated out. The effective pair potential between two particles is a way to reduce the complexity of a system and gives a lot of physical insight. To use an effective pair potential in a many-body system is an attractive approach to study large systems with a reduced computational cost. Moreover, the approximate treatment of both the solvent and 1:1 salt have in many cases shown good agreement with experiments (Israelachvili & Adams (1978); Pashley (1981); Israelachvili (2011)).

For anisotropic particles such as clay platelets, the potential of mean force as a function of merely the separation can not be used in most cases due to the additional rotational

degrees of freedom. A possible but very expensive way (in a computational sense) would be to find the potential of mean force,  $W(r, \theta, \phi)$ , as a function of the separation and the two angles,  $\theta$  and  $\phi$ . Moreover, clay platelets are flexible which would also introduce too many degrees of freedom into the potential of mean force for any kind of practical usage. In Paper II, a free-energy matching method was developed to solve the above mentioned problem within certain limits.

### 3.3 Coarse-grained modeling

A coarse-grained (CG) model is a simplified description of a system where the number of degrees of freedom is reduced. For example, two clay platelets can be modeled as two charged surfaces. The two main reasons to coarse-grain an atomistic system is to be able to study large-scale systems at a reduced computational cost and to reduce the complexity of the system in order to understand the molecular mechanisms. The disadvantage of a simplified model is that the quantitative correspondence with experiments is usually not achievable, instead a qualitative agreement can be found where the overall trends can be understood. When developing a CG model it is important to define the goals of the study and determine the essential physics that the model should capture.

A simple way to describe any colloidal particle is to replace a set of atoms with a CG site. The number of atoms that the site represents sets the resolution of the model. To maintain a desired shape, the sites within the colloidal particle is held together by bonded interactions, for example, harmonic stretching potentials and/or harmonic angle potentials. The CG sites interact through non-bonded effective pair potentials, described in Section 3.2.5, where the parameters are chosen from either a more detailed model and/or experimental data.

In this thesis all coarse-graining are done on the level of the *primitive model*, i.e., the charged species are treated as charged hard or soft spheres, and the water molecules are treated through a dielectric constant which is uniform throughout all space.

#### 3.3.1 Clay platelets and ions

The CG model of clay platelets have been described in different ways in this thesis depending on the goal of the study. The first model represents two parallel clay platelets as two negatively charged planar surfaces neutralized by mobile counterions (see Fig 13). The surfaces are uniformly charged with a surface charge density  $\sigma$ , and the ions interact with the charged surfaces. The ions interact pairwise with each other by combining Eq. (20) with Eq. (30), and the diameter of the ions was set to 0.4 nm. In practice, the simulation box is finite with volume  $V = hL^2$ , where  $h$  is the separation between the

surfaces, and  $L$  is the length in the directions parallel to the surfaces. *Periodic boundary conditions* are used for the ions, i.e., if an ion moves outside the box ( $x > L/2$ ) in a direction parallel to the surfaces, it will reappear at  $x = x - L$ . The *minimum image convention* is used to calculate the distance between two ions, i.e., if the separation,  $r_x$ , in a direction parallel of the surfaces is larger than  $L/2$  then  $r_x = |r_x - L|$ . An external potential is included to account for the interactions outside the simulation box.

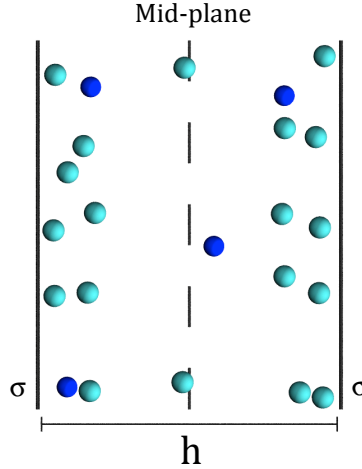


**Figure 13:** Schematic picture of the first model. Two parallel clay platelets are coarse-grained as two negatively charged planar surfaces with surface charge density  $\sigma$  (represented as the two black vertical lines) neutralized by mobile counterions (represented as blue and cyan spheres). The mid-plane is represented by the dashed line.

The second model represents a clay platelet as a finite hexagonal monolayer of connected CG sites. The sites are negatively charged and the diameter,  $d_{site} = 1$  nm, was chosen to mimic the surface charge density and the thickness of a clay platelet. The number of sites of a platelet and the separation between the sites determines the area of a platelet (see Fig. 14). The platelets are considered to be either rigid or flexible. For the latter, all neighboring sites within a platelet are connected by a harmonic bond-stretching potential,

$$u_b(r_{ij}) = \frac{1}{2}k^b(r_{ij} - b)^2 \quad (34)$$

where  $k^b$  is the force constant,  $r_{ij}$  is the separation between site  $i$  and  $j$ , and  $b = 1$  nm is the equilibrium bond separation. The platelet flexibility is controlled by a harmonic bending potential between triplets of bonded sites,

$$u_a(\theta_{ijk}) = \frac{1}{2}k^\theta(\theta_{ijk} - \theta^0)^2 \quad (35)$$

where  $k^\theta$  is the force constant,  $\theta_{ijk}$  is the bond angle between the sites  $i, j$ , and  $k$ , and  $\theta^0 = \pi$  rad.

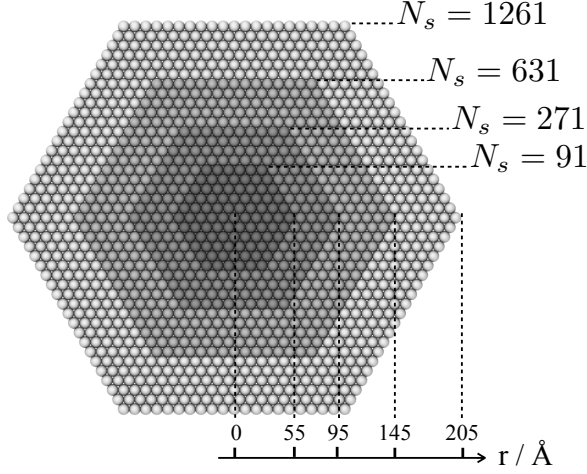


**Figure 14:** Schematic picture of the second model. The clay platelets are represented as hexagonal monolayer of connected charged spheres. For a given number of platelet sites ( $N_s$ ) a certain platelet radius ( $r$ ) is obtained in the given direction.

The counterions and additional salt are modeled as freely moving charges with diameter  $d_{ion} = 0.4$  nm. All particles of the system, except adjacent platelet sites, interact pairwise by combining Eq. (20) with Eq. (30) or Eq. (31).

### 3.3.2 Polyethylene oxide

PEG is modeled as a set of connected CG sites denoted as beads. The single hydrogen and hydroxyl group at the ends are neglected and each bead represents a ethylene oxide unit. Non-adjacent beads interact through the truncated and shifted LJ potential (Eq. (31)) and adjacent beads are connected by a harmonic bond-stretching potential (Eq. (34)). The parameters for Eq. (31) and Eq. (34) have been chosen to give similar osmotic pressure and radius of gyration to values measured experimentally (Xie et al. (2016)). The LJ potential (Eq. (32)) was chosen between the polymer bead and platelet site where  $\sigma = (d_{site} + d_{bead})/2$  and the strength of the interaction was chosen to resemble the adsorption isotherm that has been measured experimentally (Paper III, Mongondry et al. (2004)).

### 3.4 Monte Carlo simulations

The osmotic pressure can be found analytically in some special cases, e.g., for two charged surfaces mediated by only counterions within the PB equation (Section 3.2.2), the SC theory or the SM (Section 3.2.3). Each theory contains a large number of approximations but is found to be valid for certain cases and important physical insight concerning the interaction between charged colloids is gained. An alternative approach to find, for example, the osmotic pressure in a system is to use simulations. The advantage of using simulations is that many approximations can be removed, e.g., the mean-field approximation or the restriction to include only one counterion. Hence, more complex and realistic systems can be considered with simulations. The disadvantage is that the physical insight can be hard to gain if the model is too complex and involves too many parameters. The spirit of the simulations in this thesis is to include as few parameters as possible in the model such that the mechanisms can be understood.

Two of the most popular simulation methods in classical statistical mechanics are Monte Carlo (MC) simulations and Molecular Dynamics (MD) simulations. The connection between MD and MC is to consider the ergodic hypothesis where (i) the average value of a certain property after a long time is equal to (ii) the ensemble average. In MD, the particles of a system evolve through Newton's laws of motion and hence the average value of a property is found after a long time (i). In MC, the notion of time is absent, instead a large number of states (configurations) within the ensemble is considered and the average value of a property is found by the ensemble average (ii).

In a canonical system, the thermal average of any observable,  $\Upsilon$ , can be calculated by generalizing Eq. (18) as,

$$\langle \Upsilon \rangle = \frac{\int_V \Upsilon(\mathbf{\Gamma}) e^{-\beta U(\mathbf{\Gamma})} d\mathbf{\Gamma}}{Z_N} \quad (36)$$

An analytical solution to the multidimensional integral above is limited to small and simple systems. For larger and more complex systems, an approximated average value of the observable can be found by for example a brute force MC method where the coordinates of the particles are chosen randomly for a large set of configurations. The disadvantage of such an approach is that it is very inefficient since most of the generated configurations in a dense system will not give a significant contribution. For example, overlapping particles will increase the energy of a configuration due to the short-ranged repulsive interactions and the total energy of a dense system is easily found to be above  $k_B T$ , i.e.,  $e^{-\beta U(\mathbf{\Gamma})} \ll 1$ , in a randomly generated configuration.

### 3.4.1 Metropolis method

An efficient and robust way around the above mentioned problem is to use the Metropolis method (Metropolis et al. (1953); Allen & Tildesley (1989)). The Metropolis method is a sampling method where configurations are generated proportional to the Boltzmann weight,  $e^{-\beta U(\Gamma)}$ , and a new configuration is only dependent on the previous. The criterion of *detailed balance* is enforced such that the equilibrium of a system can be found. Detailed balance means that:

$$\rho_o \pi_{o \rightarrow n} = \rho_n \pi_{n \rightarrow o} \quad (37)$$

where  $\rho_o = e^{-\beta U(\Gamma_o)} / Z_N$ ,  $\rho_n = e^{-\beta U(\Gamma_n)} / Z_N$ ,  $\Gamma_o$ , and  $\Gamma_n$  are the probability densities and coordinates of the old and new configuration, respectively.  $\pi_{o \rightarrow n}$  and  $\pi_{n \rightarrow o}$  are the transition probability densities from the old configuration to the new configuration and vice versa. In the Metropolis scheme, Eq. (37) is fulfilled by choosing  $\pi_{o \rightarrow n}$  to be,

$$\pi_{o \rightarrow n} = \begin{cases} \gamma_{o \rightarrow n} & \text{if } \rho_n \geq \rho_o \\ \gamma_{o \rightarrow n} \cdot \alpha & \text{if } \rho_n < \rho_o \end{cases} \quad (38)$$

where  $\gamma_{o \rightarrow n} = \gamma_{n \rightarrow o}$  describes a symmetric random *trial move* (explained in Section 3.4.2). In the case of translation of a single particle,  $\gamma_{o \rightarrow n}$  describes the uniform probability to move in any direction within a maximum allowed distance (see Section 3.4.2).  $\gamma_{o \rightarrow n}$  is symmetric because the probability of finding a certain new position is the same as finding the old position when in the new position. The acceptance ratio,  $\alpha$ , from an old configuration to a new configuration is found by rewriting Eq. (37):

$$\alpha = \frac{\pi_{o \rightarrow n}}{\pi_{n \rightarrow o}} = \frac{\rho_n}{\rho_o} = \frac{e^{-\beta U(\Gamma_n)}}{Z_N} \frac{Z_N}{e^{-\beta U(\Gamma_o)}} = e^{-\beta(U(\Gamma_n) - U(\Gamma_o))}. \quad (39)$$

Before the Metropolis method can be applied it is necessary to define the geometry and boundary conditions of the system. After an initial configuration of the particle positions has been created, the method can be described in the following steps,

1. Select a random trial move.
2. Select a random particle or a set of particles as required by the trial move and perform the move to generate a new configuration.
3. Calculate Eq. (39) and accept the new configuration if  $\alpha \geq 1$  ( $\rho_n \geq \rho_o$ ) or  $\alpha > R$  (when  $\rho_n < \rho_o$ ), where  $R$  is a random number between zero and one, otherwise keep the old configuration.
4. Sample the observables of interest (only after the system has equilibrated, i.e., skip the initial configurations until the system has reached equilibrium).

## 5. Start over from step 1.

To check whether a system is in equilibrium or not requires knowledge about the system. Necessary criteria are typically that the energy of the system is converged and that independent simulations from different initial configurations give the same observable averages. But this could also be the case for a system that is not in equilibrium. If, for example, the trial moves and the initial configurations are chosen such that important parts of the phase space are inaccessible, the true equilibrium will never be found. Hence, intelligent trial moves and simulation techniques are important in order to find equilibrium as well as efficiently sample the observable averages.

An advantage of the Metropolis algorithm is that unphysical moves, such as translation of an ion through a platelet (described in the next section), are possible. The disadvantage is that a configuration can only be generated by knowing the previous configuration, hence parallelization of the simulation program is usually non-optimal. Moreover, intelligent trial moves are required to reduce the simulation time, which may be time consuming to invent/implement and are usually system dependent.

### 3.4.2 Trial moves

There exist a vast number of trial moves in the literature, optimized for different types of colloids and systems (Allen & Tildesley (1989)). In this section, the trial moves that are relevant for the simulated systems in this thesis will be described.

**Single particle displacement:** A single particle (e.g. a clay platelet or an ion) is chosen randomly. The chosen particle is translated or rotated randomly. A maximum allowed displacement is chosen to optimize the efficiency of the displacement for a given system. Within the maximum allowed displacement there should be an equal probability for any of the accessible states such that the symmetric condition  $\gamma_{0 \rightarrow n} = \gamma_{n \rightarrow 0}$  is fulfilled. In this thesis, the maximum translation for the ions ( $d_{max}$ ) was typically chosen as  $d_{max} > d_{ion} + d_{site}$ , such that the ions could translate through a platelet. Moreover, as a rule of thumb the maximum displacement was chosen such that the acceptance probability was  $\sim 30\%$ .

**Cluster displacement:** The location of the counterions is typically very close to a clay platelet due to the electrostatic attraction. Hence, most displacements of a single platelet are rejected since an overlap between the platelet and an ion, where the short-ranged repulsive interactions dominate, is very likely. An alternative trial move is to perform a cluster displacement where a platelet including a set of surrounding ions and/or platelets are displaced together. A platelet is chosen randomly. The set of particles that are within a certain volume (e.g. a cylinder or sphere) around the center of mass of the platelet

will be translated or rotated randomly (see Fig. 15).

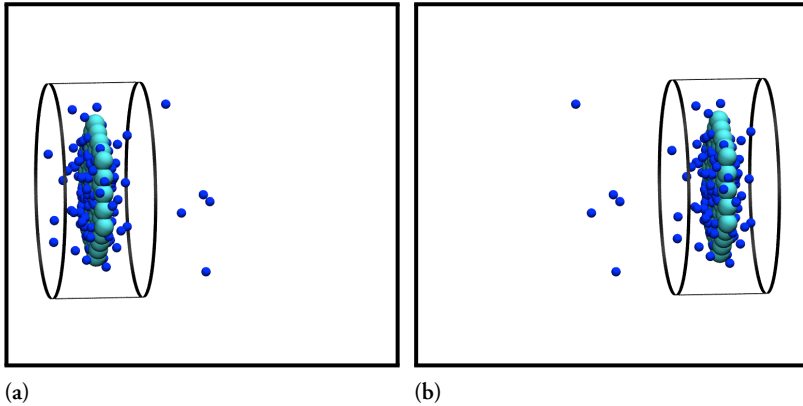


Figure 15: Schematic picture of a cluster displacement. The platelet and ions are represented by the cyan and blue sphere, respectively. (a) All particles within the cylinder are translated together to a new location shown in (b).

To maintain detailed balance, the simplest extra criterion for rejecting a cluster displacement was used in this thesis. That is, if a new particle is introduced into the displaced volume, the configuration is rejected.

**Grand canonical salt:** In the grand canonical ensemble, the number of particles can vary whereas the chemical potential is constant. In some of the simulations of this thesis, the numbers of platelets and corresponding counterions are fixed and additional salt is determined by a chemical potential,  $\mu$ , that represents a certain salt concentration in the reservoir. To maintain electroneutrality of the system, salt particles are inserted and deleted in groups such that the total charge is zero. The acceptance ratio, valid in the canonical ensemble (Eq. (39)) is modified as,

$$\alpha_{\text{insertion}} = \frac{V}{\Lambda^3(N+1)} e^{-\beta(U(\mathbf{\Gamma}_{\text{new}}) - U(\mathbf{\Gamma}_{\text{old}}) - \mu)} \quad (40)$$

for insertion of a particle. The acceptance ratio for deletion of a particle is,

$$\alpha_{\text{deletion}} = \frac{\Lambda^3 N}{V} e^{-\beta(U(\mathbf{\Gamma}_{\text{new}}) - U(\mathbf{\Gamma}_{\text{old}}) + \mu)} \quad (41)$$

### 3.5 Molecular dynamics simulations

A popular alternative to the Metropolis algorithm is molecular dynamics (MD) simulations where the particles of the system move according to Newton's laws of motion.

The advantage of MD is that parallelization is straightforward, the dynamics of a system is obtained, and the algorithms are universal for most types of systems. The disadvantage of traditional MD is that it takes a long time for particles to cross energy barriers much larger than  $k_B T$ , and for most MD packages (e.g. Gromacs (Pronk et al. (2013); Abraham et al. (2014))), the interaction potentials and the forces must be continuous functions.

Newton's second law of motion states,  $\mathbf{F} = m \mathbf{a}$  where  $\mathbf{F}$  is the force,  $m$  is the mass, and  $\mathbf{a}$  is the acceleration. In a system with many particles, the force acting on particle  $i$  at time  $t$  is,

$$\mathbf{F}_i(t) = - \sum_{j \neq i} \nabla u_{ij}(|\mathbf{r}_i(t) - \mathbf{r}_j(t)|) = - \sum_{j \neq i} \nabla u_{ij}(r_{ij}(t)) \quad (42)$$

where the sum is over all particles except the particle  $i$  itself,  $\mathbf{r}_i(t)$  is the position of particle  $i$ , and  $u_{ij}(r)$  is the pair potential between the particles  $i$  and  $j$ . To integrate the equation of motion numerically one can use the Velocity Verlet algorithm. In the Velocity Verlet algorithm, the initial position and velocity of a particle at time  $t$  is defined. The algorithm can then be described in the following steps,

1. Calculate the position of the particle at time  $t + \delta t$ :

$$\mathbf{r}(t + \delta t) = \mathbf{r}(t) + \mathbf{v}(t)\delta t + \frac{\mathbf{a}(t)}{2} \delta t^2 \quad (43)$$

where  $\delta t$  is the timestep,  $\mathbf{a}(t) = \mathbf{F}(t)/m$  is the acceleration (obtained from Eq. (42)),  $\mathbf{v}(t)$  is the velocity, and  $\mathbf{r}(t)$  is the particle position.

2. Calculate  $\mathbf{a}(t + \delta t)$  where the particle position is  $\mathbf{r}(t + \delta t)$ .
3. Calculate the velocity of the particle at time  $t + \delta t$ :

$$\mathbf{v}(t + \delta t) = \mathbf{v}(t) + \frac{\mathbf{a}(t) + \mathbf{a}(t + \delta t)}{2} \delta t \quad (44)$$

4. Start over from step 1 to find the position at time  $t + 2\delta t$ .

MD integrators conserve the number of particles, the volume, and the energy of a system, i.e., represent the microcanonical ensemble, if the timestep,  $\delta t$ , is small enough. To simulate within the canonical ensemble or isobaric ensemble, thermostats (Berendsen et al. (1984); Bussi et al. (2007); Nosé (1984); Hoover (1985)) and barostats (Berendsen et al. (1984); Parrinello & Rahman (1981); Nosé & Klein (1983)) are used. These methods are not described in the thesis. For the interested reader the references above are recommended.

## 3.6 Simulation techniques

### 3.6.1 Boundary conditions

In the simulations, it is necessary to insert some type of boundary to limit the system size due to the finite amount of calculation power. Depending on the system properties and the goal of the study, different types of boundary conditions can be used. Consider that an interaction potential is truncated at a distance  $r_c$ . The interaction,  $u_c$ , beyond  $r_c$  can be estimated as,

$$u_c = \int_{r_c}^{+\infty} u(r) 4\pi r^2 \rho dr \quad (45)$$

where  $\rho$  is the density of the system, and  $u(r)$  is the interaction potential. If  $u(r) \propto r^{-n}$  where  $n > 3$ , then  $u_c$  will be a finite value and the truncation error can be controlled. Thus, a truncation of the van der Waals forces seems to be an appealing approach. On the other hand, if  $n \leq 3$ ,  $u_c$  will diverge for all finite values of  $r_c$ . Hence, depending on what boundary condition that is used one should be aware that interaction potentials such as the Coulomb interaction,  $u(r) \propto r^{-1}$ , needs to be dealt with care.

In this thesis, two types of boundary conditions were considered (see Fig. 16), (i) all particles where located inside a closed volume, or (ii) all particles where located inside a volume with periodic boundary conditions.

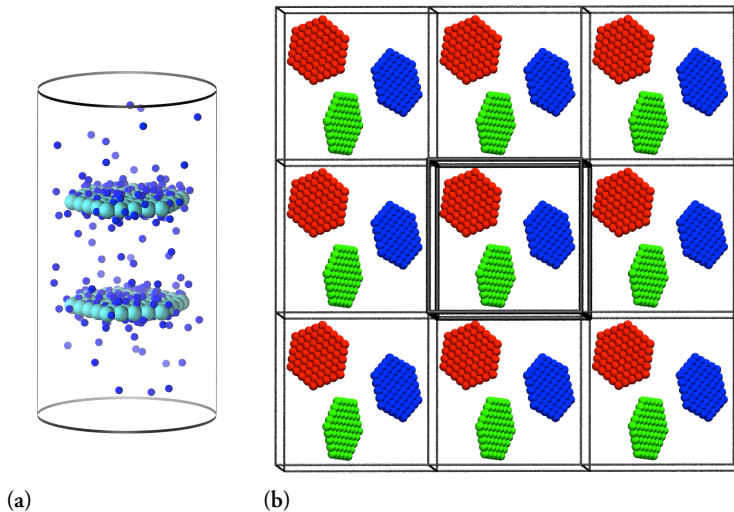


**Figure 16:** Schematic picture of the two types of boundary conditions used in this thesis. (a) All particles are located inside a closed cylinder (the platelets and the ions are represented by the cyan and blue sphere, respectively), and (b) all particles are located inside a cubic box with periodic boundary conditions, eight nearby images surrounding the central image are shown (the three platelets are represented as red, green and blue spheres).

By considering Eq. (45), case (i) seems to be a doomed setup for charged colloids since  $u_c$  diverges. But if one considers a dilute system with a small amount of salt, the interaction between the charged colloid is screened, and to a good approximation, the system can be closed. Moreover, it has been shown that the effective pair potential from a closed system can be used in a many-body system up to reasonable volume fractions (Turesson et al. (2012)). The reason to close the system, is to study the two-body interaction solely and limit the entropy of the counterions. Boundary effects between charged colloidal particles will become more and more apparent as they approach the surface of the closed geometry due to the confinement of the ions. If salt is introduced into the system, the boundary effect will be reduced since the long-ranged interaction is screened. A method to reduce the boundary effect between two charged platelets was used in Paper I. The boundary effect that a single colloidal particle experiences was estimated by calculating the effective pair potential between a ghost particle and a single colloidal particle with its corresponding ions. That potential was then subtracted twice from the effective pair potential between two colloids.

An example of case (ii) has been described in Section 3.3.1 where two parallel surfaces represented the clay platelets and periodic boundary conditions existed in the directions parallel to the surfaces. An external potential was used to take care of the long-range interactions outside the box. The purpose of using periodic boundary conditions in three dimensions is to resemble an infinite (large) system. To simulate a many-body system, the long-ranged interactions can be dealt with the Ewald summation method. An infinite number of images of the simulation box are applied in all dimensions. Within a cut-off, the interaction is calculated in real space. For larger separations, including all images, the interaction is calculated in reciprocal space. The highly efficient implementation of the Ewald summation method, the particle-mesh Ewald summation, was used in this thesis. It is important to use a simulation box that is large enough such that the periodicity does not affect the results. To ensure that this was not the case, the system size was doubled and thermal averages were compared.

## 4 Main Results of the Research Papers

The six papers included in this thesis can be divided into three different groups:

1. Paper I and II: The tactoid formation and the microstructure of negatively charged platelets were investigated by simulations. The effects of surface charge density, platelet size, platelet flexibility, ion valency, and salt concentration were considered.
2. Paper III and IV: The tactoid formation and the microstructure were investigated

for flocculated Laponite, with and without the addition of PEG20k, by SAXS, Cryo-TEM, and computer simulations. The results were compared to flocculated montmorillonite in order to study the effect of varying the platelet size.

3. Paper v and vi: The temperature response of montmorillonite was investigated by free swelling, swelling pressure measurements in a test cell, SAXS, and computer simulations.

A short summary of the main results of each paper is presented below.

#### **4.1 Paper I: Monte Carlo Simulations of Parallel Charged Platelets as an Approach to Tactoid Formation in Clay.**

In the first paper, the free energy of interaction between parallel charged platelets with divalent counterions was calculated using MC simulations. A schematic picture of the model can be seen in Fig. 17. The aim was to investigate the electrostatic effects on aggregation. The platelets are primarily intended to represent clay particles. With divalent counterions, the free energy for two platelets or two tactoids (clusters of parallel platelets) shows a minimum at a short separation due to the attraction caused by ion-ion correlations. In a salt-free system, the free energy of interaction has a long-ranged repulsive tail beyond the minimum. The repulsion increases for tactoids with larger aggregation numbers, whereas the depth of the free-energy minimum is gradually reduced. For large enough aggregation numbers, the repulsion is dominating and the minimum is no longer a global free-energy minimum. This is an effect of the depletion of counterions free in solution (outside tactoids), as counterions and platelets aggregate into tactoids, and the resulting redistribution of counterions in the system changes the effective interactions between platelets and tactoids. The difference in tactoid-tactoid interactions as a function of aggregation number can be removed by adding enough salt to mask the depletion. Adding salt also reduces the repulsive tail of the free energy of interaction and enhances the minimum. No dependence on the aggregation number suggests that an isodesmic model with a monotonically decaying distribution of aggregation numbers can be used to describe a clay system. This may help to explain the experimental observations of low average numbers of platelets in tactoids, although factors not included in the simulation model, for example, rotation, congestion, and polydispersity, may also play an important role.

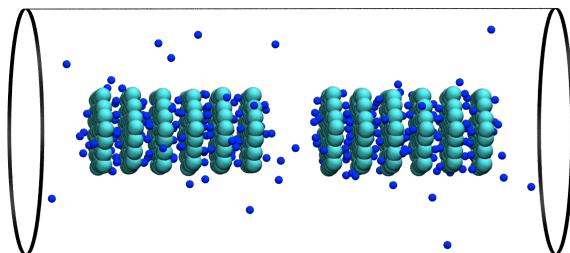


Figure 17: Schematic picture of the model that was used in Paper I. Two parallel tactoids containing six platelets each (cyan spheres) mediated by counterions (blue spheres) are located inside a cylindrical cell.

#### 4.2 Paper II: Interaction and Aggregation of Charged Platelets in Electrolyte Solutions: A Coarse-Graining Approach.

In the second paper, the constraint to consider only parallel platelets, as in Paper I, was removed, i.e., bulk simulations were performed. A schematic picture of the bulk simulations can be seen in Fig. 18. The bulk simulations were used to study the effects of platelet size, flexibility, and surface charge density on platelet aggregation in an aqueous 2:1 electrolyte. Additionally, some systems in a 1:1 electrolyte were also investigated. Furthermore, a coarse-graining approach was developed to replace the effect of explicit ions with an effective pair potential between charged sites in anisotropic colloidal particles by optimizing a potential of mean force against the results of simulations of two such colloidal particles with all ions in a cell model. Bulk simulations of many platelets interacting via the effective pair potentials are in excellent agreement with the corresponding bulk simulations with all mobile charges present.

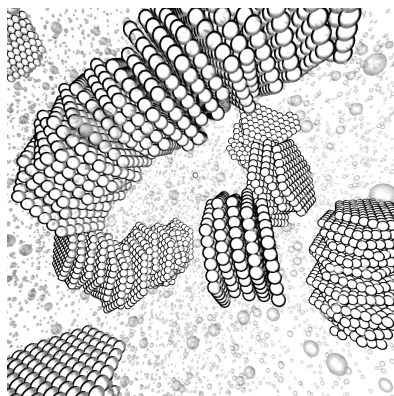


Figure 18: Schematic picture of the microstructure from the bulk simulations in Paper II. The highly charged platelets aggregate and form tactoids with divalent counterions and 2:1 salt.

### 4.3 Paper III: Flocculated Laponite-PEG/PEO Dispersions with Monovalent Salt, a SAXS and Simulation Study.

In this study, SAXS in combination with coarse-grained modeling and molecular dynamics simulations were utilized to study flocculated and sedimented Laponite-PEG/PEO dispersions at elevated monovalent salt concentrations (150 mM–1 M). It was shown that it is possible to induce tactoids for Laponite if two constraints are fulfilled:

1. Addition of a large amount of salt such as NaCl.
2. Addition of a neutral polymer such as PEG.

The role of the salt is to screen the repulsive interactions between the platelets, and the role of the polymer is to bridge between the platelets: hence the loss in configurational entropy of the polymer is counteracted by the gain in attractive polymer-platelet interactions. As the concentration of NaCl and/or PEG increases, the Bragg peak becomes sharper, which is an indication that larger tactoids are formed. The total structure factor for three different polymer concentrations can be seen in Fig. 19. Comparison between Laponite and montmorillonite shows that the interlayer distance between the platelets increases linearly with an increased Debye screening length for both types of clay, whereas the structure peaks of Laponite are broader compared to the ones from montmorillonite. We argue that the main reason for the latter is due to the size of the platelets:

1. Smaller platelets are less rotationally restricted.
2. The effect of positive edge charges is larger when the platelets are smaller, which results in more irregular aggregates.

In the absence of the polymer, montmorillonite forms tactoids above 0.3 M NaCl whereas Laponite does not. Even though the model used is simple, we find qualitative agreement between experiments and simulations, which verifies that the underlying physics for tactoid formation is captured.

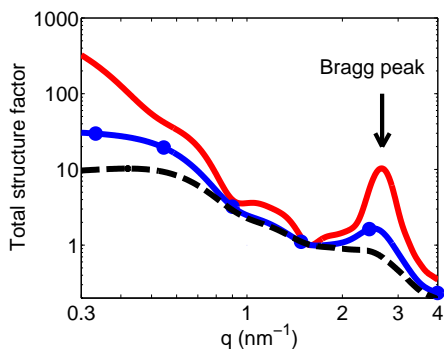


Figure 19: Total structure factor for three different concentrations of the adsorbing polymer at a high 1:1 salt concentration calculated from the computer simulations. Three different polymer concentrations are shown: Low, medium, and high, which corresponds to black dashed, blue circle, and red line, respectively. The location of the Bragg peak is indicated by the vertical arrow. The Bragg peak becomes sharper as the polymer concentration increases, which is an indication that larger tactoids are formed.

#### 4.4 Paper IV: Flocculated Laponite-PEG/PEO Dispersions with Multivalent Salt: A SAXS, Cryo-TEM, and Computer Simulation Study.

In this paper, which is a follow-up study of Paper III, flocculated and sedimented Laponite-PEG/PEO dispersions were studied at elevated multivalent salt concentrations. The effect of having either monovalent salt or multivalent salt was studied by SAXS, USAXS, and Cryo-TEM. In the case of multivalent salt, the coarse-grained molecular dynamics simulations indicate that ion-ion correlations are not enough to induce large tactoids if the platelets are small, and the absolute charge is low, more specifically, in the size and charge range of Laponite. When a polymer is introduced into the system, the tactoid size grows, and the results can be explained by weak attractive electrostatic correlation forces and polymer bridging. It is shown that when the salt concentration increases, the long-ranged electrostatic repulsion is screened, and a free energy minimum appears at short distances due to the ion-ion correlations effects. When a strongly adsorbing polymer is introduced into the system, a second free energy minimum appears at a slightly larger separation. The latter dominates if the polymer is relatively long and/or the polymer concentration is high enough. The potential of mean force (free energy) between two parallel platelets with and without an adsorbing polymer is shown in Fig. 20.

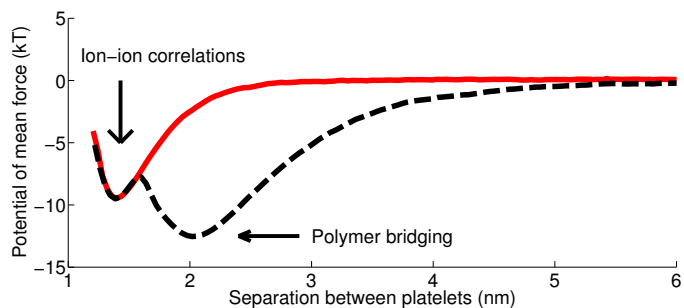


Figure 20: The potential of mean force between two parallel platelets at a high 2:1 salt concentration. Without an adsorbing polymer, a minimum is found due to the ion-ion correlations (red line), whereas by including an adsorbing polymer to the system, polymer bridging occurs (black dashed), and a second minimum is found at a greater distance.

#### 4.5 Paper v: Anomalous Temperature Behavior in Clay Swelling due to Ion-Ion Correlations.

Free swelling, swelling pressure measurements in a test cell, and simulations show that the swelling of both natural and refined clays has an anomalous temperature behavior depending on the counterion valency. In an aqueous clay dispersion dominated by monovalent counterions, the swelling pressure increases with temperature as expected from entropic arguments. In a clay with predominantly divalent counterions, the opposite behavior is found. The explanation is due to the fact that ion-ion correlations increase with temperature, which is a mechanism that is important at strong electrostatic coupling. In an aqueous solution the dielectric constant,  $\epsilon_r$ , decreases with increased temperature,  $T$ , in such a way that the product  $\epsilon_r T$  also decreases. Thus, the Bjerrum length increases and the net effect is an increased coupling.

#### 4.6 Paper vi: Temperature Response of Charged Colloidal Particles by Mixing Counterions Utilizing $\text{Ca}^{2+}/\text{Na}^+$ Montmorillonite as Model System.

The osmotic pressure and the aggregation of charged colloids as a function of temperature were investigated using MC and MD simulations for different ratios of monovalent and divalent counterions. It was found that the temperature response can be controlled, i.e., the osmotic pressure can increase, decrease, or be kept constant, as a function of temperature, depending on the monovalent/divalent counterion ratio. The increase in osmotic pressure with temperature, which occurs at low enough surface charge density, and/or low fraction of divalent ions, can be understood from the DLVO-theory. The origin of the opposite behavior can be explained by the enhanced attractive electrostatic ion-ion correlation interactions with temperature. The constraint is that the absolute

value of the surface charge density of the colloids must be above a certain threshold, i.e., high enough such that the attractive ion-ion correlations can dominate for the divalent ions. The current conclusions are supported by the microstructural characterization of  $\text{Ca}^{2+}/\text{Na}^{+}$ -montmorillonite clay using SAXS. A qualitative agreement is observed between the simulations and the experimental data. The results of the simulations are shown in Fig. 21.

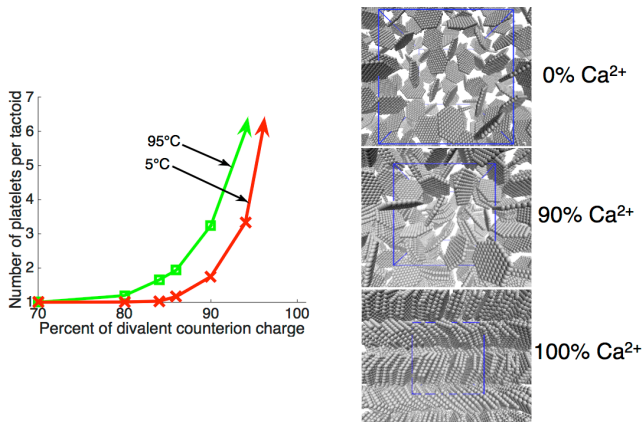


**Figure 21:** Number of platelets per tactoid as a function of the fraction of divalent ions in percent. The size of the tactoids increases with temperature (left graph). The microstructure of three different systems with 0%, 90%, and 100% fraction of divalent ions are shown in the schematic pictures to the right. With 0%  $\text{Ca}^{2+}$  the platelets repel each other and there are no tactoids, with 90%  $\text{Ca}^{2+}$  some tactoids are formed, and with 100%  $\text{Ca}^{2+}$  all platelets have aggregated.

## 5 Conclusions and Future Perspectives

In this thesis, I have performed coarse-grained simulations of negatively charged platelets that are intended to represent clay platelets. The microstructure and the tactoid formation of these platelets have been investigated by varying the platelet surface charge density, platelet size, platelet flexibility, valency of ions, salt concentration, temperature, and addition of adsorbing polymers.

The purpose of the simulations was to try to connect theory with experimental findings in literature as well as my own experiments. A number of different experimental techniques have been used in an attempt to characterize the swelling and the microstructure of the clay minerals Laponite and montmorillonite (SAXS, Cryo-TEM, swelling pressure measurements, and free swelling).

During my PhD studies, a number of theoretical investigations of charged nanoplatelets have appeared in the literature. Various assumptions and simplifications have been made in order to be able to simulate a many-platelet system to derive a phase diagram and/or

study the microstructure: (i) platelets interacting through an effective pair potential obtained within nonlinear PB formalism (Jabbari-Farouji et al. (2014)), (ii) platelets with anisotropic charge (negative face charges and positive edge charges) interacting through a screened Coulomb potential (Delhorme et al. (2012, 2014)), and (iii) platelets interacting through an effective Gay-Berne potential parametrized from atomistic simulations (Ebrahimi et al. (2014)), to mention a few.

I believe that all the above mentioned references as well as this thesis contain some pieces of the puzzle to understand the complex behavior of clays within the assumptions that were made. The simulations in this thesis have been limited to either small uniformly charged platelets, or infinite uniformly charged surfaces, where all ions have been treated explicitly. It is my belief that fruitful extensions of this work would be to increase the diameter of the platelets, include a polydisperse distribution of the platelet diameter, and to include charge anisotropy while still including all the ions explicitly. In that way both monovalent and multivalent ions can be included, and thereby to study more realistic and detailed systems. For example it would be interesting to study the temperature response, the dynamic response of adding an adsorbing polymer, and the tactoid formation. Some simulations of the suggested extended model have been performed, but none of the results have been published. In Fig. 22, two examples of the microstructure are shown for nanoplatelets with positive edge charges, mediated by monovalent ions.

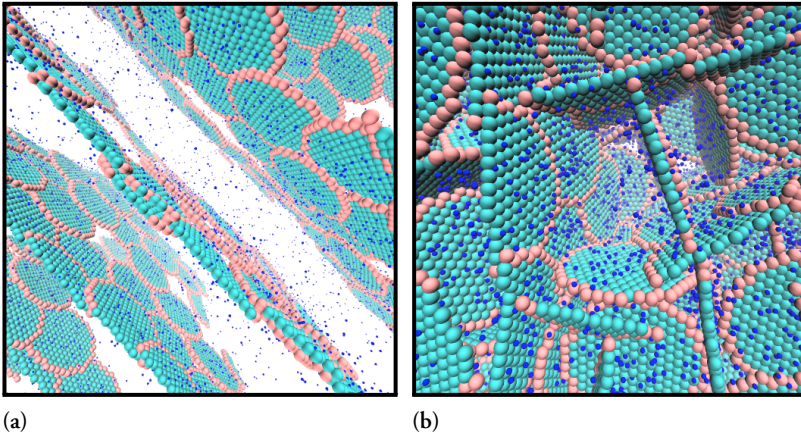


**Figure 22:** Representative configurations (unpublished work) of platelets with diameter 15 nm at two different volume fractions. The platelets are negatively charged on the surface and have positively charged edges. The negatively, and positively charged sites are represented as cyan, and red spheres respectively. The monovalent ions are represented as blue spheres.

## 6 References

- Abraham, M. J., van der Spoel, D., Lindahl, E., Hess, B., & the GROMACS development team. 2014, GROMACS User Manual version 5.0.1, [www.gromacs.org](http://www.gromacs.org)
- Allen, M. P. & Tildesley, D. J. 1989, *Computer Simulation of Liquids* (Oxford University Press)
- Almgren, M., Edwards, K., & Karlsson, G. 2000, *Colloids and Surfaces A: Physicochemical and Engineering Aspects*, 174, 3
- Anderson, R. L., Ratcliffe, I., Greenwell, H. C., et al. 2010, *Earth-Science Reviews*, 98, 201
- Bailey, S. W. 1980, *Clay Minerals*, 15, 85
- Berendsen, H. J. C., Postma, J. P. M., van Gunsteren, W. F., DiNola, A., & Haak, J. R. 1984, *The Journal of Chemical Physics*, 81, 3684
- Bergaya, F., Theng, B. K. G., & Lagaly, G. 2006, *Developments in Clay Science, Vol. 1, Handbook of Clay Science* (Elsevier)
- Birgersson, M., Karnland, O., & Nilsson, U. 2010, SKB Technical Report, TR-10-40
- Bussi, G., Donadio, D., & Parrinello, M. 2007, *The Journal of Chemical Physics*, 126, 014101
- BYK. 2016, Technical Information B-RI 21 LAPONITE® Performance Additives
- Callen, H. B. 1985, *Thermodynamics and an Introduction to Thermostatistics*, 2nd edn. (Wiley)
- Chen, B., Evans, J. R. G., Greenwell, H. C., et al. 2008, *Chemical Society Reviews*, 37, 568
- Choi, E., Mondal, J., & Yethiraj, A. 2014, *The Journal of Physical Chemistry B*, 118, 323
- Delhomme, M., Jönsson, B., & Labbez, C. 2012, *Soft Matter*, 8, 9691
- Delhomme, M., Jönsson, B., & Labbez, C. 2014, *RSC Advances*, 4, 34793
- Derjaguin, B. V. & Landau, L. 1941, *Acta Physico Chemica URSS*, 14, 633
- Ebrahimi, D., Whittle, A. J., & Pellenq, R. J.-M. 2014, *The Journal of Chemical Physics*, 140, 154309

- Evans, D. F. & Wennerström, H. 1999, *The Colloidal Domain: Where Physics, Chemistry, Biology, and Technology Meet*, 2nd edn. (Wiley-VCH)
- Glatter, O. & Kratky, O. 1982, *Small Angle X-ray Scattering* (Academic Press, London)
- Grim, R. E. 1953, *Clay Mineralogy* (McGraw-Hill, New York)
- Guggenheim, S. & Martin, R. T. 1995, *Clays and Clay Minerals*, 43, 255
- Gutiérrez, G. & Johansson, B. 2002, *Physical Review B*, 65, 104202
- Hill, T. L. 1986, *An Introduction to Statistical Thermodynamics* (Dover Publications Inc., New York)
- Hoover, W. G. 1985, *Physical Review A*, 31, 1695
- Israelachvili, J. N. 2011, *Intermolecular and Surface Forces*, 3rd edn. (Academic press)
- Israelachvili, J. N. & Adams, G. E. 1978, *Journal of the Chemical Society, Faraday Transactions 1*, 74, 975
- Jabbari-Farouji, S., Weis, J.-J., Davidson, P., Levitz, P., & Trizac, E. 2014, *The Journal of Chemical Physics*, 141, 224510
- Jönsson, B., Nonat, A., Labbez, C., Cabane, B., & Wennerström, H. 2005, *Langmuir*, 21, 9211
- Jönsson, B. & Wennerström, H. 2001, *Electrostatic Effects in Soft Matter and Biophysics* (Springer Netherlands), 171–204
- Karnland, O., Olsson, S., & Nilsson, U. 2006, SKB Technical Report, TR-06-30
- Martin, C., Pignon, F., Magnin, A., et al. 2006, *Langmuir*, 22, 4065
- Mauroy, H., Plivelic, T. S., Hansen, E. L., et al. 2013, *The Journal of Physical Chemistry C*, 117, 19656
- Metropolis, N., Rosenbluth, A. W., Rosenbluth, M. N., Teller, A. H., & Teller, E. 1953, *The Journal of Chemical Physics*, 21, 1087
- Michot, L. J., Bihannic, I., Porsch, K., et al. 2004, *Langmuir*, 20, 10829
- Mongondry, P., Nicolai, T., & Tassin, J. F. 2004, *Journal of Colloid and Interface Science*, 275, 191
- Moreira, A. G. & Netz, R. R. 2002, *The European Physical Journal E*, 8, 33
- Netz, R. R. 2001, *The European Physical Journal E*, 5, 557

- Nosé, S. 1984, *Molecular Physics*, 52, 255
- Nosé, S. & Klein, M. 1983, *Molecular Physics*, 50, 1055
- Parrinello, M. & Rahman, A. 1981, *Journal of Applied Physics*, 52, 7182
- Pashley, R. M. 1981, *Journal of Colloid and Interface Science*, 83, 531
- Patterson, A. L. 1939, *Physical Review*, 56, 978
- Pronk, S., Páll, S., Schulz, R., et al. 2013, *Bioinformatics*, 29, 845
- Ruzicka, B. & Zaccarelli, E. 2011, *Soft Matter*, 7, 1268
- Schnablegger, H. & Singh, Y. 2013, *The SAXS Guide* (Anton Paar GmbH, Austria)
- Segad, M. 2013, *Journal of Applied Crystallography*, 46, 1316
- Segad, M., Cabane, B., & Jönsson, B. 2015, *Nanoscale*, 7, 16290
- Segad, M., Jönsson, B., Åkesson, T., & Cabane, B. 2010, *Langmuir*, 26, 5782
- SKB. 2011, SKB Technical Report, TR-11-01
- Svensson, P. D. 2015, PhD thesis, Lund University, Lund, Sweden
- Turesson, M., Jönsson, B., & Labbez, C. 2012, *Langmuir*, 28, 4926
- Verwey, E. J. W. & Overbeek, J. T. G. 1948, *Theory of the Stability of Lyophobic Colloids* (Amsterdam: Elsevier Publishing Company Inc.)
- Xie, F., Turesson, M., Jansson, M., Skepö, M., & Forsman, J. 2016, *Polymer*, 84, 132

# Scientific Publications

## Author Contributions

### **Paper I: Monte Carlo Simulations of Parallel Charged Platelets as an Approach to Tactoid Formation in Clay.**

Involved in planning and wrote the first version of the manuscript. Performed all simulations and analyses.

### **Paper II: Interaction and Aggregation of Charged Platelets in Electrolyte Solutions: A Coarse-Graining Approach.**

Initiated, planned, and formulated the scientific questions and hypotheses together with the co-authors. Wrote the manuscript together with my co-authors. Developed and implemented the coarse-graining method. Performed all MC simulations.

### **Paper III: Flocculated Laponite-PEG/PEO Dispersions with Monovalent Salt, a SAXS and Simulation Study.**

Planned and formulated the scientific questions and hypotheses together with the co-authors. Main responsible for writing the manuscript with input from my co-authors. Planned and performed most of the experiments as well as all the simulations with their corresponding analyses. Responsible for the submission and the revision process.

**Paper iv: Flocculated Laponite-PEG/PEO Dispersions with Multivalent Salt: A SAXS, Cryo-TEM, and Computer Simulation Study.**

Planned and formulated the scientific questions and hypotheses together with the co-authors. Main responsible for writing the manuscript with input from my co-authors. Planned and performed most of the experiments as well as all the simulations with their corresponding analyses. Responsible for the submission and the revision process.

**Paper v: Anomalous Temperature Behavior in Clay Swelling due to Ion-Ion Correlations.**

Initiated, planned, and formulated the scientific questions and hypotheses together with the co-authors. Planned, performed, and analyzed all the experiments together with my co-authors. Participated in writing the manuscript. Responsible for the submission and the revision process.

**Paper vi: Temperature Response of Charged Colloidal Particles by Mixing Counterions Utilizing  $\text{Ca}^{2+}/\text{Na}^+$  Montmorillonite as Model System.**

Initiated, planned, and formulated the scientific questions and hypotheses. Main responsible for writing the manuscript with input from my co-authors. Assisted the second author in performing the simulations and the corresponding analyses. Assisted my co-authors in planning the experiments. I conducted all the analyses of the experiments. Responsible for the submission and the revision process.

Reprinted with permission from *Langmuir*, 2013, 29, 9216-9223  
A. Thuresson, M. Ullner, T. Åkesson, C. Labbez and B. Jönsson  
©2013 American Chemical Society.



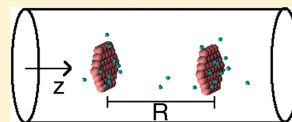
## Monte Carlo Simulations of Parallel Charged Platelets as an Approach to Tactoid Formation in Clay

Axel Thuresson,<sup>†</sup> Magnus Ullner,<sup>\*,†</sup> Torbjörn, Åkesson,<sup>†</sup> Christophe Labbez,<sup>‡</sup> and Bo Jönsson<sup>†</sup>

<sup>†</sup>Theoretical Chemistry, Lund University, POB 124, SE-221 00 Lund, Sweden

<sup>‡</sup>Laboratoire Interdisciplinaire Carnot de Bourgogne, UMR 6303 CNRS, Université de Bourgogne, F-21078 Dijon Cedex, France

**ABSTRACT:** The free energy of interaction between parallel charged platelets with divalent counterions has been calculated using Monte Carlo simulations to investigate the electrostatic effects on aggregation. The platelets are primarily intended to represent clay particles. With divalent counterions, the free energy for two platelets or two tactoids (clusters of parallel platelets) shows a minimum at a short separation due to the attraction caused by ion–ion correlations. In a salt-free system, the free energy of interaction has a long-range repulsive tail beyond the minimum. The repulsion increases for tactoids with larger aggregation numbers, whereas the depth of the free-energy minimum is gradually reduced. For large enough aggregation numbers, the repulsion is dominating and the minimum is no longer a global free-energy minimum. This is an effect of the depletion of counterions free in solution (outside tactoids) as counterions and platelets aggregate into tactoids and the resulting redistribution of counterions in the system changes the effective interactions between platelets and tactoids. The difference in tactoid–tactoid interactions as a function of aggregation number can be removed by adding enough salt to mask the depletion. Adding salt also reduces the repulsive tail of the free energy of interaction and enhances the minimum. No dependence on the aggregation number suggests that an isodesmic model with a monotonically decaying distribution of aggregation numbers can be used to describe a clay system. This may help to explain the experimental observations of low average numbers of platelets in tactoids, although factors not included in the simulation model may also play an important role.



### INTRODUCTION

Clay is available in large natural deposits and has many industrial applications such as paint, cosmetics, drilling fluids, and paper fillers. Moreover, several countries plan to deposit spent nuclear fuel for long-term storage in deep geological repositories with bentonite clay as a buffer to protect the containers and prevent radioactive leakage into the environment. Both the mechanical stability and the properties as a barrier are related to the internal structure of the clay and the ability to swell. A typical clay mineral consists of large negatively charged sheets, and depending on whether the counterions are (predominantly) monovalent or divalent, the swelling can be unlimited or restricted. The differences can also be seen on a microscopic level. Whereas the mineral sheets repel each other with monovalent counterions, the clay platelets aggregate into so-called tactoids when the counterions are divalent. Studies have shown an average number of platelets in tactoids of calcium montmorillonite of about 5–20.<sup>1–8</sup> The aggregation can be understood because previous theoretical work has shown that there is a strong attraction between highly charged surfaces with multivalent counterions as a result of ion–ion correlations.<sup>9–14</sup> However, given the strong attraction between two platelets, a naive guess would be that all platelets would aggregate into a macroscopic ordered phase. The purpose of this investigation is to look for a reason that this is not happening.

To study the interactions between charged colloids (such as clay platelets), one approach is to use the Derjaguin–Landau–Verwey–Overbeek (DLVO) theory,<sup>15,16</sup> which combines

attractive van der Waals forces with an electrostatic double-layer repulsion obtained from the Poisson–Boltzmann (PB) equation. Although the mean-field approximation of the PB equation has proven useful when the electrostatic coupling is not too strong, it fails for highly charged colloids with divalent counterions because of the neglect of ion–ion correlations. We would therefore not expect the DLVO approach to offer a correct explanation of the tactoid formation in the presence of divalent ions. To catch the attractive effect of ion–ion correlations, we have performed Monte Carlo simulations with explicit counterions.

The outline of the article is as follows. The model and simulation details are described in the Methods section. In Results and Discussion, we first consider two single platelets (singlets) in a cylindrical cell. The effect of changing the cell volume, surface charge density, and size of the singlets will be discussed. This is followed by a study of tactoids with different aggregation numbers and a discussion of the distribution of aggregation numbers. Finally, we end with Conclusions.

### METHODS

**Model.** The interactions are described within the primitive model (i.e., the particles are hard, charged spheres and the solvent is treated as a continuum with a dielectric constant  $\epsilon_r$

Received: April 5, 2013

Revised: June 16, 2013

Published: July 8, 2013

that is uniform throughout the system). Particles are interacting pairwise with the potential

$$u_{ij}(r_{ij}) = \begin{cases} \frac{Z_i Z_j e^2}{4\pi\epsilon_0\epsilon_r r_{ij}} & \text{if } r_{ij} > R_i + R_j \\ +\infty & \text{otherwise} \end{cases} \quad (1)$$

where  $e$  is the charge of a proton,  $\epsilon_0$  is the permittivity of vacuum,  $R_i$  is the radius and  $Z_i$  is the valency of particle  $i$ , and  $r_{ij}$  is the distance between two particles.

A platelet is constructed from spheres with a charge of  $-1e$  and a radius of 5 Å arranged as a hexagon on a lattice with a distance of 6.8 Å between lattice points for a charge density  $\sigma = -0.025 \text{ e}/\text{Å}^2$  and 7.5 Å for  $\sigma = -0.020 \text{ e}/\text{Å}^2$  when viewed from one side. A typical one-sided charge density for montmorillonite would be  $-0.015 \text{ e}/\text{Å}^2$ , based on a cationic exchange capacity of 1 mequiv/g<sup>17,18</sup> and a specific (two-sided) surface area of 800 m<sup>2</sup>/g,<sup>19</sup> which corresponds to a density of 2.5 g/cm<sup>3</sup> using a platelet thickness of 10 Å. To avoid symmetry artifacts, the platelet sites are randomly displaced in the plane of the hexagon. Each sphere is displaced within a square with a 1 Å side and centered on the hexagonal lattice point. Because a hexagonal platelet has an odd number of sites, the central site is uncharged to allow one platelet to be neutralized by an integral number of divalent counterions. The radius of the ions, counterions as well as any added salt ions, is 2 Å.

The system is confined in a cylindrical cell. The aim is to study the interactions involved in the formation of tactoids, where the platelets are stacked in parallel. The simulated platelets are therefore kept parallel and are allowed to move only in the  $z$  direction along the central axis of the cylinder. A sketch of the system is shown in Figure 1. Unless stated

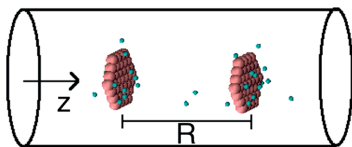


**Figure 1.** Schematic representation of a cylindrical cell with a snapshot from a simulation of two platelets (hexagonal discs composed of large spheres) and counterions (small spheres). The platelets are parallel and are allowed to move only in the  $z$  direction, but the counterions can move freely inside the cell.

otherwise, the interacting platelets/tactoids are moved in unison symmetrically around the center of the cell. The counterions are allowed to explore the entire cell.

It should be noted that we are not interested in the actual process of tactoid formation but in the equilibrium properties of the system, in particular, electrostatic effects and differences between tactoids with different numbers of platelets. The calculated interactions thus primarily serve to gauge differences in free energies under different conditions and for different species. This is one reason that we allow ourselves the simplification of parallel platelets. The tactoids consist by definition of parallel platelets, and to a first approximation, rotations would give similar contributions to the free energies of interaction between tactoids with different aggregation numbers. The latter may be questionable for our model with comparatively thick platelets but would be a better approx-

imation for a real system where the clay platelets are thin and wide, which means that the aspect ratio changes slowly with aggregation number, and rotations may be hindered, even at relatively low volume fractions. In other words, by not allowing rotations, we may even avoid introducing artifacts due to the small size of our platelets, although this is a conjecture.

A similar argument can be made about the use of the primitive model, which with a uniform dielectric constant and implicit solvent ignores short-range solvent effects, such as hydration, and the changes in the dielectric environment between the bulk and the slits in tactoids. As long as the errors cancel in the free-energy differences, the general conclusions will remain valid. Furthermore, there are many cases where the continuum model appears to be applicable down to surprisingly short separations.<sup>20,21</sup>

The “standard” concentration of platelets is chosen to be large enough for the system to display a global free-energy minimum at short separations for two platelets. The length  $L_{\text{cell}}$  and radius  $R_{\text{cell}}$  of the cylinder are set so that the average counterion concentration on the cylindrical surface is approximately the same as on the capping circular surfaces, which can be shown to give an optimal aspect ratio and corresponds to a consistent osmotic pressure.<sup>22</sup> For the chosen standard concentration, an aspect ratio of  $L_{\text{cell}}/R_{\text{cell}} = 4$  was found to give a reasonably consistent osmotic pressure.

If nothing else is stated, then the simulation results are for platelets with 37 sites,  $\sigma = -0.025 \text{ e}/\text{Å}^2$ , and a platelet concentration corresponding to two platelets in a cylindrical cell with  $L_{\text{cell}} = 200 \text{ Å}$  and  $R_{\text{cell}} = 50 \text{ Å}$  (i.e., a counterion concentration of 38 mM and a platelet volume fraction of  $\phi \approx 0.02$ ).

**Monte Carlo Simulations.** Canonical Monte Carlo (MC) simulations are performed with the Metropolis algorithm,<sup>23</sup> and umbrella sampling is used to allow parallel execution and more efficient sampling using the Faunus molecular simulation framework.<sup>24</sup> The possible platelet separations are divided into (slightly overlapping) windows, where each window is used to calculate the free energy  $A(R)$  for a certain interval of platelet separations  $R$ . The free energies from the different windows can be joined to give the free energy for the full range of separations by requiring that the free energy should be continuous and have the same value in different windows for a given  $R$ .

A cluster move<sup>25,26</sup> is used where counterions within a cylindrical volume around the platelets are moved together with the platelets. Apart from the normal acceptance criterion depending on the difference in energy for old and new positions, a platelet move is rejected if new counterions are found within the selection volume after the move. The radius of the selection volume is approximately the radius of a hexagonal platelet, and the cylinder extends 10 Å on either side of a single platelet or the outermost platelets in a tactoid. Note that the platelet sites have a radius of 5 Å, and the selected counterions outside a platelet/tactoid are therefore within a 5-Å-wide slit on either side. An exception is the simulation windows containing separations corresponding to “contact” between the two platelets/tactoids. In these cases, the cylindrical extension on the side facing the other platelet/tactoid is only 7 Å (2-Å-wide slit for counterions) to allow separations down to 14 Å.

**Free Energy.** We are interested in the free energy as a function of the separation  $R$  between two tactoids,

$$\beta A(R) = -\ln \int d\mathbf{r}^N \exp(-\beta U(R, \mathbf{r}^N)) + \text{const} \quad (2)$$

where  $\beta \equiv 1/k_B T$ , with  $k_B$  being Boltzmann's constant and  $T$  being the absolute temperature.  $\mathbf{r}^N$  represents the coordinates of the  $N$  counterions, and  $U(R, \mathbf{r}^N) = \sum_{i>j} u_{ij}(r_{ij})$  is the sum of interactions between all combinations of platelet sites and counterions in a given configuration. However, what we measure is the difference in free energy for different values of  $R$  or the probability density

$$P(R) = \frac{\exp(-\beta A(R))}{Z} = \frac{\int d\mathbf{r}^N \exp(-\beta U(R, \mathbf{r}^N))}{\int dR \int d\mathbf{r}^N \exp(-\beta U(R, \mathbf{r}^N))} \quad (3)$$

where  $Z$  is the configuration integral of the simulated system. The configuration integral is not obtained separately, and the free energy is determined only to within an unknown constant, as indicated in eq 2.

The outer tail of the counterion cloud in the  $z$  direction for each platelet gets squeezed between the boundary and the platelet, giving rise to an increasing free energy at large separations (Figure 2). To remove this effect, the free energy is

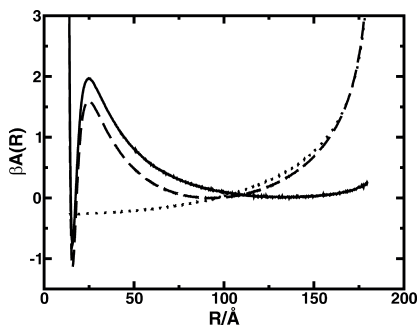


**Figure 2.** Demonstration of the boundary effect and its removal. The free energy is calculated as a function of the separation between two platelets (dashed line) and between a single platelet and a “ghost” (dotted line, multiplied by a factor of 2). The excess free energy (solid line) is obtained as the difference between the singlet–singlet free energy and 2 times the singlet–ghost free energy.

calculated for each tactoid alone in the system. The free energy is still calculated as a function of  $R$ , which is now the separation to a nonexistent tactoid, a “ghost”. The “boundary-corrected” excess free energy of interaction is then obtained by subtracting the free energies of the single tactoids from the free energy of the system with two interacting tactoids. Thus, the zero level of the free energy can be regarded as two noninteracting tactoids (including counterions).

## RESULTS AND DISCUSSION

Tactoids will be labeled by how many platelets they contain. A single platelet will be called a singlet, two platelets with a fixed, small separation will be called a doublet, and three stacked platelets will be called a triplet and so forth.

**Singlet–Singlet Interactions.** The excess free energy of interaction between two singlets in a salt-free system with divalent counterions, illustrated by Figure 2, shows a repulsive

part (i.e., increasing free energy as the separation decreases). This can be seen as the normal double-layer repulsion mainly caused by the compression of ion clouds outside the charged surfaces. At short separations, however, there is a minimum due to the attraction caused by the electrostatic ion–ion correlations opposed by a strong repulsion due to the confinement of the ions. This repulsion is partially entropic and partially due to direct interactions. The minimum distance between platelets when ions can still fit in the slit as hard spheres is roughly 14 Å (the platelets are not smooth but also consist of hard spheres). However, such close packing is unlikely because of the other interactions and the entropic loss, and the free-energy minimum is found slightly further out, at 16 Å. Stronger attraction can push the minimum to shorter separations but only very little because the repulsion rises sharply. As we will show, the position of the minimum stays rather constant when we change the conditions because the size and charge of the counterions are not changed and the repulsive interactions at very short separations are therefore more or less the same.

Because the ion–ion correlations are electrostatic in origin, increasing the electrostatic coupling increases the effect. One way of doing that is to increase the valency of the counterions, which we have done by choosing divalent ions instead of monovalent ions. Under normal conditions, monovalent counterions would give only double-layer repulsion. Another option is to increase the surface charge density. Figure 3 shows

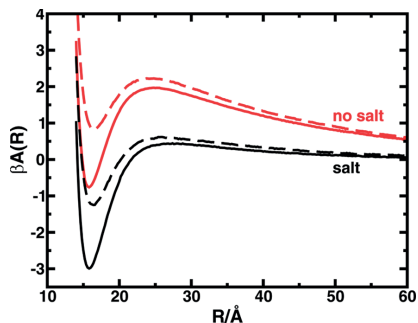


**Figure 3.** Singlet–singlet excess free energy of interaction for different surface charge densities,  $\sigma = -0.025 \text{ e}/\text{\AA}^2$  (solid lines) and  $-0.020 \text{ e}/\text{\AA}^2$  (dashed lines), without added salt (red curves) and with 10 mM 2:1 salt (black curves).

how the minimum becomes deeper for a higher surface charge density. The figure also shows the effect of adding salt. The repulsive part is reduced because the extension of the electrical double layer becomes smaller and the minimum becomes more pronounced as a result of the reduced repulsion.

Because the simulated platelets have a finite size, there are additional effects. For infinite walls, the amount of counterion charge between platelets is expected to balance the surface charges. With finite platelets, it is possible to reduce the number of counterions between the platelets by dilution (i.e., by increasing the total volume of the system). Fewer counterions in the solution between the platelets will reduce the ion–ion correlations and thus the attraction. The entropic double-layer repulsion will also be reduced, but the lower

degree of (local) neutralization will expose some of the platelet charges across the slit, leading to an electrostatic platelet–platelet repulsion. Figure 4 shows the effect of increasing the

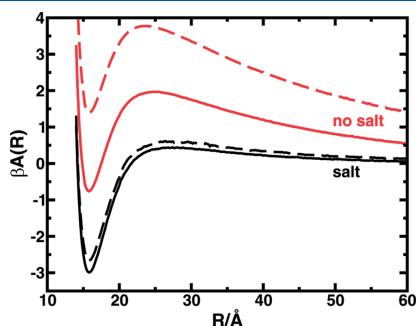


**Figure 4.** Singlet–singlet excess free energy of interaction for different cell volumes without added salt (red curves) and with 10 mM 2:1 salt (black curves). The dashed curves represent a volume that is 3.4 times larger than the volume for the solid curves, which are the same as in Figure 3 ( $\sigma = -0.025 e/\text{\AA}^2$ ).

cell volume, which gives a slightly shallower minimum and stronger and more long-ranged repulsion. If extra counterions are added as part of a salt and the salt concentration is kept constant as the volume is increased, then the dilution effect is masked and the free energy of interaction does not change very much. Compared to the salt-free case, adding salt means better screening of the platelets and an increase in the counterion density in between the platelets, which makes the minimum more pronounced because there are more counterions available for the correlation effect.

The effect of increasing the size of the platelets while maintaining the total counterion concentration is shown in Figure 5. Larger platelets allow more ion–platelet interactions, which gives a higher degree of (local) neutralization with a stronger ion–ion correlation effect and a deeper minimum in

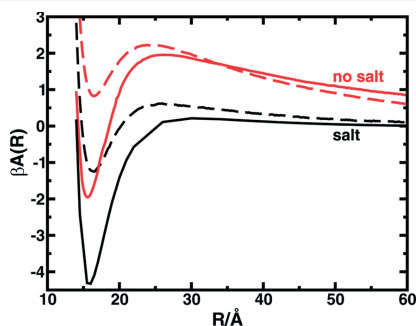


**Figure 5.** Singlet–singlet excess free energy of interaction for different numbers of sites in a platelet, 37 (dashed lines) and 127 (solid lines, scaled by a factor of 36/126, the relative number of charges in a small/large platelet) at constant counterion concentration for  $\sigma = -0.020 e/\text{\AA}^2$ , without added salt (red curves) and with 10 mM 2:1 salt (black curves).

both the salt-free case and with added salt. The repulsion beyond the minimum is much less affected, which could also be said about the effect of changing the surface charge density in Figure 3. This is in agreement with SAXS studies on size-fractionated calcium montmorillonite, where larger platelets form larger tactoids whereas small platelets do not form tactoids to a significant degree.<sup>8,27</sup>

**Tactoid–Tactoid Interactions.** The simplest and most time-saving representation of a tactoid is to keep platelets at a fixed separation that corresponds to the minimum in the free energy of interaction. To confirm that the minimum found for two singlets forming a doublet is also valid for larger tactoids, simulations were performed with one singlet fixed at the origin and two other singlets allowed to move independently in the  $z$  direction on each side of the fixed singlet. The results showed a free-energy minimum when both mobile singlets were 16 Å from the central singlet, which is indeed the same separation as the free-energy minimum of the singlet–singlet simulations. Thus, this separation was used throughout as the fixed internal distance of doublets, triplets, and so forth.

In Figure 6, the free energy is shown as a function of the separation between tactoids consisting of different numbers of

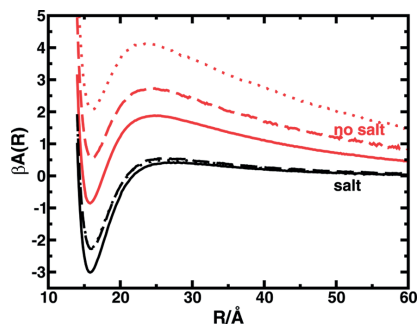


**Figure 6.** Excess free energy of interaction for tactoids with different aggregation numbers, singlet–singlet (solid lines), doublet–doublet (dashed lines), and hexet–hexet (dotted lines), without added salt (red curves) and with 10 mM 2:1 salt (black curves) at constant platelet concentration.

platelets. The short-range free-energy minimum is consistently found at  $R = 16$  Å, which is also the distance between platelets in the tactoids. However, as the tactoids grow in aggregation number, in the absence of salt, the minimum is becoming more shallow while the repulsive tail of the free energy curve shifts upward, raising the minimum value further and changing it from a global minimum to a local one.

This can be explained as follows: When more and more platelets are joined into tactoids, they bring with them counterions to be sandwiched in a new layer between adjoining platelets. The concentration of “free”, nonaggregated counterions is thus reduced. With a lower concentration of free counterions, the density of counterions in the electrical double layers between tactoids is also reduced to compensate partially for the loss in entropy. Fewer neutralizing counterions mean less attraction due to ion–ion correlations and more electrostatic repulsion between platelets. However, when salt is added, the concentration of counterions outside tactoids stays nearly

constant and there is no dependence on aggregation number, apart from a slightly deeper minimum for the singlet–singlet case.

To confirm the entropic mechanism, we need to calculate the free energy of interaction for tactoids with different aggregation numbers at the same concentration of free counterions. To this end, we have performed simulations in what we call a buffer model, illustrated in Figure 7. The system contains a moving

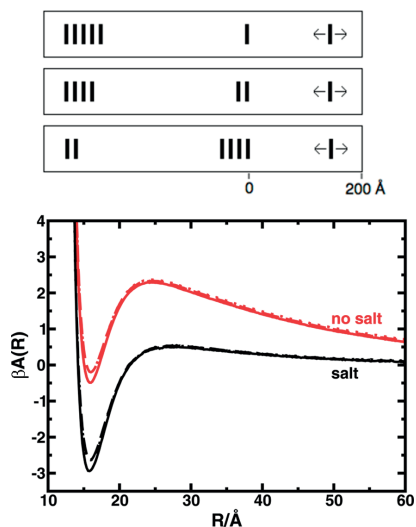


**Figure 7.** Free energy (no removal of boundary effects) of a singlet (solid lines), doublet (dashed lines), and quartet (dotted lines) interacting with a moving singlet in a system also containing a buffer tactoid. (See the text.) A schematic representation of the buffer model is also shown ( $L_{\text{cell}} = 700 \text{ \AA}$ ,  $R_{\text{cell}} = 50 \text{ \AA}$ ). Results are shown for simulations without added salt (red curves) and with 10 mM 2:1 salt (black curves).

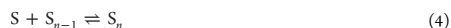
singlet interacting with a fixed tactoid, the tactoid of interest. Thus far, the cell would resemble our normal system, but it also contains an additional fixed tactoid, the buffer tactoid. When a larger tactoid of interest is simulated, the extra platelets are removed from the buffer tactoid to keep the number of platelets in tactoids constant. Because the dimensions of the cell are also kept fixed, a constant concentration of free counterions is maintained when the aggregation number of the tactoid of interest is changed. Furthermore, the moving singlet will experience the same boundary effects as a function of separation, and there is no need to subtract the boundary effects for the comparison in the buffer model.

Figure 7 shows the free energies for a singlet interacting with tactoids with different aggregation numbers in the buffer model. Apart from the singlet–singlet interaction, there is very little difference, which indicates that, under the same conditions, it is the nearest platelet that determines the interaction and the aggregation number does not matter (much). The difference for the singlet–singlet case can be understood by the fact that the opposite side of a singlet is neutralized by a diffuse double layer whereas the end platelet in a tactoid with two or more

platelets is adjacent to a narrow layer of counterions, which counteracts its charge more efficiently. Thus, the effective charge density seen when approaching a singlet is slightly higher than for a larger tactoid, giving a stronger interaction, as discussed in the context of Figure 3. Because adding salt removes most of the entropic dilution effect, the picture should be more or less the same with or without the buffer, as the figure also confirms. If anything, the buffer just makes the variation between different aggregation numbers in the presence of salt even smaller because the concentration of free counterions from the platelets are kept constant.

The difference between simulations with only two tactoids, showing a mechanism opposing the formation of large tactoids in the salt-free case, and the buffer model, where the aggregation number is of little consequence, lies in their representation of the system as a whole. Two tactoids (no buffer) implies that all platelets in the system undergo the same change; for example, a system of singlets becomes a system of doublets, and the number of slits is changing. In the buffer model, the platelets are just redistributed whereas the number of slits is kept constant.

**Tactoid Distributions.** The formation of a tactoid with  $n$  platelets,  $S_n$ , can be written as a series of reactions where singlets,  $S$ , are added one by one:



Each step is governed by an equilibrium constant:

$$K_n = \frac{[S_n]}{[S][S_{n-1}]} \quad (5)$$

Formally, the various  $[S_n]$  represent activities, but with the simplifying approximation that there are no interactions beside the tactoid formation itself (i.e., ideal conditions), they represent concentrations. The concentration of a tactoid with aggregation number  $n$  can then be written as

$$[S_n] = [S]K_n[S_{n-1}] = [S] \prod_{m=2}^n K_m[S] \quad (6)$$

If the free energy of interaction between tactoids is more or less independent of aggregation number, as seen in our cases with added salt, then the equilibrium constant,  $K$ , is also  $n$ -independent and we have an isodesmic system with a probability distribution function for tactoids with different aggregation numbers.<sup>28</sup>

$$P(n) = \frac{[S_n]}{\sum_{m=1}^{\infty} [S_m]} = \frac{(K[S])^{n-1}}{\sum_{m=0}^{\infty} (K[S])^m} \quad (7)$$

If  $K[S] < 1$ , then

$$P(n) = (K[S])^{n-1}(1 - K[S]) \quad (8)$$

In other words, the distribution peaks at  $n = 1$  and decays for larger  $n$ . When  $K[S]$  is small, this decay is rapid, and it is natural that the average

$$\langle n \rangle = \sum_{m=1}^{\infty} mP(m) = (1 - K[S])^{-1} \quad (9)$$

is small.

The total concentration of platelets,  $[S]_{\text{tot}}$ , is given by

$$K[S]_{\text{tot}} = K \sum_{m=1}^{\infty} m[S_m] = \frac{K[S]}{(1 - K[S])^2} \quad (10)$$

using eq 6 (with a single constant  $K$ ) and  $K[S] < 1$ . Solving for  $K[S]$  gives

$$K[S] = 1 + \frac{1}{2K[S]_{\text{tot}}} - \sqrt{\frac{1}{K[S]_{\text{tot}}} + \frac{1}{4(K[S]_{\text{tot}})^2}} \quad (11)$$

Concentrations  $[S]$  and  $[S]_{\text{tot}}$  may be expressed as volume fractions of platelets. By representing  $K$  as

$$K = \exp(-\beta A_{\text{eff}}) \quad (12)$$

we can relate the total volume fraction  $\phi$  and an effective free energy of association  $\beta A_{\text{eff}}$  to an average aggregation number using eqs 9 and 11.  $\beta A_{\text{eff}}$  can be seen as an association energy (nearest-neighbor pair interaction) in a 1D lattice model, where a lattice site represents the volume of a platelet and a tactoid slit at low volume fractions, but at higher volume fractions, space limitations also affect  $\langle n \rangle$  and the assumption of ideality breaks down.

As shown by the buffer model, the salt-free system is also essentially isodesmic at a given concentration of slits. Thus, the dilution effect would be to reduce  $K$  as tactoids form and  $\langle n \rangle$  would be lower than for the same system with salt.

Figure 8 shows the results of the isodesmic model for  $\langle n \rangle$  as a function of  $\phi$  for different  $\beta A_{\text{eff}}$  values. It is possible to find

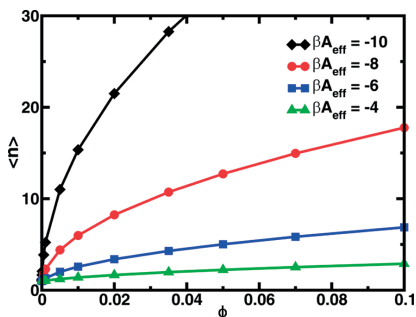


**Figure 8.** Average aggregation number as a function of volume fraction according to the isodesmic model for  $\beta A_{\text{eff}} = -4$  (green triangles),  $-6$  (blue squares),  $-8$  (red circles), and  $-10$  (black diamonds).

values of  $\beta A_{\text{eff}}$  where the aggregation number stays within reasonable values (5–20) for a large range of volume fractions. However, a more direct comparison with the experimental values in Table 1 shows that the observed aggregation numbers are much less sensitive to the concentration than the model, assuming a constant  $\beta A_{\text{eff}}$ . If anything, we would expect a weaker interaction when the system is dilute, unless it is in equilibrium with a salt reservoir, and the agreement would be worse.

The isodesmic results in Table 1 were calculated with the platelet volume fractions given in the table. As mentioned above,  $\beta A_{\text{eff}}$  can be thought of as the association energy in a lattice model where the volume fraction includes a tactoid slit for each platelet. For clay, this would mean a volume fraction that is double that of the volume fraction of only the platelets because experimentally the slit is roughly as wide as a clay

**Table 1. Average Aggregation Numbers for Different Effective Free Energies of the Isodesmic Model and Experimental Values for Calcium Montmorillonite at Different Concentrations<sup>a</sup>**

mass%	$\phi$	$-\beta A_{\text{eff}}$						exp
		4	6	8	10	12		
0.025	0.0001	1.0	1.0	1.2	2.0	4.4	10.88 <sup>b</sup>	
0.2	0.0007	1.0	1.2	2.1	4.6	12	4.2, <sup>c</sup> 5–7 <sup>d</sup>	
0.5	0.002	1.1	1.5	2.9	6.9	18	9 <sup>e</sup>	
1	0.004	1.2	1.8	3.9	9.6	25	16.1 <sup>f</sup>	
3	0.01	1.4	2.7	6.3	16	43	19 <sup>g</sup>	
15	0.06	2.4	5.5	14	37	100	10 <sup>h</sup>	
25	0.11	3.0	7.2	19	50	130	5.3 (max pressure) <sup>i</sup>	
38	0.18	3.7	9.2	24	64	170	6.2 (max pressure) <sup>i</sup>	
44	0.23	4.0	10	26	71	190	6.0 (max pressure) <sup>i</sup>	

<sup>a</sup>A clay density of 2.7 g/cm<sup>3</sup> was used to convert between mass percent and volume fraction,  $\phi$ .<sup>29</sup> <sup>b</sup>From Banin and Lahav.<sup>2</sup> <sup>c</sup>From Shainberg and Otoh.<sup>3</sup> <sup>d</sup>From Schramm and Kwak.<sup>6</sup> <sup>e</sup>From Levy.<sup>4</sup> <sup>f</sup>From Shomer and Mingelgrin.<sup>5</sup> <sup>g</sup>From Segad, Jönsson, and Cabane.<sup>8</sup> <sup>h</sup>From Segad et al.<sup>7</sup> <sup>i</sup>From Blackmore and Miller.<sup>1</sup>

platelet.<sup>1,2,7,8</sup> Using a doubled volume fraction increases the average aggregation number, but it does not change the conclusion that the isodesmic model is more sensitive to concentration than the experimental results.

On the other hand, the experimental data represent varying conditions with respect to composition and sample preparation, which also give differences in particle size, and cannot be taken as a representation of a universal concentration dependence of the average aggregation number of tactoids. An interesting point is that Blackmore and Miller, who compressed calcium montmorillonite and made measurements as the system was allowed to reswell, found that the average aggregation number was a function of the maximum pressure (and concentration) that the system had been exposed to rather than the pressure/concentration at the time of measurement.<sup>1</sup> Thus, if equilibration is very slow, measured values may represent a memory in the system and not equilibrium.

The prediction that the distribution of aggregation numbers is a monotonically decaying function is at odds with a distribution obtained from counting the number of different tactoids in cryo-TEM images.<sup>7</sup> This distribution has a maximum that is close to the average value. It would be possible to produce a maximum by modifying the isodesmic model if we were allowed to play with the spectrum of equilibrium constants, in particular, increasing the values for only low aggregation numbers. However, we currently do not have any clear physical justification for doing so. Furthermore, there are some technical difficulties with the cryo-TEM analysis. For example, the film thickness is of the same order as the platelet diameter, which means that only tactoids with smaller platelets can stand perpendicular and be seen edge on to count the number of platelets. Smaller platelets would be less likely to form tactoids, though. In other words, we are not convinced that the cryo-TEM analysis gives the correct distribution, although we are not in a position to dismiss it either. We will therefore leave any reevaluation of the theoretical distribution until we have made a more thorough investigation of the limitations of our model, which is indeed rather simplified and neglects a number of effects.

First, we consider only parallel platelets in our simulation model. Allowing rotations would add a repulsive term to the free energy of interaction,<sup>30</sup> but perhaps more importantly, the picture of well-dispersed independent particles, echoed in the isodesmic model, is not correct. With typical diameters of around 300 nm and a thickness of just 1 nm for montmorillonite,<sup>7,8,18</sup> rotation is hindered even at very low volume fractions, which may lead to an increased aggregation of singlets for entropic reasons. As a rough estimate, we may define an overlap concentration as the volume fraction of a circular platelet in a cube with the same side as the platelet diameter, which with the numbers above yields  $\phi_c \approx 0.003$ . Another important point that is likely to affect the distribution of aggregation numbers is that the particles in natural clay vary in size and shape. The size distribution is very broad and can be rather broad even after fractionation. Standard deviations of about 200 nm have been measured.<sup>7,18</sup>

Clay particles have titratable charges on the edges with a net positive charge at low pH and a negative charge at high pH. Our platelets represent the latter. Results vary for the point of zero charge,<sup>31–33</sup> but most often, the pH found in clay soils would be expected to give rise to a negative or neutral rim charge. Besides, rim charges amount to only 5–10% of the total charge, and with our small platelets, a positive edge charge would need to be made disproportionately large to be significant.

Adding van der Waals interactions would strengthen the attraction, which would increase the average number of platelets per tactoid, but the tactoids would still grow one-dimensionally and as long as the van der Waals interactions are reasonably short-ranged the distribution of aggregation numbers would be expected to decay monotonically with an isodesmic tail.

To summarize, in the isodesmic model, we have found a principle that may offer a partial explanation for the experimental observation that the average aggregation number of tactoids is limited to about 5–20,<sup>1–5</sup> but it gives a rather simplified picture. It is clear that further investigations are needed to prove or disprove the isodesmic model as an explanation for the limited aggregation number of tactoids.

## CONCLUSIONS

We have investigated how the excess free energy of interaction between highly charged platelets varies as the conditions are changed, focusing on electrostatic effects. The platelets were always parallel and could move only along the axis of the cylindrical cell whereas ions could move freely inside the cell.

**Singlet–Singlet Interactions.** Without added salt and for strong enough electrostatic coupling, the free energy of interaction between two singlets displays a minimum at short separations and a repulsive tail at larger separations with a maximum in between. The minimum is due to ion–ion correlations and is made deeper by a higher charge density, a smaller volume (higher platelet concentration), and larger platelets. With added salt, the repulsion is reduced and the minimum is enhanced. Changing the volume has little effect if the salt concentration is kept constant.

**Singlet–Singlet–Singlet Interactions.** The optimum separation for three singlets forming a triplet is found to be the same as for the minimum in the singlet–singlet free energy. This leads to the conclusion that the internal distance between platelets in a tactoid can be fixed at the position of this minimum.

**Tactoid–Tactoid Interactions.** The free energy of interaction between two tactoids has a minimum at the same separation as two singlets. At a constant total concentration of platelets and counterions, with no salt, the minimum becomes more shallow and the repulsive part increases as more platelets form tactoids. The change in interactions is due to a reduction in the concentration of counterions in the tactoids to compensate partially for the depletion “outside” as counterions are aggregated together with platelets. If instead the concentration of free counterions is kept constant, either by adding salt or by keeping the concentration of slits fixed, then there is very little difference between tactoids with different aggregation numbers.

**Tactoid Distributions.** Our result that the free energy of interaction is independent of aggregation number with salt present (and at constant slit concentration for a salt-free system) suggests that an isodesmic model can be used to describe a clay system. In this model, the distribution of aggregation numbers peaks at singlets and decays monotonically for larger tactoids, which may help explain the low average number of platelets in tactoids found experimentally.<sup>1–8</sup> However, the results were obtained with a rather simplified model, neglecting, for example, rotation, congestion, and polydispersity. Further investigations are needed to confirm that the isodesmic model can be applied to a real clay system.

## AUTHOR INFORMATION

### Corresponding Author

\*E-mail: magnus.ullner@teokem.lu.se

### Notes

The authors declare no competing financial interest.

## ACKNOWLEDGMENTS

Computational resources were provided by the Swedish National Infrastructure for Computing (SNIC) through Lunarc, the Center for Scientific and Technical Computing at Lund University. This work was performed within the framework of the Swedish national strategic e-science research program eSENCE.

## REFERENCES

- (1) Blackmore, A. V.; Miller, R. D. Tactoid Size and Osmotic Swelling in Calcium Montmorillonite. *Soil Sci. Soc. Am. Proc.* **1961**, *24*, 169–173.
- (2) Banin, A.; Lahav, N. Particle Size and Optical Properties of Montmorillonite in Suspensions. *Isr. J. Chem.* **1968**, *6*, 235–250.
- (3) Shainberg, I.; Otoh, H. Size and Shape of Montmorillonite Particles Saturated with Na/Ca Ions (Inferred from Viscosity and Optical Measurements). *Isr. J. Chem.* **1968**, *6*, 251–259.
- (4) Levy, R. Size of Sodium-Calcium Montmorillonite Crystallites. *J. Colloid Interface Sci.* **1976**, *57*, 572–574.
- (5) Shomer, I.; Mingelgrin, U. A Direct Procedure for Determining the Number of Plates in Tactoids of Smectites: The Na/Ca-Montmorillonite Case. *Clays Clay Miner.* **1978**, *26*, 135–138.
- (6) Schramm, L. L.; Kwak, J. C. T. Influence of Exchangeable Cation Composition on the Size and Shape of Montmorillonite Particles in Dilute Suspension. *Clays Clay Miner.* **1982**, *30*, 40–48.
- (7) Segad, M.; Hanski, S.; Olsson, U.; Ruokolainen, J.; Åkesson, T.; Jönsson, B. Microstructural and Swelling Properties of Ca and Na Montmorillonite: (In Situ) Observations with Cryo-TEM and SAXS. *J. Phys. Chem. C* **2012**, *116*, 7596–7601.
- (8) Segad, M.; Jönsson, B.; Cabane, B. Tactoid Formation in Montmorillonite. *J. Phys. Chem. C* **2012**, *116*, 25425–25433.

- (9) Guldbrand, L.; Jönsson, B.; Wennerström, H.; Linse, P. Electrical Double Layer Forces. A Monte Carlo Study. *J. Chem. Phys.* **1984**, *80*, 2221–2228.
- (10) Kjellander, R.; Marčelja, S. Correlation and Image Charge Effects in Electric Double-Layers. *Chem. Phys. Lett.* **1984**, *112*, 49–53.
- (11) Kjellander, R.; Marčelja, S. Inhomogeneous Coulomb Fluids with Image Interactions between Planar Surfaces. I. *J. Chem. Phys.* **1985**, *82*, 2122–2135.
- (12) Attard, P.; Mitchell, D. J.; Ninham, B. W. Beyond Poisson-Boltzmann: Images and Correlations in the Electric Double Layer. I. Counterions Only. *J. Chem. Phys.* **1988**, *88*, 4987–4996.
- (13) Valleau, J. P.; Ivkov, R.; Torrie, G. M. Colloid Stability: The Forces between Charged Surfaces in an Electrolyte. *J. Chem. Phys.* **1991**, *95*, 520–532.
- (14) Jönsson, B.; Wennerström, H. In *Electrostatic Effects in Soft Matter and Biophysics*; Holm, C., Kékicheff, P., Podgornik, R., Eds.; NATO Science Series II - Mathematics, Physics and Chemistry; Kluwer Academic Publishers: Dordrecht, The Netherlands, 2001; Vol. 46, pp 171–204.
- (15) Derjaguin, B. V.; Landau, L. Theory of the Stability of Strongly Charged Lyophobic Soils and of the Adhesion of Strongly Charged Particles in Solutions of Electrolytes. *Acta Physicochim. URSS* **1941**, *14*, 633–662.
- (16) Verwey, E. J. W.; Overbeek, J. T. G. *Theory of the Stability of Lyophobic Colloids*; Elsevier: Amsterdam, 1948.
- (17) Peigneur, P.; Maes, A.; Cremers, A. Heterogeneity of Charge Density Distribution in Montmorillonite as Inferred from Cobalt Adsorption. *Clays Clay Miner.* **1973**, *23*, 71–75.
- (18) Michot, L. J.; Bihannic, I.; Porsch, K.; Maddi, S.; Baravian, C.; Mougél, J.; Levitz, P. Phase Diagrams of Wyoming Na-Montmorillonite Clay. Influence of Particle Anisotropy. *Langmuir* **2004**, *20*, 10829–10837.
- (19) Warkentin, B. P.; Bolt, G. H.; Miller, R. D. Swelling Pressure of Montmorillonite. *Soil Sci. Soc. Am. Proc.* **1957**, *21*, 495–497.
- (20) Shubin, V. E.; Kékicheff, P. Electrical Double Layer Structure Revisited via a Surface Force Apparatus: Mica Interfaces in Lithium Nitrate Solutions. *J. Colloid Interface Sci.* **1993**, *155*, 108–123.
- (21) Sonnevile-Aubrun, O.; Bergeron, V.; Gulik-Krzywicki, T.; Jönsson, B.; Wennerström, H.; Lindner, P.; Cabane, B. Surfactant Films in Biliquid Foams. *Langmuir* **2000**, *16*, 1566–1579.
- (22) Antypov, D.; Holm, C. Optimal Cell Approach to Osmotic Properties of Finite Stiff-Chain Polyelectrolytes. *Phys. Rev. Lett.* **2006**, *96*, 088302.
- (23) Metropolis, N. A.; Rosenbluth, A. W.; Rosenbluth, M. N.; Teller, A.; Teller, E. Equation of State Calculations by Fast Computing Machines. *J. Chem. Phys.* **1953**, *21*, 1087–1097.
- (24) Lund, M.; Trulsson, M.; Persson, B. Faunus: An Object Oriented Framework for Molecular Simulation. *Source Code Biol. Med.* **2008**, *3*, 1.
- (25) Gordon, H. L.; Valleau, J. P. A Partially Clothed Pivot Algorithm for Model Polyelectrolyte Solutions. *Mol. Sim.* **1995**, *14*, 361–379.
- (26) Lobaskin, V.; Lyubartsev, A.; Linse, P. Simulation of an Asymmetric Electrolyte with Charge Asymmetry 60:1 Using Hard-Sphere and Soft-Sphere Models. *J. Chem. Phys.* **1999**, *111*, 4300–4309.
- (27) Michot, L. J.; Bihannic, I.; Thomas, F.; Lartiges, B. S.; Waldvogel, Y.; Caillet, C.; Thieme, J.; Funari, S. S.; Levitz, P. Coagulation of Na-Montmorillonite by Inorganic Cations at Neutral pH. A Combined Transmission X-ray Microscopy, Small Angle and Wide Angle X-ray Scattering Study. *Langmuir* **2013**, *29*, 3500–3510.
- (28) Evans, D. F.; Wennerström, H. *The Colloidal Domain: Where Physics, Chemistry, Biology, and Technology Meet*, 2nd ed.; Wiley-VCH: New York, 1999.
- (29) Morvan, M.; Espinat, D.; Lambard, J.; Zemb, T. Ultrasmall- and Small-Angle X-ray Scattering of Smectite Clay Suspensions. *Colloids Surf., A* **1994**, *82*, 193–203.
- (30) Delhomme, M. Thermodynamics and Structure of Plate-Like Particle Dispersions. Ph.D. Thesis, Lund University, Lund, Sweden, 2012.
- (31) Thomas, F.; Michot, L. J.; Vantelon, D.; Montargés, E.; Prêlot, B.; Cruchaudet, M.; Delon, J. F. Layer Charge and Electrostatic Mobility of Smectites. *Colloids Surf. A* **1999**, *159*, 351–358.
- (32) Duc, M.; Gaboriaud, F.; Thomas, F. Sensitivity of the Acid-Base Properties of Clays to the Methods of Preparation and Measurement I. Literature Review. *J. Colloid Interface Sci.* **2005**, *289*, 139–147.
- (33) Delhomme, M.; Labbez, C.; Caillet, C.; Thomas, F. Acid-Base Properties of 2:1 Clays. I. Modeling the Role of Electrostatics. *Langmuir* **2010**, *26*, 9240–9249.

Reprinted with permission from *J. Phys. Chem. B.*, 2014, **118**, 7405-7413  
A. Thuresson, M. Ullner and M. Turesson  
©2014 American Chemical Society.



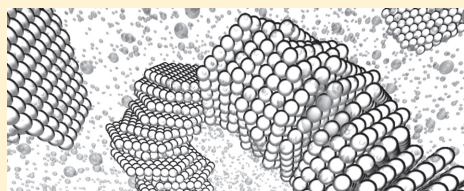
# Interaction and Aggregation of Charged Platelets in Electrolyte Solutions: A Coarse-Graining Approach

Axel Thuresson,\* Magnus Ullner, and Martin Turesson\*

Theoretical Chemistry, Lund University, P.O. Box 124, S-221 00 Lund, Sweden

## Supporting Information

**ABSTRACT:** A coarse-graining approach has been developed to replace the effect of explicit ions with an effective pair potential between charged sites in anisotropic colloidal particles by optimizing a potential of mean force against the results of simulations of two such colloidal particles with all ions in a cell model. More specifically, effective pair potentials were obtained for charged platelets in electrolyte solutions by simulating two rotating parallel platelets with ions at the primitive model level, enclosed in a cylindrical cell. One-component bulk simulations of many platelets interacting via the effective pair potentials are in excellent agreement with the



corresponding bulk simulations with all mobile charges present. The bulk simulations were mainly used to study the effects of platelet size, flexibility, and surface charge density on platelet aggregation in an aqueous 2:1 electrolyte, but systems in a 1:1 electrolyte were also investigated.

## INTRODUCTION

Atomistic simulations of aqueous suspensions containing clay minerals present a great challenge due to the highly anisotropic shape of the clay platelets and the long-range electrostatic interactions. As an example, montmorillonite consists of charged, flexible, anisotropic platelets with a thickness of 1 nm and lateral size of 100–1000 nm. Even coarse-grained primitive model (PM) simulations where the atomistic details are neglected would require about  $10^5$  ions just to neutralize a single circular platelet of diameter 400 nm with a typical surface charge density of  $-0.015 \text{ e}/\text{\AA}^2$ . To find the corresponding equilibrium in a bulk system with such platelets would require an enormous amount of calculation power. Much would therefore be gained by treating the ions implicitly. This is done in approximate mean-field theories, such as the DLVO approach. However, standard mean-field theories fail in the high electrostatic coupling regime, for example, in systems containing divalent counterions where ion–ion correlations are important.<sup>1–6</sup> Therefore, finding an accurate model, valid over a wider electrostatic coupling regime and with a low computational cost, would be highly desirable.

It has been shown that mono- and divalent counterions can be treated implicitly for isotropically charged spheres in the PM with excellent agreement up to about 7% volume fraction.<sup>7</sup> The idea is to extract an effective pair potential from a two-body simulation including the explicit counterions. The density-dependent effective pair potential is then used in the one-component bulk simulation. Such coarse-graining, treating ions implicitly, leads to a computational speed up of several orders of magnitude. Moreover, the understanding of the system is enhanced because the effect of the counterions is condensed into an effective pair potential.

However, for anisotropic colloidal particles, such as charged platelets, the potential of mean force (PMF) depends on the relative orientation of the particles. There are numerous ways of coarse-graining platelets and their interaction. For example, stiff platelets can be modeled as square-well oblate ellipsoids<sup>8</sup> and with an orientation-dependent potential for spherocylinders.<sup>9,10</sup> Flexible platelets can be modeled as nodes connected in a 3D lattice.<sup>11</sup>

Finding an effective potential from a more accurate model can be done with iterative methods, for example, inverse Monte Carlo (MC).<sup>12</sup> To avoid an iterative procedure, the force-matching method, suggested by Ercolessi and Adams<sup>13</sup> and further developed by Izvekov and Voth,<sup>14</sup> minimizes, in a linear least-squares sense, the error between an atomistic force and a coarse-grained force over a number of configurations. The method was later described in a formal statistical mechanical framework by Noid et al.<sup>15,16</sup>

Our method is in some ways similar to the force-matching of Izvekov and Voth but simpler by construction partly because it is not designed to reduce the number of interaction sites in the molecules of interest but to replace entire species with an effective potential. As the name implies, the force-matching optimizes effective forces, which after integration would correspond to a PMF. Our starting point is instead to optimize the PMF.

More specifically, our approach is to minimize the error in the PMF for two parallel platelets interacting with an effective site–site potential compared to two parallel platelets in a

Received: February 26, 2014

Revised: May 28, 2014

Published: June 4, 2014

cylindrical cell with explicit ions. In general, the minimization problem is nonlinear because the Boltzmann factor is a nonlinear function. By assuming that the Boltzmann weighted distribution of mutual orientations of the platelets is the same for implicit ions as that for explicit ions, the minimization problem becomes linear and can be solved with the linear least-squares method. An advantage of this method is that the effective site–site potential is obtained simply from a two-body simulation without any iterative procedure.

In this work, we focus on the strong coupling regime, where platelets aggregate into stacks (tactoids) due to ion–ion correlations between divalent ions. In a previous study, the aggregation between parallel platelets was shown to be isodesmic at a high enough concentration of 2:1 salt, that is, the free energy of interaction between tactoids was independent of the aggregation number.<sup>17</sup> Isodesmic behavior implies that the effective potential must be short-ranged. Replacing the electrostatic interactions and effects of ions with a short-ranged effective potential decreases the computational demand by several orders of magnitude. Our coarse-graining approach is able to treat ions implicitly for uniformly charged flexible platelets within the PM. We believe that the PM describing the electrostatic interactions (going beyond mean-field theories) is able to capture the fundamental physics responsible for the aggregation of clay platelets in bulk suspensions. This is a first step toward more realistic (still not atomistic) simulations for large platelets.

The outline of the article is as follows. The potentials, platelets, and simulation details are explained together with the coarse-graining scheme in the Model and Simulations section. In the Results section, radial distribution functions are shown for different parameters: size, flexibility, and surface charge density of the platelets. In the Discussion, the coarse-graining method is evaluated.

## MODEL AND SIMULATIONS

In this work, three types of canonical ensemble (NVT) simulations have been employed, namely

- bulk-PM: Multiplatelet molecular dynamics (MD) simulations of platelets *and* explicit ions at the PM level. These simulations were used to sample radial distribution functions  $g(r)$  with respect to the center of mass (CoM) of the platelets.

- cyl-PM: Two-platelet MC simulations with explicit ions in a closed cylindrical cell. These simulations were the basis for effective potentials acting between sites on different platelets.

- bulk-OCM: Multiplatelet MC one-component model (OCM) simulations of platelets interacting via the effective pair potential (implicit ions) extracted from the cyl-PM simulations. Resulting radial distribution functions were compared to bulk-PM simulations.

**Interaction Potentials.** In the bulk-PM and cyl-PM simulations, the solvent is treated as a continuum with a uniform dielectric constant  $\epsilon_r = 78.3$ . Particles are interacting pairwise. The electrostatic pair potential is defined as

$$u_{ij}^{\text{EL}}(r_{ij}) = \frac{e^2 z_i z_j}{4\pi\epsilon_0\epsilon_r r_{ij}} \quad (1)$$

where  $e$  is the elementary unit charge,  $\epsilon_0$  is the permittivity of vacuum,  $z_i$  is the valency of particle  $i$ , and  $r_{ij}$  is the distance between particles  $i$  and  $j$ . In addition, particles interact via a

strictly repulsive truncated and shifted Lennard-Jones (LJ) potential

$$u_{ij}^{\text{LJ}}(r_{ij}) = \begin{cases} \epsilon_{\text{LJ}} \left[ \left( \frac{\sigma_{ij}}{r_{ij}} \right)^{12} - 2 \left( \frac{\sigma_{ij}}{r_{ij}} \right)^6 + 1 \right] & \text{if } r_{ij} < \sigma_{ij} \\ 0 & \text{otherwise} \end{cases} \quad (2)$$

$\beta\epsilon_{\text{LJ}}$  determines the strength of the short-ranged repulsion and was set to 1.  $\beta = 1/kT$ , with  $k$  being the Boltzmann constant and  $T = 300$  K as the temperature. Furthermore,  $\sigma_{\text{ion-ion}} = 4$  Å,  $\sigma_{\text{ion-site}} = 7$  Å, and  $\sigma_{\text{site-site}} = 10$  Å. The total potential between all pairs is thus defined as

$$u_{ij}(r_{ij}) = u_{ij}^{\text{LJ}}(r_{ij}) + u_{ij}^{\text{EL}}(r_{ij}) \quad (3)$$

**Platelet Description.** A platelet was modeled as a symmetric hexagon, built from a monolayer of  $N_s$  charged LJ spheres (henceforth denoted as sites), arranged in a hexagonal pattern; see Figure 1.

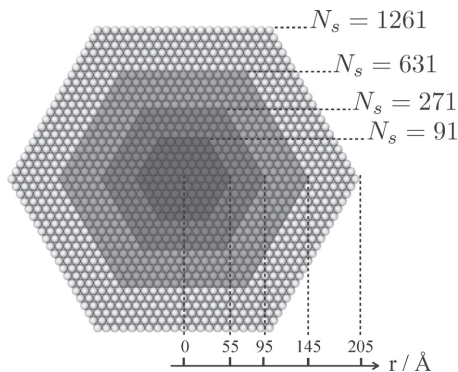


**Figure 1.** Schematic representation showing the hexagonally placed sites and dimensions for a number of platelet sizes.  $N_s$  refers to the number of sites per platelet.

A total electrical charge of  $Q_p$  unit charges was equally divided among the  $N_s$  sites, that is, giving each site  $Q_p/N_s$  unit charges, located in the center of the site. The surface charge density,  $\sigma_s$ , was estimated from an infinite plane of sites arranged in a hexagonal pattern. In this work,  $\sigma_s$  was either  $-0.026$  or  $-0.013$   $e/\text{Å}^2$ . The latter value roughly corresponds to a (one-sided) surface charge density of the clay mineral montmorillonite.<sup>18–20</sup>

Two adjacent sites,  $i$  and  $j$ , separated by a distance  $r_{ij}$ , were connected by a harmonic bond-stretching potential

$$u_b(r_{ij}) = \frac{1}{2} k^b (r_{ij} - b)^2 \quad (4)$$

with  $b$  being the equilibrium bond length. The spring constant  $k^b$  was set to  $40$   $\text{kJ}/\text{Å}^2$  to render practically rigid bonds. (In fact, rigid bonds were employed in the cyl-PM simulations.) In our work,  $b = 10$  Å, the same as the platelet thickness ( $\sigma_{\text{site-site}}$ ). In order to induce platelet rigidity, the sites were also restrained by a harmonic bending potential, acting on the angle  $\theta_{ijk}$  between triplets of bonded sites  $i$ ,  $j$ , and  $k$ . The potential reads

$$u_s(\theta_{jk}) = \frac{1}{2}k^\theta(\theta_{jk} - \theta^0)^2 \quad (5)$$

with  $\theta^0 = \pi$  rad. Three values of  $k^\theta$  were used in order to render platelets with varying flexibilities, ranging between “soft” platelets ( $k^\theta = 4$  kT/rad<sup>2</sup>), “medium stiff” platelets ( $k^\theta = 40$  kT/rad<sup>2</sup>), and “stiff” platelets ( $k^\theta = 4000$  kT/rad<sup>2</sup>). The volume fraction  $\phi$ , was defined as

$$\phi = \frac{\pi N_p N_s \sigma_{\text{site-site}}^3}{6V} \quad (6)$$

where  $V$  is the volume of the simulation box and  $N_p$  is the number of platelets.

**Ions.** Ions were modeled as freely moving charges centered in truncated and shifted LJ spheres. The total platelet charge was neutralized by either divalent or monovalent counterions. 1:1 salt or 2:1 salt was also added to the system.

**Bulk-PM Simulations.** MD simulations were performed with the software package GROMACS (version 4.5.4).<sup>21</sup> The platelets were allowed to rotate and translate freely in a cubic simulation box with three-dimensional periodic boundary conditions. The intermolecular interaction potentials were given by eqs 3–5. Newton’s equations of motion for the freely moving species (platelets + ions) were integrated using a velocity Verlet algorithm. The temperature for each species was thermostated using velocity rescaling with a stochastic term, ensuring the generation of a proper canonical ensemble.<sup>22</sup> A time step of 10 fs was usually employed, but to check the convergence of the sampled radial distribution functions, simulations with a 1 fs time step were also performed for some of the systems. To account for the long-ranged electrostatic contribution, fast particle-mesh Ewald summation (PME) was used with a 60 Å real space Coulomb cutoff and a Fourier spacing equal to 6 Å. For an in-depth description of the input parameters, see the online user manual.<sup>23</sup> Radial distribution functions,  $g(r)$ , were sampled during long enough simulations (typically 50 ns) to obtain converged system energies. In general, 50 platelets were simulated, and for some of the systems, we checked the size dependence by doubling the number of platelets, observing negligible differences in  $g(r)$ .

**Cyl-PM Simulations.** For isotropically charged spheres, the PMF between pairs as a function of their separation can be used as an effective potential in an OCM.<sup>7</sup> For anisotropic particles, the situation is more complicated because the PMF depends on the relative orientation of the particles. In our coarse-graining approach, the construction of an effective potential between platelets makes use of the PMF,  $W(r)$ , between two parallel platelets rotating about the  $z$ -axis as a function of their CoM distance  $r$ .

All particles are enclosed in a cylindrical cell at the PM level, including all ions explicitly. The cylinder length  $L_{\text{cyl}}$  and cylinder radius  $R_{\text{cyl}}$  set the concentration of ions and the volume fraction of platelet sites.  $W(r)$ , which is density-dependent, can be written as

$$W(r) = - \int_{-\infty}^{\infty} \bar{F}_z(r') \, dr' \quad (7)$$

where  $\bar{F}_z(r') = \langle F_z(r'; r^N, \theta) \rangle$  is the mean force in the  $z$ -direction between the two platelets, placed symmetrically around the origin along the  $z$ -axis at a fixed CoM distance  $r'$  (see Figure 3).  $r^N$  represents the coordinates of  $N$  ions, and  $\theta$  is the angle representing the relative rotation of the parallel platelets. The configurational space of the freely moving ions was explored by

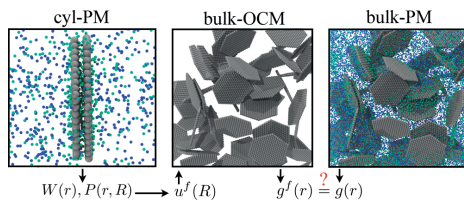


**Figure 2.** In the cyl-PM simulations, the PMF  $W(r)$  between two parallel platelets (rotating about the  $z$ -axis) and the distribution of site–site distances  $P(r,R)$  are calculated as functions of the platelet–platelet CoM separation  $r$ . After extracting an effective site–site potential  $u^I(R)$ , acting between pairs of platelet sites, the bulk radial distribution function  $g^I(r)$  is calculated in a bulk-OCM simulation with implicit ions. The result is compared with the corresponding  $g(r)$  sampled in a bulk-PM simulation with explicit ions.

single-particle translations using the standard Metropolis MC algorithm<sup>24</sup> in the canonical ( $NVT$ ) ensemble. The platelet configurations were sampled with platelet rotations and cluster rotations, the latter meaning that attempts were made to rotate a platelet and its neighboring ions simultaneously. All MC simulations were performed using software from the Faunus project.<sup>25</sup>

**Mean-force calculations.** For each system,  $\bar{F}_z(r)$  was evaluated for roughly 30 CoM distances and integrated according to eq 7 using the trapezoidal rule in order to obtain  $W(r)$ .  $\bar{F}_z(r)$ , for a given  $r$ , was calculated using a midplane approach<sup>1</sup> and can be written as

$$\bar{F}_z(r) = \bar{F}_z^p(r) + \bar{F}_z^{\text{id}}(r) \quad (8)$$

where  $\bar{F}_z^p(r)$  is the  $z$ -component of the mean force (originating from the pair potential in eq 3) between species residing on different sides of the midplane. The ideal contribution to the mean force,  $\bar{F}_z^{\text{id}}(r)$ , was calculated according to

$$\beta \bar{F}_z^{\text{id}}(r) = A[\rho_1(z=0) - \rho_1(z=L_{\text{cyl}}/2)] \quad (9)$$

where  $\rho_1(z=0)$  and  $\rho_1(z=L_{\text{cyl}}/2)$  are the ion densities at the midplane and the cylinder edges, respectively.  $A$  is the cross-sectional cylinder area. We were able to reduce the standard deviation in  $\bar{F}_z(r)$  to less than 0.05 kT/Å, which is necessary in order to accurately fit an effective site–site potential to  $W(r)$  (see the next section). A complete list of simulated cyl-PM cases is provided in the Supporting Information.

**Coarse-Graining Method.** In this section, we present a method to fit an effective PMF,  $W^I(r)$ , as closely as possible to the  $W(r)$  extracted from the cyl-PM simulations. We have chosen to construct  $W^I(r)$  as a *single* site–site potential  $u^I(R_{ij})$ , acting between pairs of platelet sites  $i$  and  $j$ , separated by a distance  $R_{ij}$ . The aim is to reproduce radial distribution functions from bulk-PM simulations using  $u^I(R_{ij})$  in bulk-OCM simulations; see Figure 2.

The form chosen for  $u^I(R_{ij})$  was a truncated and shifted 12–8–6 potential with a hard-sphere cutoff. Note that the choice is somewhat arbitrary, but  $u^I(R_{ij})$  should be able to reproduce the shape of  $W(r)$ .

$$u^f(R_{ij}) = \begin{cases} +\infty & R_{ij} \leq \sigma_{\text{hs}} \\ u^{12-8-6}(R_{ij}) - u^{12-8-6}(\sigma_{\text{cut}}) & \sigma_{\text{hs}} < R_{ij} < \sigma_{\text{cut}} \\ 0 & R_{ij} \geq \sigma_{\text{cut}} \end{cases} \quad (10)$$

where

$$u^{12-8-6}(R_{ij}) = \frac{A_1}{R_{ij}^{12}} + \frac{A_2}{R_{ij}^8} + \frac{A_3}{R_{ij}^6} \quad (11)$$

For a given choice of  $u^f(R_{ij})$ , an optimal  $W^f(r, A_1, A_2, A_3)$  would be found by minimizing the following function with respect to  $A_1, A_2$ , and  $A_3$

$$f(A_1, A_2, A_3) = \sum_{i=1}^N [W(r_i) - W^f(r_i, A_1, A_2, A_3)]^2 \quad (12)$$

When the force is averaged to obtain  $W^f(r, A_1, A_2, A_3)$ ,  $u^f(R_{ij})$  determines both the force itself and the Boltzmann weight for each configuration, which makes minimizing  $f(A_1, A_2, A_3)$  a nonlinear problem. It can be solved iteratively by sampling a new  $W^f(r, A_1, A_2, A_3)$  for every updated set of  $A_1, A_2$ , and  $A_3$ , but if it is assumed that the Boltzmann weights are the same as those in the cyl-PM simulations, simulated distribution functions can be used to calculate a free energy of interaction, denoted  $W_{\text{PM}}^f(r, A_1, A_2, A_3)$ , which makes the problem linear, and  $f(A_1, A_2, A_3)$  can be minimized with the linear least-squares method. If  $u^f(R_{ij})$  was a perfect effective potential, it should, of course, reproduce the Boltzmann weights of the simulations.

Because the distribution functions can be saved, the free energy of interaction can be calculated after the simulations for any choice of  $u^f(R_{ij})$

$$\begin{aligned} W_{\text{PM}}^f(r, A_1, A_2, A_3) \\ = - \int_0^r \sum_{k=1}^M P(r', R_k) N_1 N_2 \left( - \frac{d}{dz} u^f(R') \right) \Big|_{R'=R_k} dr' \end{aligned} \quad (13)$$

where  $P(r', R_k)$  is the probability of site–site distances ( $R_k$ ) from the cyl-PM simulation for a given CoM distance  $r'$  and is sampled in a histogram with  $M$  bins during the cyl-PM simulations (see Figure 3);  $N_1$  and  $N_2$  are the number of sites for platelet 1 and 2, respectively; and  $-(d/dz)u^f(R')$  is the force in the  $z$ -direction for a given site–site distance  $R'$ .

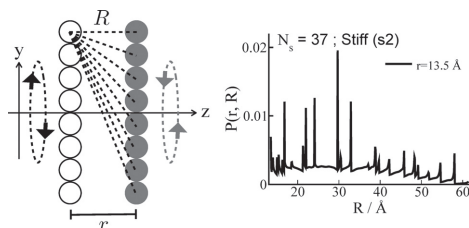


**Figure 3.** 2D schematics of two parallel platelets rotating about the  $z$ -axis in a cyl-PM simulation (left). The dashed lines show a selection of site–site distances  $R_{ij}$  which are sampled during the simulation and saved in a histogram  $P(r, R)$ . An example of such a histogram is shown on the right (bin size of 0.1 Å).

Thus,  $\sum_{k=1}^M P(r', R_k) N_1 N_2 [-(d/dz)u^f(R')] \Big|_{R'=R_k}$  is the effective mean force in the  $z$ -direction using the Boltzmann weighted platelet rotations from the cyl-PM simulation (a general derivation of eq 13 is given in the Appendix).

Once  $A_1, A_2$ , and  $A_3$  were determined, we performed bulk-OCM simulations with freely rotating platelets in three dimensions and the sites interacting via  $u^f(R_{ij})$ . Radial distribution functions were calculated and compared with the corresponding bulk-PM simulations.

## RESULTS

In this section, we present radial distribution functions for a number of systems, sampled in bulk-PM simulations with explicit ions and the full interaction potentials. The systems are listed in Table 1 (the corresponding simulation parameters are

**Table 1. Systems in the Bulk-PM and Bulk-OCM Simulations<sup>a</sup>**

ID	$N_s$	$\sigma_s / (e/\text{Å}^2)$	$\rho(i:1)/\text{mM}$	$i$	$k^{\theta} / (\text{kT}/\text{rad}^2)$	$\phi$	$\sigma_{\text{cut}}/\text{Å}$
$s_1$	19	-0.026	40	2	4000	0.03	23.4
$s_2$	37	-0.026	40	2	4000	0.03	23.4
$s_3$	37	-0.026	40	2	40	0.03	23.4
$s_4$	37	-0.026	40	2	4	0.03	23.4
$s_5$	61	-0.026	40	2	4000	0.03	23.4
$s_6$	61	-0.026	40	2	40	0.03	23.4
$s_7$	61	-0.026	40	2	4	0.03	23.4
$s_8$	91	-0.026	40	2	4000	0.03	23.4
$s_9$	91	-0.026	40	2	40	0.03	23.4
$s_{10}$	91	-0.026	40	2	4	0.03	23.4
$s_{11}$	271	-0.013	40	2	4000	0.03	25.0
$s_{12}$	61	-0.026	0	1	4000	0.03	100.0
$s_{13}$	61	-0.026	80	1	4000	0.03	100.0
$s_{14}$	61	-0.026	80	1	4000	0.1	100.0

<sup>a</sup>The columns give the simulation identifier (ID), number of sites per platelet ( $N_s$ ), surface charge density ( $\sigma_s$ ), added salt concentration ( $\rho(i:1)$ ), electrolyte type ( $i$ ), force constant for the angle potential ( $k^{\theta}$ ) [see eq 5], volume fraction ( $\phi$ ), and the site–site potential cutoff ( $\sigma_{\text{cut}}$ ).

given in the Supporting Information) with a system identifier  $s_i$ , which will be used throughout the text to represent the systems. For each system, a comparison with the corresponding bulk-OCM simulation is provided. Effects of varying the platelet size, flexibility, surface charge density, and electrolyte type will be analyzed.

**Tactoid Formation in 2:1 Electrolytes.** We start by analyzing systems  $s_2$ – $s_{10}$  (see Figure 4), containing roughly 40 mM added 2:1 salt. Furthermore,  $\sigma_s = -0.026 e/\text{Å}^2$  and  $\phi = 0.03$ . These systems only differ with respect to platelet size and platelet flexibility (see columns 2 and 6 in Table 1).

**Effects of Platelet Size.** By comparing stiff platelets of different sizes (systems  $s_2, s_5$ , and  $s_8$ ), see panels (a), (d), and (g) in Figure 4, we notice a pronounced buildup of the primary peak at  $r = 15 \text{ Å}$ , going from  $N_s = 37$  to 91 (note the different scales on the  $y$ -axes). The peaks correspond to face-to-face configurations of adjacent platelets, induced by a strong ion–ion correlation attraction. Furthermore, the probability to form larger tactoids increases with platelet size, manifested by a more structured  $g(r)$  at large  $r$ . The same trend is seen for medium stiff platelets (systems  $s_3, s_6$ , and  $s_9$ ) and for soft platelets (systems  $s_4, s_7$ , and  $s_{10}$ ). For the investigated surface charge

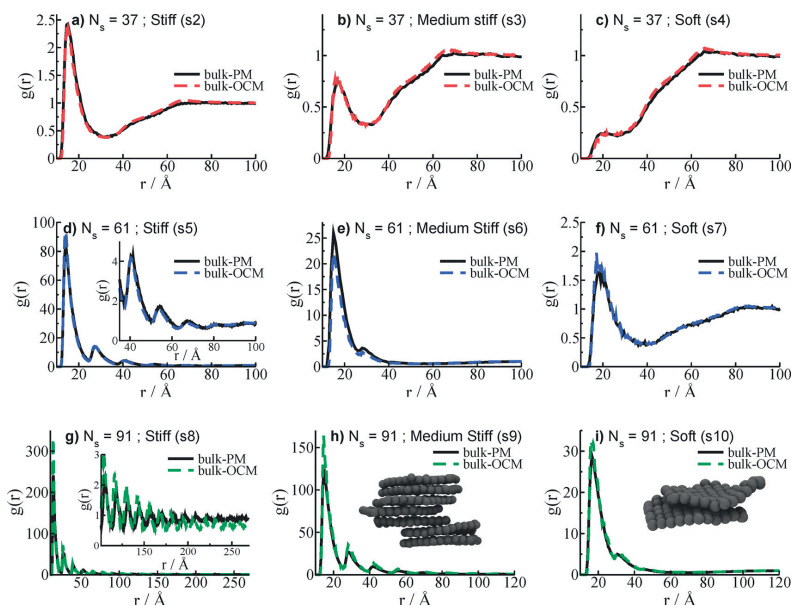


**Figure 4.** Bulk radial distribution functions for systems  $s_2$ – $s_{10}$ . Solid and dashed lines correspond to bulk-PM and bulk-OCM results, respectively. The insets in (d) and (g) magnify the regions at large  $r$ , and the snapshots in (h) and (i) show the bent platelet conformations resulting from the introduction of platelet flexibility. Note the different scales on the  $y$ -axes.  $\sigma_s = -0.026 e/\text{Å}^2$ , and  $\phi = 0.03$ .

density, the aggregation is almost complete for system  $s_8$ . This is highlighted in the inset of Figure 4g, showing an oscillating structure over the full  $r$  range (half of the size of the simulation box).

**Effects of Platelet Flexibility.** Introducing platelet flexibility has a dramatic effect on the aggregation state. In Figure 4a–c ( $N_s = 37$ ), the parameter  $k^\theta$  is gradually decreased, leading to an increased flexibility. This introduces a platelet–platelet repulsion, seen by the decrease of the primary peak. The same trend is seen for all platelet sizes, that is, compare the series  $s_3$ – $s_7$  and  $s_8$ – $s_{10}$ . The tactoid size distribution,  $P_{\text{clust}}(N)$ , in Figure 5 for series  $s_5$ – $s_7$ , decays exponentially (typical for

isodesmic aggregation<sup>26</sup>) as a function of the aggregation size,  $N$ . Two platelets are here defined to be in the same tactoid if the CoM distance is within 20 Å. A simulation snapshot from the bulk-PM simulations is included in Figure 4h (medium stiff platelets), showing one selected tactoid containing seven platelets (simple ions are omitted for clarity). Note the slightly buckled platelet shape. The snapshot in Figure 4i shows a characteristic pair configuration for soft platelets, displaying an even more bent platelet shape compared to the medium stiff platelets. The flexibility-induced repulsion can be understood as an entropic effect, that is, apart from the rotational entropy cost, flexible platelets lose more internal degrees of freedom relative to stiff platelets when brought into close contact.

**Effects of Surface Charge Density.** Figure 6 shows the simulated  $g(r)$  for system  $s_{11}$ , which contains larger stiff platelets ( $N_s = 271$ ) with a lower surface charge density ( $\sigma_s = -0.013 e/\text{Å}^2$ ). If we look at the trend in structure evolution as a function of increasing platelet size for stiff platelets in Figure 4 ( $\sigma_s = -0.026 e/\text{Å}^2$ ), we conclude that the surface charge density has a very strong impact on the aggregation state. For example, the radial distribution function in Figure 6 is comparable to the one found for system  $s_2$  ( $N_s = 37$ ), even though the platelet surface has been increased more than a factor of 7.

**Repulsive Systems: 1:1 Electrolyte.** It turns out that our established coarse-graining method can not only be used to find effective site–site potentials for platelet aggregation at high electrostatic coupling. With slight modifications of  $u^i$  (see the Discussion), the same fitting method was used for systems

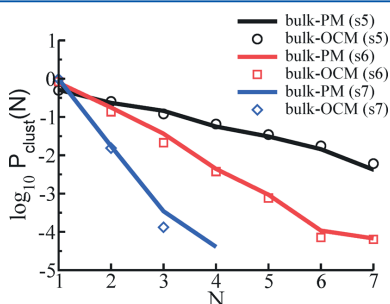


**Figure 5.** Tactoid size distribution for systems  $s_5$ – $s_7$ . Platelets within a CoM distance of 20 Å are counted as belonging to a tactoid.

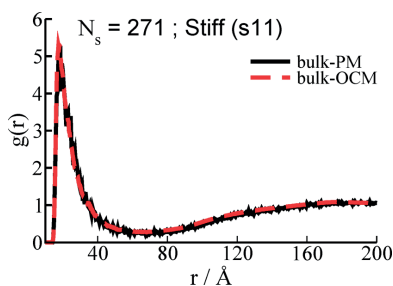


**Figure 6.** Radial distribution functions for system  $s_{11}$ . Solid and dashed lines correspond to bulk-PM and bulk-OCM results, respectively.  $\sigma_s = -0.013 \text{ e}/\text{\AA}^2$ , and  $\phi = 0.03$ .

containing monovalent counterions and added 1:1 salt, as shown in Figure 7.

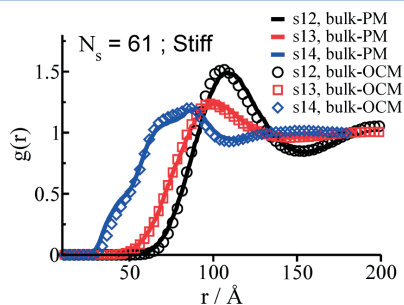


**Figure 7.** Bulk radial distribution functions for systems  $s_{12}$  ( $\phi = 0.03$ ),  $s_{13}$  ( $\phi = 0.03$ ), and  $s_{14}$  ( $\phi = 0.1$ ). Solid lines and symbols correspond to bulk-PM and bulk-OCM results, respectively.  $N_s = 61$ , and  $\sigma_s = -0.026 \text{ e}/\text{\AA}^2$ .

System  $s_{12}$  ( $\phi = 0.03$ ) is a salt-free system (counterions + platelets only), displaying a characteristic shape of  $g(r)$  found in purely repulsive systems, that is, the position of the first peak is located at  $r = \rho_p^{-1/3}$ .  $\rho_p$  is the platelet number density. Adding 80 mM of 1:1 salt (system  $s_{13}$ ,  $\phi = 0.03$ ) screens the site–site interactions, resulting in a lower primary peak in the  $g(r)$ , slightly shifted toward smaller  $r$ .

System  $s_{14}$  also contains 80 mM 1:1 salt, but the volume fraction has been increased to 10%. The kinks in  $g(r)$  are found in both the bulk-PM and the bulk-OCM simulations and appear due to excluded volume effects because we are above the platelet overlap concentration, that is,  $\rho_p^{-1/3} \approx 68 \text{ \AA}$ , which is less than the maximum platelet dimension (90  $\text{\AA}$ ).

## DISCUSSION

The overall agreement between the bulk-OCM and bulk-PM radial distribution functions is excellent, as seen in Figures 4, 6, and 7. Remarkably, a near-quantitative agreement is found even for flexible platelets that interact with a site–site potential obtained for stiff platelets. The flexibility was only introduced via the bond potential in eq 4 and angle potential in eq 5. This shows that flexibility can be introduced additively, keeping the attractive ion–ion correlation constant.

**Comments on the Coarse-Graining Method. Choice of Effective Site–Site Potential.** In a previous study, we showed that parallel, negatively charged platelets at high enough 2:1 salt concentrations is an isodesmic system.<sup>17</sup> This implies that platelets in a tactoid only interact with their nearest neighbors. Therefore,  $\sigma_{\text{cut}}$  was chosen to be just below  $2r_{\text{min}}$ .  $r_{\text{min}}$  is the interlamellar spacing between platelets in a tactoid and was approximated from  $W(r_{\text{min}}) = \min(W(r))$ ; see Figure 8. Indeed,

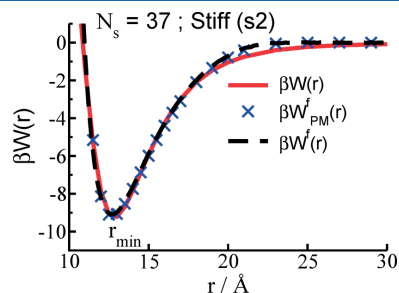


**Figure 8.** System  $s_2$ :  $\phi = 0.03$ ,  $N_s = 37$ ,  $\sigma_s = -0.026 \text{ e}/\text{\AA}^2$ , and  $\rho(2:1) = 40 \text{ mM}$ . Comparison between  $W(r)$ ,  $W^{\text{PM}}(r)$  and  $W_{\text{PM}}^{\text{W}}(r)$ .

if  $\sigma_{\text{cut}} \geq 2r_{\text{min}}$ , the platelet aggregation is overestimated (not shown) because the mean force between two platelets is not negligible at distances larger than  $2r_{\text{min}}$  if there are only ions between the platelets. Thus, in a tactoid, intervening layers of platelets and ions “screen” these interactions, which is a many-body effect that is taken care of by the cutoff.

For the attractive systems, a short-ranged cutoff was also used in the minimization of eq 12 by ignoring short distances where  $W(r) > 0$  to avoid fitting to a steep repulsive part of  $W(r)$ , whose exact form is of lesser importance. The hard-sphere cutoff,  $\sigma_{\text{hs}}$ , in the effective potential (eq 10) is introduced for even shorter separations to allow negative values of the coefficient for the  $1/R_{ij}^{12}$  term.

To obtain good agreement between bulk-PM and bulk-OCM for the repulsive systems (1:1 electrolyte), a different effective potential was used,  $u^{\text{monovalent}}(R_{ij}) = (A_1^*/R_{ij}^{10}) + (A_2^*/R_{ij}^8) + (A_3^*/R_{ij}^6) + (A_4^*/R_{ij}^4)$  for  $\sigma_{\text{hs}} < R_{ij} < \sigma_{\text{cut}}$ . Moreover, due to the repulsion,  $r_{\text{min}} \rightarrow \infty$ . In this case,  $\sigma_{\text{cut}}$  was limited to  $L_{\text{cyl}}/2$  to avoid boundary effects when calculating  $W(r)$  in the cyl-PM simulations. For system  $s_{14}$ , the volume fraction in the cyl-PM simulation was set to 7%, instead of 10%, in order to obtain a reasonable cutoff ( $\sigma_{\text{cut}} = 45 \text{ \AA}$ ).

**Validity of Assumptions.** Two main assumptions were made in our coarse-graining method. The first assumption is that we can represent the free energy of the full model (explicit ions) as a single site–site potential (of mean force) of the chosen form. The second is that we can use a preaveraged distance distribution ( $P(r, R_k)$ ) to represent the site–site distances in the fitting procedure. The latter assumption allows for a postsimulation determination of the coefficients in  $u^{\text{f}}$  and the possibility to modify its functional form, without the need to sample a new  $W^{\text{f}}(r)$  for each choice of  $u^{\text{f}}$ .

To show that the preaveraging is valid, the requirement is that  $W_{\text{PM}}^{\text{f}}(r)$  in eq 13 should be approximately equal to  $W^{\text{f}}(r)$  for the optimal parameters ( $A_1$ ,  $A_2$ , and  $A_3$ ) found in the fitting procedure.  $W^{\text{f}}(r)$  is the PMF between two parallel platelets

rotating about the  $z$ -axis interacting with the effective site–site potential  $u^f$

$$\beta W^f(r, A_1, A_2, A_3) = -\ln \left( \frac{\int e^{-\beta U^f(r, \theta)} d\theta}{\int d\theta} \right) \quad (14)$$

where  $U^f(r, \theta) = \sum_{i=1}^{N_s} \sum_{j=1}^{N_s} u^f(r_{ij})$  is the configurational energy for a CoM distance  $r$  and relative platelet orientation  $\theta$ . The reference point (zero-level of free energy) is two non-interacting, rotating parallel platelets.

An example is shown for system  $s_2$  in Figure 8.  $W(r)$  is sampled in the cyl-PM simulation. We see that  $W^f(r, A_1, A_2, A_3) \approx W_{\text{PM}}^f(r, A_1, A_2, A_3)$ , which confirms that using a preaveraged distance distribution is a good approximation. The slight difference between  $W(r)$  and  $W_{\text{PM}}^f(r, A_1, A_2, A_3)$  around 20 Å is due to the introduction of the cutoff ( $\sigma_{\text{cut}}$ ) to account for many-body effects in the tactoid and maintain an isodesmic system. Figure 4a shows a comparison of the radial distribution function between the bulk-PM simulation and the corresponding bulk-OCM simulation for this system. The agreement is excellent over the full  $r$  range.

The advantage of using parallel platelets compared to freely rotating platelets is that (i) the mean force is sampled with high precision, (ii) boundary artifacts of the cyl-PM cell are small, and (iii) the site–site distances are sampled at constant  $z$  for a given CoM separation, which means that no distribution of mean  $z$ -averages is required (cf. Appendix) and the calculation of the force in eq 12 is more straightforward.

**Simulating Larger Platelet Sizes.** Our coarse-graining method allows us to simulate systems at a lower computational cost for two reasons, (i) the implicit treatment of counterions and salt and (ii) the possibility (in the case of 2:1 electrolyte) to introduce cutoff schemes when evaluating energy differences in the MC algorithm, thanks to the short-ranged effective site–site potential. In Figure 9, we show the evolution of the free-energy

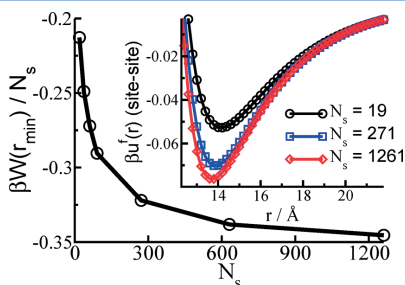


**Figure 9.** Free-energy minimum per site as a function of platelet size. The inset shows the corresponding effective site–site potentials for a number of  $N_s$ .  $\sigma_s = -0.026 e/\text{Å}^2$ ,  $\phi = 0.03$ ,  $\rho(2:1) = 40 \text{ mM}$ , and  $\sigma_{\text{cut}} = 23.4 \text{ Å}$ .

minimum per site,  $W(r_{\text{min}})/N_s$ , as a function of  $N_s$ , in the range  $[19 \leq N_s \leq 1261]$ . We see that an increase in platelet size does not only trivially increase the attraction due to a larger interacting area but also increases the attraction per unit area (also observed in ref 17) because of the finite size of the platelets, that is, a decreasing rim to surface ratio. The inset of Figure 9 shows the underlying effective site–site potentials for a selection of platelet sizes.

We also note that the finite-size effect becomes less significant for large platelets, and  $W(r_{\text{min}})/N_s$  quite rapidly converges to a constant value, meaning that the global free-energy minimum will scale as  $N_s/N_s$ , when changing the platelet size from  $N_s$  to  $N_s$ . This means that beyond a sufficiently large platelet size, the effective site–site potential can be kept constant, allowing us to simulate very large platelets and still accurately map the bulk-PM system.

## CONCLUSIONS

We have successfully developed a coarse-graining method able to treat ions and salt implicitly in systems containing charged nanoplatelets. The method is based on numerically sampling the PMF between two parallel platelets with an in-plane rotation about the  $z$ -axis in a closed cylindrical cell with explicit salt and counterions (implicit solvent). By using distributions of site–site distances obtained from such simulations, an effective site–site potential is obtained with the linear least-squares method as a postprocessing step, which also allows the functional form of the effective potential to be changed without performing new simulations. Effective site–site potentials were used in multiplatelet simulations without ions, giving quantitative agreement with radial distribution functions sampled in the PM with explicit ions.

In this work, we focused on the self-assembly of platelets into stacks (tactoid formation) solely held together via ion–ion correlations of divalent ions. The platelet size, surface charge density, and flexibility seem to play a crucial role with respect to tactoid formation. As the platelets grow bigger, the interaction between adjacent platelets will increase partly by a trivial effect of making the interacting surfaces bigger, but we also see that the interaction per site is increasing with size as the relative influence of the rim becomes smaller. Assuming that the asymptotic limit has been reached, the site–site potential can be considered to be constant, thus providing a route to simulate very large multiplatelet systems. Adding flexibility to the platelets greatly reduces the tendency to form tactoids. Furthermore, we show that the ion–ion correlations can be represented as a short-ranged site–site potential and that the flexibility can be introduced additionally, keeping the site–site potential constant. The computational gain of using a short-ranged effective site–site potential compared with the full long-ranged electrostatic potentials is significant.

A coarse-grained model is crucial when modeling multiplatelet systems containing realistic platelet sizes, for example, montmorillonite clay sheets. Moreover, by a careful implementation of the coarse-graining method presented here, a variety of particle geometries for both attractive and repulsive systems can be studied. For example, we have demonstrated that the method can be adapted to systems with only monovalent counterions, that is, purely repulsive systems.

## APPENDIX

### General Derivation

The construction of an effective potential between platelets in this paper uses the PMF between two parallel platelets rotating about the  $z$ -axis as a function of their CoM distance  $r$ . This method can be generalized for two fully rotating particles. The general expression for the free energy of interaction  $W(r)$ , which is density-dependent, can be written as

$$\begin{aligned}
 W(r) &= - \int_{-\infty}^r \bar{F}_z(r') dr' \\
 &= - \int_{-\infty}^r \iint \bar{E}_z(r', \mathbf{r}^N, \Omega) p(r', \mathbf{r}^N, \Omega) d\mathbf{r}^N d\Omega dr'
 \end{aligned}
 \quad (15)$$

where  $\bar{F}_z(r')$  is the mean force in the z-direction between the two particles, placed symmetrically around the origin along the z-axis at a fixed CoM distance  $r'$ .  $\mathbf{r}^N$  represents the coordinates of  $N$  ions, and  $\Omega$  represents the relative orientation of the particles.  $p(r', \mathbf{r}^N, \Omega) = e^{-\beta U(r', \mathbf{r}^N, \Omega)} / \int \int e^{-\beta U(r', \mathbf{r}^N, \Omega)} d\mathbf{r}^N d\Omega$  is the probability density and  $U(r', \mathbf{r}^N, \Omega)$  is the total energy of the system for the specific configuration.

The goal of the method is to find the  $m$  fitting parameters  $A_i$ , such that  $f(A_1, \dots, A_m)$  is minimized

$$f(A_1, \dots, A_m) = \int [W^f(r, A_1, \dots, A_m) - W(r)]^2 dr \quad (16)$$

$W^f$  is the PMF between two particles interacting with an effective site-site potential

$$\begin{aligned}
 W^f(r, A_1, \dots, A_m) &= - \int_{-\infty}^r \int \bar{F}_z^f(r', \Omega, A_1, \dots, A_m) \\
 &\quad \times p^f(r', \Omega, A_1, \dots, A_m) d\Omega dr'
 \end{aligned}
 \quad (17)$$

where  $p^f(r', \Omega, A_1, \dots, A_m) = e^{-\beta U^f(r', \Omega, A_1, \dots, A_m)} / \int e^{-\beta U^f(r', \Omega, A_1, \dots, A_m)} d\Omega$  is the probability density and  $U^f(r', \Omega, A_1, \dots, A_m) = \sum_{k=1}^{N_{s,1}} \sum_{l=1}^{N_{s,2}} u^f(R_{kl})$  is the energy of the given configuration with CoM distance  $r'$ .  $N_{s,1}$  and  $N_{s,2}$  are the number of sites in particle 1 and 2, respectively.  $u^f(R_{kl})$  is the site-site potential defined as

$$u^f(R) = \sum_{i=1}^m \frac{A_i}{R^{v_i}} \quad (18)$$

where  $R$  is the site-site distance and  $v_i$  is a positive integer.

By assuming that the particle configurations have the same Boltzmann weights with an effective site-site potential as that in the cyl-PM model, that is,  $p^f(r', \Omega, A_1, \dots, A_m) = \int p(r', \mathbf{r}^N, \Omega) d\mathbf{r}^N$ , then eq 16 can be minimized with the linear least-squares method.  $W^f$  can be written as

$$\begin{aligned}
 W^f(r, A_1, \dots, A_m) &= - \int_{-\infty}^r \int \bar{F}_z^f(r', \Omega, A_1, \dots, A_m) \\
 &\quad \times \int p(r', \mathbf{r}^N, \Omega) d\mathbf{r}^N d\Omega dr'
 \end{aligned}
 \quad (19)$$

$$\begin{aligned}
 &= - \sum_{i=1}^m A_i \int_{-\infty}^r \int \xi_i(r', \Omega) \\
 &\quad \times \int p(r', \mathbf{r}^N, \Omega) d\mathbf{r}^N d\Omega dr'
 \end{aligned}
 \quad (20)$$

where

$$\xi_i(r', \Omega) = \sum_{k=1}^{N_{s,1}} \sum_{l=1}^{N_{s,2}} \frac{v_i z}{R_{kl}^{v_i+2}} \quad (21)$$

For a given  $r'$  and  $R_{kl}$ , the factors  $v_i/R_{kl}^{v_i+2}$  are constant. The different  $z$ -values can therefore be separated out and collected as a function of  $r'$  and  $R_{kl}$  in the averaging over orientations. After this operation, we find

$$\begin{aligned}
 &\int \xi_i(r', \Omega) \int p(r', \mathbf{r}^N, \Omega) d\mathbf{r}^N d\Omega \\
 &= v_i N_{s,1} N_{s,2} \int_0^{\infty} \frac{\bar{z}(r', R)}{R^{v_i+2}} P(r', R) dR
 \end{aligned}
 \quad (22)$$

where  $\bar{z}(r', R)$  is the mean z-distance and  $P(r', R)$  is the probability density for a certain site-site distance  $R$  for a fixed CoM distance  $r'$ . Both  $\bar{z}(r', R)$  and  $P(r', R) dR$  are collected from cyl-PM simulations for discrete values of  $R$ , which leads to

$$\begin{aligned}
 W^f(r, A_1, A_2, A_3) &= - \sum_i A_i v_i N_{s,1} N_{s,2} \\
 &\quad \times \int_{-\infty}^r \sum_{k=0}^M \frac{\bar{z}(r', R_k)}{R_k^{v_i+2}} P(r', R_k) dr'
 \end{aligned}
 \quad (23)$$

where  $P(r', R_k)$  now is the probability of a site-site distance  $R_k$  at a given CoM distance  $r'$ .

## ■ ASSOCIATED CONTENT

### ● Supporting Information

The simulation parameters for bulk-PM and cyl-PM and the fitting parameters for the effective site-site potential are provided. This material is available free of charge via the Internet at <http://pubs.acs.org>.

## ■ AUTHOR INFORMATION

### Corresponding Authors

\*E-mail: axel.thuresson@teokem.lu.se (A.T.).

\*E-mail: martin.turesson@teokem.lu.se (M.T.).

### Notes

The authors declare no competing financial interest.

## ■ ACKNOWLEDGMENTS

Computational resources were provided by the Swedish National Infrastructure for Computing (SNIC) through Lunarc, the Center for Scientific and Technical Computing at Lund University. The work was performed within the framework of the Swedish national strategic e-science research program eSENCE.

## ■ REFERENCES

- (1) Guldbbrand, L.; Jönsson, B.; Wennerström, H.; Linse, P. Electrical Double Layer Forces. A Monte Carlo Study. *J. Chem. Phys.* **1984**, *80*, 2221–2228.
- (2) Kjellander, R.; Marčelja, S. Correlation and Image Charge Effects in Electric Double-Layers. *Chem. Phys. Lett.* **1984**, *112*, 49–53.
- (3) Kjellander, R.; Marčelja, S. Inhomogeneous Coulomb Fluids with Image Interactions between Planar Surfaces. I. *J. Chem. Phys.* **1985**, *82*, 2122–2135.
- (4) Attard, P.; Mitchell, D. J.; Ninham, B. W. Beyond Poisson–Boltzmann: Images and Correlations in the Electric Double Layer. I. Counterions Only. *J. Chem. Phys.* **1988**, *88*, 4987–4996.
- (5) Valteau, J. P.; Ivkov, R.; Torrie, G. M. Colloid Stability: The Forces Between Charged Surfaces in an Electrolyte. *J. Chem. Phys.* **1991**, *95*, 520–532.
- (6) Jönsson, B.; Wennerström, H. In *Electrostatic Effects in Soft Matter and Biophysics*; Holm, C., Kékicheff, P., Podgornik, R., Eds.; NATO Science Series II - Mathematics, Physics and Chemistry; Kluwer Academic Publishers: Dordrecht, The Netherlands, 2001; Vol. 46, pp 171–204.
- (7) Turesson, M.; Jönsson, B.; Labbez, C. Coarse-Graining Intermolecular Interactions in Dispersions of Highly Charged Colloids. *Langmuir* **2013**, *28*, 4926–4930.

- (8) Meneses-Juarez, E.; Varga, S.; Orea, P.; Odriozola, G. Towards Understanding the Empty Liquid of Colloidal Platelets: Vapour–Liquid Phase Coexistence of Square-Well Oblate Ellipsoids. *Soft Matter* **2013**, *9*, 5277–5284.
- (9) Martinez-Haya, B.; Cuetos, A.; Lago, S.; Rull, L. F. A Novel Orientation-Dependent Potential Model for Prolate Mesogens. *J. Chem. Phys.* **2005**, *122*, 024908.
- (10) Martinez-Haya, B.; Cuetos, A. Columnar Phases of Discotics with Orientation-Dependent Interactions. *J. Chem. Phys.* **2009**, *131*, 074901.
- (11) Pandey, R. B.; Anderson, K. L.; Farmer, B. L. Exfoliation of Stacked Sheets: Effects of Temperature, Platelet Size, and Quality of Solvent by a Monte Carlo Simulation. *J. Polym. Sci., Part B: Polym. Phys.* **2006**, *44*, 3580–3589.
- (12) Lyubartsev, A. P.; Laaksonen, A. Calculation of Effective Interaction Potentials from Radial Distribution Functions: A Reverse Monte Carlo Approach. *Phys. Rev. E* **1995**, *52*, 3730–3737.
- (13) Ercolessi, F.; Adams, J. B. Interatomic Potentials from First-Principles Calculations: The Force-Matching Method. *Europhys. Lett.* **1994**, *26*, 583.
- (14) Izvekov, S.; Voth, G. A. Multiscale Coarse Graining of Liquid-State Systems. *J. Chem. Phys.* **2005**, *123*, 134105.
- (15) Noid, W. G.; Chu, J.-W.; Ayton, G. S.; Krishna, V.; Izvekov, S.; Voth, G. A.; Das, A.; Andersen, H. C. The Multiscale Coarse-Graining Method. I. A Rigorous Bridge between Atomistic and Coarse-Grained Models. *J. Chem. Phys.* **2008**, *128*, 244114.
- (16) Noid, W. G.; Chu, J.-W.; Ayton, G. S.; Krishna, V.; Izvekov, S.; Voth, G. A.; Das, A.; Andersen, H. C. The Multiscale Coarse-Graining Method. II. Numerical Implementation for Coarse-Grained Molecular Models. *J. Chem. Phys.* **2008**, *128*, 244115.
- (17) Thuresson, A.; Ullner, M.; Åkesson, T.; Labbez, C.; Jönsson, B. Monte Carlo Simulations of Parallel Charged Platelets as an Approach to Tactoid Formation in Clay. *Langmuir* **2013**, *29*, 9216–9223.
- (18) Peigneur, P.; Maes, A.; Cremers, A. Heterogeneity of Charge Density Distribution in Montmorillonite as Inferred from Cobalt Adsorption. *Clays Clay Miner.* **1973**, *23*, 71–75.
- (19) Michot, L. J.; Bihannic, I.; Porsch, K.; Maddi, S.; Baravian, C.; Mougel, J.; Levitz, P. Phase Diagrams of Wyoming Na-Montmorillonite Clay. Influence of Particle Anisotropy. *Langmuir* **2004**, *20*, 10829–10837.
- (20) Warkentin, B. P.; Bolt, G. H.; Miller, R. D. Swelling Pressure of Montmorillonite. *Soil Sci. Soc. Am. Proc.* **1957**, *21*, 495–497.
- (21) Hess, B.; Kutzner, C.; van der Spoel, D.; Lindahl, E. GROMACS 4: Algorithms for Highly Efficient, Load-Balanced, and Scalable Molecular Simulation. *J. Chem. Theory Comput.* **2008**, *4*, 435–447.
- (22) Bussi, G.; Donadio, D.; Parrinello, M. Canonical Sampling through Velocity Rescaling. *J. Chem. Phys.* **2007**, *126*, 014101.
- (23) van der Spoel, D.; Lindahl, E.; Hess, B.; van Buuren, E.; Apol, E.; Meulenhoff, P. J.; Tieleman, D. P.; Sijbers, A. L. T. M.; Feenstra, K. A.; van Drunen, R.; et al. *Gromacs User Manual version 4.5.4*; <http://www.gromacs.org/>, 2010.
- (24) Metropolis, N. A.; Rosenbluth, A. W.; Rosenbluth, M. N.; Teller, A.; Teller, E. Equation of State Calculations by Fast Computing Machines. *J. Chem. Phys.* **1953**, *21*, 1087–1097.
- (25) Lund, M.; Trulsson, M.; Persson, B. Faunus: An Object Oriented Framework for Molecular Simulation. *Source Code Biol. Med.* **2008**, *3*, 1.
- (26) Evans, D. F.; Wennerström, H. *The Colloidal Domain: Where Physics, Chemistry, Biology, and Technology Meet*, 2nd ed.; Wiley-VCH: New York, 1999.



## Paper III

Reprinted from *J. Colloid Interface Sci.*, **466**

A. Thuresson, M. Segad, M. Turesson and M. Skepö

Flocculated Laponite-PEG/PEO Dispersions with Monovalent Salt, a SAXS and Simulation Study., 330-342, 2016

©2016 with permission from Elsevier.





Contents lists available at ScienceDirect

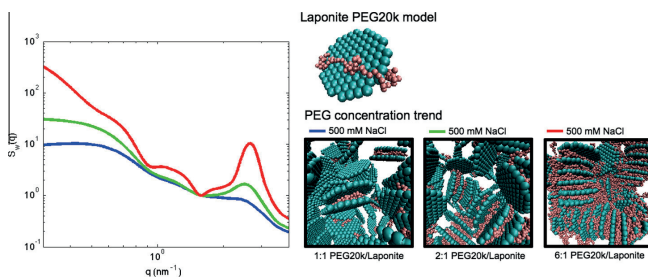
Journal of Colloid and Interface Science

journal homepage: [www.elsevier.com/locate/jcis](http://www.elsevier.com/locate/jcis)

## Flocculated Laponite–PEG/PEO dispersions with monovalent salt, a SAXS and simulation study

A. Thuresson<sup>a,\*</sup>, M. Segad<sup>b</sup>, M. Turesson<sup>a</sup>, M. Sköpö<sup>a</sup><sup>a</sup>Theoretical Chemistry, Lund University, POB 124, SE-221 00 Lund, Sweden<sup>b</sup>Advanced Light Source, Lawrence Berkeley National Laboratory, Berkeley, CA 94720, United States

### GRAPHICAL ABSTRACT



### ARTICLE INFO

#### Article history:

Received 5 October 2015

Revised 15 December 2015

Accepted 17 December 2015

Available online 18 December 2015

#### Keywords:

Laponite  
 Polyethylene glycol  
 Polyethylene oxide  
 Polymer bridging  
 Laponite–PEG composites  
 Laponite–PEO composites  
 Coarse-grained simulation  
 Molecular dynamics  
 Electrostatic interactions  
 Salt effects  
 Platelet polymer interaction  
 Tactoid  
 Bragg peak

### ABSTRACT

It is well-known that clay can form lamellar structures i.e. tactoids, and recently it has been shown that the tactoid formation is dependent on the platelet diameter. To the authors knowledge, no tactoid formation has been observed for montmorillonite platelets with a diameter less than 60 nm. In this study, small angle X-ray scattering in combination with coarse-grained modeling and molecular dynamics simulations have been utilized to study the sediment of Laponite–polyethylene glycol/polyethylene oxide (PEG/PEO) at elevated salt concentrations (150 mM–1 M). Laponite consists of platelets with a diameter of 25 nm and it is known to have a relatively monodisperse size-distribution. At pH 10, the face of the platelets has a strong negative charge, whereas the rim is slightly positive. Here we show that it is possible to induce tactoids for Laponite if two constraints are fulfilled: (1) addition of high amount of salt such as NaCl, and (2) addition of a neutral polymer such as PEG. The role of the salt is to screen the repulsive interactions between the platelets and the role of the polymer is to bridge the platelets together: hence the loss in configurational entropy of the polymer is counteracted by the gain in attractive polymer–platelet interaction. As the concentration of NaCl and/or PEG increases, the Bragg peak becomes sharper, which is an indication of that larger tactoids are formed.

Comparison between Laponite and montmorillonite shows that the interlayer distance between the platelets increases linearly with an increased Debye screening length for both type of clays, whereas the structure peaks of Laponite are broader compared to the montmorillonite. We argue that the main reason to the latter is due to the size of the platelets: (i) smaller platelets are less rotationally restricted

\* Corresponding author.

E-mail address: [axel.thuresson@teokem.lu.se](mailto:axel.thuresson@teokem.lu.se) (A. Thuresson).<http://dx.doi.org/10.1016/j.jcis.2015.12.033>

0021-9797/© 2015 Elsevier Inc. All rights reserved.

Total structure factor  
Aggregate

and (ii) the effect of positive edge charges is larger when the platelets are smaller, which results in more irregular aggregates. In absence of the polymer, montmorillonite form tactoids above  $\sim 0.3$  M NaCl whereas Laponite does not.

Even though the model used is simple, we find qualitative agreement between experiments and simulations, which verifies that the underlying physics for tactoid formation is captured.

© 2015 Elsevier Inc. All rights reserved.

## 1. Introduction

Many clay minerals swell in water and yield aqueous dispersions with unusual properties. Swelling 2:1 clays are made of platelets with a thickness of about 1 nm and lateral dimensions varying from 25 nm in synthetic Laponite clays to 1000 nm in natural montmorillonite. Previous experimental studies [1,2] have shown that Laponite exists in dilute suspensions as mono-disperse disc-shaped particles. When water is added, the clay platelets become ionized and a rising osmotic pressure in the solution causes the clay to swell [3–5]. Semi-dilute dispersions with volume fractions above 0.5% can behave as gels (they have a yield stress) [5–7]. Upon drying, they form films with excellent barrier properties. These are often used in surface coatings, paper and polymer films, household, and personal care products. Another very interesting area for clay is as storing alternative for the nuclear waste; where the nuclear waste is put into copper containers embedded in bentonite or other source of clay and placed underground [8].

Depending on the size, the platelets can form a lamellar structure making it a seemingly perfect model system for an electrical double layer, where the swelling and stability in saline solution depend strongly on counterion valency and surface charge density [9–11]. The situation is, however, from a structural point slightly less ideal. Clay is normally not a homogeneous lamellar material, it is rather better described as a disordered structure of stacks of platelets, sometimes called tactoids [12–14].

In a tactoid the platelets have agglomerated in a face-to-face conformation with equidistant separation [15]. The tactoid formation of montmorillonite has been studied for several decades [16–19], where Blackmore and Miller [20] were first to introduce the term in clay science. In their study, Ca-montmorillonite was analyzed with X-ray diffraction and a diffraction peak was found at  $1.9 \text{ nm}^{-1}$ . The diffraction peak gives an estimation of the repeat distance between platelets and the average number of platelets per tactoid. The repeat distance for Na-montmorillonite decreases with increasing NaCl concentration due to the electrostatic screening effect. At high enough NaCl concentration tactoids are formed [21].

Recently, it has been shown that the average diameter of Ca-montmorillonite platelets is related to the average number of platelets per tactoid [22]. By increasing the diameter of the clay platelets, the number of platelets per tactoid increases. To the authors knowledge, it has not been observed that montmorillonite platelets with a diameter less than 60 nm can form tactoids in water with neither NaCl nor  $\text{CaCl}_2$ . By generalizing this fact for Laponite, where the diameter is roughly 25 nm (model system for this study), tactoids will not be formed.

Clay/polymer complexes are of considerable importance in the field of colloid science, finding use in a wide range of applications from drilling muds [23,24] to paint. Studies that explore the nature of clay/polymer interactions and how it is affected by the physico-chemical properties of the solution are of fundamental importance since it can affect the bulk properties of the colloidal system such as the stability and the flow. It has been proposed that the polymers are disrupting hydrogen bonding between the water molecules and the silica or alumina functionalities of the clay surface,

and that the glycol molecules competes with water for these sites and also with water hydrating interlayer cations [23].

In the review by Anderson et al. [25] three different mechanisms are discussed for inhibition of clay swelling by addition of polyethylene glycol (PEG): (i) PEG diffuses into and displace water molecules from the interlayer; (ii) enthalpic terms i.e. the energy of the clay-PEG interaction is driving the reaction; or (iii) osmotic dewatering of the clay system. Smalley [26] has suggested a bridging flocculation method; but there has been, and still is, a dispute regarding the main mechanism, as stated by Liu et al. in 2004 [27].

It is well-known that PEG adsorbs onto the Laponite platelets, and at low salt concentration, relatively short PEG inhibits aggregation between the face and edge by steric hindrance [28]. Lal and Auvray [29,30] studied Laponite-PEG composites with Small Angle Neutron Scattering (SANS) using contrast variation techniques. They found that for 2 wt% Laponite with an addition of 1 wt% PEG suspension, the polymers adsorb and saturate the Laponite platelets with a 2–3 nm thick layer. Later, Nelson and Cosgrove [31] used SANS with contrast variation for a range of different molecular weights of PEG and found that the edge adsorption increases slightly with the polymer size whereas the adsorption on the face is more or less constant. By Dynamic Light Scattering studies (DLS) it was shown that the hydrodynamic thickness increases with molecular weight, indicating that the conformation of the adsorbed layer is very compact and it is much smaller than those normally observed for polymer adsorption on flat interfaces [32]. Nuclear Magnetic Resonance (NMR) studies of Na-montmorillonite and PEG have shown that ethylene oxide chains are in closest proximity with the surface [33].

In this article, we present results from our study of sedimented Laponite-PEG composites at pH 10 and at high salt concentrations. A relatively short PEG of molecular weight 20 kDa has been used. The experimental results were obtained by Small Angle X-ray Scattering (SAXS) and complemented by coarse-grained modeling and Molecular Dynamics simulations (MD). At pH 10, Laponite has a strong negative face charge and a weak positive edge charge [34]. Experimentally we show that, despite the small size of the Laponite platelets, it is possible to induce tactoids if two conditions are fulfilled: (1) high ionic strength, and (2) presence of PEG. Hence, it is not enough to only have a high amount of NaCl (as generalized above for montmorillonite) or a high amount of PEG. As the concentration of PEG increases, the number of platelets per tactoid increases and reaches a plateau value. The saturation concentration of PEG is in the same regime as the PEG adsorption isotherm to Laponite found by Mongondry et al. [28].

The experimental findings are compared to MD simulations where the platelets are modeled as negatively charged discs with explicit ions and adsorbing polymers. In the given model, we assume that the effect of the weakly positively charged rim is negligible, therefore only the face charge is taken into consideration. From the simulations, the total structure factor is calculated and compared to the experimental SAXS data. We find the corresponding polymer and salt concentration trends in the simulations as in the experiments. Simulations show that the system can be understood by a competition of electrostatic repulsive forces between the platelets and attractive bridging forces between the platelets

and polymers; which shed light to the dispute regarding the underlying mechanism for clay–PEG tactoid formation.

## 2. Material and methods

### 2.1. Experimental details

#### 2.1.1. Material

The source of clay used throughout this work was sodium Laponite from ROCKWOOD ADDITIVES. Analytical grade sodium chloride (purity, 99.5%) was purchased from MERCK and millipore water was used to prepare the solutions. PEG of molecular weight 20,000 g/mol, further denoted PEG20k, (purity, 98%) were purchased from ALDRICH.

#### 2.1.2. Sample preparation

The salt was dissolved in millipore water at least one week in advance. PEG20k was added to the suspension and shaken overnight until complete dispersion. Finally the Laponite was added (0.125 g Laponite in a suspension of total 5 g) and shaken overnight. The mass fraction for Laponite was set to 2.5 wt%, which corresponds to roughly 1% volume fraction (the density of Laponite is 2.53 kg/dm<sup>3</sup> [35]). The pH was set to 10 by addition of NaOH. The sample was set vertically for at least 48 h, and a clear sediment was noticed for all samples with a salt concentration >20 mM.

#### 2.1.3. SAXS

The SAXS experiments were performed at the synchrotron radiation facility MAX II in Lund using beamline I911-4 [36]. A monochromatic beam of 0.091 nm wavelength was used together with point collimation and a two-dimensional position-sensitive CCD detector. The sample to detector distance was 1.9 m (0.1 <  $q$  < 5 nm<sup>-1</sup>). The SAXS data were analyzed with the program FIT2D [37].

Laponite samples at varying PEG20k as well as NaCl concentrations were measured in 1 mm quartz capillaries. The background scattering of pure water at different polymer and salt concentrations were subtracted.

In order to estimate the size of aggregates i.e., the number of clay platelets per aggregate, a model scattering peak has been fitted to the experimental data. The scattering function can be approximated with a Lorentzian line shape:

$$q^2 I(q) \propto \frac{w}{(q - q_{max})^2 + w^2} \quad (1)$$

where  $I(q)$  is the scattering intensity and  $w$  is a measure of the width. The full width at half maximum (FWHM) of the peak is equal to  $2w$  and the average tactoid size can be expressed as  $\langle N \rangle \approx q_{max}/w$  [38,39,22,40,41]. In order to make the fitting procedure as reasonable as possible we have chosen to fit the data between  $q_{max} \pm 1$  nm<sup>-1</sup>. It should be noted that the fitted average tactoid size is a rough estimation and should not be taken as an exact number. All the fitted data can be found in the [Supplementary Material](#).

### 2.2. Simulation details

#### 2.2.1. Interaction potentials

The platelets are defined by a set of sites and the polymers are defined by a set of beads. In the simulations, the solvent is treated as a continuum with a uniform dielectric constant  $\epsilon_r = 78.3$ . All interactions are assumed to be pairwise additive. The electrostatic pair potential is defined as:

$$u_{ij}^{el}(r_{ij}) = \frac{e^2 z_i z_j}{4\pi\epsilon_0\epsilon_r r_{ij}} \quad (2)$$

where  $e$  is the elementary unit charge,  $\epsilon_0$  is the permittivity of vacuum,  $z_i$  is the valency of particle  $i$  and  $r_{ij}$  is the distance between particles  $i$  and  $j$ . The tripartite repulsive, truncated and shifted Lennard-Jones (TLJ) potential, is defined as:

$$u_{ij}^{TLJ}(r_{ij}) = \begin{cases} \epsilon_{TLJ} \left[ \left( \frac{\sigma_{ij}}{r_{ij}} \right)^{12} - 2 \left( \frac{\sigma_{ij}}{r_{ij}} \right)^6 + 1 \right] & \text{if } r_{ij} < \sigma_{ij} \\ 0 & \text{otherwise.} \end{cases} \quad (3)$$

The Lennard-Jones (LJ) potential is defined as:

$$u_{ij}^{LJ}(r_{ij}) = 4\epsilon_{LJ} \left[ \left( \frac{\sigma_{ij}}{r_{ij}} \right)^{12} - \left( \frac{\sigma_{ij}}{r_{ij}} \right)^6 \right]. \quad (4)$$

where the strength of the short-ranged potential was chosen to be  $\beta\epsilon_{TLJ_{site-site}} = \beta\epsilon_{TLJ_{ion-site}} = \beta\epsilon_{TLJ_{ion-bead}} = \beta\epsilon_{TLJ_{ion-ion}} = 1$ ,  $\beta = 1/kT$  with  $k$  being the Boltzmann constant and  $T = 300$  K is the temperature.  $\sigma_{ij} = (\sigma_i + \sigma_j)/2$  where  $\sigma_{ion} = 4$  Å,  $\sigma_{site} = 10$  Å, and  $\sigma_{bead} = 5.5$  Å. The total potential between all pairs is thus defined as:

$$u_{ij}(r_{ij}) = u_{ij}^L(r_{ij}) + u_{ij}^{TLJ}(r_{ij}). \quad (5)$$

where  $x$  can be either LJ or TLJ. The harmonic bond-stretching potential is defined as:

$$u_{b_j}(r_{ij}) = \frac{1}{2} k_{b_j} (r_{ij} - b_{ij})^2, \quad (6)$$

with  $b$  being the equilibrium bond length and  $k_b$  is the spring constant.

The harmonic bending potential is defined as:

$$u_a(\theta_{ijk}) = \frac{1}{2} k^\theta (\theta_{ijk} - \theta^\theta)^2, \quad (7)$$

where  $k^\theta$  is the spring constant,  $\theta_{ijk}$  is the angle between triplets of bonded sites  $i, j$ , and  $k$ , and  $\theta^\theta = \pi$  rad.

#### 2.2.2. Platelet and polymer description

A schematic representation of the platelet and polymer is shown in [Fig. 1](#). The model size is smaller than the experimental size in order to reduce the computational simulation time.

A platelet is modeled by 85 sites, where each site has a charge of  $z_{site} = -1$ , unless otherwise stated. Two adjacent platelet sites are connected by a harmonic bond-stretching potential with  $k_{b_{site-site}} = 40$  kT/Å<sup>2</sup> and  $b_{site-site} = 10$  Å and a harmonic bending potential with  $k^\theta = 4000$  kT/rad<sup>2</sup>.

A polymer consists of 68 beads. The polymer beads and the platelet sites are interacting by a LJ potential with  $\beta\epsilon_{LJ_{bead-site}} = 0.3$  kT.

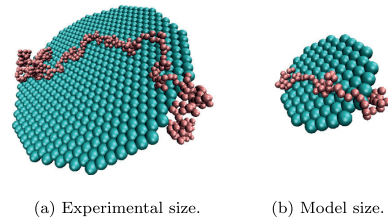


**Fig. 1.** Schematic representation of the experimental system size (a) and the model system size (b). In the experimental system, the platelet has a diameter of 25 nm and a thickness 1 nm. The polymer is PEG20k and consists of 455 beads, which gives a radius of gyration of  $R_g = 7$  nm [42]. The molar mass of each bead corresponds to one ethylene oxide group i.e. 44 g/mol. In the model system, the size of the platelet is 10 nm and 1 nm, for the diameter and thickness, respectively. The model polymer corresponds to PEG3000 i.e., 68 beads and a  $R_g = 2$  nm.

The non-adjacent beads and ions are interacting by a TLJ potential with  $\beta\epsilon_{TLJ\text{bead-bead}} = 8 \cdot 10^{-6}$ . Two adjacent polymer beads are connected by a harmonic bond-stretching potential with  $k_{b\text{bead-bead}} = 40 \text{ kT}/\text{\AA}^2$  and  $b_{b\text{bead-bead}} = 5.5 \text{ \AA}$ . The particular choice of bead-bead potential was used to produce a near identical equation of state to Cohen 2009 [43,44],  $k_{b\text{site-site}}$ ,  $k_{b\text{bead-bead}}$ , and  $k^{\theta}$  was chosen to resemble stiff bonds.

### 2.2.3. Ions

All ions were modeled as freely moving charges, and an excluded volume, using a TLJ potential. The total platelet charge was neutralized by monovalent counterions. Except for the platelets, its counterions, as well as neutral polymers; explicit monovalent (1:1) salt was also added to the system.

### 2.2.4. Simulations

Molecular dynamics simulations were performed with the software package GROMACS (version 4.5.4) [45]. The platelets were allowed to rotate and translate freely in a cubic simulation box with three-dimensional periodic boundary conditions. Newton's equations of motion of the freely moving species (platelets + polymers + ions) were integrated using a velocity Verlet algorithm. The temperature for each species was thermostated using velocity rescaling with a stochastic term, ensuring the generation of a proper canonical ensemble [46]. A time step of 10 fs was usually employed, and to check the convergence of the sampled radial distribution functions  $g(r)$ , simulations with a 1 fs time step were also performed for some of the systems. To account for the long-ranged electrostatic contribution, fast particle-mesh Ewald summation (PME) was used with a 60 Å real-space Coulomb cut-off and a Fourier spacing equal to 6 Å. For an in-depth description of the input parameters, see the online user manual [47]. Radial distribution functions were sampled during typically 50 ns of the simulation to obtain converged system energies.

The bulk systems in this work consist of 80 platelets with ions and polymers of varying amount in a cubic box of length 36.5 nm, unless otherwise stated. The volume of the box was chosen such that each platelet can be confined within a sphere with radius equal to the platelets radius. No boundary effects are expected for the polymer c.f.  $R_g = 2 \text{ nm}$  [42].

The adsorption isotherms for the model system were made with a single platelet placed inside a cubic box with its center of mass located at the box origin and the normal of the platelet is parallel to the z-axis. The cubic box has periodic boundary conditions and the length of the box is  $L = 20 \text{ nm}$ . The density of the beads from the PEG-molecules,  $\Gamma(z)$ , is calculated by counting the number of beads in each slice divided by the respective volume. The bulk concentration is found at the end of the box,  $c_{\text{bulk}} = \Gamma(L/2)$ , and the excess amount of beads adsorbed is calculated as,  $\Gamma_{\text{excess}} = 2L^2 \int_{\sigma_{\text{site}}/2}^{L/2} (\Gamma(z) - c_{\text{bulk}}) dz$ , where the factor of two is included because the platelet have two faces. Finally the excess amount of beads adsorbed is rescaled to an accessible experimental value by multiplying with the bead molar mass 44 g/mol and divide with the 85 site platelet molar mass. The molar mass of the 85 site platelet (radius 5 nm and thickness 1 nm) is estimated from the Laponite density as:  $2530 \text{ g dm}^{-3} \cdot (1 \cdot 5^2 \pi) \cdot 10^{-24} \text{ dm}^3 \cdot 6 \cdot 10^{23} \text{ mol}^{-1} \approx 10^5 \text{ g/mol}$ .

### 2.2.5. Structural information obtained from simulations

The form factor of a solid object is calculated as:

$$P(q) = \frac{1}{N_p^2} \sum_{m=1}^{N_p} \sum_{n=1}^{N_p} \frac{\sin(qr_{mn})}{qr_{mn}} \quad (8)$$

where  $N_p$  is the number of sites in a platelet and  $r_{mn}$  is the distance between site  $m$  and site  $n$ .

The total structure factor between the platelets is defined as:

$$S(q) = \left\langle \frac{1}{N} \sum_{i=1}^N \sum_{j=1}^N \frac{\sin(qr_{ij})}{qr_{ij}} \right\rangle \quad (9)$$

where  $N$  is the total number of platelet sites in the system.

The above equation can be rewritten to:

$$S(q) = 1 + 4\pi \frac{N}{V} \int_0^{\infty} (g(r) - 1) r^2 \frac{\sin(qr)}{qr} dr \quad (10)$$

where  $g(r)$  is the radial distribution function between all platelet sites in the system. If  $g(r)$  is not approaching one due to the finite length of the box, a window function can be used to reduce artifacts:

$$S_w(q) = 1 + 4\pi \frac{N}{V} \int_0^{\infty} (g(r) - 1) r^2 \frac{\sin(qr)}{qr} \frac{\sin(\pi r/R_c)}{\pi r/R_c} dr \quad (11)$$

where  $R_c$  is the maximum distance in  $g(r)$  [48]. The total structure factor from a simulation of neutral platelets (no ions present) where the sites are interacting with a LJ-potential ( $\sigma = 2.6 \text{ nm}$  and  $\epsilon = 0.02$  or  $0.05 \text{ kT}$ ) are shown in Fig. 2a and b. The simulated  $S_w(q)$  has been compared to *StackedDiskModel* in SASVIEW with reasonable agreement. The parameters in SASVIEW were set such that the scattering from the solvent and layer is zero, core thickness 0.1 nm, layer thickness 1.3 nm, radius of disc 5 nm, and  $\sigma_{\text{d}} 0.1$ . By increasing the short-ranged attractive interaction parameter,  $\epsilon$ , in the computer simulations, larger tactoids are obtained (Fig. 2c and d). In the SASVIEW application the stack corresponds to either four or 30 platelets.

## 3. Results and discussion

### 3.1. Small angle X-ray scattering

The experimental analysis in this work is based on structure peaks as have been measured with SAXS. A structure peak corresponds to the average repetitive separation distance between the Laponite platelets. If the degree of order in the system is such that the intensity scattering function show a structure peak that is clearly visible in the log-log plot, we define it as a Bragg peak. Throughout this article, our results will be compared to the results in the literature regarding montmorillonite.

In Fig. 3 the Kratky plot of three intensity scattering functions are shown for Laponite in pure water at high volume fractions, 14 vol% (blue circle), 20 vol% (black dashed), and 22 vol% (red line). As shown, the structure peaks are shifted to higher  $q$ -values i.e. smaller average separation distances between the platelets, when the volume fraction of Laponite is increased.

It has earlier been shown that the spacing between clay platelets in Na-montmorillonite between 4 vol% and 25 vol% is a linear function of the inverse volume fraction corresponding to an almost perfect exfoliated one-dimensional system [38]. The structure peaks depicted in Fig. 3 are very broad compared to Na-montmorillonite at high volume fraction, which is due to the fact that the average radius of a montmorillonite platelet is approximately ten times larger than the radius of a Laponite platelet. Smaller platelets are rotationally less restricted and the positive edge charges have a larger impact to create a more disordered state. Using the relation  $d = 2\pi/q$ , the average repeat distance between the platelets is estimated from the X-ray scattering intensity to be located at  $\sim 7.8 \text{ nm}$ ,  $\sim 5.4 \text{ nm}$ , and  $\sim 4.2 \text{ nm}$ . The corresponding inverse volume fractions multiplied by the platelet thickness,  $1 \cdot \phi_c^{-1} \text{ nm}$  (the platelet is assumed to have a thickness

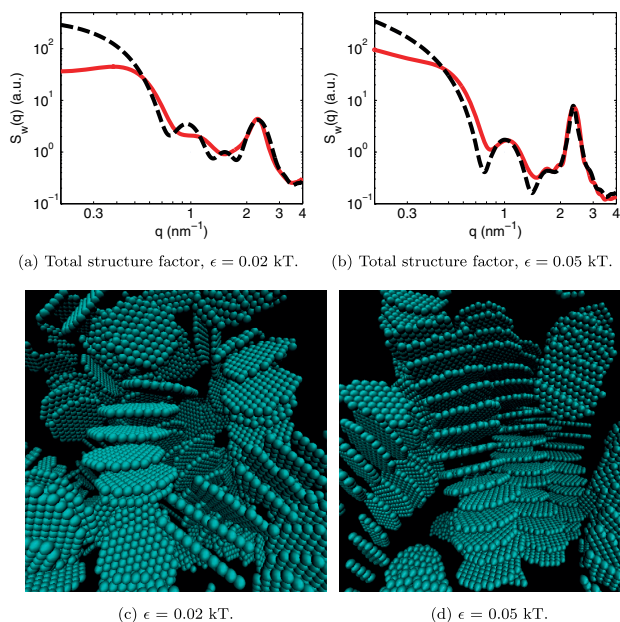


**Fig. 2.** (a) and (b) Simulated  $S_w(q)$  for platelet sites interacting with a LJ-potential with  $\sigma = 2.6$  nm and  $\epsilon = 0.02$  kT or  $\epsilon = 0.05$  kT (red line), compared with *StackedDiskModel* in SASVIEW (black dashed). (c) and (d) Illustrative configurations obtained from the simulations. (For interpretation of the references to colour in this figure legend, the reader is referred to the web version of this article.)

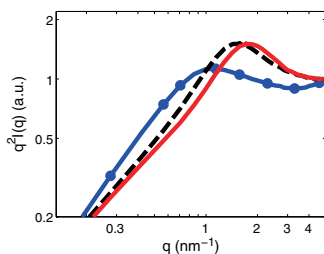


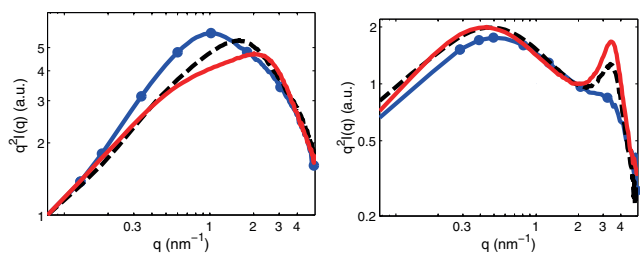
**Fig. 3.** Kratky plot of the intensity scattering functions as a function of the wave vector for Laponite–water (no salt) dispersions. The scattering intensities are normalized at the highest  $q$ -value. The structure peak is shifted to higher  $q$ -values (smaller average separation between the platelets) with increasing volume fraction. The used volume fractions of Laponite are 14%, 20%, and 22%, which corresponds to the blue circle, black dashed, and red line respectively. (For interpretation of the references to colour in this figure legend, the reader is referred to the web version of this article.)

of 1 nm), is  $\sim 7.1$  nm,  $\sim 5.0$  nm, and  $\sim 4.5$  nm. Thus, a reasonable agreement is obtained given the difficulty to locate the average repeat distance of the structure peaks.

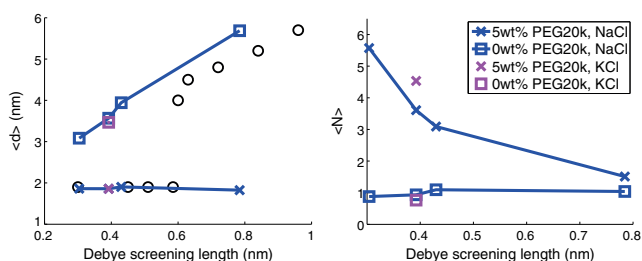
Flocculation (and sedimentation) of a 2.5 wt% Laponite dispersion is known to occur at NaCl concentrations above 20 mM [4]. In Fig. 4a the Kratky plot of the intensity scattering function is shown for sedimented Laponite at three different NaCl concentra-

tions. For each of the curves there is a broad structure peak with a maximum value,  $q_{max}$ , which gives the average distance between the platelets. Fig. 4c and d display the average distance between the platelets and the average number of platelets per tactoid as a function of the Debye screening length. As shown, the average distance between the Laponite platelets increases linearly as a function of the Debye screening length (linear regression coefficient of 0.998), which confirms that the system is driven by electrostatic interactions. The same linear trend has also been shown for montmorillonite (data from Norrish[21]). For Na-montmorillonite the tactoid formation starts at  $\sim 0.3$ – $0.5$  M NaCl, and two spacings are observed initially, the first at 1.9 nm and the second at 4 nm. A separation of 1.9 nm corresponds to three water layers ( $\sim 0.9$  nm) between the  $\sim 1$  nm thick platelets. At lower salt concentrations the average distance between platelets is proportional to  $1/\sqrt{C}$  where  $C$  is the molar concentration of salt [21,49]. In Fig. 4d, the average number of platelets per tactoid for Laponite with NaCl is found to be one and hence there is no tactoid formation (the platelets are not very well ordered).

Fig. 4b shows the effect of adding 5 wt% of the neutral polymer, PEG20k, to the system i.e. there is an excess of polymer. The structure in the sample has now completely changed compared to the sediment where no PEG is added, see Fig. 4a. At the higher salt concentrations a Bragg peak is found at  $\sim 3.4$  nm $^{-1}$ , which corresponds to a repeat distance between the platelets of  $\sim 1.8$  nm. A structure peak is depicted for 0.15 M NaCl and with additional salt the FWHM decreases. The average number of platelets per tactoid was estimated to be smaller than two for 0.15 M and roughly six for 1 M NaCl. Comparing Fig. 4a with Fig. 4b it is clear that a high



(a) Salt concentration trend for Laponite with 0 wt% PEG and 0.15 M (blue circle), 0.5 M (black dashed) or 1 M (red line) NaCl. (b) Salt concentration trend on Laponite with 5 wt% PEG 20k and 0.15 M (blue circle), 0.5 M (black dashed) or 1 M (red line) NaCl.



(c) Average platelet distance between Laponite platelets as a function of the Debye length with NaCl (blue), KCl (purple) and 0 wt% PEG20k (square) and 5 wt% PEG20k (cross). Comparison with data by Norrish and Na-montmorillonite (black circle). [21] (d) Average number of platelets per tactoid for Laponite as a function of the Debye length.

**Fig. 4.** (a) and (b) Kratky plot of the intensity scattering function for 2.5 wt% Laponite in NaCl solutions of varied concentration (0.15 M (blue circle), 0.5 M (black dashed), and 1 M (red line)), with 0 wt% PEG20k and 5 wt% PEG20k respectively. The scattering intensities are normalized at the lowest  $q$ -value for (a) and at  $q \approx 2 \text{ nm}^{-1}$  for (b). (c) The average distance between platelets as a function of the Debye screening length. The crosses and squares show the maximum value in each Kratky plot with PEG20k and without PEG20k respectively. The circles show the result for Na-montmorillonite from Norrish [21]. (d) The average number of platelets per tactoid estimated by applying Eq. (1). (For interpretation of the references to colour in this figure legend, the reader is referred to the web version of this article.)

amount of salt is not enough to form tactoids, an addition of PEG is necessary. It should be noted that there are two peaks in Fig. 4b. We attribute the peak at low  $q$ -value ( $\sim 0.4 \text{ nm}^{-1}$ ) to be the characteristic tactoid–tactoid distance.

It is well-known that potassium binds stronger to the montmorillonite platelets than sodium and thereby inhibit clay swelling [21]. This has for example been used in oilfield applications. A comparison of the scattering intensity functions of the sediment when 0.6 M KCl or 0.6 M NaCl have been added to the Laponite suspension is found in the Supplementary Material. In Fig. 4c and d it is shown that the average distance between the platelets and that the average tactoid size is similar for KCl and NaCl:  $\langle d \rangle \sim 3.5 \text{ nm}$  without PEG20k and  $\langle d \rangle \sim 1.8 \text{ nm}$  with 5 wt% PEG20k ( $\langle N \rangle \sim 4$ –5).

It is reasonable to find a platelet–platelet separation of approximately 1.8 nm, in the literature the same separation distance has been found for tactoids in many types of clays and Laponite–PEG composites. For example, a separation of 1.8 nm was found with X-ray Diffraction (XRD) for multilayered films of Laponite–PEG composites [50], and 1.89 nm was found for freeze-dried Laponite–PEG composites with XRD [51]. PEG2k and PEG35k in the molten state at  $70^\circ\text{C}$  were mixed with Laponite (salt free solution) and measured with SANS and XRD. In the former no clear Bragg peak was reported but with the latter it was shown that an addition of polymer enhance the order of the clay platelets [52].

In order to not misinterpret the results in this study compared to the salt free Laponite–PEG composites measured with XRD, the reader should notice that XRD was applied to dry samples. The

sediment in our SAXS measurements has not been subjected to any pre-treatment, hence water still exist in the samples.

The separation of  $\sim 1.9$  nm is typically found for Namontmorillonite and montmorillonite at high NaCl solutions with multivalent counterions such as  $Mg^{2+}$ ,  $Ca^{2+}$ ,  $La^{3+}$  [21,38,15,49]. Despite the fact that Laponite is a synthetic trioctahedral clay and montmorillonite is a natural dioctahedral clay i.e. dissimilarity in atomistic structure, similar separation distances between the two types of clay are obtained. One main difference between Laponite and montmorillonite is the average size of the platelets, where the average diameter of a montmorillonite platelet is typically one order of magnitude larger than Laponite platelet [15]. Another dissimilarity is the polydispersity, where the size distribution of montmorillonite platelets is large, and the smallest platelets is typically of the same size as Laponite, which is known to be relatively monodisperse [15]. For size fractionated Ca-montmorillonite, it has been shown that the average number of platelets per tactoid is related to the average platelet diameter. Platelets with diameter less than  $\sim 60$  nm show no tendency to form tactoids [39,22].

In Fig. 5 the scattering intensity functions are shown for three different concentrations of PEG20k supplemented with 1 M NaCl. The molar mass of a Laponite platelet is estimated from the density to be  $2530 \text{ g dm}^{-3} \cdot (1 \cdot 12.5^2 \pi) \cdot 10^{-24} \text{ dm}^3 \cdot 6 \cdot 10^{23} \text{ mol}^{-1} \approx 7 \cdot 10^5 \text{ g/mol}$  and hence the mass of a Laponite platelets is about 35 times the mass of a PEG20k molecule. Here 0.05 wt % corresponds to a system which is undersaturated with PEG molecules with respect to the number ratio clay platelets/PEG molecules, 0.4 wt% corresponds to a number ratio of approximately six, whereas for 5 wt% there is a large excess of PEG molecules. By increasing the PEG concentration, the structure peak becomes a Bragg peak with a maximum at  $\sim 3.4 \text{ nm}^{-1}$ . The corresponding scattering intensity functions for 10 wt% and 15 wt% PEG20k have also been measured (data not shown) and the location of the Bragg peaks are approximately at the same  $q$ -value as for 5 wt%. At an addition of 5 wt% PEG20k the system seems to have reached a plateau value with respect to the number of tactoids and their size. For 0.4 wt% and 5 wt% PEG20k there is  $\sim 0.16 \text{ g/g}$  and  $2 \text{ g/g}$  (g PEG20k/g Laponite) respectively. Hence, the saturation is located somewhere between 0.16 and  $2 \text{ g/g}$ , which is in agreement with the adsorption isotherm for PEG20k in Laponite dispersion ( $\sim 1.4 \text{ g/g}$ ) [28].

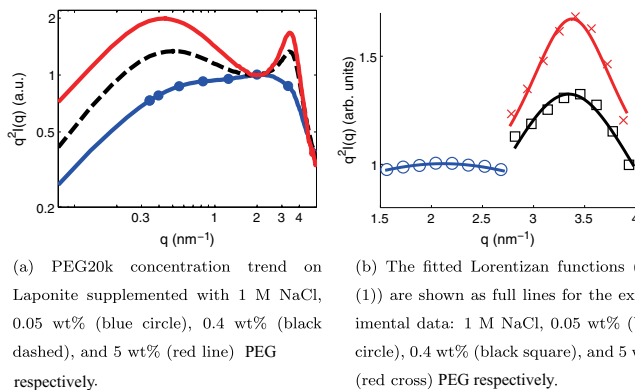


**Fig. 5.** (a) Kratky plot of the scattering intensity function for 2.5 wt% Laponite in 1 M NaCl solution with varied PEG20k concentration; 0.05 wt% (blue circle), 0.4 wt% (black dashed), and 5 wt% (red line), PEG respectively. The intensities are normalized at  $q \approx 2 \text{ nm}^{-1}$ . The average number of platelets per tactoid was estimated to be  $\langle N \rangle < 2$  for 0.05 wt%,  $\langle N \rangle \approx 3$  for 0.4 wt%, and  $\langle N \rangle \approx 6$  for 4 wt% PEG20k obtained by applying Eq. (1). (For interpretation of the references to colour in this figure legend, the reader is referred to the web version of this article.)

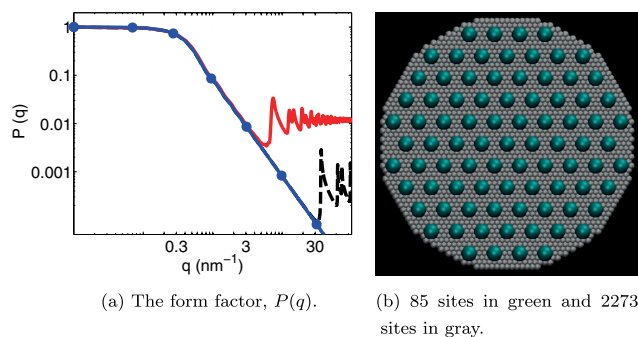
## 3.2. Simulations

### 3.2.1. The form factor

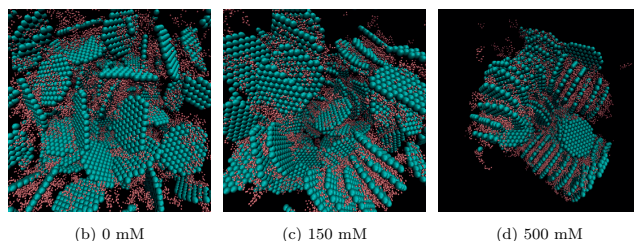
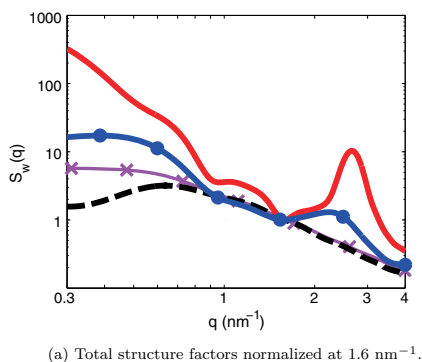
In the simulations the clay platelets are represented as a set of points in a hexagonal lattice with a 5 nm radial cut off. In Fig. 6a the form factor according to Eq. (8) is calculated for a discrete platelet with 85 sites, a discrete platelet with 2273 sites (Fig. 6b), and a homogeneous thin cylinder with 5 nm radius and 0.01 nm thickness (calculated with SASVIEW). The only visible difference is noticed at high  $q$ -values, at approximately  $6 \text{ nm}^{-1}$  for the platelet with 85 sites and  $32 \text{ nm}^{-1}$  for the platelet with 2273 sites corresponding to 1 nm and 0.2 nm respectively (c.f. 1 nm site–site distance of the model). From these  $q$ -values, and the fact that the highest possible  $q$ -value from the experiment is  $5 \text{ nm}^{-1}$ , the conclusion is that the discretization of a platelet only introduces artifacts between nearest sites on a platelet, and that an 85 site platelet can be used for comparison.

### 3.2.2. Bulk simulations: Salt and polymer trends

In the simulations, there is a competition between the repulsive and the attractive forces between the polymer and platelets, where the repulsive forces between the platelets are due to electrostatic repulsion, translational, and rotational entropy. The attractive forces have their origin in the polymers that would like to bridge between the platelets. When salt is added to the system the electrostatic repulsion is screened, and at high enough salt concentrations, the electrostatic barrier is significantly reduced, which implies that the polymers have to overcome the rotational and translational entropic components between the platelets, as well as the loss in their own configuration entropy, to form tactoids. In Fig. 7 the total structure factor according to Eq. (11) has been calculated for simulations with converged energies of 80 platelets in a cubic box with, on average, six polymers per platelet c.f. experiment. With an increased amount of salt, the Bragg peak FWHM becomes smaller corresponding to larger tactoids. With zero mM salt, no Bragg peak is visible i.e. there are no tactoids in the system (Fig. 7a). When the salt concentration is increased, the polymers can bridge the platelets in a parallel arrangement where the platelet–platelet distance becomes  $\sim 2.4$  nm and small aggregates are found, see 150 mM salt (Fig. 7c). When the salt concentration is increased further to 500 mM, all the tactoids aggregate into one



**Fig. 6.** The form factor is shown for a platelet of 85 (red line) and 2273 sites (black dashed) and compared to a homogeneous thin cylinder of thickness 0.01 nm (blue circle). The later is obtained by applying SASVIEW. The radius of the platelets is 5 nm in all approaches. (For interpretation of the references to colour in this figure legend, the reader is referred to the web version of this article.)

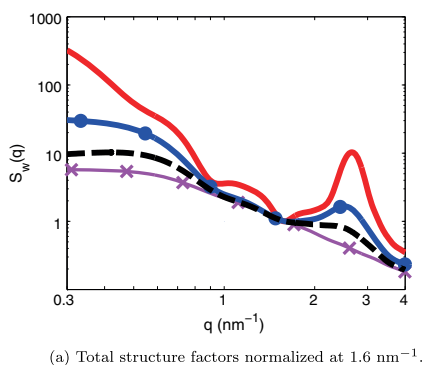
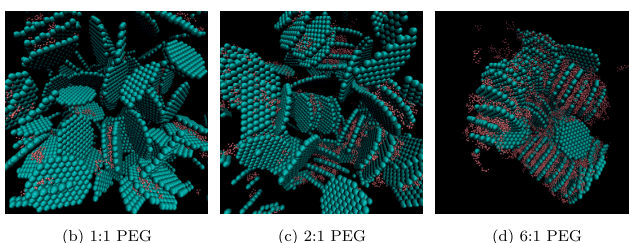


**Fig. 7.** (a) Total structure factor,  $S_w(q)$ , from the simulations for 80 platelets with LJ-eps = 0.3 kT, on average there are six polymers per platelet. The salt concentration is varied between 0 mM (black dashed), 150 mM (blue circle), and 500 mM (red line). The corresponding structure factor for platelets only (purple cross), i.e. when only excluded volume is taken into account and no polymers and ions exist, is included for comparison. Figure (b)–(d) show three illustrative configurations obtained from the simulations. All small ions are omitted due to clarity, the platelets are shown in green, and the polymers in red. (For interpretation of the references to colour in this figure legend, the reader is referred to the web version of this article.)

cluster, as shown in the snapshot in Fig. 7d. The salt trend found in the simulations can qualitatively be compared to the experimental data in Fig. 4b.

Introducing more polymers into the system increases the effective attraction between the platelets since more polymers are con-

tributing to the bridging, until saturation is reached. In Fig. 8, the salt concentration is kept constant at 500 mM and the polymer concentration is varied as X:1 where X is the number of polymers per platelet. The total structure factor reveals that the Bragg peak FWHM is decreased with an increased polymer concentration. In

(a) Total structure factors normalized at  $1.6 \text{ nm}^{-1}$ .

(b) 1:1 PEG

(c) 2:1 PEG

(d) 6:1 PEG

**Fig. 8.** (a) Total structure factor,  $S_w(q)$ , for 80 platelets with the short-ranged attractive interaction parameter set to  $\epsilon = 0.3 \text{ kT}$ , and 500 mM 1:1 salt was added. The polymer concentration is varied, and the number ratios are 1:1 (black dashed), 2:1 (blue circle), 6:1 (red line), with respect to PEG. The corresponding structure factor for platelets only (purple cross), i.e. when only excluded volume is taken into account and no polymers and ions exist, is included for comparison. (b)–(d) Three illustrative and typical configurations from the simulations. In the snapshots, all the small ions are omitted due to clarity, the platelets are shown in green, and the polymers in red. (For interpretation of the references to colour in this figure legend, the reader is referred to the web version of this article.)

Fig. 8b–d the corresponding configurations from the simulations are shown. With an unsaturated amount of PEG (1:1 and 2:1) the polymers prefer to bridge a few of the platelets and not adsorb onto the single platelets.

Three possible scenarios for a system with an unsaturated amount of polymers and a fixed amount of salt are schematically shown in Fig. 9. Scenario A has been optimized with respect to the electrostatic repulsion where the platelets are far apart and the polymers can only adsorb onto single platelets. Scenario B has been optimized with respect to the electrostatic repulsion for the single platelets and the minimization in energy for the bridging polymers at the cost of bringing two of the platelets close to each

other. Scenario C has been optimized with respect to the minimization in energy for the bridging polymers only. The hypothesis is that scenario B is the best compromise between bridging and electrostatic repulsion. The thermodynamical reason to bridge two platelets is to minimize the energy and gain configurational entropy since the polymers obtain two surfaces to adsorb onto instead of only one i.e. the amount of contact points can be increased while still being able to attain many configurations. Forming few aggregates is more favorable since the distance can be increased between the single platelets, and hence the electrostatic repulsion is lowered and the translational and rotational entropy is increased. The polymer concentration trend obtained from the simulations can qualitatively be compared to the one achieved from SAXS, see Fig. 5.

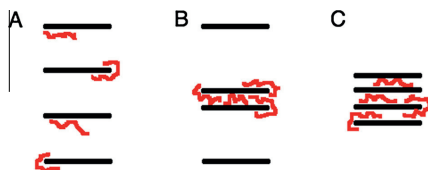


**Fig. 9.** Three schematic scenarios optimized for the electrostatic repulsion, entropy and/or the polymer bridging for a system of charged platelets and an unsaturated amount of adsorbing polymer. The platelets are represented by the black bars and the polymers by the red lines. (For interpretation of the references to colour in this figure legend, the reader is referred to the web version of this article.)

### 3.2.3. Charged compared to uncharged platelets

In Fig. 10 the total structure factors are shown for solutions consisting of: (i) 80 charged platelets, 500 mM 1:1 salt, and 160 polymers; (ii) 80 uncharged platelets, zero salt, and 160 polymers, and (iii) uncharged platelets only i.e. in the latter neither salt nor polymers are included. The Bragg peak in system (ii) is translocated to higher  $q$ -values when all charges and thereby also counterions are omitted. This indicates that the platelet–platelet distance becomes shorter and larger tactoids are formed, which of course is an effect of the lack of electrostatic repulsion in the uncharged system, in combination with the absence of counterions. Hence, despite the fact that the electrostatic repulsion would like to separate the

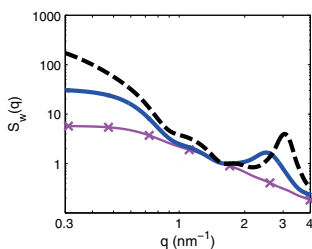


**Fig. 10.** Total structure factor (normalized at  $1.6 \text{ nm}^{-1}$ ) for 80 platelets and 160 polymers. The short-ranged attractive interaction parameter was set to  $\epsilon = 0.3 \text{ kT}$ . To the charged system, 500 mM salt is added, see blue curve, the corresponding uncharged system i.e. platelets and polymers only, are given in the black dashed curve, and the structure factor where only neutral platelets with excluded volumes are taken into consideration (no salt and no polymer) is shown as the purple cross. (For interpretation of the references to colour in this figure legend, the reader is referred to the web version of this article.)

platelets, there is also a competition of the available space in the interlayer in the tactoids as well; and in the charged system, the excluded volume of the counterions plays an important role in that respect. For a system with only neutral platelets; no Bragg peak is visible, see the purple cross line.

### 3.2.4. Adsorption isotherm and conformational properties of the polymer

The adsorption isotherm as function of bulk concentration and polymer length is shown in Fig. 11. A polymer that is one fourth (17 beads) and two times (136 beads) the length of the reference polymer (68 beads) that was used in the bulk simulations has been included, as well. A longer polymer can obtain more contact points compared to a shorter polymer. Hence a longer polymer adsorbs more strongly to the platelet. At  $\sim 20 \text{ g/L}$  polymer bulk concentration, the 136 bead polymer has completely saturated the platelet. The 68 and 17 bead long polymer requires a higher bulk concentration to find their saturation points. These results can qualitatively be compared to the adsorption isotherms by Mongondry et al. [28].

Due to the additive van der Waals (vdw) interaction in the model, the polymers can roughly lower their energy by a factor of two when located between two platelets instead of adsorbing onto a single platelet. Thus, the concentration of polymer between two platelets is higher than the concentration outside a single platelet. In Fig. 12, there are 80 polymers with 17 beads, 20 polymers

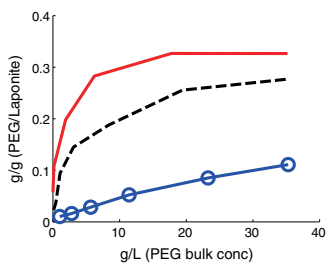


**Fig. 11.** Adsorption isotherm of the polymers onto a single platelet with short-ranged Lennard-Jones interaction parameter of  $\epsilon = 0.3 \text{ kT}$  for 17 bead long polymers (blue circle), 68 bead long polymers (black dashed), and 136 bead long polymers (red line). (For interpretation of the references to colour in this figure legend, the reader is referred to the web version of this article.)

with 68 beads or 10 polymers with 136 beads. Two parallel platelets with their center of mass fixed at  $x = 0, y = 0$  and  $z = \pm 1.2 \text{ nm}$  (a separation of 2.4 nm was found for the tactoids in Fig. 7) inside a cubic box with periodic boundary conditions and length  $L = 20 \text{ nm}$ . The bead concentration is calculated within  $\sqrt{x^2 + y^2} < 4 \text{ nm}$ . It is found that the radius of gyration of the 68 bead polymer between the two platelets is 1.8 nm whereas the corresponding radius of gyration in bulk is 2 nm, hence the polymer is slightly contracted. A deeper analyze of the configurational properties of the 68 bead polymer is obtained by studying the individual Cartesian coordinate of the polymers:  $R_x := \sqrt{\frac{1}{N} \left\langle \sum_{i=1}^N (x_i - x_{\text{mean}})^2 \right\rangle}$  where  $N = 68$  and  $R_x$  is either in the  $x$ -,  $y$ - or  $z$ -direction. Obviously the polymer in bulk has  $R_x = R_y = R_z$  since there is no directional preference. The polymer between two platelets has  $R_x = R_y$  since the platelets are circular but  $R_z$  could denote. In fact,  $R_z = 0.32 \text{ nm}$  and  $R_x = R_y = 1.25 \text{ nm}$  for the polymers between the platelets and  $R_x = R_y = R_z = 1.10 \text{ nm}$  for the polymers in bulk. In this respect, a comparison between radius of gyration in bulk and in adsorbed state is not sensitive enough. Even though a deviance of 10% contraction is shown when adsorbed to surfaces, the microstructure of the polymer is much more affected. In the adsorbed state, the polymer is compressed in the  $z$ -direction and much more extended in the  $x$ - and  $y$ -direction and achieves an anisotropic shape.

## 4. Conclusions

In this study we have shown that coarse-grained modeling and molecular dynamics simulations can be used to capture the qualitative trends for Laponite-PEG sediments that were observed in the SAXS-experiments. Moreover, we have shown that even though Laponite is synthetic and trioctahedral, and montmorillonite is natural and dioctahedral, they have many similarities but also some differences. One example of the latter is that the structure peaks of Laponite are broader compared to the ones obtained by montmorillonite. We argue that the main reason for this is the size of the platelets. Smaller platelets are less rotationally restricted and the effect of positive edge charges is larger, hence the formed aggregates are more irregular.

We have also shown that it is possible to induce tactoids for sedimented clays where the platelets radius is less than 60 nm by adding NaCl and PEG. For that scenario, two constraints need to be fulfilled: (1) high amount of salt to screen the repulsive interactions between the platelets, and (2) addition of a neutral polymer for example PEG20k, as used in this work. The role of the polymer is to bridge the platelets together and the loss in configurational entropy of the polymer is counteracted by gain in attractive polymer-platelet interaction. As the concentration of NaCl and/or PEG20k concentration increases, the Bragg peak becomes sharper, which is an indication of that larger tactoids are formed.

By the results obtained in this study we can now extend the schematic picture from Atmuri et al. [53] with an extra column with addition of NaCl (see Fig. 13). With no adsorbing polymer we find a rather random but sedimented structure where the average distance between the platelets is proportional to the Debye screening length. Below adsorbing polymer saturation concentration, small tactoids are found, and above the saturation concentration, larger tactoids are formed in the sediment.

The simulations show that there is a competition between the electrostatic repulsion and the attractive polymer bridging. Even though the model is simple, it is possible to capture the underlying physics for tactoid formation and to obtain a molecular picture.

Finally, by tuning the parameters  $\epsilon$  and  $\sigma$ , the same repeat distance within the tactoids in the simulations as in the experiments

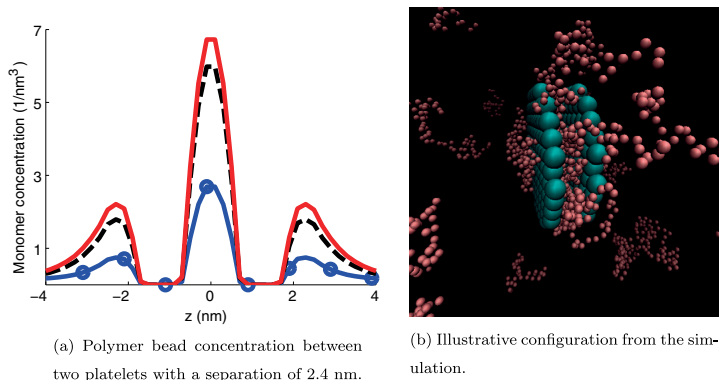


**Fig. 12.** (a) Bead-platelet concentration profile between two platelets with a separation of 2.4 nm for 17 bead long polymers (blue circle), 68 bead long polymers (black dashed), and 136 bead long polymers (red line). (b) A representative configuration from the simulation with the 68 bead polymers. The small ions are omitted due to clarity, the platelets are shown in green, and the polymers in red. (For interpretation of the references to colour in this figure legend, the reader is referred to the web version of this article.)

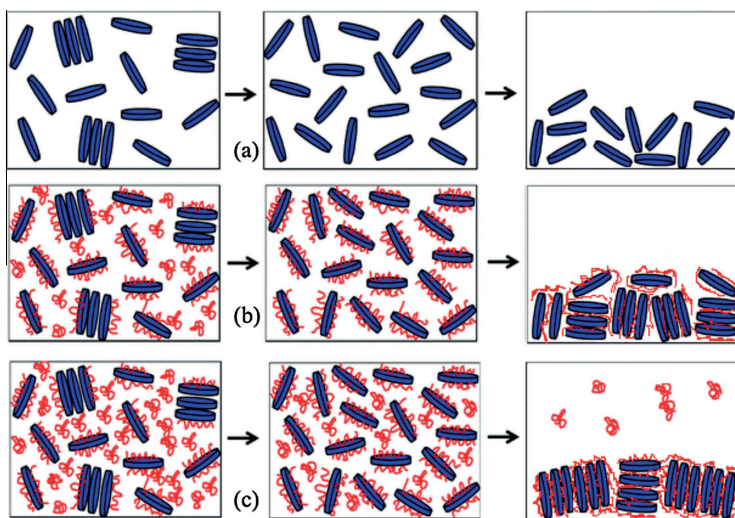


**Fig. 13.** Extension of schematic Laponite dispersions from Atmuri et al. [53]. Showing initial structure (left), structure after aging (middle), and after addition of salt (right) with (a) no polymer, (b) adsorbing polymer below saturation concentration, and (c) adsorbing polymer above saturation concentration. The right column is added by this work.

could be found. However, fitting parameters for a simple model rarely gives any additional physical insight. A more reasonable approach to improve our model would be to use real size platelets and polymers, include a more advance salt–polymer interaction, include positive charges on the edge of the platelets, and include a gravitational force (on-going research).

#### Acknowledgements

We appreciate all help from the staff and especially Sebastian Lages at MAX-lab, Lund University. Computational resources were provided by the Swedish National Infrastructure for Computing (SNIC) through Lunarc, the Center for Scientific and Technical

Computing at Lund University. The work was performed within the framework of the Swedish national strategic e-science research program eSENCE.

## Appendix A. Supplementary data

Supplementary data associated with this article can be found, in the online version, at <http://dx.doi.org/10.1016/j.jcis.2015.12.033>. These data include MOL files and InChIKeys of the most important compounds described in this article.

## References

- [1] R. Avery, J. Ramsay, Colloidal properties of synthetic hectorite clay dispersions: II. Light and small angle neutron scattering, *J. Colloid Interface Sci.* 109 (2) (1986) 448–454, [http://dx.doi.org/10.1016/0021-9797\(86\)90322-X](http://dx.doi.org/10.1016/0021-9797(86)90322-X).
- [2] D.W. Thompson, J.T. Butterworth, The nature of Laponite and its aqueous dispersions, *J. Colloid Interface Sci.* 151 (1) (1992) 236–243, [http://dx.doi.org/10.1016/0021-9797\(92\)90254-4](http://dx.doi.org/10.1016/0021-9797(92)90254-4).
- [3] P. Mongondry, J.F.T. Tassin, T. Nicolai, Revised state diagram of Laponite dispersions, *J. Colloid Interface Sci.* 283 (2) (2005) 397–405, <http://dx.doi.org/10.1016/j.jcis.2004.09.043>.
- [4] A. Mourchid, E. Lcolier, H.V. Damme, P. Levitz, On viscoelastic, birefringent, and swelling properties of Laponite clay suspensions? Revisited phase diagram, *Langmuir* 14 (17) (1998) 4718–4723, <http://dx.doi.org/10.1021/la980117p>.
- [5] F. Pignon, A. Magnin, J.-M. Piau, B. Cabane, P. Lindner, O. Diat, Yield stress thixotropic clay suspension: investigations of structure by light, neutron, and X-ray scattering, *Phys. Rev. E* 56 (3) (1997) 3281, <http://dx.doi.org/10.1103/PhysRevE.56.3281>.
- [6] S. Cocard, J.F. Tassin, T. Nicolai, Dynamical mechanical properties of gelling colloidal disks, *J. Rheol.* (1978–present) 44 (3) (2000) 585–594, <http://dx.doi.org/10.1122/1.551107>.
- [7] C. Martin, F. Pignon, A. Magnin, M. Meireles, V. Lelièvre, P. Lindner, B. Cabane, Osmotic compression and expansion of highly ordered clay dispersions, *Langmuir* 22 (9) (2006) 4065–4075, <http://dx.doi.org/10.1021/la052605k>.
- [8] O. Buzzi, M. Boulon, F. Deleruyelle, F. Besnus, Hydromechanical behaviour of rock-bentonite interfaces under compression, *Rock Mech. Rock Eng.* 41 (2) (2009) 343–371, <http://dx.doi.org/10.1007/s00603-006-0099-2>.
- [9] A.V. Blackmore, B.P. Warkentin, Swelling of calcium montmorillonite, *Nature* 186 (9) (1960) 823–824, <http://dx.doi.org/10.1038/186823a0>.
- [10] B. Jönsson, H. Wennerström, When ion-ion correlations are important in charged colloidal systems, in: *Electrostatic Effects in Soft Matter and Biophysics*, Springer, 2001, pp. 171–204, [http://dx.doi.org/10.1007/978-94-010-0577-7\\_7](http://dx.doi.org/10.1007/978-94-010-0577-7_7).
- [11] O. Karnland, S. Olsson, U. Nilsson, P. Sellin, Experimentally determined swelling pressures and geochanical interactions of compacted Wyoming bentonite with highly alkaline solutions, *Phys. Chem. Earth, Parts A/B/C* 32 (1) (2007) 275–286, <http://dx.doi.org/10.1016/j.pce.2006.01.012>.
- [12] A. Babin, Tactoid formation in montmorillonite: effect on ion exchange kinetics, *Science* 155 (3758) (1967) 71–72, <http://dx.doi.org/10.1126/science.155.3758.71>.
- [13] A. Meunier, *Clays*, Springer Science & Business Media, 2005.
- [14] A. Shalkevich, A. Stradner, S.K. Bhat, F. Muller, P. Schurtenberger, Cluster, glass, and gel formation and viscoelastic phase separation in aqueous clay suspensions, *Langmuir* 23 (7) (2007) 3570–3580, <http://dx.doi.org/10.1021/la062996i>.
- [15] L.J. Michot, I. Bihannic, F. Thomas, B.S. Lartiges, Y. Waldvogel, C. Cailliet, J. Thieime, S.S. Funari, P. Levitz, Coagulation of Na-montmorillonite by inorganic cations at neutral pH. A combined transmission X-ray microscopy, small angle and wide angle X-ray scattering study, *Langmuir* 29 (10) (2013) 3500–3510, <http://dx.doi.org/10.1021/la400245n>.
- [16] S.D. Lubetkin, S.R. Middleton, R.H. Ottewill, P. Barnes, P. Nadeau, J. Fripiat, Some properties of clay-water dispersions [and discussion], *Philos. Trans. Roy. Soc. Lond. A: Math. Phys. Eng. Sci.* 311 (1517) (1984) 353–368, <http://dx.doi.org/10.1098/rsta.1984.0033>.
- [17] P.F. Luckham, S. Rossi, The colloidal and rheological properties of bentonite suspensions, *Adv. Colloid Interface Sci.* 82 (1) (1999) 43–92, [http://dx.doi.org/10.1016/S0001-8688\(99\)00005-6](http://dx.doi.org/10.1016/S0001-8688(99)00005-6).
- [18] S.L. Swartzan-Allen, E. Matijevic, Surface and colloid chemistry of clays, *Chem. Rev.* 74 (3) (1974) 385–400, <http://dx.doi.org/10.1021/cr60289a004>.
- [19] F. Bergaya, G. Lagaly, *Handbook of Clay Science*, vol. 5, Newnes, 2013.
- [20] A.V. Blackmore, R.D. Miller, Tactoid size and osmotic swelling in calcium montmorillonite, *Soil Sci. Soc. Am. J.* 25 (1961) 169–173, <http://dx.doi.org/10.2136/sssaj1961.03615995002500030009x>.
- [21] K. Norrish, The swelling of montmorillonite, *Discuss. Faraday Soc.* 18 (1954) 120–134, <http://dx.doi.org/10.1039/DF9541800120>.
- [22] M. Segad, Microstructure determination of IQ-WB clays: a direct procedure by small-angle X-ray scattering, *J. Appl. Cryst.* 46 (2013) 1316–1322, <http://dx.doi.org/10.1107/S0021889813020991>.
- [23] L. Quintero, An overview of surfactant applications in drilling fluids for the petroleum industry, *J. Dispers. Sci. Technol.* 23 (1–3) (2002) 393–404, <http://dx.doi.org/10.1080/01932690208984212>.
- [24] B. Bloys, N. Davis, B. Smolen, L. Bailey, O. Houwen, P. Reid, J. Sherwood, L. Fraser, M. Hodder, Designing and managing drilling fluid, *Oilfield Rev.* 6 (2) (1994) 33–43.
- [25] R.L. Anderson, I. Ratcliffe, H.C. Greenwell, P.A. Williams, S. Cliffe, P. Coveney, Clay swelling – a challenge in the oilfield, *Earth-Sci. Rev.* 98 (3) (2010) 201–216, <http://dx.doi.org/10.1016/j.earscirev.2009.11.003>.
- [26] M.V. Smalley, *Clay Swelling and Colloid Stability*, CRC Press, 2006.
- [27] S. Liu, X. Mo, C. Zhang, D. Sun, C. Mu, Swelling inhibition by polyglycols in montmorillonite dispersions, *J. Dispers. Sci. Technol.* 25 (1) (2004) 63–66, <http://dx.doi.org/10.1081/DIS-120027669>.
- [28] P. Mongondry, T. Nicolai, J.F. Tassin, Influence of pyrophosphate or polyethylene oxide on the aggregation and gelation of aqueous Laponite dispersions, *J. Colloid Interface Sci.* 275 (2004) 191–196, <http://dx.doi.org/10.1016/j.jcis.2004.01.037>.
- [29] J. Lal, L. Auvray, Interaction of polymer with clays, *J. Appl. Cryst.* 33 (2000) 673–676, <http://dx.doi.org/10.1107/S0021889899013308>.
- [30] J. Lal, L. Auvray, Interaction of polymer with discotic clay particles, *Mol. Cryst. Liq. Cryst.* 356 (2001) 503–515, <http://dx.doi.org/10.1080/105872501080327325>.
- [31] A. Nelson, T. Cosgrove, A small-angle neutron scattering study of adsorbed poly(ethylene oxide) on Laponite, *Langmuir* 20 (6) (2004) 2298–2304, <http://dx.doi.org/10.1021/la035268t>.
- [32] A. Nelson, T. Cosgrove, Dynamic light scattering studies of poly(ethylene oxide) adsorbed on Laponite: layer conformation and its effect on particle stability, *Langmuir* 20 (24) (2004) 10382–10388, <http://dx.doi.org/10.1021/la049323p>.
- [33] S. Rossi, P.F. Luckham, N. Green, T. Cosgrove, NMR solvent relaxation studies of Na<sup>+</sup>-montmorillonite clay suspensions containing non-ionic polymers, *Colloid. Surf. A: Physicochem. Eng. Aspects* 215 (1) (2003) 11–24, [http://dx.doi.org/10.1016/S0927-7757\(02\)00447-8](http://dx.doi.org/10.1016/S0927-7757(02)00447-8).
- [34] S.L. Tawari, D.L. Koch, C. Cohen, Electrical double-layer effects on the Brownian diffusivity and aggregation rate of Laponite clay particles, *J. Colloid Interface Sci.* 240 (1) (2001) 54–66, <http://dx.doi.org/10.1006/jcis.2001.7646>.
- [35] H.Z. Cummins, Liquid, glass, gel: the phases of colloidal laponite, *J. Non-Cryst. Solids* 353 (41–43) (2007) 3891–3905, <http://dx.doi.org/10.1016/j.jncr.2007.02.066>.
- [36] M. Knaipila, C. Svensson, J. Barauskas, M. Zackrisson, S.S. Nielsen, K.N. Toft, B. Vestergaard, L. Arleth, U. Olsson, J.S. Pedersen, V.J. Cerenius, A new small-angle X-ray scattering set-up on the crystallography beamline i711 at max-lab, *J. Synchrotron Rad.* 16 (2009) 498–504, <http://dx.doi.org/10.1107/S0909049509018986>.
- [37] A.P. Hammersley, S.O. Svensson, A. Thompson, H. Graafsma, Å. Kvick, J.P. Moy, Calibration and correction of distortions in two-dimensional detector systems, *Rev. Sci. Instrum.* 66 (3) (1995) 2729–2733, <http://dx.doi.org/10.1063/1.1145618>.
- [38] M. Segad, S. Hanski, U. Olsson, J. Ruokolainen, T. Åkesson, B. Jönsson, Microstructural and swelling properties of ca and na montmorillonite: (in situ) observations with cryo-TEM and SAXS, *J. Phys. Chem. C* 116 (13) (2012) 7596–7601, <http://dx.doi.org/10.1021/jp300531y>.
- [39] M. Segad, B. Jönsson, B. Cabane, Tactoid formation in montmorillonite, *J. Phys. Chem. C* 116 (48) (2012) 25425–25433, <http://dx.doi.org/10.1021/jp3094929>.
- [40] A.L. Patterson, The Scherrer formula for X-ray particle size determination, *Phys. Rev.* 56 (1939) 978–982, <http://dx.doi.org/10.1103/PhysRev.56.978>.
- [41] F.W. Jones, The measurement of particle size by the X-ray method, *Proc. Roy. Soc. Lond. A* 166 (1938) 16–43, <http://dx.doi.org/10.1098/rspa.1938.0079>.
- [42] K. Devanand, J.C. Selsler, Asymptotic behavior and long-range interactions in aqueous solutions of poly(ethylene oxide), *Macromolecules* 24 (22) (1991) 5943–5947, <http://dx.doi.org/10.1021/ma00022a008>.
- [43] F. Xie, M. Turesson, M. Jansson, M. Skögl, J. Forsman, A simple and versatile implicit solvent model for Polyethylene Glycol in aqueous solution at room temperature, *Polymer* (2015), <http://dx.doi.org/10.1016/j.polymer.2015.12.034>.
- [44] J.A. Cohen, R. Podgornik, P.L. Hansen, V.A. Parsegian, A phenomenological one-parameter equation of state for osmotic pressures of PEG and other neutral flexible polymers in good solvent, *J. Phys. Chem. B* 113 (2009) 3709–3714, <http://dx.doi.org/10.1021/jp908893a>.
- [45] B. Hess, C. Kutzner, D. van der Spoel, E. Lindahl, Gromacs 4: algorithms for highly efficient, load-balanced, and scalable molecular simulation, *J. Chem. Theory Comput.* 4 (3) (2008) 435–447, <http://dx.doi.org/10.1021/ct700301q>.
- [46] G. Bussi, D. Donadio, M. Parrinello, Canonical sampling through velocity rescaling, *J. Chem. Phys.* 126 (2007) 014101, <http://dx.doi.org/10.1063/1.2408420>.
- [47] D. van der Spoel, E. Lindahl, B. Hess, E. van Buuren, E. Apol, P.J. Meulenhoff, D.P. Tieleman, A.L.T.M. Sijbers, K.A. Feenstra, R. van Drunen, et al., *Gromacs User Manual* Version 4.5.4.
- [48] G. Gutiérrez, B. Johansson, Molecular dynamics study of structural properties of amorphous Al<sub>2</sub>O<sub>3</sub>, *Phys. Rev. B* 65 (2002) 104202, <http://dx.doi.org/10.1103/PhysRevB.65.104202>.
- [49] P.D. Svensson, S. Hansen, Combined salt and temperature impact on montmorillonite hydration, *Clays Clay Miner.* 61 (4) (2013) 328–341, <http://dx.doi.org/10.1346/CCMN.2013.0610412>.

- [50] E.A. Stefanescu, C. Stefanescu, B.C. Donose, J.C. Garno, W.H. Daly, G. Schmidt, I. I. Negulescu, Polymer/clay nanocomposites: influence of ionic strength on the structure and adhesion characteristics in multilayered films, *Macromol. Mater. Eng.* 293 (9) (2008) 771–780, <http://dx.doi.org/10.1002/mame.200800139>.
- [51] A. Loiseau, J. Tassin, Model nanocomposites based on Laponite and poly (ethylene oxide): preparation and rheology, *Macromolecules* 39 (26) (2006) 9185–9191, <http://dx.doi.org/10.1021/ma061324w>.
- [52] G. Lazzara, S. Milioto, M. Gradzielski, S. Prevost, Small angle neutron scattering, X-ray diffraction, differential scanning calorimetry, and thermogravimetry studies to characterize the properties of clay nanocomposites, *J. Phys. Chem. C* 113 (28) (2009) 12213–12219, <http://dx.doi.org/10.1021/jp901909w>.
- [53] A.K. Atmuri, G.A. Pecklaris, S. Kishore, S.R. Bhatia, A re-entrant glass transition in colloidal disks with adsorbing polymer, *Soft Matter* 8 (34) (2012) 8965–8971, <http://dx.doi.org/10.1039/C2SM25311A>.



## Paper IV



Reprinted with permission from *J. Phys. Chem. C.*, 2017, **121**, 7387-7396  
A. Thuresson, M. Segad, T. S. Plivelic and M. Skepö  
©2017 American Chemical Society.



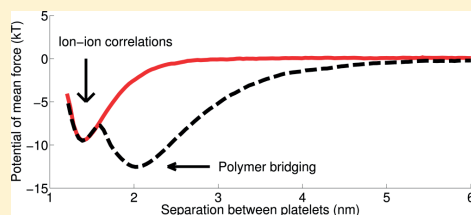
# Flocculated Laponite-PEG/PEO Dispersions with Multivalent Salt: A SAXS, Cryo-TEM, and Computer Simulation Study

Axel Thuresson,<sup>\*,†</sup> M. Segad,<sup>‡</sup> Tomás S. Plivelic,<sup>§</sup> and Marie Sképö<sup>\*,†</sup><sup>†</sup>Theoretical Chemistry, Lund University, P.O. Box 124, SE-221 00 Lund, Sweden<sup>‡</sup>Advanced Light Source, Lawrence Berkeley National Laboratory, Berkeley, California 94720, United States<sup>§</sup>MAX IV Laboratory, Lund University, P.O. Box 118, SE-221 00 Lund, Sweden

## Supporting Information

**ABSTRACT:** The aim of this study is to scrutinize the mechanism behind aggregation, i.e., tactoid formation of nanostructures with the shape of a platelet. For that purpose, the clay minerals Laponite and montmorillonite have been used as model systems. More specifically, we are interested in the role of: the platelet size, the electrostatic interactions, and adsorbing polymers. Our hypothesis is that the presence of PEG is crucial for tactoid formation if the system is constituted by small nanometric platelets. For this purpose, SAXS, USAXS, Cryo-TEM, and coarse-grained molecular dynamics simulations have been used to study how the formation and the morphology of the tactoids are affected by the platelet size.

The simulations indicate that ion–ion correlations are not enough to induce large tactoids solely if the platelets are small and the absolute charge is too low, i.e., in the size and charge range of Laponite. When a polymer is introduced into the system, the tactoid size grows, and the results can be explained by weak attractive electrostatic correlation forces and polymer bridging. It is shown that when the salt concentration increases the long-ranged electrostatic repulsion is screened, and a free energy minimum appears at short distances due to the ion–ion correlation effects. When a strongly adsorbing polymer is introduced into the system, a second free energy minimum appears at a slightly larger separation. The latter dominates if the polymer is relatively long and/or the polymer concentration is high enough.



## INTRODUCTION

Generally, swelling 2:1 clay minerals are constituted of platelets with a thickness of about 1 nm and lateral dimensions varying from 25 nm in synthetic Laponite clays up to 1000 nm in natural montmorillonite. Previous experimental studies<sup>1,2</sup> have shown that Laponite exists in dilute suspensions as monodisperse disc-shaped particles. When water is added, the clay platelets become ionized, and a rising osmotic pressure in the solution causes the clay to swell.<sup>3–5</sup> Semidilute dispersions with volume fractions above 0.5% can behave as gels; i.e., they possess a yield stress.<sup>5–7</sup> Upon drying they form films with excellent barrier properties. These are often used in surface coatings, paper and polymer films, as well as household and personal care products.

Another very interesting application for clay is as a storing alternative for the nuclear waste, where the nuclear waste is put into copper containers embedded in bentonite or another source of clay and placed underground.<sup>8</sup> The success for such containment depends on the clay structure and its stability under varying conditions. The clay should be able to sustain changes in the surrounding groundwater including salinities of glacial meltwater as well as seawater, while still being an effective hydraulic barrier. Equilibrium with the surrounding water will eventually be established. Hence, the salt content in the clay will be determined by the surroundings and not by the

initial preparation. For most, if not all, saline waters this means that the clay will be dominated by calcium ions, and the structure of the dispersion will be that of calcium clay.

Depending on the size, the platelets can form a lamellar structure making it a seemingly perfect model system for an electrical double layer, where the swelling and the stability in saline solution depend strongly on the counterion valency and the surface charge density.<sup>9–11</sup> The situation is, however, from a structural point slightly less ideal. Clay is normally not a homogeneous lamellar material, and it might better be described as a disordered structure of stacks of platelets, also denoted tactoids.<sup>12–14</sup> In a tactoid the platelets have agglomerated in a face-to-face conformation with equidistant separation.<sup>15</sup> The tactoid formation of montmorillonite has been studied for several decades.<sup>16–19</sup> In a study by Blackmore and Miller,<sup>20</sup> Ca-montmorillonite was analyzed with X-ray diffraction, and a diffraction peak was found at 1.9 nm. The diffraction peak gives an estimation of the distance between the platelets and the average number of platelets per tactoid. The repeat distance for Na-montmorillonite platelets decreases with increasing NaCl concentration due to the electrostatic

Received: February 21, 2017

Revised: March 9, 2017

Published: March 13, 2017



screening effect, and at high enough NaCl concentration, tactoids are formed.<sup>21</sup> Recently, it has been shown that the average diameter of Ca-montmorillonite platelets is related to the average number of platelets per tactoid.<sup>22</sup> By increasing the diameter of the clay platelets, the number of platelets per tactoid increases. To the authors knowledge, it has not been observed that montmorillonite platelets with a diameter less than 60 nm can form tactoids in water with neither NaCl nor CaCl<sub>2</sub>. By generalizing this fact for Laponite, where the diameter is roughly 25 nm, tactoids will either contain a low number of platelets per tactoid or not be formed. Moreover, the surface charge density, which is related to the strength of the attractive ion–ion correlations,<sup>23,24</sup> is lower for Laponite (cation exchange capacity ~0.5 mequiv/g<sup>25</sup>) compared to montmorillonite purified from Wyoming bentonite (cation exchange capacity ~0.8 mequiv/g<sup>26</sup>). Hence, the attraction between the Laponite platelets mediated by multivalent cations should theoretically be less significant compared to montmorillonite platelets of the same size.

It is well-known that PEG adsorbs onto the Laponite platelets.<sup>27–32</sup> More than four decades ago, Parfitt and Greenland<sup>33</sup> found that PEG was strongly adsorbed to montmorillonite and that cations of a higher valency gave rise to a larger separation between the platelets. Studies that explore the nature of clay/polymer interactions and how it is affected by the physicochemical properties of the solution are of fundamental importance since it can affect the bulk properties of the colloidal system such as the stability and the flow. It has been proposed that the polymers are disrupting hydrogen bonding between the water molecules and the silica or alumina functionalities of the clay surface and that the glycol molecules compete with water for these sites and also with water-hydrating interlayer cations.<sup>34</sup> Our coarse-grained model is simple, and it neglects how the polymer–clay interactions are affected by the addition of salt. Although, we would like to emphasize that it has been suggested that the clay–polymer interaction is enhanced with addition of salt due to the disrupted hydrogen bonding between the water molecules and PEG.<sup>35,36</sup>

Recently we have shown that, despite the small size of the Laponite platelets, it is possible to induce tactoids if two conditions are fulfilled: (1) high ionic strength and (2) presence of PEG.<sup>37</sup> Hence, in that study we focused on the electrostatic screening effects, by utilizing monovalent ions solely.

In this study the aim is to study the role of attractive electrostatic correlation forces by adding multivalent ions. For that purpose Ca-, Mg-, and La-ions have been added to the Laponite/PEG and montmorillonite/PEG dispersions and thoroughly analyzed. To achieve a molecular understanding of the observed macroscopic phenomena and as an attempt to comprehend the underlying physics, coarse-grained molecular dynamic simulations have been used in combination with experimental data from SAXS, USAXS, and Cryo-TEM.

## MATERIAL AND METHODS

**Experimental Details.** *Material.* The source of clays used in this work was sodium Laponite XLG from ROCKWOOD ADDITIVES and purified Wyoming Bentonite (MX-80) whose main component is sodium montmorillonite. The cleaning procedure for MX-80 has been described elsewhere.<sup>38</sup> This study will mainly focus on Laponite, but montmorillonite is included for comparison. Analytical grade sodium chloride

(purity, 99.5%) was purchased from MERCK, and Millipore water was used to prepare the solutions. PEG of molecular weight 20 000 g/mol, further denoted PEG20k, (purity, 98%) was purchased from Aldrich.

**Sample Preparation.** The salt was dissolved in Millipore water at least one week in advance. PEG20k was added to the suspension and shaken overnight until complete dispersion. Finally the clay, Laponite or montmorillonite, was added (0.125 g of clay in a suspension of total 5 g) and shaken overnight. The mass fraction of the clay was set to 2.5 wt %, which corresponds to roughly 1% volume fraction (the density of Laponite is 2.53 kg/dm<sup>3</sup>,<sup>39</sup> and the density of montmorillonite is 2.75 kg/dm<sup>326</sup>). The pH was set to 10 by addition of NaOH for the Laponite samples. The samples were set vertically for at least 48 h.

**SAXS.** Synchrotron SAXS experiments were performed for most of the samples at MAXlab synchrotron in Lund-Sweden using beamline I911-4,<sup>40</sup> ID02 at ESRF in Grenoble-France,<sup>41</sup> and at an in-house pinhole instrument (Ganesha, from SAXSLAB AB) in Lund (Sweden) for the montmorillonite samples. At the MAXlab, a monochromatic beam of 0.091 nm wavelength was used together with point collimation and a two-dimensional position-sensitive hybrid pixel X-ray detector (Pilatus 1M, Dectris). The sample to detector distance was 1.9 m covering the scattering vector  $q$ -range  $0.1 < q < 5 \text{ nm}^{-1}$ , where  $q = 4\pi \sin(\theta)/\lambda$  and  $2\theta$  the scattering angle. The SAXS data were normalized by the transmitted intensity and corrected for the solvent scattering contribution using the software bli9114. At ESRF, 2D SAXS data were measured at two different sample detector distances covering the  $q$ -range:  $4 \times 10^{-3} < q < 5 \text{ nm}^{-1}$ . The detector used was the CCD Rayonix MX 170HS with binning  $4 \times 4$ . The software SAXSUtilities<sup>42</sup> was used for data reduction.

Laponite and montmorillonite samples at different PEG20k and salt concentrations were measured in 1 mm quartz capillaries. The background scattering of pure water at different polymer and salt concentrations was subtracted for the Laponite samples but not for the montmorillonite samples.

In order to estimate the average size of aggregates  $\langle N \rangle$ , i.e., the number of clay platelets per aggregate, a model scattering peak has been fitted to the experimental data. The scattering function can be approximated with a Lorentzian line shape

$$I(q) - C(q) \propto \frac{w}{(q - q_{\text{max}})^2 + w^2} \quad (1)$$

where  $I(q)$  is the scattering intensity;  $C(q)$  is a polynomial function for the background contribution around the peak; and  $w$  is a measure of the width. The full width at half-maximum (fwhm) of the peak is equal to  $2w$ , and the average tactoid size can be expressed as  $\langle N \rangle \approx q_{\text{max}}/w$ .<sup>22,27,43,44</sup> All the fitted data can be found in the Supporting Information.

The fitting of the data in the  $q$ -range  $0.0035\text{--}5 \text{ nm}^{-1}$  (USAXS/SAXS) has been done utilizing the software SasView.<sup>45</sup> For this purpose, two contributions have been combined: (i) a power law in the very low  $q$ -regime ( $I_1(q)$ ) and (ii) the scattering from a polydisperse system of flat particles, with a thickness of 1 nm, for intermediate and high  $q$ -range ( $I_2(q)$ ), the intensity,  $I(q)$ , becomes

$$\begin{aligned}
 I(q) &= I_1(q) + I_2(q) + b \\
 I_1(q) &= Aq^{-\alpha} \\
 I_2(q) &= B \int_0^{\infty} g(R)(\Delta\rho)^2 v(R)^2 f(q, R)^2 dR
 \end{aligned}
 \quad (2)$$

where  $A$  and  $B$  are scaling factors;  $b$  is a constant that accounts for the background contribution;  $\alpha$  is the coefficient of the power law;  $R$  is the radius of the flat particles;  $\Delta\rho$  is the contrast;  $v(R)$  is the volume;  $g(R)$  is a Gaussian distribution of the particles radii; and  $f(q, R)$  is the form factor of flat particles.<sup>46</sup>

**Cryo-TEM.** Specimens for electron microscopy were prepared in a controlled environment vitrification system (CEVS) to ensure stable temperature and to avoid loss of solution during sample preparation. The specimens were prepared as thin liquid films, <300 nm thick, on lacey carbon filmed copper grids, and plunged into liquid ethane at  $-180$  °C. This leads to vitrified specimens, avoiding component segmentation and rearrangement, and water crystallization, thereby preserving original microstructures. The vitrified specimens were stored under liquid nitrogen until measured. An Oxford CT3500 cryoholder and its workstation were used to transfer the specimen into the electron microscope (Philips CM120 BioTWIN Cryo) equipped with a postcolumn energy filter (Gatan GIF100). The acceleration voltage was 120 kV. The images were recorded digitally with a CCD camera under low electron dose conditions.

**Simulation Details.** Molecular dynamics simulations were performed with the software package GROMACS (version 5.1.2).<sup>47</sup> The choice of the parameters and the setup of the model are described in detail in our previous work.<sup>37</sup> As a brief description of the model, the platelets are 1 nm in thick, and the diameter is varied from 25 to 10 nm in order to reduce the computational cost. Due to the decreased diameter of the platelets, the polymer size is reduced from PEG20k to PEG3k, where the latter is coarse-grained into 68 connected beads (see Table 1).

**Table 1.** Comparison between the Coarse-Grained and Experimental System

property	coarse-grained system	experimental system
Laponite diameter	10 nm	25 nm
Laponite thickness	1 nm	1 nm
polymer $R_g$	2 nm (PEG3k)	7 nm (PEG20k)
polymer length	37 nm	250 nm

Two parallel charged platelets were immersed in a cubic box with its center of mass (COM) located at the box origin, and the normal of the platelet is parallel to the  $z$ -axis. The cubic box has periodic boundary conditions, and the length of the box is  $L = 20$  nm. Divalent counterions, 2:1 salt, and polymers were added to the system, and equilibration was performed for at least 50 ns. The COM separation between the platelets was initially set to 1.2 nm. The *pull code*<sup>47</sup> was used to pull apart the parallel platelets along the  $z$ -axis using a spring constant of 1000 kJ/(mol nm<sup>2</sup>), with a pull rate of 10 nm/ns, to find starting configurations for the umbrella sampling. The starting configurations were typically 0.2 nm apart for the total sampling interval 1.2–8 nm. Each configuration was sampled for at least 1 ms with zero pull rate, and the equilibration was typically 100 ns to ensure convergence. Finally, the free energy of interaction

(potential of mean force) was extracted by using the weighted histogram analysis method (WHAM).<sup>48</sup>

## RESULTS AND DISCUSSION

**Small-Angle X-ray Scattering.** In Figure 1a–1b, the scattering intensity and Kratky plot for 2.5 wt % Laponite with 0 or 5 wt % PEG20k show the difference between multivalent salts such as CaCl<sub>2</sub>, MgCl<sub>2</sub>, or LaCl<sub>3</sub> with monovalent salt at a constant Debye screening length of 0.4 nm. Due to the high salt concentration, all the Laponite samples have flocculated (and sedimented). With monovalent salt and 0 wt % PEG20k, a broad structure peak is found, and the average separation is found to be  $\sim 3.6$  nm. For the multivalent salt and 0 wt % PEG20k, a structure peak is found at  $\sim 2.6$  nm for the divalent cations and  $\sim 2.4$  nm for the trivalent. Hence, as the valency of the cation is increasing for a given Debye screening length, the separation between the platelets reduces. The fwhm of the structure peak is reducing as the valency of the cation increases. By introducing 5 wt % PEG20k (Figure 1b), a Bragg peak is found for all the systems. The average distance between the platelets in the tactoids is  $\sim 1.8$  nm or  $\sim 2.9$  nm, with monovalent or multivalent salt, respectively. Furthermore, it is shown that the nature of the salt does not make any difference, and it is rather the valency of the cations that is of importance. As shown, two trends are visible; SAXS spectra for monovalent salts superimpose into one curve;<sup>37</sup> and the SAXS spectra for salts with a valency >1 superimpose into one curve. No effects are detectable when changing from calcium/magnesium to lanthanum. The reader should notice that lanthanum has a tendency to hydrolyze. Around pH 10, La(OH)<sub>3</sub> is the dominant hydrolytic form with a very low solubility,<sup>49</sup> although no signs of precipitation in the pure salt solutions were visible during the preparation.

The scattering intensities for montmorillonite in Figure 1c,d reveal a similar difference in the average distance with PEG20k depending on the valency of the cation of the salt. For a high amount of NaCl or CaCl<sub>2</sub>, an average distance  $\sim 1.9$  nm is found, and an addition of PEG20k alters the distance to  $\sim 1.8$  nm and  $\sim 2.3$  nm for NaCl and CaCl<sub>2</sub>, respectively.

Due to the small size of Laponite, the tactoids will contain a low number of platelets or not be formed by adding multivalent salt solely, cf. size-fractionated montmorillonite. By introducing PEG to montmorillonite or Laponite, two separations are found to coincide: (i) with monovalent cations and PEG, the average platelet separation becomes  $\sim 1.8$  nm, and (ii) with divalent cations, an addition of PEG increases the average platelet separation by  $\sim 0.3$ – $0.4$  nm.

By analyzing the SAXS data according to eq 1, the average distance between the Laponite platelets and average number of platelets per tactoid can be estimated (see Figure 2). With CaCl<sub>2</sub> but without PEG, the flocculated clay is not very well ordered since the number of platelets per tactoid is small,  $\langle N \rangle \approx 3$  (compare with montmorillonite in Figure 1c,  $\langle N \rangle \approx 20$ ). The position of the structure peak reveals that with added CaCl<sub>2</sub> the average distance is linearly increasing as a function of the Debye screening length. In comparison with NaCl,<sup>37</sup> shorter distances are found, and the slope is less dependent on the salt concentration. With 5 wt % PEG20k, the number of platelets per tactoid increases, and the separation between the platelets in the tactoids is linearly increasing as a function of the Debye screening length for CaCl<sub>2</sub>, although systematically  $\sim 0.3$  nm larger than the PEG-free case. Between 5 wt % PEG20k and 15 wt % PEG20k (the maximum concentration in our

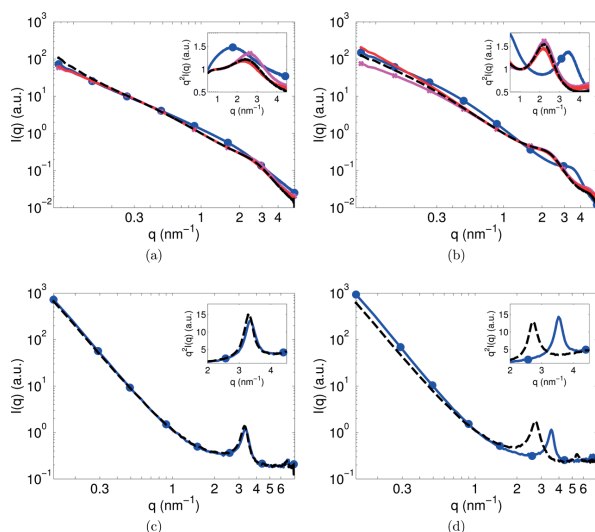


**Figure 1.** (a) Intensity scattering functions as a function of the wave vector of Laponite with 0 wt % PEG20k at constant Debye screening length: 0.6 M NaCl (blue circle), 0.2 M CaCl<sub>2</sub> (black dashed), 0.2 M MgCl<sub>2</sub> (red line), and 0.1 M LaCl<sub>3</sub> (magenta cross). The insets show the Kratky plot over a narrow  $q$ -range. The scattering intensities are normalized at  $q \approx 0.4 \text{ nm}^{-1}$ . (b) Same as (a) with 5 wt % PEG20k, the scattering intensities are normalized at  $q \approx 1.4 \text{ nm}^{-1}$ . (c) Intensity scattering functions as a function of the wave vector of montmorillonite with 0 wt % PEG20k at constant Debye screening length: 1.5 M NaCl (blue circle) and 0.5 M CaCl<sub>2</sub> (black dashed). The scattering intensities are normalized at  $q \approx 1 \text{ nm}^{-1}$ . (d) Same as (c) with 5 wt % PEG20k.

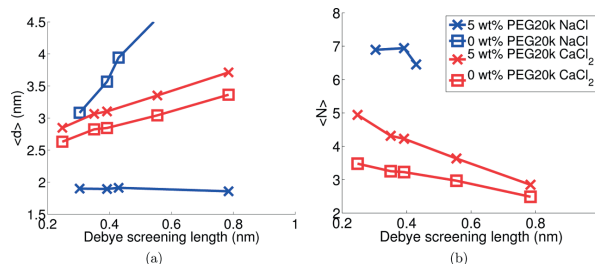


**Figure 2.** (a) Average distance between Laponite platelets as a function of the Debye screening length. The crosses and squares show the maximum value in each Kratky plot with 5 wt % PEG20k and 0 wt % PEG20k, respectively. CaCl<sub>2</sub> is shown in red and NaCl from Thuresson et al.<sup>37</sup> in blue. (b) The average number of platelets per tactoid as estimated by applying eq 1 as a function of the Debye length.

experiments), the number of platelets per tactoid did not change for 0.25 M and 0.5 M CaCl<sub>2</sub> (data not shown). Thus, 2 g/g (g PEG20k/g Laponite) is above the saturation of PEG20k on Laponite with respect to the tactoid size. The saturation of PEG20k has been found to be  $\sim 1.4 \text{ g/g}$  by Mongondry et al.,<sup>27</sup> whereas for larger PEG molecules,  $\sim 0.4 \text{ g/g}$  and  $\sim 0.6\text{--}0.9 \text{ g/g}$  were found by Cosgrove et al.<sup>30</sup> and Lal et al.,<sup>28</sup> respectively. The conformation of the adsorbed PEG onto Laponite has been found to be flat, and the thickness of the polymer layer on the face of single platelets has been estimated to about 1 nm for PEG20k and 1.6 nm for larger PEG molecules.<sup>30</sup> This is also suggested from the simulations of our previous work,<sup>37</sup> where the thickness of the polymer layer onto single platelets was found to be within a few nanometers; i.e., the attractive

component between the platelet and the polymer beads dominates over the configurational entropy to a large extent.

The lack of order in the flocculated Laponite system, even with PEG20k, is significant, and the amount of CaCl<sub>2</sub> has to be above 100 mM (0.55 nm Debye screening length) in order to find an average tactoid size above four. This is in contrast to unfractionated montmorillonite where a salt-free system with divalent counterions induces formation of large tactoids.<sup>38</sup> The key parameter seems to be the size of platelets, and it has been shown that the tactoid size is decreasing with the platelet diameter for Ca-montmorillonite.<sup>15,38</sup> If the average diameter is below  $\sim 60 \text{ nm}$ , no Bragg peak is visible at high  $q$ -values in the flocculated clay.<sup>22,44</sup> This should be compared with Laponite where the average diameter is approximately 25 nm. From a

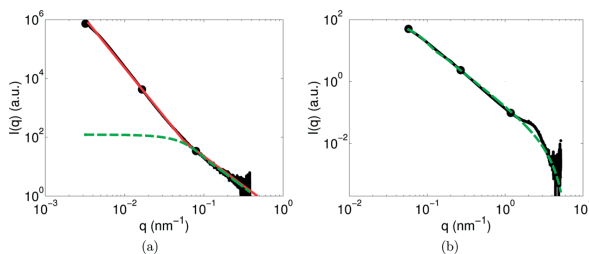


**Figure 3.** Scattering intensity for Laponite in 5 wt % PEG20k with 0.1 M  $\text{LaCl}_3$  (black circle). (a)  $0.0035 < q < 0.35 \text{ nm}^{-1}$  and (b)  $0.06 < q < 5 \text{ nm}^{-1}$ . The overall fit of the scattering curve (red line) is the result of adding the contribution of a power law with  $\alpha = 3.38$  and platelets scattering (green dashed).

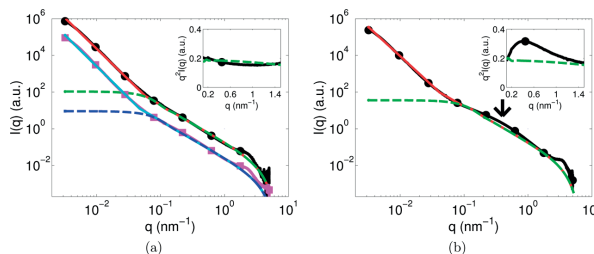


**Figure 4.** (a) Scattering intensity in the complete experimental  $q$ -range  $0.0035\text{--}5 \text{ nm}^{-1}$  for Laponite in 5 wt % PEG20k with 0.1 M  $\text{LaCl}_3$  (black circle) and 0.2 M  $\text{CaCl}_2$  (magenta square). The overall fit is shown as a red and cyan line, respectively. The curves for  $\text{CaCl}_2$  have been scaled to avoid superpositioning the data. (b) Scattering intensity for Laponite in 5 wt % PEG20k with 0.6 M  $\text{NaCl}$  (black circle). The overall fit to the experimental data is indicated as a red line. Platelet scattering contribution is added as a reference (green dashed). The black arrow indicates where the scattering curve deviates from the fit, and the insets show the Kratky plot over a narrow  $q$ -range.

theoretical point of view, it seems reasonable that the attractive forces (e.g., dispersion forces and ion–ion correlations) between two platelets are to a first approximation proportional to the diameter squared; i.e., the force is proportional to the area. In the case of attractive ion–ion correlations, an increase in platelet size does not only increase the attraction due to a larger interacting area but also increases the attraction per unit area because of the finite size of the platelets, that is, a decreasing rim to surface ratio.<sup>23,24</sup> Thus, it seems reasonable that smaller platelets give rise to smaller tactoids.

Complementary structural information on the system was obtained by performing ultrasmall angle X-ray scattering experiments (USAXS) combined with SAXS measurements at the ID02 beamline of ESRF, Grenoble. USAXS probes larger length scales than the platelet–platelet distance described above, giving information on the tactoid morphology or even larger finite-size aggregates. Using two sample detector distances at the ID02 beamline, the  $q$ -range covered was larger than three decades,  $\Delta q = 0.0035\text{--}5 \text{ nm}^{-1}$ . The scattering data (over the complete range) for the three samples of Laponite in 5 wt % PEG20k with 0.6 M  $\text{NaCl}$ , 0.2 M  $\text{CaCl}_2$ , and 0.1 M  $\text{LaCl}_3$  were investigated, and most of the data show similarities over the entire  $q$ -range. For the sake of clarity, the scattering data are discussed in selected  $q$ -regions. Figure 3 shows the USAXS data for 0.1 M  $\text{LaCl}_3$  utilizing log–log representation in the  $q$ -range  $0.0035\text{--}0.35 \text{ nm}^{-1}$  and  $q$ -range  $0.06\text{--}5 \text{ nm}^{-1}$  (note that the data as well as the fitting in Figure 3a and Figure 3b are combined over the whole  $q$ -range in Figure 4a). Two regions can be observed: (i) the low  $q$ -region, extending for almost one

decade ( $\Delta q = 0.004\text{--}0.045 \text{ nm}^{-1}$ ) and following the relationship  $I(q) \propto q^{-\alpha}$  with  $3 < \alpha < 4$ , and (ii) the high  $q$ -region for  $q > 0.07 \text{ nm}^{-1}$  with the same power law relationship but with a different coefficient,  $\alpha = 2$ .

Exponents of  $\alpha$  between three and four can be interpreted as characteristic for a system with well-defined fractal rough surfaces<sup>50</sup> or a very polydisperse distribution of heterogeneities.<sup>15,51,52</sup> In the former, the fractal dimension  $D_s$  can be obtained using the equation  $D_s = 6 - \alpha$ , and this parameter is related to the nature of the surface aggregates. For  $D_s$  approaching two, a well-correlated smooth surface on the aggregate is assumed, and for  $D_s$  tending to three, the surface will be more tightly crumpled.<sup>53</sup> All three samples show similar behavior at low- $q$  region of the USAXS data. The  $D_s$  values were obtained for the three samples where  $D_s = 2.80$ ,  $D_s = 2.54$ , and  $D_s = 2.62$  for 0.6 M  $\text{NaCl}$ , 0.2 M  $\text{CaCl}_2$ , and 0.1 M  $\text{LaCl}_3$ .

A scattering behavior of ( $3 < \alpha < 4$ ) has been observed in the literature previously for colloidal attractive glasses.<sup>54</sup> Interestingly, most USAXS data reported in the literature for montmorillonite clay dispersions show exponential laws with  $1 < \alpha < 3$ .<sup>15,55</sup>

The dependency of the scattering for  $q > 0.07 \text{ nm}^{-1}$  presented in Figure 3b shows the  $q^{-2}$  behavior, which is typical of flat particles (platelets).<sup>46</sup> Since the contribution of the Bragg peak is very localized in the SAXS curve of Figure 3b, a reasonable fitting of the data can be obtained using a description of a polydisperse system (polydispersity of 10%) of flat particles with 1 nm thickness<sup>36</sup> and average platelet radius,  $R_p$ . The values estimated were  $R_p = 24.2 \text{ nm}$  and  $R_p =$

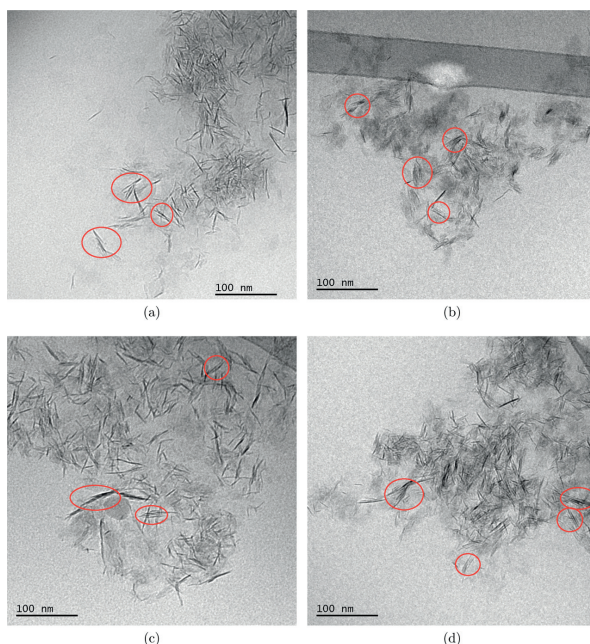


**Figure 5.** Representative Cryo-TEM images for flocculated and sedimented Laponite. (a) 0.25 wt % Laponite in 1 M NaCl and 0 wt % PEG20k. (b) 0.25 wt % Laponite in 1 M NaCl and 5 wt % PEG20k. (c) 2.5 wt % Laponite in 0.5 M CaCl<sub>2</sub> and 0 wt % PEG20k. (d) 2.5 wt % Laponite in 0.5 M CaCl<sub>2</sub> and 5 wt % PEG20k.

29.6 nm for 0.2 M CaCl<sub>2</sub> and 0.1 M LaCl<sub>3</sub>, respectively. This number is larger than the expected value for a single Laponite platelet but can be explained as if the platelets in the tactoids are not perfectly aligned instead slightly mismatched (see also Cryo-TEM section). Tactoids with a larger average diameter than the individual platelets have also been found for flocculated montmorillonite.<sup>15</sup> Noticeably, a good fitting was achieved for CaCl<sub>2</sub> and LaCl<sub>3</sub> samples (see Figure 4a) but not for NaCl (see Figure 4b). Clearly, for NaCl, the fitting does not follow the scattering curve in the  $q$ -range 0.2–0.7 nm<sup>-1</sup>.

The reason for the poor agreement might be due to the existence of platelet–platelet interactions that are not included in the tactoid stacks but as individual scattering elements with a characteristic average distance. An estimation of the distance could be obtained as  $d_1 = 2\pi/q_0 \approx 15$  nm where  $q_0$  is the position of the local maxima in the  $q$ -range: 0.2–0.7 nm<sup>-1</sup> (see arrow and the Kratky plot in Figure 4b).

**Cryo-TEM.** Cryo-TEM has been used to study the microstructure of the flocculated Laponite suspensions at high salt concentrations. Due to the fact that the suspensions are very dense, it was necessary to reduce the Laponite concentration by a factor of 10 for a system containing 1 M NaCl. Nevertheless, we still believe that qualitative information can be obtained using this technique. In Figure 5a, the outer parts of a dense aggregate with 1 M NaCl and 0.25 wt % Laponite are shown. In the top right corner of the image, the aggregate seems to consist of several layers of Laponite platelets, and hence, it is difficult to make any predictions.

Further, it is slightly easier to depict the dark lines that represent the Laponite platelets, especially if they are oriented more or less orthogonal to the film. In the Cryo-TEM measurements, one pixel corresponds to 0.47 nm, and the thickness of the dark lines was found to be approximately two–three pixels; hence, a thickness of two pixels corresponds to the thickness of a single platelet. The reason for a platelet to be represented by three pixels is probably because the platelet is not oriented completely orthogonal to the film. As shown, the platelets are not very well ordered, although some slightly mismatched pair of platelets is found and depicted in the figure. In Figure 5b, when 5 wt % of PEG20k has been added to the system, it is possible to detect some tactoids. From the Cryo-TEM measurements it is possible to locate tactoids consisting of two–six platelets that are aggregating face-to-face. The distance between dark lines representing the platelets is between two and three pixels, and thus, in decent agreement with SAXS, which suggests a repetition distance of  $\sim 1.8$  nm from center-to-center.

In Figure 5c the suspension contains 0.5 M CaCl<sub>2</sub> and 2.5 wt % Laponite. Also here, the thickness of the platelets was found to be two to three pixels, and some pairs of platelets or possibly larger aggregates were found to be stacked face-to-face (depicted in the figure), although the majority of the platelets is randomly oriented. In Figure 5d, 5 wt % of PEG20k has been added to the system, and in correspondence with the Cryo-TEM image in Figure 5b, the Laponite platelets seem to form larger tactoids. The separation between the platelets was, on

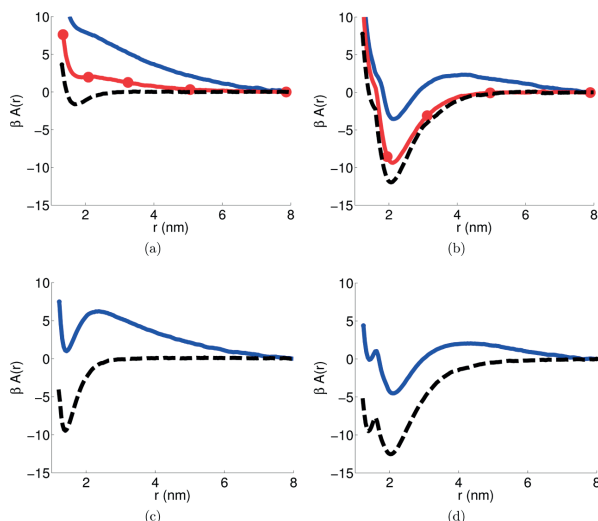


**Figure 6.** Free energy between two parallel platelets is shown as a function of the separation, with and without the 68 bead polymer. (a)  $\sigma = -1.15$   $e/\text{nm}^2$  without polymer with 0 M  $\text{CaCl}_2$  (blue line), 0.01 M  $\text{CaCl}_2$  (red circle), and 0.1 M  $\text{CaCl}_2$  (black dashed). (b) Same as (a) including one 68 bead polymer. (c)  $\sigma = -1.85$   $e/\text{nm}^2$  without polymer with 0 M  $\text{CaCl}_2$  (blue line) and 0.1 M  $\text{CaCl}_2$  (black dashed). (d) Same as (c) including one 68 bead polymer. The short-ranged attractive interaction parameter is  $\epsilon = 0.3$  kT.

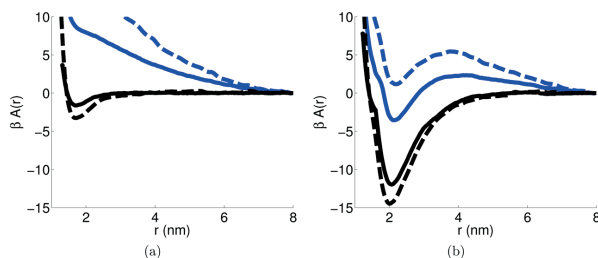


**Figure 7.** (a) Free energy between two parallel platelets as a function of the separation, without the 68 bead polymer.  $\sigma = -1.15$   $e/\text{nm}^2$  with 0 M  $\text{CaCl}_2$  (blue) and 0.1 M  $\text{CaCl}_2$  (black) for two different platelet diameters: 10 nm (line) and 14 nm (dashed). (b) Same as (a) including one 68 bead polymer. The short-ranged attractive interaction parameter is  $\epsilon = 0.3$  kT.

average, found to be three pixels, which is in agreement with the SAXS measurements; i.e., the platelet separation in the tactoids is slightly larger with  $\text{CaCl}_2$  and PEG compared to tactoids formed in a suspension containing NaCl and PEG. The images also show that most of the platelets in the tactoids are slightly mismatched (red circles), which was also found for coagulated montmorillonite by TXM.<sup>15</sup> Such microstructure supports our scattering model of polydisperse flat particles with average size larger than single Laponite platelets.

**Free Energy between Parallel Platelets: Salt and Polymer Trends.** Experimentally, it has been shown that the average separation between the platelets increases and that the average size of the tactoids grows, for Laponite with multivalent salt upon addition of PEG20k. To gain some physical insight into these findings, we have calculated the free energy of interaction between two parallel platelets including counterions, salt, and adsorbing polymers, utilizing a coarse-grained model

and molecular dynamics simulations. From an electrostatic point of view, replacing monovalent cations with multivalent ones in a system containing negatively charged colloids will affect the interaction, from purely repulsive to repulsive and/or attractive, depending on the surface charge density. Therefore, two different systems have been studied with respect to the surface charge densities: a relatively high surface charge density ( $z_{\text{site}} = -1.6$ ,  $\sigma = -1.85$   $e/\text{nm}^2$ ) and the one from our previous study ( $z_{\text{site}} = -1$ ,  $\sigma = -1.15$   $e/\text{nm}^2$ ). Figure 6a shows the free energy between two parallel platelets ( $\sigma = -1.15$   $e/\text{nm}^2$ ) for different salt concentrations without any addition of polymers. For the salt-free case with divalent counterions (blue line), the free energy increases as the platelets approach each other, i.e., a nonaggregated system. By including 0.01 M  $\text{CaCl}_2$  (red circle), the long-ranged repulsion is screened to some extent, and a weak local minima is found at  $\sim 1.8$  nm. By increasing the salt concentration to 0.1 M (black dashed), the long-ranged

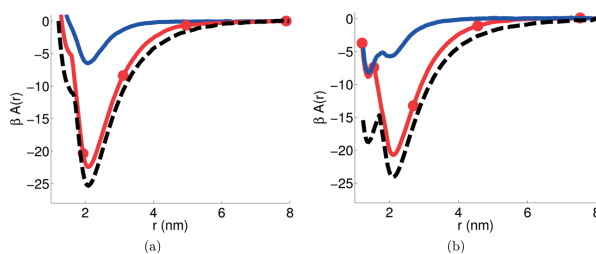


**Figure 8.** Free energy between two parallel platelets is shown as a function of the separation with 0.1 M CaCl<sub>2</sub> and different lengths of the adsorbing polymer at equal monomer density: eight 17 bead polymers (blue line), two 68 bead polymers (red circle), and one 136 bead polymer (black dashed). The surface charge density is  $-1.15 \text{ e/nm}^2$  in (a) and  $-1.85 \text{ e/nm}^2$  in (b). The short-ranged attractive interaction parameter is  $\epsilon = 0.3 \text{ kT}$ .

repulsion is completely screened, and a global minimum of 1.7 kT occurs at  $\sim 1.7 \text{ nm}$ ; i.e., small aggregates can be formed. If one adsorbing 68 bead polymer is introduced in the system (Figure 6b), the long-ranged repulsion is lowered due to polymer bridging, and global free energy minima of 4 kT at  $\sim 2.1 \text{ nm}$  and 12 kT at  $\sim 2.0 \text{ nm}$  for the salt-free system and 0.1 M CaCl<sub>2</sub> are introduced, respectively. Hence, larger tactoids are formed by including the adsorbing polymer; by increasing the salt concentration, the tactoid size increases, and the platelet–platelet separation decreases slightly. Even though the coarse-grained model is very simple, the results seem to be in qualitative agreement with the experimental results. Similar findings are found for  $\sigma = -1.85 \text{ e/nm}^2$  (Figure 6c) with the difference that the minima originating from the electrostatic interactions are enhanced. The adsorbing polymer prefers a separation of  $\sim 2.0 \text{ nm}$ , whereas the preferable separation for the electrostatic ion correlations is  $\sim 1.4 \text{ nm}$  at 0.1 M CaCl<sub>2</sub>, leading to a competition between the two separations or rather mechanisms, i.e., polymer bridging versus electrostatic attractive ion correlation effects, which is shown in Figure 6d.

The diameter of the platelet has been increased from 10 to 14 nm to study the effect of the platelet size with and without one 68 bead polymer. As mentioned in the SAXS section, the interaction scales to a first approximation with the diameter squared of the platelet; i.e., the electrostatic repulsion and electrostatic attraction when changing the diameter from 10 to 14 nm increase a factor of  $(14 \text{ nm}/10 \text{ nm})^2 \approx 2$ . Thus, larger tactoids are formed for the larger platelet at high enough salt concentration with or without the polymer (compare black line and black dashed in Figure 7). On the contrary, for the salt-free case, the polymer bridging with one 68 bead polymer can not reduce the long-range repulsion enough to introduce a global free energy minima for the larger platelet (blue dashed in Figure 7b); i.e., the number of polymers need to be increased to overcome the electrostatic repulsion.

The effect of the polymer length was analyzed for a given monomer density (i.e., the number of monomers was kept constant, whereas the number of polymers varied) with the two selected surface charge densities, upon addition of 0.1 M CaCl<sub>2</sub> (see Figure 8a). As mentioned in our previous work,<sup>37</sup> a longer polymer can obtain more contact points compared to a shorter polymer, and as a consequence, the separation where the polymer starts to bridge the platelets increases with the polymer length. Moreover, the electrostatic ion correlation minima at  $\sim 1.4 \text{ nm}$  is able to compete with the 17 bead polymer minima at  $\sim 2.0 \text{ nm}$  (blue line in Figure 8b). The radius of gyration of the 136 bead polymer decreased slightly

from 3 nm in bulk to 2.5 nm when situated between the two platelets at the free energy minima  $r = 2 \text{ nm}$ . To further analyze the conformation of the polymer, the individual Cartesian coordinate of the polymer changes from  $R_x = R_y = R_z = 1.7 \text{ nm}$  in bulk to  $R_x = R_y = 1.8 \text{ nm}$ , and  $R_z = 0.2 \text{ nm}$  between the two platelets where  $R_x = \sqrt{\frac{1}{N} \langle \sum_{i=1}^N (x_i - x_{\text{mean}})^2 \rangle}$ ,  $N = 136$ , and  $R_x$  is either the  $x$ -,  $y$ -, or  $z$ -direction. Hence, the polymer is compressed in the direction orthogonal to the platelet surface ( $z$ -direction) and extended in the directions along the platelet surface.

## CONCLUSIONS

The aim of this study was to scrutinize the mechanism behind aggregation, i.e., tactoid formation of nanostructures with the shape of a platelet. For that purpose two clay mineral dispersions have been used based on either Laponite or montmorillonite. The results obtained in this study can be explained by weak attractive electrostatic correlation forces and polymer bridging. It is also shown that as the salt concentration increases the long-ranged electrostatic repulsion is screened, and a free energy minimum at short distances appears due to the ion–ion correlations. When a strongly adsorbing polymer is introduced into the system, a second free energy minimum appears at a slightly larger separation. The latter dominates if the polymer is relatively long and/or the polymer concentration is high enough. The Debye screening length was found to be proportional to the platelet–platelet separation above 50 mM CaCl<sub>2</sub>. With the addition of PEG, the separation between the platelets systematically increased about 0.3 nm, and the number of platelets per tactoid increased. Comparison with montmorillonite showed similar separation distances between platelets; hence, the nature of the clay does not seem to be of importance for this matter. Notice though that the larger diameter of the montmorillonite platelets forms tactoids that contains a significantly larger number of platelets compared with Laponite tactoids.

Most of the experimental trends could be correlated with qualitative agreement in the simulations using a coarse-grained model with divalent cations. As the salt concentration increases, the long-ranged repulsion reduces, and a free energy minimum from the electrostatic ion–ion correlation is found. The electrostatic interactions between the platelets are proportional to the platelet area to a first approximation. Hence, from a theoretical point of view it is expected that smaller platelets will give rise to a lower number of platelets per tactoid. The adsorbing polymer bridged the platelets, although a second free

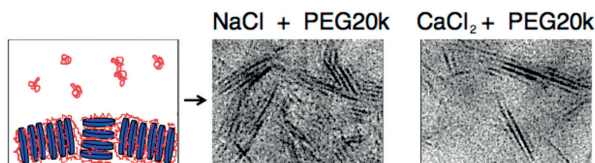


**Figure 9.** Replacement of the schematic description for Laponite-PEG dispersion<sup>37</sup> by a realistic sedimented structure from the Cryo-TEM results. Tactoid formation of Laponite platelets occurs at high enough salt concentration from both NaCl and CaCl<sub>2</sub> including the adsorbing polymer above the saturation concentration.

energy minimum occurred at slightly larger separations. These two minimas compete for the equilibrium separation, where the key parameters are the surface charge density, length of the polymer, and concentration of the polymer for the given adsorption strength.

In our previous study<sup>37</sup> we extended the schematic picture of Laponite dispersions with and without PEG from Atmuri et al.<sup>36</sup> with an extra column by adding NaCl. In this work we can replace the schematic picture by a realistic sedimented structure from the Cryo-TEM results and extend the observation for both 1:1 and 2:1 salt. Some of the tactoids that were found at high enough salt concentration from both NaCl and CaCl<sub>2</sub>, including the adsorbing polymer above the saturation concentration are shown in Figure 9.

This study could provide the colloidal community with important information regarding the aggregation of platelet nanostructures, as well as the role of multivalent ions and adsorbing polymers. The take-home message is that indeed the size of the disc is of importance, and it correlates with the size of formed tactoids. Moreover, our simulations suggest that there exists a threshold when the size of the platelets overrules the attractive electrostatic correlation forces. When adsorbing polymers are introduced into the system, there is a competition for the equilibrium platelet–platelet separation due to the two mechanisms: attractive ion–ion correlations and polymer bridging.

Future studies include synchrotron X-ray scattering techniques to obtain further detailed information about the system and thereby a deeper understanding of the forces and the morphology in a broader size range (from nano- to micrometer scale).

## ■ ASSOCIATED CONTENT

### ● Supporting Information

The Supporting Information is available free of charge on the ACS Publications website at DOI: 10.1021/acs.jpcc.7b01715.

Scattering intensities in log–log, Kratky, and fitting of the peaks for Laponite with different concentration of CaCl<sub>2</sub> for 0 and 5 wt % PEG20k (PDF)

## ■ AUTHOR INFORMATION

### Corresponding Authors

\*E-mail: axel.thuresson@teokem.lu.se

\*E-mail: marie.skepo@teokem.lu.se.

### ORCID

Axel Thuresson: 0000-0001-8459-1394

### Notes

The authors declare no competing financial interest.

## ■ ACKNOWLEDGMENTS

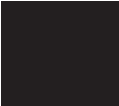
We acknowledge MAX IV Laboratory at Lund University, Sweden, proposal ID 20140385. We acknowledge Dr. S. Lages as well as Dr. T. Narayanan and Dr. J. Möller, for providing assistance during measurements at MAX IV Laboratory and ESRF, respectively. We would also like to acknowledge Gunnel Karlsson at Biomicroscopy Unit, Polymer and Materials Chemistry, Chemical Centre, Lund University, Sweden for the Cryo-TEM work. Computational resources were provided by the Swedish National Infrastructure for Computing (SNIC) through LUNARC, the Center for Scientific and Technical Computing at Lund University. This work was performed within the framework of the Swedish national strategic e-science research program, eSENCE. Lars Hierta Memorial Foundation is also acknowledged for financial support. M. Segad gratefully acknowledges the Royal Physiographic Society of Lund (KFS) for a number of traveling and research grants.

## ■ REFERENCES

- (1) Avery, R.; Ramsay, J. Colloidal properties of synthetic hectorite clay dispersions: II. Light and small angle neutron scattering. *J. Colloid Interface Sci.* **1986**, *109*, 448–454.
- (2) Thompson, D. W.; Butterworth, J. T. The nature of Laponite and its aqueous dispersions. *J. Colloid Interface Sci.* **1992**, *151*, 236–243.
- (3) Mongondry, P.; Tassin, J. F. T.; Nicolai, T. Revised state diagram of Laponite dispersions. *J. Colloid Interface Sci.* **2005**, *283*, 397–405.
- (4) Mourchid, A.; Lécolier, E.; Damme, H. V.; Levitz, P. On viscoelastic, birefringent, and swelling properties of Laponite clay suspensions: Revised phase diagram. *Langmuir* **1998**, *14*, 4718–4723.
- (5) Pignon, F.; Magnin, A.; Piau, J.-M.; Cabane, B.; Lindner, P.; Diat, O. Yield stress thixotropic clay suspension: Investigations of structure by light, neutron, and X-ray scattering. *Phys. Rev. E: Stat. Phys., Plasmas, Fluids, Relat. Interdiscip. Top.* **1997**, *56*, 3281.
- (6) Cocard, S.; Tassin, J. F.; Nicolai, T. Dynamical mechanical properties of gelling colloidal disks. *J. Rheol.* **2000**, *44*, 585–594.
- (7) Martin, C.; Pignon, F.; Magnin, A.; Meireles, M.; Lelièvre, V.; Lindner, P.; Cabane, B. Osmotic compression and expansion of highly ordered clay dispersions. *Langmuir* **2006**, *22*, 4065–4075.
- (8) SKB-Long-term safety for the final repository for spent nuclear fuel at Forsmark. 2011, TR-11-01, 1.
- (9) Blackmore, A. V.; Warkentin, B. P. Swelling of calcium montmorillonite. *Nature* **1960**, *186*, 823–824.
- (10) Jönsson, B.; Wennerström, H. *Electrostatic effects in soft matter and biophysics*; Springer: Netherlands, 2001; pp 171–204.
- (11) Karlund, O.; Olsson, S.; Nilsson, U.; Sellin, P. Experimentally determined swelling pressures and geochemical interactions of compacted Wyoming bentonite with highly alkaline solutions. *Phys. Chem. Earth, Parts A/B/C* **2007**, *32*, 275.
- (12) Banin, A. Tactoid formation in montmorillonite: effect on ion exchange kinetics. *Science* **1967**, *155*, 71–72.
- (13) Meunier, A. *Clays*; Springer Science & Business Media, 2005.
- (14) Shalkevich, A.; Stradner, A.; Bhat, S. K.; Muller, F.; Schurtenberger, P. Cluster, glass, and gel formation and viscoelastic

- phase separation in aqueous clay suspensions. *Langmuir* **2007**, *23*, 3570–3580.
- (15) Michot, L. J.; Bihannic, I.; Thomas, F.; Lartiges, B. S.; Waldvogel, Y.; Caillet, C.; Thieme, J.; Funari, S. S.; Levitz, P. Coagulation of Na-montmorillonite by inorganic cations at neutral pH. A combined transmission X-ray microscopy, small angle and wide angle X-ray scattering study. *Langmuir* **2013**, *29*, 3500–3510.
- (16) Lubetkin, S. D.; Middleton, S. R.; Ottey, R. H.; Barnes, P.; Nadeau, P.; Fripiat, J. Some properties of clay-water dispersions [and discussion]. *Philos. Trans. R. Soc., A* **1984**, *311*, 353–368.
- (17) Luckham, P. F.; Rossi, S. The colloidal and rheological properties of bentonite suspensions. *Adv. Colloid Interface Sci.* **1999**, *82*, 43–92.
- (18) Swartzan-Allen, S. L.; Matijevic, E. Surface and colloid chemistry of clays. *Chem. Rev.* **1974**, *74*, 385–400.
- (19) Bergaya, F.; Lagaly, G. *Handbook of clay science*; Newnes, 2013; Vol. 5.
- (20) Blackmore, A. V.; Miller, R. D. Tactoid size and osmotic swelling in calcium montmorillonite. *Soil Sci. Soc. Am. J.* **1961**, *25*, 169–173.
- (21) Norrish, K. The swelling of montmorillonite. *Discuss. Faraday Soc.* **1954**, *18*, 120–134.
- (22) Segad, M. Microstructure determination of IQ-WB clays: a direct procedure by small-angle X-ray scattering. *J. Appl. Crystallogr.* **2013**, *46*, 1316–1322.
- (23) Thuresson, A.; Ullner, M.; Åkesson, T.; Labbez, C.; Jönsson, B. Monte Carlo simulations of parallel charged platelets as an approach to tactoid formation in clay. *Langmuir* **2013**, *29*, 9216–9223.
- (24) Thuresson, A.; Ullner, M.; Turesson, M. Interaction and aggregation of charged platelets in electrolyte solutions: A coarse-graining approach. *J. Phys. Chem. B* **2014**, *118*, 7405–7413.
- (25) BYK, Technical information B-RI 21 Laponite performance additives. 2016.
- (26) Karnland, O.; Olsson, S.; Nilsson, U. Mineralogy and sealing properties of various bentonites and smectite-rich clay materials. *SKB Technical Report* **2006**, TR-06–30, 1–1.
- (27) Mongondry, P.; Nicolai, T.; Tassin, J. F. Influence of pyrophosphate or polyethylene oxide on the aggregation and gelation of aqueous Laponite dispersions. *J. Colloid Interface Sci.* **2004**, *275*, 191–196.
- (28) Lal, J.; Auvray, L. Interaction of polymer with clays. *J. Appl. Crystallogr.* **2000**, *33*, 673–676.
- (29) Lal, J.; Auvray, L. Interaction of polymer with discotic clay particles. *Mol. Cryst. Liq. Cryst. Sci. Technol., Sect. A* **2001**, *356*, 503–515.
- (30) Nelson, A.; Cosgrove, T. A small-angle neutron scattering study of adsorbed poly(ethylene oxide) on Laponite. *Langmuir* **2004**, *20*, 2298–2304.
- (31) Nelson, A.; Cosgrove, T. Dynamic light scattering studies of poly(ethylene oxide) adsorbed on Laponite: Layer conformation and its effect on particle stability. *Langmuir* **2004**, *20*, 10382–10388.
- (32) Rossi, S.; Luckham, P. F.; Green, N.; Cosgrove, T. NMR solvent relaxation studies of Na<sup>+</sup>-montmorillonite clay suspensions containing non-ionic polymers. *Colloids Surf., A* **2003**, *215*, 11–24.
- (33) Parfitt, R. L.; Greenland, D. The adsorption of poly(ethylene glycols) on clay minerals. *Clay Miner.* **1970**, *8*, 305–315.
- (34) Quintero, L. An overview of surfactant applications in drilling fluids for the petroleum industry. *J. Dispersion Sci. Technol.* **2002**, *23*, 393–404.
- (35) Stefanescu, E. A.; Stefanescu, C.; Donose, B. C.; Garno, J. C.; Daly, W. H.; Schmidt, G.; Negulescu, I. I. Polymer/clay nanocomposites: Influence of ionic strength on the structure and adhesion characteristics in multilayered films. *Macromol. Mater. Eng.* **2008**, *293*, 771–780.
- (36) Stefanescu, E. A.; Stefanescu, C.; Negulescu, I. I.; Daly, W. H. Effect of ionic species on the structures and properties of salt-containing PEO/montmorillonite nanocomposites. *Macromol. Chem. Phys.* **2008**, *209*, 2320–2330.
- (37) Thuresson, A.; Segad, M.; Turesson, M.; Skepö, M. Flocculated Laponite-PEG/PEO dispersions with monovalent salt, a SAXS and simulation study. *J. Colloid Interface Sci.* **2016**, *466*, 330–342.
- (38) Segad, M.; Jönsson, B.; Åkesson, T.; Cabane, B. Ca/Na montmorillonite: Structure, forces and swelling properties. *Langmuir* **2010**, *26*, 5782–5790.
- (39) Cummins, H. Z. Liquid, glass, gel: The phases of colloidal Laponite. *J. Non-Cryst. Solids* **2007**, *353*, 3891–3905.
- (40) Labrador, A.; Cerenius, Y.; Svensson, C.; Theodor, K.; Plivelic, T. The yellow mini-hutch for SAXS experiments at MAX IV Laboratory. *J. Phys.: Conf. Ser.* **2013**, *425*, 072019.
- (41) van Vaerenbergh, P.; Léonard, J.; Sztucki, M.; Boesecke, P.; Gorini, J.; Claustre, L.; Sever, F.; Morse, J.; Narayanan, T. An upgrade beamline for combined wide, small and ultra small-angle X-ray scattering at the ESRF. *AIP Conf. Proc.* **2015**, *1741*, 030034.
- (42) Sztucki, M. (2011) SAXSUtilities download page. <http://www.sztucki.de/SAXSUtilities> (accessed Mar 2017).
- (43) Segad, M.; Hanski, S.; Olsson, U.; Ruokolainen, J.; Åkesson, T.; Jönsson, B. Microstructural and swelling properties of Ca and Na montmorillonite: (In situ) Observations with Cryo-TEM and SAXS. *J. Phys. Chem. C* **2012**, *116*, 7596–7601.
- (44) Segad, M.; Jönsson, B.; Cabane, B. Tactoid formation in montmorillonite. *J. Phys. Chem. C* **2012**, *116*, 25425–25433.
- (45) SasView, version 3.1.2. <http://www.sasview.org> (accessed Mar 2017).
- (46) Glatter, O.; Kratky, O. *Small angle X-ray scattering*; Academic Press: London, 1982.
- (47) Abraham, M. J.; van der Spoel, D.; Lindahl, E.; Hess, B. The GROMACS development team, GROMACS user manual version 5.1.2., 2016.
- (48) Kumar, S.; Rosenberg, J. M.; Bouzida, D.; Swendsen, R. H.; Kollman, P. A. The weighted histogram analysis method for free-energy calculations on biomolecules. I. The method. *J. Comput. Chem.* **1992**, *13*, 1011–1021.
- (49) Bouyer, F.; Sanson, N.; Destarac, M.; Gerardin, C. Hydrophilic block copolymer-directed growth of lanthanum hydroxide nanoparticles. *New J. Chem.* **2006**, *30*, 399–408.
- (50) Beaucage, G. Small-angle scattering from polymeric mass fractals of arbitrary mass-fractal dimension. *J. Appl. Crystallogr.* **1996**, *29*, 134–146.
- (51) Bihannic, I.; Delville, A.; Demé, B.; Plazanet, M.; Villieras, F.; Michot, L. J. *Neutron applications in earth, energy and environmental sciences*; Springer: US, 2009; Chapter 18, pp 521–546.
- (52) Botet, R.; Cabane, B. Simple inversion formula for the small-angle X-ray scattering intensity from polydisperse systems of spheres. *J. Appl. Crystallogr.* **2012**, *45*, 406–416.
- (53) Chiarello, R.; Panella, V.; Krim, J.; Thompson, C. X-ray reflectivity and adsorption isotherm study of fractal scaling in vapor-deposited films. *Phys. Rev. Lett.* **1991**, *67*, 3408.
- (54) Bhatia, S. R. Ultra-small-angle scattering studies of complex fluids. *Curr. Opin. Colloid Interface Sci.* **2005**, *9*, 404–411.
- (55) Yoonessi, M.; Toghiani, H.; Daulton, T. L.; Lin, J.-S.; Pittman, C. U. Clay delamination in clay/poly(dicyclopentadiene) nanocomposites quantified by small angle neutron scattering and high-resolution transmission electron microscopy. *Macromolecules* **2005**, *38*, 818–831.
- (56) Atmuri, A. K.; Peklaris, G. A.; Kishore, S.; Bhatia, S. R. A re-entrant glass transition in colloidal disks with adsorbing polymer. *Soft Matter* **2012**, *8*, 8965–8971.

# Paper v



Reprinted with permission from *EPL*, 2016 **114**, 38002  
A. Thuresson, O. Karnland and B. Jönsson  
©2016 EPLA.



# Anomalous temperature behavior in clay swelling due to ion-ion correlations

A. THURESSON<sup>1</sup>, O. KARNLAND<sup>2</sup> and B. JÖNSSON<sup>1</sup>

<sup>1</sup> *Theoretical Chemistry, Chemical Center - POB 124, S-221 00 Lund, Sweden*

<sup>2</sup> *Clay Technology AB, IDEON Research Center - S-223 70 Lund, Sweden*

received 8 April 2016; accepted in final form 12 May 2016

published online 27 May 2016

PACS 82.70.Dd – Colloids

PACS 87.10.Rt – Monte Carlo simulations

PACS 05.20.-y – Classical statistical mechanics

**Abstract** – We show, experimentally and theoretically, that swelling of both natural and refined clays has an anomalous temperature behavior depending on counterion valency. In an aqueous clay dispersion dominated by monovalent counterions the swelling pressure increases with temperature as expected from entropic arguments. In a clay with predominantly divalent counterions, the opposite behavior is found. The explanation is due to the fact that ion-ion correlations increase with temperature. Ion-ion correlations are important at strong electrostatic coupling and in an aqueous solution the dielectric permittivity,  $\epsilon_r$ , drops with increased temperature,  $T$ , in such a way that the product  $\epsilon_r T$  also decreases. Thus, the net effect is an increased coupling.

Copyright © EPLA, 2016

**Introduction.** – The interaction between charged particles has successfully been described within the dielectric continuum model using the Poisson-Boltzmann (PB) equation. This so-called DLVO theory [1,2] has been extensively applied to charged aqueous colloidal suspensions containing monovalent salt. The number and diversity of applications, where it has been successfully applied is so large that we are led to the conclusion that both the primitive model and the mean-field approach are legitimate approximations. The numerically most striking examples of the accuracy of the theory have come from direct surface force measurements [3,4].

Rather well known, the theory fails completely when divalent counterions are present. The origin of the breakdown of the mean-field approach is its neglect of ionic correlations, which become important for divalent species. The electrostatic correlations reduce the entropic repulsion and also contributes an attractive component to the osmotic pressure, which will eventually make the net osmotic pressure attractive.

In order to describe these correlations quantitatively one generally needs to perform Monte Carlo (MC) simulations [5] and it turns out that many systems in real life are indeed determined by ionic correlations due to the presence of divalent counterions. The list can be made long –ranging from mineral suspensions like clay [6] and cement [7] to DNA [8,9] solutions.

Our interest in clay dispersions stems from the plan to deposit high-level nuclear waste in geological repositories using clay in the sealing procedure [10–12]. The success for such a containment depends on the clay structure and its stability under varying conditions [10,13,14]. In this context stable means that the clay should be able to sustain considerable changes in surrounding water including salinities of glacial melt water as well as sea water, while still being an effective hydraulic barrier. Another factor of concern is the heat production by the nuclear waste leading initially to a temperature increase.

Dry bentonite, or more correctly its main component montmorillonite, is built from two tetrahedral and one octahedral unit forming a mineral *platelet* with a thickness of approximately 10 Å. The octahedral part consists of oxygen coordinating Al atoms, and is surrounded by two tetrahedral sheets consisting of oxygen coordinating Si atoms. The platelets are negatively charged due to an exchange of  $\text{Al}^{3+}$  with, for example,  $\text{Mg}^{2+}$  and/or  $\text{Fe}^{2+}$ . Electroneutrality is conserved through mobile counterions such as  $\text{Na}^+$  or  $\text{Ca}^{2+}$  between the platelets.

The platelets form a lamellar structure, making bentonite clay a seemingly perfect model system for an electrical double layer [15–17]. The situation is, however, from a structural viewpoint slightly less ideal. With monovalent counterions, the swelling in solutions with low salt concentration seems to lead to a homogeneous dispersion of fully

exfoliated platelets, while with divalent counterions stacks of platelets are formed, usually referred to as *tactoids* [18] —which typically consist of 5–20 platelets [19]. The tactoid size is related to the correlation attraction between the platelets and increases with increased coupling. The number of platelets/tactoid also increases with the size of the platelets and it has been shown that small platelets do not form tactoids [20,21].

Clay swelling as a function of temperature has been studied by several groups [22–28]. A general result seems to be that the pressure increases with increasing temperature for  $\text{Na}^+$ -dominated bentonite below  $\sim 4$  MPa [27]. At higher pressures, that is thinner water layers, the opposite trend has been found [22,25,27,28]. On the contrary, a decreasing pressure with increased temperature is mostly found for  $\text{Ca}^{2+}/\text{Mg}^{2+}$ -dominated bentonites [24–26,28]. Conflicting experimental results for  $\text{Ca}^{2+}$ -dominated bentonite have been reported by Cho *et al.* [23], who found the pressure to increase with temperature.

In this letter, we have performed two sets of experiments that demonstrates the anomalous temperature behavior in clay swelling. We show that the MC simulations are in qualitative agreement with experimental results but in disagreement with the PB approximation. Furthermore, a simple one-dimensional model is derived to clarify the underlying physics. The physics behind the anomalous temperature behavior is a very general result and is most likely to be found in other colloidal systems.

**Materials.** – In this study we focus on clays from two different sources. The first, MX80, is a bentonite from Wyoming, Montana, and/or South Dakota in USA, with predominantly monovalent  $\text{Na}^+$  counterions [14]. The second clay, WB, originates from a natural source in Wadi Bashira in Iraq with a large fraction of divalent  $\text{Ca}^{2+}$  counterions [29]. Both these clays have been used as delivered, but we have also purified MX80 and performed ion exchange in order to obtain pure Na-MX80 and Ca-MX80 —the cleaning procedure has been described elsewhere [30].

**Clay swelling.** – A simple experiment illustrating the forces acting in a dispersion is to add one gram of clay into semipermeable membrane pockets. The pockets are placed into beakers with pure water at different temperatures and the swelling (weight) is followed on a daily basis. Figure 1 shows the difference in swelling at  $T = 60$  and  $25^\circ\text{C}$  for sodium-dominated MX80 and for calcium-dominated WB clays. Results from refined and calcium-exchanged MX80 is also included. MX80 shows the expected increase in swelling with temperature, while the WB clay exhibits the opposite behavior in conflict with mean-field predictions. The PB equation has a closed solution for the salt-free double layer and it is straightforward to show that  $\partial\Pi/\partial T > 0$  for both mono- and divalent counterions in aqueous solution. This is, however not the case if ion correlations are included as we will demonstrate below. The reduced swelling in the presence of divalent counterions

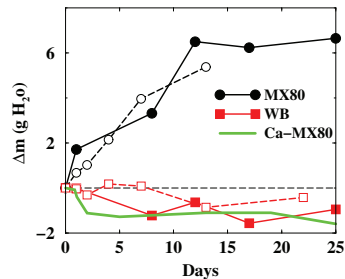


Fig. 1: (Colour online) The difference in swelling in pure water at  $T = 60$  and  $25^\circ\text{C}$ . The dialysis bags are tightened with either clips (solid lines) or knots (dashed lines). MX80 is Na dominated but contains Ca as well and vice versa for WB. The thick green line without symbols shows the swelling difference for refined and Ca-enriched MX80.

upon a temperature increase has three components: i) the clay forms larger tactoids, ii) the repulsion between the free platelets (those which do not form tactoids) is reduced, and iii) the thickness of the water layer between platelets in a tactoid decreases. The last factor is probably the least significant, but has been accurately measured in a scattering experiment [31], see below.

It is also possible to directly measure the pressure in a test cell [14,28]. A few grams of clay are placed into the cell and confined by a piston, which is attached to a force transducer. The bentonite is set to equilibrate with water through a semi-permeable membrane, which is permeable to water, but not to clay particles. The arrangement is placed in a climate chamber and the temperature can be varied between 5 and  $50^\circ\text{C}$ . The resulting osmotic pressure is calculated from the recorded force and piston contact area. It is difficult to prepare the cell to give an exact final volume, and two measurements are thus seldom identical. It is, however, possible to accurately determine the clay water content,  $w$ , at the end of an experiment, according to  $w = m_w/m_s$ , where  $m_w$  is the mass of water and  $m_s$  is the mass of solids. The clay dry density defined as  $D_d = m_s/V$  may then be calculated from  $D_d = D_w/(w + D_w/D_s)$ , where  $V$  is the total volume,  $D_w$  ( $1000\text{ kg/m}^3$ ) is the density of water and  $D_s$  ( $2750\text{ kg/m}^3$ ) is the density of the solids. Figure 2 clearly illustrates the difference between a clay with mainly monovalent counterions (MX80; fig. 2(a)) and one dominated by divalent counterions (WB; fig. 2(b)). Thus, the interpretation of the free swelling results (fig. 1) is confirmed by direct force measurements. The different temperature behavior between MX80 and WB could of course be due to their different mineralogical origin. The Ca-MX80 curve in fig. 1 indicates that this is not the case and it is further corroborated by the results in fig. 3, which show that the pressure response of pure Na-MX80 and Ca-MX80 is principally the same as that of the naturally

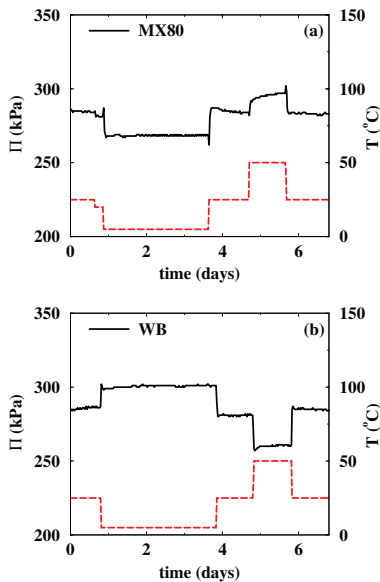


Fig. 2: (Colour online) Monitoring the swelling pressure in the cell while varying the temperature between 5 and 50 °C. (a) Na<sup>+</sup>-rich MX80 clay ( $D_d = 980 \text{ kg/m}^3$ ) and (b) Ca<sup>2+</sup>-rich WB clay ( $D_d = 950 \text{ kg/m}^3$ ). The red dashed lines show the temperature variation and the black lines the swelling pressure.

Na-rich MX80 and Ca-rich WB clay, respectively. The temperature response observed for Na and Ca bentonites also coincides well with previous studies [26,28].

**Monte Carlo simulations.** – A common model for montmorillonite swelling [16,32–34] is to treat it as two planar negatively charged surfaces neutralized by mobile counterions. The water molecules are treated as a dielectric continuum with a temperature,  $T$ , dependent relative dielectric permittivity,  $\epsilon_r = \epsilon_r(T)$ . In this *primitive model* all charged species are treated as hard spheres and the interaction, between two particles  $i$  and  $j$  separated by a distance  $r$ , is defined as  $u(r) = Z_i Z_j e^2 / (4\pi\epsilon_0\epsilon_r r)$  if  $r > d_{hc}$ , otherwise  $u(r) \rightarrow \infty$ , where  $Z_i$  is the ion valency,  $e$  the elementary charge,  $\epsilon_0$  the permittivity of vacuum and  $d_{hc}$  is the ion diameter. It is straightforward to perform an MC simulation of this system and the technicalities have been described elsewhere [35–37]. The osmotic pressure of the confined solution,  $\Pi$ , may be calculated according to [5,36]

$$\Pi = k_B T \sum_i c_i(\text{mp}) + \Pi^{\text{corr}} + \Pi^{\text{hc}}, \quad (1)$$

where  $k_B$  is the Boltzmann constant,  $c_i$  is the concentration of species  $i$  and  $mp$  stands for mid-plane. The term

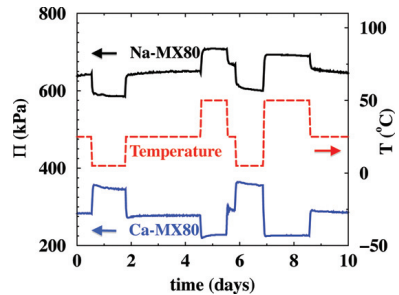


Fig. 3: (Colour online) Monitoring the swelling pressure in the cell while varying the temperature between 5 and 50 °C for sodium- and calcium-exchanged MX80. The red dashed lines show the temperature variation, the black and blue lines show the swelling pressure for Na-MX80 ( $D_d = 780 \text{ kg/m}^3$ ) and Ca-MX80 ( $D_d = 970 \text{ kg/m}^3$ ), respectively. The arrows indicate the corresponding  $y$ -scale.

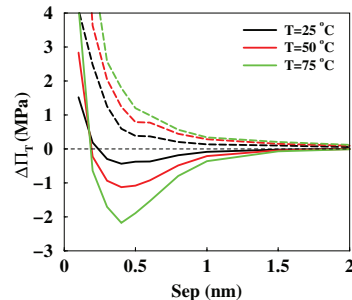


Fig. 4: (Colour online) The difference in simulated osmotic pressure taking  $T = 5^\circ\text{C}$  as our reference,  $\Delta\Pi_T = \Pi_T - \Pi_{T=5^\circ\text{C}}$ . Solid curves are for divalent counterions and dashed curves for monovalent ones.

$\Pi^{\text{corr}}$  comes from the fact that ions on either side of the mid-plane correlate and give an attractive contribution to the pressure. The finite ion size,  $d_{hc} = 4 \text{ \AA}$ , gives rise to the term  $\Pi^{\text{hc}}$ .

The osmotic pressure of the model described above has been calculated (note that the bulk water osmotic pressure is zero, since we study a salt-free system) at four different temperatures, 5, 25, 50 and 75 °C. The corresponding dielectric permittivities of water are 85.76, 78.30, 69.91 and 62.43, respectively [38]. Figure 4 shows the simulated pressures for both monovalent and divalent counterions. For clarity, we present the pressure difference,  $\Delta\Pi_T = \Pi_T - \Pi_{T=5^\circ\text{C}}$ . The simulations show the same trends as observed experimentally. That is, with monovalent counterions the pressure increases with temperature, while with divalent it decreases. It would be tempting to

make more quantitative comparisons between the simulated results in fig. 4 and the experimental ones in figs. 2, 3. It could be possible for the monovalent case as we presumably have a fully exfoliated system. In the divalent case, we have a mixture of tactoids and freely moving platelets whose structural details are unknown. We note, however, that the pressure changes in both theory and experiments are in the range of 100 kPa. As mentioned above, there is a small but significant temperature induced change in platelet separation in the tactoids. From X-ray scattering of Ca-montmorillonite [31], it was found that the water layer in a tactoid shrinks from 19.9 to 19.5 Å when temperature increases from 20 to 60 °C. A further decrease to about 19.35 Å takes place between 60 and 90 °C. These results can be directly compared to our simulation data. Simulations predict, from the point of zero pressure, a reduction of the layer thickness of 0.2 Å when the temperature increases from 25 to 75 °C in fair agreement with experiments.

**Simple model.** – Obviously, the mean-field approximation applied to the model system with two infinite planar charged walls neglects ion-ion correlations. Another simple model (SM) of the electric double layer, akin to the strong-coupling theory (SC) suggested by Netz [39] that incorporates correlation, is to regard it as completely correlated [40]. Consider a model system where we from a system with two infinitely charged walls and neutralizing counterions cut out a cylinder containing two circular charged plates and in between one neutralizing counterion. This system is straightforward to solve numerically, but it can also be further simplified by treating it as a one-dimensional system with three charges on a line. Assuming that the wall charges are fixed at positions  $\pm(h/2 + \delta)$  and that the counterion is free to move between  $\pm h/2$ , we may estimate the free energy as

$$A(h) = -\frac{7}{4} \frac{Z^2 e^2}{4\pi\epsilon_0\epsilon_r(h+2\delta)} - k_B T \ln(h/C), \quad (2)$$

where  $C$  is a constant that is independent of  $h$  and  $T$ . In eq. (2) we overestimate the entropy by assuming a uniform counterion distribution on the line and we also overestimate the energy by assuming that the counterion is situated in the middle of the line. The force then becomes

$$F(h) = -\frac{7}{4} \frac{Z^2 e^2}{4\pi\epsilon_0\epsilon_r(h+2\delta)^2} + \frac{k_B T}{h}, \quad (3)$$

and by taking the derivative with respect to  $T$ , we get

$$\frac{\partial F}{\partial T} = \frac{7}{4} \frac{Z^2 e^2}{4\pi\epsilon_0\epsilon_r^2(h+2\delta)^2} \frac{\partial\epsilon_r}{\partial T} + \frac{k_B}{h}. \quad (4)$$

The derivative  $\partial\epsilon_r/\partial T < 0$ , and hence,  $\partial F/\partial T$  can be both positive and negative in agreement with MC simulations but in disagreement with the PB approximation. It, however, explains the difference in swelling behavior between clays neutralized by monovalent and divalent counterions seen in figs. 1–3.

By comparing SM with SC it can be shown that the entropy terms are identical, while the energy term in SM has distance and valency dependence, which is absent in the SC case. This means that the SM can describe the transition between weak and strong coupling.

**Limitations of the primitive model.** – The swelling pressure above  $\sim 4$  MPa decrease with increasing temperature also for sodium-dominated MX80 [27,28]. As shown in fig. 4 the primitive model fails to predict this behavior. The dry density at 4 MPa for MX80 is approximately 1400 kg/m<sup>3</sup> and hence the estimated average distance between the platelets is smaller than 1 nm [14,28]. Thus, for short separations, smaller than a few layers of water, it seems that water cannot be treated as a uniform dielectric continuum with a dielectric permittivity of bulk water.

**Conclusions.** – We have demonstrated experimentally that the swelling pressure increases or decreases with temperature for clays dominated by monovalent or divalent counterions, respectively. We showed that the exact solution to the primitive model predicts the correct behavior down to a few layers of water. With monovalent counterions, the pressure increases with temperature as expected from the DLVO theory. With divalent counterions, the results can be understood by the fact that the dielectric permittivity drops as the temperature increases, which leads to an increase in electrostatic interaction and thereby enhanced ion-ion correlation. This correlation effect leads to attractive forces, which is significant for divalent counterions. The pressure in the divalent system is consequently expected to decrease with increasing temperature.

Finally, the anomalous temperature behavior described above is most likely to be found in other colloidal systems where divalent counterions prevail. One example is cement, where it is known that, on a microscopic level, a harder material, *i.e.* calcium silicate hydrate, is formed at elevated temperature. On the macroscopic scale, however, an elevated temperature leads to a more porous concrete [41].

\*\*\*

The work was performed within the framework of the Swedish national strategic e-science research program ESSENCE.

## REFERENCES

- [1] DERJAGUIN B. V. and LANDAU L., *Acta Phys. Chim. URSS*, **14** (1941) 633.
- [2] VERWEY E. J. W. and OVERBEEK J. T. G., *Theory of the Stability of Lyophobic Colloids* (Elsevier Publishing Company Inc., Amsterdam) 1948.
- [3] PASHLEY R. M., *J. Colloid Interface Sci.*, **83** (1981) 531.
- [4] ISRAELACHVILI J. N. and ADAMS G. E., *J. Chem. Soc. Faraday Trans. 1*, **74** (1978) 975.

- [5] GULDBRAND L., JÖNSSON B., WENNERSTRÖM H. and LINSE P., *J. Chem. Phys.*, **80** (1984) 2221.
- [6] KJELLANDER R., MARČELJA S., PASHLEY R. M. and QUIRK J. P., *J. Phys. Chem.*, **92** (1988) 6489.
- [7] PELLENQ R., CAILLOT J. and DELVILLE A., *J. Phys. Chem. B*, **101** (1997) 8584.
- [8] GULDBRAND L., NILSSON L. and NORDENSKIÖLD L., *J. Chem. Phys.*, **85** (1986) 6686.
- [9] MEL'NIKOV S. M., KHAN M. O., LINDMAN B. and JÖNSSON B., *J. Am. Chem. Soc.*, **121** (1999) 1130.
- [10] SKB, SKB Technical Report, TR-11-01 (2011) 1.
- [11] KOMINE H. and OGATA N., *Soils Found.*, **39** (1999) 83.
- [12] BUZZI O., BOULON M., DELERUVELLE F. and BESNUS F., *Rock Mech. Rock Eng.*, **41** (2008) 343.
- [13] KOMINE H. and OGATA N., *Can. Geotech. J.*, **40** (2003) 460.
- [14] KARNLAND O., OLSSON S. and NILSSON U., SKB Technical Report, TR-06-30 (2006) 1.
- [15] BLACKMORE A. V. and WARKENTIN B. P., *Nature*, **186** (1960) 823.
- [16] OLPHEN H. V., *J. Colloid Sci.*, **17** (1962) 660.
- [17] JÖNSSON B. and WENNERSTRÖM H., in *Electrostatic Effects in Soft Matter and Biophysics* (Springer Netherlands, Dordrecht) 2001, Chapt. *When Ion-Ion Correlations are Important in Charged Colloidal Systems*, pp. 171–204.
- [18] LANGMUIR I., *J. Chem. Phys.*, **38** (1938) 873.
- [19] BANIN A., *Science*, **155** (1967) 71.
- [20] THURESSON A., ULLNER M. and TURESSON M., *J. Phys. Chem. B*, **118** (2014) 7405.
- [21] SEGAD M., CABANE B. and JÖNSSON B., *Nanoscale*, **7** (2015) 16290.
- [22] LINGNAU B., GRAHAM J., YARECHEWSKI D., TANAKA N. and GRAY M., *Eng. Geol.*, **41** (1996) 103.
- [23] CHO W. J., LEE J. O. and KANG C. H., *Ann. Nucl. Energy*, **27** (2000) 1271.
- [24] VILLAR M. V. and LLORET A., *Appl. Clay Sci.*, **26** (2004) 337.
- [25] VILLAR M. V. and GÓMEZ-ESPINA R., in *Experimental Unsaturated Soil Mechanics* (Springer, Berlin, Heidelberg) 2007, Chapt. *Retention Curves of Two Bentonites at High Temperature*, pp. 267–274.
- [26] ARIFIN Y. F. and SCHANZ T., in *Experimental Unsaturated Soil Mechanics* (Springer, Berlin, Heidelberg) 2007, Chapt. *Modified Isochoric Cell for Temperature Controlled Swelling Pressure Tests*, pp. 229–241.
- [27] BIRGERSSON M., KARNLAND O. and NILSSON U., *Phys. Chem. Earth, Parts A/B/C*, **33** (2008) S527.
- [28] BIRGERSSON M., KARNLAND O. and NILSSON U., SKB Technical Report, TR-10-40 (2010) 1.
- [29] SEGAD M., *J. Appl. Crystallogr.*, **46** (2013) 1316.
- [30] SEGAD M., JÖNSSON B., ÅKESSON T. and CABANE B., *Langmuir*, **26** (2010) 5782.
- [31] SVENSSON P. D. and HANSEN S., *Clays Clay Miner.*, **61** (2013) 328.
- [32] NORRISH K. and QUIRKE J. P., *Nature*, **18** (1954) 120.
- [33] SPITZER J. J., *Langmuir*, **5** (1989) 199.
- [34] KARNLAND O., SKB Technical Report, TR-97-31 (1997) 1.
- [35] JÖNSSON B., WENNERSTRÖM H. and HALLE B., *J. Phys. Chem.*, **84** (1980) 2179.
- [36] VALLEAU J. P., IVKOV R. and TORRIE G. M., *J. Chem. Phys.*, **95** (1991) 520.
- [37] GREBERG H., KJELLANDER R. and ÅKESSON T., *Mol. Phys.*, **87** (1996) 407.
- [38] MALMBERG C. G. and MARYOTT A. A., *J. Res. Natl. Bur. Stand.*, **56** (1956) 1.
- [39] NETZ R., *Eur. Phys. J. E*, **5** (2001) 557.
- [40] JÖNSSON B., NONAT A., LABBEZ C., CABANE B. and WENNERSTRÖM H., *Langmuir*, **21** (2005) 9211.
- [41] ZAJAC M., PhD Thesis, Université de Bourgogne, Dijon, France (2007).



## Paper VI



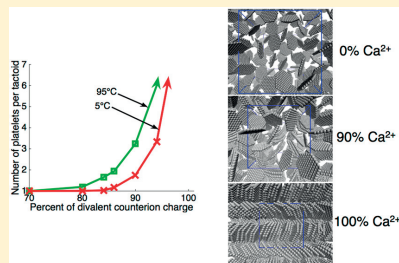
Reprinted with permission from *J. Phys. Chem. C.*, 2017 121, 7951-7958  
A. Thuresson, M. Jansson, T. S. Plivelic and M. Skepö  
©2017 American Chemical Society.



# Temperature Response of Charged Colloidal Particles by Mixing Counterions Utilizing $\text{Ca}^{2+}/\text{Na}^+$ Montmorillonite as Model System

Axel Thuresson,<sup>\*,†</sup> Maria Jansson,<sup>†</sup> Tomás S. Plivelic,<sup>‡</sup> and Marie Skepö<sup>\*,†</sup><sup>†</sup>Theoretical Chemistry and <sup>‡</sup>MAX IV Laboratory, Lund University, SE-221 00 Lund, Sweden

**ABSTRACT:** The osmotic pressure and the aggregation of charged colloids as a function of temperature have been investigated using Monte Carlo and molecular dynamics simulations for different ratios of monovalent and divalent counterions. In the simulations the water is treated as a temperature-dependent dielectric continuum, and only the electrostatic interactions are considered. It was found that the temperature response can be controlled, i.e., the osmotic pressure can increase, decrease, or be kept constant, as a function of temperature depending on the monovalent/divalent counterion ratio. The increase in osmotic pressure with temperature, which occurs at low enough surface charge density and/or low fraction of divalent ions, can be understood from the DLVO theory. The origin of the opposite behavior can be explained by the enhanced attractive electrostatic ion–ion correlation interactions with temperature. The constraint is that the absolute value of the surface charge density of the colloids must be above a certain threshold, i.e., high enough such that the attractive ion–ion correlations can dominate the interaction regarding the divalent ions. The current conclusions are supported by the microstructural characterization of  $\text{Ca}^{2+}/\text{Na}^+$ -montmorillonite clay using small-angle X-ray scattering. A qualitative agreement is observed between the simulations and the experimental data.



## INTRODUCTION

When a charged colloid is dissolved in aqueous or polar solvents, the macromolecule becomes ionized, and there will be a release of counterions. Since macromolecules usually are highly charged, there will be counterions that confer enormous entropies of mixing. The counterions will form an electrical double layer, where the first layer is the surface charge of the macromolecule, and the second layer is composed of oppositely charged ions screening the first layer. Upon addition of multivalent ions to a system comprising monovalent counterions, there will be an ionic exchange in the double layer, and monovalent counterions will be released. With monovalent counterions in the system solely, the electrostatic interaction between the particles is repulsive, whereas when multivalent counterions are introduced, the interaction can be attractive due to the electrostatic ion–ion correlation effects. The latter is only valid under the constraint that the surface charge density is above a certain threshold.<sup>1–8</sup>

The above given mechanisms along with the charge distribution, the volume, the size, and the shape of the macromolecule, as well as the hydrophobic interactions, are the parameters that primarily determines the physicochemical properties of macromolecular solutions.

The model system of this study is montmorillonite, although we would like to emphasize that the obtained results are generally valid. Swelling 2:1 clay minerals consist of platelets with a thickness of about 1 nm and lateral dimensions varying from 25 nm in synthetic Laponite clays up to 1000 nm in natural montmorillonite. When water is added, the clay

platelets become ionized, and the rising osmotic pressure in the solution causes the clay to swell.<sup>9–11</sup> Depending on the size, the platelets can form a lamellar structure, making it a seemingly perfect model system for an electrical double layer, where the swelling and the stability in saline solution depend strongly on the counterion valency and the surface charge density.<sup>12–14</sup> The situation is however, from a structural point, slightly less ideal. Clay is normally not a homogeneous lamellar material; it might better be described as a disordered structure of stacks of platelets, also denoted tactoids.<sup>15–17</sup>

Experimentally<sup>18</sup> and theoretically,<sup>19</sup> it has been found that for mixtures of  $\text{Ca}^{2+}/\text{Na}^+$ -montmorillonite (with ~20% sodium or more) the clay is behaving qualitatively as  $\text{Na}^+$ -montmorillonite. Recently, it has also been shown that the swelling pressure of the clay mineral in aqueous solution, as a function of temperature, can be understood from electrostatic ion–ion correlation interactions.<sup>20</sup> In an aqueous clay dispersion dominated by monovalent counterions, the swelling pressure increases with temperature due to entropic reasons, whereas in a clay with predominantly divalent counterions, the opposite behavior was found. The explanation is that the ion–ion correlations increase with temperature since the product  $\epsilon_r T$  decreases, i.e., the dielectric permittivity multiplied with temperature. The latter is an effect of the fact that  $\epsilon_r$  drops when  $T$  increases. The aim of this study is to investigate the

Received: January 27, 2017

Revised: March 15, 2017

Published: March 16, 2017



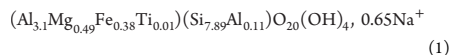
possibility to control the osmotic pressure response with temperature of charged colloidal particles by varying the ratio of monovalent/divalent counterions in the system.

For this purpose a coarse-grained model has been used, and the simulations assume that the solvent can be represented as a uniform temperature-dependent dielectric permittivity. The limitations of the model are that: (i) it does not explain the extralammellar swelling<sup>19</sup> that is found for homoionic Ca<sup>2+</sup>-montmorillonite nor, (ii) the reverse swelling pressure trend with temperature for Na<sup>+</sup>-montmorillonite, i.e., when the average distance between the platelets is smaller than 1 nm. The former is to the authors knowledge not well understood, and the latter is due to the fact that the water is represented by the dielectric permittivity of bulk water.<sup>20,21</sup> The theoretical predictions are verified by small-angle X-ray scattering (SAXS) data, and a good qualitative correspondence is achieved.

## MATERIALS AND METHODS

### Experimental Details. Material and Sample Preparation.

In this study, Wyoming Bentonite (MX-80), which consists mainly of the swelling clay mineral sodium montmorillonite, has been used. Sodium saturated montmorillonite from MX-80 has the chemical formula:<sup>22</sup>



The thickness and the average lateral size of the montmorillonite platelets are approximately 1 and 250 nm, respectively.<sup>23</sup> The purification and ion exchange procedures for MX-80 are described elsewhere.<sup>24</sup> Analytical grade sodium chloride (purity, 99.5%) and calcium chloride (purity, 99.5%) were purchased from MERCK. The purified Na<sup>+</sup>- and Ca<sup>2+</sup>-montmorillonite were dried at 105 °C overnight and milled into a fine powder. The clay powder from respective clay were mixed in different proportions to obtain different fractions of calcium (divalent) counterion charge that is neutralizing the clay:

$$\eta_{\text{Di}} = \frac{m_{\text{Ca-clay}}}{m_{\text{Ca-clay}} + m_{\text{Na-clay}}} \approx \frac{2N_{\text{Di}}}{2N_{\text{Di}} + N_{\text{Mon}}} \quad (2)$$

where  $m_{\text{Ca-clay}}$  is the mass of Ca<sup>2+</sup>-montmorillonite and  $m_{\text{Na-clay}}$  is the mass of the Na<sup>+</sup>-montmorillonite, whereas  $N_{\text{Mon}}$  and  $N_{\text{Di}}$  are the number of monovalent and divalent counterions, respectively. An excess of Millipore water was added to the mixed clay powder such that the counterions could diffuse and equilibrate within the sample for 24 h. All the Ca<sup>2+</sup>/Na<sup>+</sup>-montmorillonite mixtures were dried at 105 °C overnight and milled into a fine powder. Finally, Millipore water was added to each mixture in order to obtain a water mass ratio equal to six, and the samples were set to equilibrate for one month.  $w = 6$  corresponds to a clay volume fraction  $\phi_c \approx D_w/(D_w + D_w) = 6\%$ , where  $D_c = 2750 \text{ kg/m}^3$  is the density of the clay<sup>18</sup> and  $D_w = 1000 \text{ kg/m}^3$  is the density of water.

SAXS. SAXS experiments were performed at beamline ID02 at the European Synchrotron Radiation Facility (ESRF) in Grenoble, France.<sup>25</sup> The  $q$ -range in the measurements was  $0.2 < q < 4.5 \text{ nm}^{-1}$ , where  $q = 4\pi \sin(\theta)/\lambda$ ,  $2\theta$  is the scattering angle, and  $\lambda = 0.1 \text{ nm}$  is the monochromatic beam wavelength. The detector was a 2D CCD Raynomix MX 170 HS with binning  $4 \times 4$ . For data reduction, the software SAXSUtilities<sup>46</sup> was used. The montmorillonite samples were measured in 1 mm sealed glass capillaries, and the background scattering

(water) was subtracted. SAXS measurements were collected at different temperatures: 5, 25, 55, and 90 °C. The thermalization time of each temperature was 12 min.

In order to estimate the size of the aggregates, i.e., the average number of clay platelets per aggregate, a model scattering peak has been fitted to the experimental data. The scattering function was approximated with a Lorentzian line shape:

$$q^2 I(q) \propto \frac{w}{(q - q_{\text{max}})^2 + w^2} + b \quad (3)$$

where  $I(q)$  is the scattering intensity,  $b$  is a fitting parameter for the background contribution, and  $w$  is a measure of the width. The full width at half-maximum (fwhm) of the peak is equal to  $2w$ , and the average tactoid size can be expressed as  $\langle N \rangle \approx q_{\text{max}}/w$ .<sup>24,27,28</sup> The data was fitted between  $q_{\text{max}} \pm 0.5 \text{ nm}^{-1}$ , in order to make the peak fitting procedure as reasonable as possible.

**Model and Simulations. Bulk Simulations.** The interaction potentials and the platelet description are given elsewhere.<sup>29</sup> The electrostatic potential between particle  $i$  and  $j$  is defined as:

$$\beta u_{ij}^{\text{EL}}(r_{ij}, T) = \frac{l_{\text{B}} z_i z_j}{r_{ij}} \quad (4)$$

where  $\beta = 1/(k_{\text{B}}T)$ ,  $k_{\text{B}}$  is the Boltzmann constant,  $l_{\text{B}} = e^2/(4\pi\epsilon_0\epsilon_r(T)k_{\text{B}}T)$  is the Bjerrum length,  $e$  is the elementary unit charge,  $\epsilon_0$  is the permittivity of vacuum,  $z_i$  is the valency of particle  $i$ , and  $r_{ij}$  is distance between the particles. The solvent, i.e. the water molecules, is treated as a temperature-dependent,  $T$ , uniform dielectric permittivity,  $\epsilon_r(T)$ , with experimentally measured values of the dielectric permittivity of water.<sup>30</sup> The electrostatic interactions are enhanced as a function of temperature; i.e., the Bjerrum length increases as shown in Table 1. A truncated and shifted Lennard-Jones (TLJ) potential

**Table 1. Bjerrum Length as a Function of Temperature<sup>a</sup>**

$T$ (°C)	$T$ (K)	$\epsilon_r(T)$	$l_{\text{B}}$ (nm)
5	278.15	85.76	0.700
25	298.15	78.30	0.716
95	368.15	57.01	0.796

<sup>a</sup>The Bjerrum length,  $l_{\text{B}}$ , at three different temperatures,  $T$ , and given dielectric permittivity,  $\epsilon_r(T)$ .<sup>30</sup>

has been used to represent the excluded volume of all particles in the system and is defined as:

$$u_{ij}^{\text{TLJ}}(r_{ij}) = \begin{cases} \epsilon \left[ \left( \frac{\sigma_{ij}}{r_{ij}} \right)^{12} - 2 \left( \frac{\sigma_{ij}}{r_{ij}} \right)^6 + 1 \right] & \text{if } r_{ij} \geq \sigma_{ij} \\ 0 & \text{otherwise} \end{cases} \quad (5)$$

where  $\sigma_{ij} = (\sigma_i + \sigma_j)/2$ ,  $\sigma_{\text{ion}} = 4 \text{ \AA}$ , and  $\sigma_{\text{site}} = 10 \text{ \AA}$ . This potential has been chosen to be temperature independent and the strength of the short-ranged potential was set to  $\epsilon = k_{\text{B}}298 \text{ J}$ . Hence, the distribution of uncharged particles behaves independently of the temperature, with the aim to study the electrostatic effects solely.

The bulk molecular dynamics (MD) simulations were performed with the software package GROMACS (version 5.0.4).<sup>31</sup> Fifty negatively charged platelets with their corre-

sponding counterions were placed into a cubic simulation box with three-dimensional periodic boundary conditions. The platelets consist of 91 connected charged sites, and the one-sided surface charge density  $\sigma = -2.6 \text{ e/nm}^2$ .<sup>29</sup> The absolute value of the surface charge density is chosen much higher than that of montmorillonite due to the small size of the simulated platelets. If the simulated platelets would be larger, the surface charge density can be reduced to have similar probability of aggregation as the smaller ones with divalent counterions.<sup>29</sup> On average, montmorillonite has a one-sided surface charge density of  $-1.5 \text{ e/nm}^2$ .<sup>32</sup>

Newton's equations of motion of the freely moving species (platelets + ions) were integrated using the leapfrog algorithm. The time step was chosen to be 10 fs and gave the same results as using 1 fs time step (data not shown). The pressure was set by isotropic Berendsen pressure coupling for the NPT simulations, and the temperature was set by velocity-rescaling temperature coupling. All simulations assume equilibrium with salt-free water, and hence, the pressure is equal to the osmotic pressure. To account for the long-ranged electrostatic interactions, fast particle-mesh Ewald summation (PME) was used with a 6 nm real-space Coulomb cutoff (the largest and smallest box length used in the simulations are 70 and 20 nm, respectively) and a Fourier spacing equal to 0.6 nm. Different starting configurations for the equilibration simulation were performed both from a dilute and a compressed system to confirm that the mean volume and mean energy converged to the same value. For an in-depth description of the input parameters, see the online user manual.<sup>31</sup>

The volume fraction is a function of temperature,  $T$ , and osmotic pressure,  $\Pi$ , and is defined as:

$$\phi(T, \Pi) = \frac{4\pi r^3 N_{\text{sites}}}{3V_s(T, \Pi)} \quad (6)$$

where  $r = 0.5 \text{ nm}$  is the radius of a platelet site,  $N_{\text{sites}}$  is the number of connected charged sites per platelet, and  $V_s(T, \Pi)$  is the volume per platelet.

**Two Parallel Surfaces.** Two infinite parallel surfaces with a specific surface charge density and its corresponding counterions were simulated using Monte Carlo (MC) simulations described elsewhere.<sup>19</sup> The surface charge is smeared out, and the ions are treated as charged hard spheres. The electrostatic interactions between two ions are defined similarly as in the bulk simulations. The counterions in the bulk simulations are free to explore the volume between the surfaces, whereas in the MC simulations it is assumed that the counterion ratio is constant. An alternative to this simplification is to use a variant of the grand canonical ensemble.<sup>33</sup> For a given separation between the surfaces,  $h$ , and temperature, the osmotic pressure,  $\Pi = \Pi(T, h)$ , can be calculated using a midplane approach<sup>1</sup> written as:

$$\Pi = \Pi^{\text{id}} + \Pi^{\text{corr}} + \Pi^{\text{coll}} \quad (7)$$

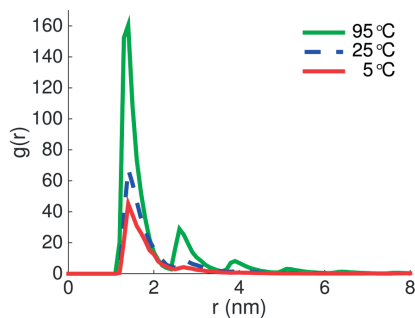
where  $\Pi^{\text{id}} = k_B T \sum_{i=1}^2 c_i(\text{mp})$  is the ideal contribution,  $c_i(\text{mp})$  is the concentration of counterions at the midplane with valency  $i$ ,  $\Pi^{\text{corr}}$  is an attractive term due to the ion-ion correlations on either side of the midplane, and  $\Pi^{\text{coll}}$  is the collision term due to the finite-sized ions. The osmotic pressure response with temperature is calculated between 25 and 95 °C:

$$\Delta \Pi = \Pi(T = 95 \text{ }^\circ\text{C}, h_{\text{fix}}) - \Pi(T = 25 \text{ }^\circ\text{C}, h_{\text{fix}}) \quad (8)$$

where  $h_{\text{fix}}$  is defined to be the separation where the osmotic pressure is 4 bar for 25 °C.

## RESULTS AND DISCUSSION

**NVT Bulk Simulations.** Three radial distribution functions (rdf's) are shown with respect to the center-of-mass between the platelets from NVT bulk simulations in Figure 1a. The



(a) Radial distribution functions for three different temperatures.

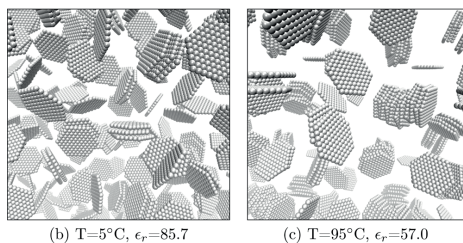


**Figure 1.** (a) Radial distribution functions between the platelets from NVT simulations at three different temperatures with  $\eta_{\text{Di}} = 0.96$ . (b, c) Representative configurations from the simulations for two temperatures. The counterions are omitted due to clarity, and the platelets are shown in gray.

volume of the platelets divided by the total volume is 4% ( $\phi = 0.04$ ), and  $\eta_{\text{Di}} = 0.96$ ; i.e., 96% of the charge of the platelets are neutralized by divalent cations. The first peak at  $\sim 1.3 \text{ nm}$  corresponds to two platelets aggregated face-to-face. The height of the peak is related to the probability of finding that configuration. If three platelets have aggregated, a second peak arises at  $\sim 1.3 \cdot 2 = 2.6 \text{ nm}$ . If four platelets have aggregated, a third peak arises at  $\sim 1.3 \cdot 3 = 3.9 \text{ nm}$  and so on. Thus, the number of visible peaks in the rdf's gives an indication of the average number of platelets per tactoid,  $\langle N \rangle$ , and it can be seen that  $\langle N \rangle$  increases with temperature. As the temperature is increasing from 5 to 95 °C, the attractive ion-ion correlations are enhanced<sup>20</sup> due to the  $\sim 14\%$  increase in Bjerrum length (see Table 1), which consequently leads to larger aggregates and a reduced osmotic pressure ( $\langle N \rangle \sim 1.5$ ,  $\Pi \sim 0.25 \text{ bar}$  at 5 °C, and  $\langle N \rangle \sim 3.0$ ,  $\Pi \sim 0.20 \text{ bar}$  at 95 °C). Typical configurations from the simulations are shown in Figure 1b,c, where it is displayed that larger aggregates are found at higher temperatures. Thus, for the particular surface charge density, volume fraction, and fraction of divalent counterions, we find:

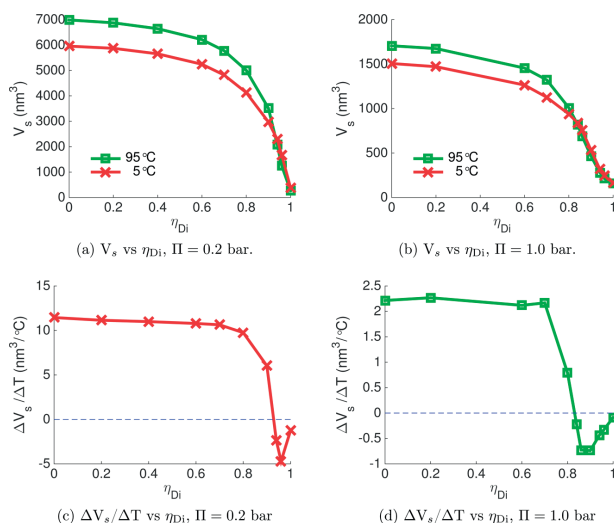


**Figure 2.** (a, b) Volume per platelet as a function of the fraction of charges that is neutralized by divalent counterions. (c, d) Difference in volume per platelet between 5 and 95 °C divided by the temperature difference as a function of  $\eta_{Di}$ . For 1 bar the crossover is found at  $\eta_{Di} \sim 0.8$ . That is, the volume per platelet is increased below  $\eta_{Di} \sim 0.8$  and reduced above  $\eta_{Di} \sim 0.8$  when the temperature is increased. For  $\Pi = 0.2$  bar the crossover is found at  $\eta_{Di} \sim 0.9$ . Because of counterion dilution at lower pressures, the crossover occurs at higher divalent content.

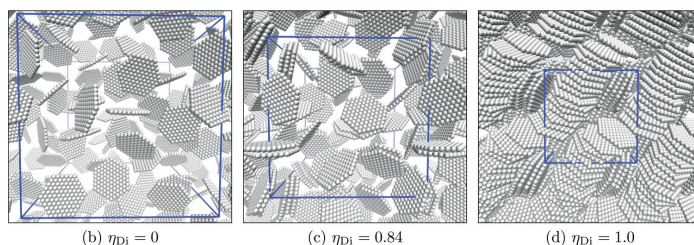
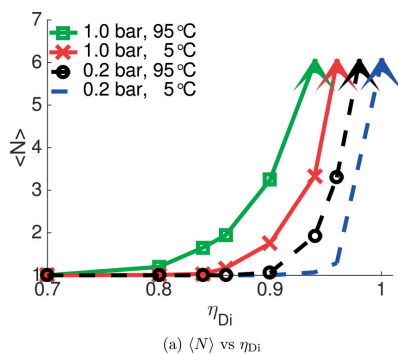


**Figure 3.** (a) The average number of platelets per tactoid, ( $N$ ), as a function of  $\eta_{Di}$  for 0.2 and 1.0 bar, respectively. The aggregation is initiated at lower fractions of divalent counterions when the temperature and/or pressure are increased. (b–d) Three configurations from the simulations for  $T = 95$  °C,  $\Pi = 1$  bar at different  $\eta_{Di}$ . The counterions are omitted due to clarity, the platelets are shown in gray, and the cubic simulation box is shown in blue (periodic images are shown outside the simulation box).

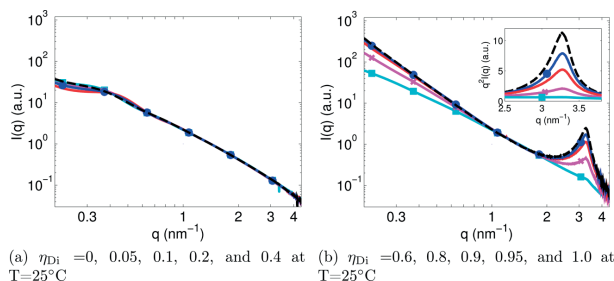


**Figure 4.** X-ray scattering intensities as a function of the scattering vector at  $T = 25\text{ }^{\circ}\text{C}$  of the  $\text{Ca}^{2+}/\text{Na}^{+}$ -montmorillonite fractions with  $\phi = 0.06$  for (a)  $\eta_{\text{Di}} = 0$  (cyan square), 0.05 (magenta cross), 0.1 (red line), 0.2 (blue circle), and 0.4 (black dashed) and, (b)  $\eta_{\text{Di}} = 0.6$  (cyan square), 0.8 (magenta cross), 0.9 (red line), 0.95 (blue circle), and 1.0 (black dashed). The scattering intensities are normalized at  $q \approx 1\text{ nm}^{-1}$ .

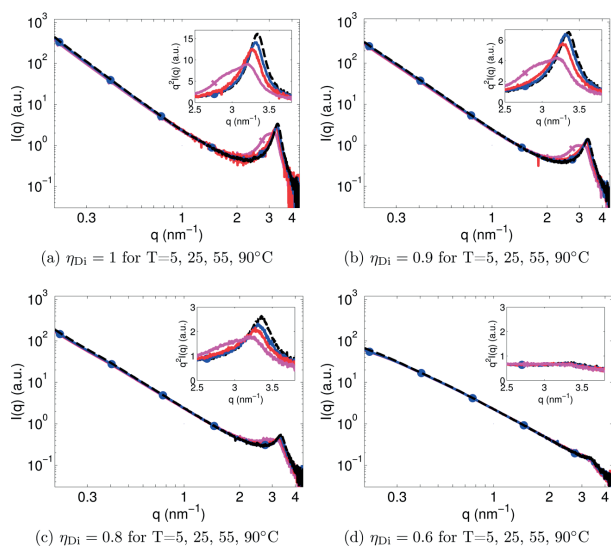


**Figure 5.** X-ray scattering intensities as a function of the scattering vector for the temperature measurements of the  $\text{Ca}^{2+}/\text{Na}^{+}$ -montmorillonite fractions with  $\phi = 0.06$  for (a)  $\eta_{\text{Di}} = 1$ , (b)  $\eta_{\text{Di}} = 0.9$ , (c)  $\eta_{\text{Di}} = 0.8$ , and (d)  $\eta_{\text{Di}} = 0.6$ . The temperatures were  $5\text{ }^{\circ}\text{C}$  (magenta cross),  $25\text{ }^{\circ}\text{C}$  (red line),  $55\text{ }^{\circ}\text{C}$  (blue circle), and  $90\text{ }^{\circ}\text{C}$  (black dashed). The inset shows the Kratky plot over a narrow  $q$ -range. The scattering intensities are normalized at  $q \approx 1\text{ nm}^{-1}$ .

$$\Delta\Pi/\Delta T = \frac{\Pi(T = 95^{\circ}\text{C}) - \Pi(T = 5^{\circ}\text{C})}{95^{\circ}\text{C} - 5^{\circ}\text{C}} \approx -60\text{ Pa}/^{\circ}\text{C}$$

which is in disagreement with the DLVO theory<sup>34,35</sup> that predicts  $\Delta\Pi/\Delta T > 0$  for both monovalent and divalent counterions. With monovalent counterions and/or low enough surface charge density of the colloids, the DLVO theory predicts the correct trend as will be shown below.

**NPT Bulk Simulations.** In Figure 2a,b the volume per platelet as a function of fraction of divalent counterions can be seen for two different temperatures at two different pressures, 0.2 and 1.0 bar. At a low fraction of divalent counterions, the entropic repulsion dominates the system and the particles prefer to be far apart, which is clearly indicated by the large

volume per platelet. At a high enough fraction of divalent counterions ( $\eta_{\text{Di}} \sim 0.8$  for  $\Pi = 1.0$  bar and  $\eta_{\text{Di}} \sim 0.9$  for  $\Pi = 0.2$  bar), the volume per platelet is decreasing rapidly, and the colloids tend to aggregate. In Figure 2c,d, the difference in volume per platelet divided by the temperature difference is shown as a function of the fraction divalent counterion charge. A crossover can be found where  $\Delta V_s/\Delta T$  changes sign from positive to negative ( $\eta_{\text{Di}} \sim 0.8$  for 1.0 bar and  $\eta_{\text{Di}} \sim 0.9$  for 0.2 bar), and hence the conclusion is that  $\Delta V_s/\Delta T$  can be chosen to be positive, negative, or kept constant by mixing counterions of different valency. Note that the volume response with temperature,  $\Delta V_s/\Delta T$ , in the NPT simulations is analogous to the osmotic pressure response,  $\Delta\Pi/\Delta T$ , in the NVT simulations. A minimum is found in the vicinity of the

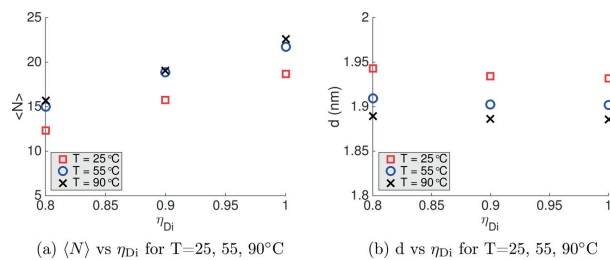


**Figure 6.** (a) Average number of platelets per tactoid,  $\langle N \rangle$ , and (b) the average distance between the platelets as a function of the fraction divalent charges neutralizing the colloids,  $\eta_{Di}$ , obtained from the temperature measurements performed with SAXS for the  $\text{Ca}^{2+}/\text{Na}^+$ -montmorillonite fractions with  $\phi = 0.06$ .

crossover where there are three effects that decreases the volume as the fraction of divalent counterions increases: (i) the single platelets form tactoids, (ii) the tactoids grow in size, and (iii) the separation between the platelets in a tactoid decreases. With 100% divalent counterions, all tactoids have aggregated at  $\Pi = 1$  bar (see Figure 3d), and the change is due to effect (iii) solely. The microstructure of the colloids is analyzed in Figure 3, where the average tactoid size is shown as a function of fraction of divalent counterions. As  $\eta_{Di}$  increases, the distance between single platelets decreases slightly (Figure 3b), and at the crossover the platelets start to aggregate into doublets and triplets (Figure 3c). The tactoids continue to grow in size, and finally, for a high enough fraction of divalent counterions and pressure ( $\eta_{Di} > 0.95$  for  $\Pi = 1$  bar), all tactoids have aggregated (Figure 3d). It should be emphasized that for  $\langle N \rangle > 6$  (indicated by the arrows) the average tactoid size cannot be calculated due to the limited size of the system, i.e., 50 platelets. The tactoid size for aggregated platelets has previously been investigated for parallel platelets with MC simulations,<sup>32</sup> and aggregates of spherical particles have been investigated with MC/MD simulations.<sup>36</sup>

**SAXS.** Scattering experiments were performed for the corresponding  $\text{Ca}^{2+}/\text{Na}^+$ -montmorillonite mixtures used in the bulk MD simulations. The scattering intensities for all mixtures at  $T = 25^\circ\text{C}$  and  $\phi_c = 0.06$  are shown in Figure 4. Bragg peaks are clearly observed for  $\eta_{Di} = 1, 0.95, 0.9$ , and  $0.8$  (Figure 4b), indicating that there are tactoids in these samples. Moreover, the fwhm of the Bragg peak is decreasing, which indicates that the tactoids are growing in size (see Figure 6a) as  $\eta_{Di}$  approaches one. For  $\eta_{Di} \leq 0.6$  (Figure 4a), all the scattering intensity curves are qualitatively equal, and no Bragg peaks are visible, indicating that the systems are dominated by repulsive interactions. Hence, the SAXS measurements are in qualitative agreement with the simulations in Figure 3 and also agree well with the study by Hedström et al.,<sup>18</sup> i.e.,  $\text{Ca}^{2+}/\text{Na}^+$ -montmorillonite with  $\sim 20\%$  sodium or more, behaves qualitatively as a  $\text{Na}^+$ -montmorillonite, whereas montmorillonite with 90% or more calcium in the interlayer behaves similar to homoionic  $\text{Ca}^{2+}$ -montmorillonite.

The scattering intensities and the Kratky plots for  $\eta_{Di} = 1, 0.9, 0.8$ , and  $0.6$  with  $\phi_c = 0.06$  at four different temperatures, 5, 25, 55, and  $90^\circ\text{C}$ , are shown in Figure 5. The positions of the Bragg peaks for  $\eta_{Di} = 1, 0.9$ , and  $0.8$  shift toward higher  $q$ -values as the temperature increases, as shown in Figure 5a–c. For  $\eta_{Di} = 0.6$  no Bragg peak is visible, indicating that there are no tactoids in the system for any of the temperatures investigated (see Figure 5d). By comparing the value of  $\langle N \rangle$  for the three

different temperatures ( $T = 25^\circ\text{C}$ ,  $T = 55^\circ\text{C}$ , and  $T = 90^\circ\text{C}$ ), it is found that there is only a small difference between 55 and  $90^\circ\text{C}$ . A larger deviation is found for  $25^\circ\text{C}$ , which can be associated with changes in the microstructure of the system. The shift toward higher  $q$ -values in the Bragg peak with temperature indicates that the average distance between the platelets decreases with an increase in temperature, from  $\sim 1.93$  to  $1.89$  nm, i.e., three water layers, for  $T = 25$ – $90^\circ\text{C}$  (see Figure 6b). At  $5^\circ\text{C}$ , the SAXS data seems to be composed by a superposition of two Bragg peaks, with an average distance of  $\sim 1.9$ – $2.1$  nm, corresponding to a combination of three and four water layers. These results are in agreement with the previous work done by Svensson and Hansen.<sup>37,38</sup>

The two trends where: (i) the spacing between the platelets in the tactoids is reducing, and (ii) the increase in number of platelets per tactoid with temperature for  $\eta_{Di} \geq 0.8$ , are found both in the simulations as well as in the experiments. Obviously, the model cannot find discrete distances between the platelets, such as three or four water layers, since the water molecules are represented as a uniform dielectric permittivity. Hence, a quantitative agreement at  $5^\circ\text{C}$  is not possible.

**Crossover for Two Parallel Surfaces.** The platelets in the bulk simulations above have a fixed surface charge density, and the crossover from positive to negative change in pressure with temperature was found to be at approximately 90% and 80% divalent counterions, for 0.2 and 1 bar, respectively (Figure 2a,b). In Figure 7 the crossover between two parallel surfaces for  $\Pi(T = 25^\circ\text{C}) = 4$  bar (eq 8) has been simulated (MC

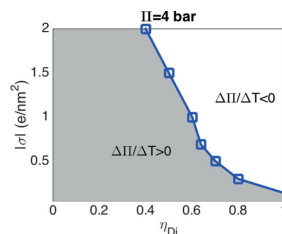


**Figure 7.** Crossover from increasing to decreasing osmotic pressure response with temperature is shown as a function of the surface charge density and the percentage of divalent counterions neutralizing the colloids. The osmotic pressure is 4 bar, and the temperature is  $25^\circ\text{C}$ . The areas left/right of the line correspond to an increased/decreased osmotic pressure with increasing temperature.

simulations) for different absolute values of the surface charge density ranging from 0.05 to 2 e/nm<sup>2</sup>. The pressure was chosen high enough to avoid any two-phase coexistence with opposite sign of  $\Delta\Pi/\Delta T$ . Furthermore, the crossover of the two parallel surfaces differs from the bulk simulations due to the exclusion of the rotational entropy, and the difference in electrostatic interaction between a small colloid and an infinite surface. The dark gray area on the left-hand side of the crossover-line corresponds to an increasing osmotic pressure with temperature, and the area on the right-hand side of the crossover-line corresponds to a decreasing osmotic pressure with temperature, as indicated in Figure 7. If  $|\sigma| < 0.2$  e/nm<sup>2</sup>, the DLVO theory is valid, even with 100% divalent counterions. As the surface charge density increases, a crossover appears, and it shifts toward a lower percentage of divalent counterions with an increased surface charge density. The latter is due to the fact that the attractive ion–ion correlations increase with increasing surface charge density.<sup>6,32</sup>

Finally, we would like to emphasize that the midplane approach is useful for understanding the importance of the different contributions to the pressure defined in eqs 7 and 8 as well as for understanding the limitations of the DLVO theory where the correlation term is neglected. In Table 2, it is shown

**Table 2. Osmotic Pressure Response from the MC Simulations<sup>a</sup>**

$\eta_{\text{Di}}$	$h_{\text{ix}}$ (nm)	$\Delta\Pi^{\text{id}}$	$\Delta\Pi^{\text{corr}}$	$\Delta\Pi$
0.6	2.6	0.69	−0.43	0.26
0.7	2.1	1.00	−0.96	0.04
0.8	1.5	2.30	−3.50	−1.20

<sup>a</sup>The osmotic pressure response,  $\Delta\Pi = \Delta\Pi^{\text{id}} + \Delta\Pi^{\text{corr}} + \Delta\Pi^{\text{coll}}$ , between 25 and 95 °C, and the main components,  $\Delta\Pi^{\text{id}}$  and  $\Delta\Pi^{\text{corr}}$ , are shown for  $|\sigma| = 0.5$  e/nm<sup>2</sup> where the osmotic pressure is 4 bar at 25 °C.

that the difference in the ideal contribution,  $\Delta\Pi^{\text{id}}$ , is found to increase with the fraction of divalent counterions mainly due to the reduced separation. Although, by taking into account the difference in the correlation contribution,  $\Delta\Pi^{\text{corr}}$ , it is found that  $\Delta\Pi/\Delta T < 0$  for  $\eta_{\text{Di}} > 0.7$ . Hence, the osmotic pressure response can be negative if the correlation difference is the leading term. The contribution  $\Delta\Pi^{\text{coll}}$  is negligible and not shown.

## CONCLUSIONS

We have shown that the electrostatic interactions alone can give a positive, negative, or constant osmotic pressure response with temperature, depending on the monovalent/divalent counterion ratio, if  $|\sigma| > 0.2$  e/nm<sup>2</sup>. The fraction of divalent counterions, where a crossover from positive to negative pressure response with temperature is found, depends on the surface charge density, the pressure (or volume fraction), and other components such as the rotational entropy and the size of the colloid. Mixtures of Ca<sup>2+</sup>-montmorillonite and Na<sup>+</sup>-montmorillonite in water were measured with SAXS at four different temperatures. It was found that Bragg peaks appear for a sodium content of ~20% or less, which indicates that tactoids exist in those compositions. As the sodium content was reduced, the number of platelets per tactoid increased. By increasing the temperature, the separation between the platelets in the tactoids decreased and the number of platelets per tactoid seems to increase slightly. For a sodium content of

~40% or more, no tactoids were found, which indicates that the interaction between the platelets are dominated by repulsive interactions. Our theoretical predictions are in good agreement with the SAXS experiments, giving a further indication that our model can explain the underlying physics. The theory presented here is general and predicts that the temperature response for all types of charged colloids can be controlled by mixing counterions of different valency if the interactions in the system are dominated by electrostatics. Even though the applied model is very simple, and only face charges are taken into consideration, we still believe that this study shed light on the fundamental physics of these systems, the formation of tactoids, and role of electrostatic interactions.

## AUTHOR INFORMATION

### Corresponding Authors

\*E-mail: axel.thuresson@teokem.lu.se (A.T.).

\*E-mail: marie.skepo@teokem.lu.se (M.S.).

### ORCID

Axel Thuresson: 0000-0001-8459-1394

### Notes

The authors declare no competing financial interest.

## ACKNOWLEDGMENTS

Computational resources were provided by the Swedish National Infrastructure for Computing (SNIC) through Lunarc, the Center for Scientific and Technical Computing at Lund University. We acknowledge Dr. T. Narayanan and Dr. J. Möller for providing assistance during measurements at ESRF. The work was performed within the framework of the Swedish national strategic e-science research program eSENCE. The Lars Hierta Memorial Foundation is greatly acknowledged for financial support.

## REFERENCES

- (1) Guldbbrand, L.; Jönsson, B.; Wennerström, H.; Linse, P. Electric double layer forces. A Monte Carlo study. *J. Chem. Phys.* **1984**, *80*, 2221–2228.
- (2) Guldbbrand, L.; Nilsson, L.; Nordenskiöld, L. A Monte Carlo simulation study of electrostatic forces between hexagonally packed DNA double helices. *J. Chem. Phys.* **1986**, *85*, 6686–6698.
- (3) Attard, P.; Kjellander, R.; Mitchell, D. J.; Jönsson, B. Electrostatic fluctuation interactions between neutral surfaces with adsorbed, mobile ions or dipoles. *J. Chem. Phys.* **1988**, *89*, 1664–1680.
- (4) Kjellander, R.; Marčelja, S. Inhomogeneous Coulomb fluids with image interactions between planar surfaces. *I. J. Chem. Phys.* **1985**, *82*, 2122–2135.
- (5) Kjellander, R.; Marčelja, S.; Pashley, R. M.; Quirk, J. P. Double-layer ion correlation forces restrict Calcium clay swelling. *J. Phys. Chem.* **1988**, *92*, 6489–6492.
- (6) Pellenq, R. J.-M.; Caillol, J. M.; Delville, A. Electrostatic attraction between two charged surfaces: A (N,V,T) Monte Carlo simulation. *J. Phys. Chem. B* **1997**, *101*, 8584–8594.
- (7) Netz, R. Electrostatics of counter-ions at and between planar charged walls: From Poisson-Boltzmann to the strong-coupling theory. *Eur. Phys. J. E: Soft Matter Biol. Phys.* **2001**, *5*, 557–574.
- (8) Jönsson, B.; Nonat, A.; Labbez, C.; Cabane, B.; Wennerström, H. Controlling the cohesion of cement paste. *Langmuir* **2005**, *21*, 9211–9221.
- (9) Mongondry, P.; Tassin, J. F. T.; Nicolai, T. Revised state diagram of Laponite dispersions. *J. Colloid Interface Sci.* **2005**, *283*, 397–405.
- (10) Mourchid, A.; Lécolier, E.; Van Damme, H.; Levitz, P. On viscoelastic, birefringent, and swelling properties of Laponite clay suspensions: Revisited phase diagram. *Langmuir* **1998**, *14*, 4718–4723.

- (11) Pignon, F.; Magnin, A.; Piau, J.-M.; Cabane, B.; Lindner, P.; Diat, O. Yield stress thixotropic clay suspension: Investigations of structure by light, neutron, and X-ray scattering. *Phys. Rev. E: Stat. Phys., Plasmas, Fluids, Relat. Interdiscip. Top.* **1997**, *56*, 3281.
- (12) Blackmore, A. V.; Warkentin, B. P. Swelling of calcium montmorillonite. *Nature* **1960**, *186*, 823–824.
- (13) Jönsson, B.; Wennerström, H. *Electrostatic Effects in Soft Matter and Biophysics*; Springer: Netherlands, 2001; pp 171–204.
- (14) Karnland, O.; Olsson, S.; Nilsson, U.; Sellin, P. Experimentally determined swelling pressures and geochemical interactions of compacted Wyoming bentonite with highly alkaline solutions. *Phys. Chem. Earth, Parts A/B/C* **2007**, *32*, 275–286.
- (15) Banin, A. Tactoid formation in montmorillonite: effect on ion exchange kinetics. *Science* **1967**, *155*, 71–72.
- (16) Meunier, A. *Clays*; Springer Science & Business Media: 2005.
- (17) Shalkevich, A.; Stradner, A.; Bhat, S. K.; Muller, F.; Schurtenberger, P. Cluster, glass, and gel formation and viscoelastic phase separation in aqueous clay suspensions. *Langmuir* **2007**, *23*, 3570–3580.
- (18) Hedström, M.; Birgersson, M.; Nilsson, U.; Karnland, O. Role of cation mixing in the sol formation of Ca/Na-montmorillonite. *Phys. Chem. Earth, PT A/B/C* **2011**, *36*, 1564–1571.
- (19) Segad, M.; Jönsson, B.; Åkesson, T.; Cabane, B. Ca/Na montmorillonite: Structure, forces and swelling properties. *Langmuir* **2010**, *26*, 5782–5790.
- (20) Thuresson, A.; Karnland, O.; Jönsson, B. Anomalous temperature behavior in clay swelling due to ion-ion correlations. *EPL* **2016**, *114*, 38002.
- (21) Birgersson, M.; Karnland, O.; Nilsson, U. Freezing of bentonite. Experimental studies and theoretical considerations. SKB Technical Report, 2010; TR-10-40, 1-1.
- (22) Karnland, O.; Olsson, S.; Nilsson, U. Mineralogy and sealing properties of various bentonites and smectite-rich clay materials. SKB Technical Report, 2006; TR-06-30, 1-1.
- (23) Michot, L. J.; Bihannic, I.; Porsch, K.; Maddi, S.; Baravian, C.; Mougel, J.; Levitz, P. Phase diagrams of Wyoming Na-montmorillonite clay. Influence of particle anisotropy. *Langmuir* **2004**, *20*, 10829–10837.
- (24) Segad, M.; Jönsson, B.; Cabane, B. Tactoid formation in montmorillonite. *J. Phys. Chem. C* **2012**, *116*, 25425–25433.
- (25) van Vaerenbergh, P.; Léonardon, J.; Sztucki, M.; Boesecke, P.; Gorini, J.; Claustre, L.; Sever, F.; Morse, J.; Narayanan, T. An upgrade beamline for combined wide, and ultra and ultra -angle X-ray scattering at the ESRF. *AIP Conf. Proc.* **2015**, *1741*, 030034.
- (26) Sztucki, M. (2011) SAXSutilities download page: <http://www.sztucki.de/SAXSutilities>, (accessed Mar 2017).
- (27) Segad, M.; Hanski, S.; Olsson, U.; Ruokolainen, J.; Åkesson, T.; Jönsson, B. Microstructural and swelling properties of Ca and Na montmorillonite: (In situ) Observations with Cryo-TEM and SAXS. *J. Phys. Chem. C* **2012**, *116*, 7596–7601.
- (28) Segad, M. Microstructure determination of IQ-WB clays: a direct procedure by small-angle X-ray scattering. *J. Appl. Crystallogr.* **2013**, *46*, 1316–1322.
- (29) Thuresson, A.; Ullner, M.; Turesson, M. Interaction and aggregation of charged platelets in electrolyte solutions: A coarse-graining approach. *J. Phys. Chem. B* **2014**, *118*, 7405–7413.
- (30) Malmberg, C. G.; Maryott, A. A. Dielectric constant of water from 0° to 100° C. *J. Res. Nat. Bureau Stand* **1956**, *56*, 1–8.
- (31) Abraham, M.; van der Spoel, D.; Lindahl, E.; Hess, B. the GROMACS development team, GROMACS User Manual version 5.0.1, 2014.
- (32) Thuresson, A.; Ullner, M.; Åkesson, T.; Labbez, C.; Jönsson, B. Monte Carlo simulations of parallel charged platelets as an approach to tactoid formation in clay. *Langmuir* **2013**, *29*, 9216–9223.
- (33) Turesson, M.; Forsman, J.; Åkesson, T.; Jönsson, B. Simulation of phase equilibria in lamellar surfactant systems. *Langmuir* **2004**, *20*, 5123–5126.
- (34) Derjaguin, B. V.; Landau, L. Theory of the stability of strongly charged lyophobic sols and of the adhesion of strongly charged particles in solutions of electrolytes. *Acta Phys. Chim. URSS* **1941**, *14*, 633–662.
- (35) Verwey, E. J. W.; Overbeek, J. T. G. *Theory of the Stability of Lyophobic Colloids*; Elsevier Publishing Company Inc.: Amsterdam, 1948.
- (36) Linse, P.; Lobaskin, V. Electrostatic attraction and phase separation in solutions of like-charged colloidal particles. *J. Chem. Phys.* **2000**, *112*, 3917–3927.
- (37) Svensson, P. D.; Hansen, S. Combined salt and temperature impact on montmorillonite hydration. *Clays Clay Miner.* **2013**, *61*, 328–341.
- (38) Svensson, P. D. Ph.D. Thesis, Lund University, Lund, Sweden, 2015.



ISBN 978-91-7422-522-8 (print)  
ISBN 978-91-7422-523-5 (pdf)

Theoretical Chemistry  
Department of Chemistry  
Lund University